Doris Prieling

Computational investigation of liquid film flow on rotating disks

---

Thesis

submitted to
Graz University of Technology

in partial fulfillment of the requirements for the degree of
Doctor of Engineering Sciences

Graz, March 2013

Deutsche Fassung:
Beschluss der Curricula-Kommission für Bachelor-, Master- und Diplomstudien vom 10.11.2008
Genehmigung des Senates am 1.12.2008

EIDESSTATTLICHE ERKLÄRUNG

Ich erkläre an Eides statt, dass ich die vorliegende Arbeit selbstständig verfasst, andere als die angegebenen Quellen/Hilfsmittel nicht benutzt, und die den benutzten Quellen wörtlich und inhaltlich entnommenen Stellen als solche kenntlich gemacht habe.

Graz, am ……. ……..
(Unterschrift)

Englische Fassung:

STATUTORY DECLARATION

I declare that I have authored this thesis independently, that I have not used other than the declared sources / resources, and that I have explicitly marked all material which has been quoted either literally or by content from the used sources.

……. ……..
date (signature)

I would like to dedicate this thesis to Bine & Amy.

My old grandmother always used to say, summer friends will meltaway like summer snows, but winter friends are friends forever.
- George R.R. Martin

ACKNOWLEDGEMENTS

I would like to thank everyone who supported me during my studies and in writing this thesis, in particular, my research supervisor Prof. Helfried Steiner for his patient guidance, assistance, and enthusiastic encouragement.
Moreover, I would like to show my gratitude to Prof. Günter Brenn for his advice and useful critiques of this research work. My grateful thanks are also extended to the second referee, Prof. Hendrik Kuhlmann, for scientific support and several constructive comments.
The research presented in this thesis has been carried out at the Institute of Fluid Mechanics and Heat Transfer at Graz University of Technology in cooperation with Lam Research AG. I am obliged to many of my colleagues from the institute who supported me and boosted me morally, in particular, Christian Walchshofer, Erich Wimmer, Klaus Czaputa, Daniel Heidorn, Tania García-Libreros, Nikolett Kiss, Bernd Langensteiner, Emil Baric, and Carole Planchette. I would also like to thank all the members of staff at the ISW, in particular, Prof. Walter Meile and Sabine Gruber.
I like to express greatest thanks to Markus Junk, Felix Staudegger, Frank Ludwig Holsteyns, and Harald Okorn-Schmidt from Lam Research AG for their support and the fruitful discussions on the various aspects and issues of the research project. I owe sincere and earnest thankfulness to various colleagues from other institutions, who delivered valuable information for this project, in particular, Bernhard Gschaider and Petr Vita from ICE Strömungsforschung GmbH.

I would like to gratefully acknowledge the financial support from the Austrian Research Promotion Agency FFG (ModSim-program) and the industrial parter Lam Research AG.

Finally I am truly thankful to my parents, my granny, my sister Astrid, my friends, and Sabine for their ongoing encouragement, their friendship and their love.

Doris Prieling

Graz, March 2013

KURZFASSUNG

Spinning-Disk-Apparate spielen eine bedeutende Rolle in einer Vielzahl von industriellen Anwendungen. Das Ziel der vorliegenden Arbeit ist die rechnerische Untersuchung der Geschwindigkeits-, Temperatur- und Konzentrationsfelder innerhalb Zentrifugalkraft getriebener Dünnfilmströmungen auf rotierenden Siliziumplatten. Da der Rechenzeitaufwand einer vollaufgelösten direkten numerischen Simulation der Strömung untragbar hoch ist, wird in der vorliegenden Arbeit eine Näherungslösung, die auf der Dünnfilmapproximation und dem von Kármán-Pohlhausen Verfahren basiert, als rechnerisch effiziente Alternative verwendet. Die Ergebnisse dieser Näherungslösung wurden mit experimentellen Daten, sowie mit numerischen Ergebnissen von achsensymmetrischen CFD Simulationen verglichen, wobei eine gute Gesamtübereinstimmung gefunden wurde. Vereinfachte Modelle für das nasschemische Ätzen in den Grenzfällen reaktions- sowie diffusionskontrollierter chemischer Prozesse, basierend auf der lokalen Temperaturverteilung, sowie dem lokalen Stofftransport des Hauptreaktanden, werden eingeführt. Die Ergebnisse dieser Näherungsmodelle sind in guter Übereinstimmung mit experimentellen Ätzabträgen.

ABSTRACT

Spinning disk devices are commonly used in a wide variety of industrial applications. The objective of the present work is to analyze computationally the hydrodynamic, thermal and species mass transfer characteristics of thin film flow on rotating disks, which is radially driven by the centrifugal forces. As a fully resolved three-dimensional direct numerical simulation of the flow is associated with prohibitively high computational costs, an integral boundary layer (IBL) approximation, which represents a computationally less costly alternative approach, is used. The results obtained with the IBL model are compared against experimental data as well as against numerical predictions from an axisymmetric CFD analysis using the Volume-of-Fluid method, where a very good overall agreement is observed. Simplified models for surface etching in the limit of reaction and diffusion controlled chemistry are introduced on top of the temperature distribution across the disk, and the mass transport of the primary etchant component, respectively. The predictions of these simplified models are compared against experimental results showing good agreement.

CONTENTS

Abstract **xi**

List of Symbols **xv**

Acronyms **xxi**

List of Figures **xxiii**

List of Tables **xxix**

1 Introduction **1**
1.1 Motivation 1
1.2 Review of previous work 4
1.2.1 Falling liquid films 4
1.2.2 Rotating films 8
1.3 Objectives of the present work 20
1.4 Structure of the thesis 21

2 Mathematical modeling and approximate solutions **23**
2.1 Governing equations 23
2.1.1 Conservation of mass 24
2.1.2 Conservation of momentum 25
2.1.3 Conservation of thermal energy 28
2.1.4 Non-dimensionalization of the governing equations 29
2.2 Thin film approximation 34
2.2.1 Governing equations and boundary conditions 34
2.2.2 Far field asymptotic solution for $Ek \gg 1$ 37
2.3 Integral boundary layer approximation 42
2.3.1 IBL approximation for hydrodynamics 42
2.3.2 IBL approximation for heat transfer 46
2.3.3 IBL approximation for species mass transfer 48
2.3.4 Steady-state smooth film solutions 51
2.4 Modeling wet chemical surface etching 61
2.4.1 Reaction controlled chemistry ($Da \ll 1$) 62
2.4.2 Diffusion controlled chemistry ($Da \gg 1$) 63

3 Numerical solutions **65**
3.1 Numerical solution of the Navier-Stokes equations 65
3.1.1 Finite Volume Method 65
3.1.2 Volume of Fluid Method 67
3.1.3 Setup 68
3.2 Numerical solution of the integral boundary layer equations 69
3.2.1 Hyperbolic systems 70
3.2.2 Numerical solution of hyperbolic PDE systems 74
3.2.3 Setup 80

4 Results and discussion **83**
4.1 Steady-state solutions 83
4.1.1 Hydrodynamics 84
4.1.2 Heat transfer 92
4.1.3 Species mass transfer 94
4.2 Effect of wavy flow 104
4.2.1 Hydrodynamics 104
4.2.2 Heat transfer 113
4.2.3 Species mass transfer 120
4.3 Validation against experiments 134
4.3.1 Small Ekman numbers 134
4.3.2 Large Ekman numbers 138

5 Conclusions and recommendations for further work **149**

Appendices **153**
1 Divergence (Gauss's) theorem 155
2 Relations and profile parameters for the IBL model 155
2.1 Quadratic approximation 155
2.2 Quartic approximation 156
3 Second-order polynomial ansatz function for the species mass fraction . . 157
4 IBL approximation for three-dimensional film flow 159

Bibliography **163**

LIST OF SYMBOLS

Roman symbols

A	prefactor in Arrhenius equation	$\mathrm{m/s}$
a	thermal diffusivity	$\mathrm{m^2/s}$
a_w	profile shape parameter	-
$b_{1,2}$	profil constants	-
C	parameter	-
c	species mass fraction, $c = \tilde{c}/c_i$	-
c_p	specific heat capacity	J/(kg K)
D	molecular diffusivity	$\mathrm{m^2/s}$
Da	Damköhler number	-
E_a	activation energy	$\mathrm{J/mol}$
Ek	Ekman number	-
Fr	Froude number	-
g	gravitational acceleration	$\mathrm{m/s^2}$
H	heater power	W
k	velocity of chemical reaction	$\mathrm{m/s}$
$k_{a,b,c}$	profile constants	-

$\hat{k}$	empirical proportionality constant	-
Le	Lewis number	-
l_0	characteristic radial length scale	m
M	molar mass	$\mathrm{kg/mol}$
n	speed of revolution, 1 rpm$\widehat{=}2\pi/60$ rad/s	rpm
Nu	Nusselt number	-
p	dimensionless pressure, $p = \tilde{p}/p_0$	-
Pr	Prandtl number	-
p_0	characteristic pressure scale	Pa
Q	volumetric flowrate	$\mathrm{m^3/s}$
q	heat flux	$\mathrm{W/m^2}$
r	dimensionless radial coordinate, $r = \tilde{r}/l_0$	-
Re	Reynolds number	-
R_g	molar gas constant	$\mathrm{J/(mol\,K)}$
Ro	Rossby number	-
Sc	Schmidt number	-
Sh	Sherwood number	-
t	dimensionless time, $t = \tilde{t}/t_0$	-
T	temperature	K
t_0	characteristic time scale	s
u	dimensionless radial velocity component, $u = \tilde{u}/u_0$	-

u_0	characteristic radial velocity scale	$\mathrm{m/s}$
v	dimensionless azimuthal velocity component, v=$\tilde{v}/u_0$	-
w	dimensionless vertical velocity component, $w = \tilde{w}/w_0$	-
W^{-1}	reduced inverse Weber number	-
w_0	characteristic axial velocity scale	$\mathrm{m/s}$
$\vec{x}$	position vector	
Δz_{etch}	etching abrasion	m
z	dimensionless vertical coordinate, $z = \tilde{z}/\delta_0$	-

Greek symbols

α	heat transfer coefficient	$\mathrm{W/(m^2K)}$
χ	volume viscosity	Pa s
δ	dimensionless film thickness, $\delta = \tilde{\delta}/\delta_0$	-
$\delta_{r,\phi}$	dimensionless boundary layer thickness of radial and azimuthal velocities	-
δ_T	dimensionless boundary layer thickness of temperature	-
δ_c	dimensionless boundary layer thickness of species mass fraction	-
δ_0	characteristic vertical length scale	m
ϵ	aspect ratio	-
γ	VoF phase marker function	-
κ	profile shape parameter	-
λ	thermal conductivity	W/(m K)
μ	dynamic viscosity	Pa s

ν	kinematic viscosity	m^2/s
Ω	angular speed	rad/s
ϕ	dimensionless azimuthal coordinate	-
π	ratio of circumference of circle to its diameter	-
ρ	density	kg/m^3
σ	surface tension	N/m
θ	dimensionless temperature	-
φ	general tensorial physical quantity	
ζ	vertical coordinate normalized with the film thickness	-

Subscripts

a	ambient
$chem$	chemical reaction
D	disk
δ	free surface
$diff$	diffusive mass transport
$etch$	wet chemical surface etching
G	gas
i	inflow
L	liquid
max	maximum
n	dispenser nozzle

0	reference quantity
w	wall

Superscripts and operators

$\overline{()}$	depth-average
$\tilde{()}$	dimensional quantity
$\gamma(a,x)$	incomplete gamma function
$\Gamma(a)$	Euler gamma function
$\mathcal{M}(a,b,c)$	confluent hypergeometric function
$\mathcal{H}(x)$	unit step function with argument x
∇	nabla operator
$\langle\rangle$	time-average
$\mathcal{D}_{1,2}$	total directional derivative
$()^T$	transpose
$\vec{()}$	vector

ACRONYMS

BLA	boundary layer assumption
CFD	computational fluid dynamics
DFA	developed film assumption
DNS	direct numerical simulation
IBL	integral boundary layer
IVP	initial value problem
LHS	left hand side
ODE	ordinary differential equation
PDE	partial differential equation
RHS	right hand side
VoF	volume-of-fluid
WRIBL	weighted-residual integral-boundary-layer

LIST OF FIGURES

1.1 Thin film flow driven by (a) gravity and (b) centrifugal acceleration. . . . 1
1.2 Spin Processor, Lam Research AG. 2
1.3 Waves encountered on a spinning disk using a high-speed camera. 3
1.4 Instantaneous film thickness profile as obtained by Woods. 11
1.5 Measurements of the film thickness (Burns et al.). 12
1.6 Temperature vs. radial distance. Exp. Staudegger. 16
1.7 Etching rate profiles for various rotational speeds (Staudegger et al.). . . . 17

2.1 Fluid material control volume. 23
2.2 Schematics of a spinning disk device. 30
2.3 Sketch of the radial development of the boundary layers of the radial velocity, azimuthal velocity, temperature, and species mass fraction, δ_r, δ_ϕ, δ_T, and δ_c, respectively. 57
2.4 Scope of boundary layer assumption (BLA) and developed film assumption (DFA). 61
2.5 Schematic representation of main rate limiting mechanisms involved in wet chemical etching. 62

3.1 Computational domain and boundary conditions. 68
3.2 Sketch of the characteristics of the linear advection equation for a characteristic speed $a > 0$ in the $x - t$ plane. 72
3.3 Sketch of the solution structure of a linear Riemann problem with $m = 5$ waves. 73
3.4 Sketch of the values of the solution in different sectors of a Riemann problem with $m = 3$ waves. 74
3.5 Piecewise constant distribution of a cell averaged state variable. 76
3.6 Initial conditions for the film thickness and position of the inflow boundary r_i for the numerical solution of the unsteady IBL equations (a) including heat transfer, (b) including species mass transfer. 80

4.1 Solutions of the steady-state IBL equations for the case C1 together with the asymptotic solutions in the radially inner and outer regions. 85
4.2 Ekman number $Ek = \nu/\Omega\tilde{\delta}^2$ vs. radial distance for the case C1. 86
4.3 Influence of the dimensionless parameter ϵFr^{-1}. Film thickness vs. radial distance obtained from the steady-state smooth film IBL model. 87

4.4 Results for a sub- and a supercritical value of ϵFr^{-1} together with asymptotic solutions for the radially inner and outer regions obtained from the steady-state smooth film IBL model. 88
4.5 Steady-state smooth film IBL predictions for the case C1 using alternatively the quadratic and quartic polynomials for the radial velocity component. 90
4.6 Influence of the two different profile assumptions in the steady-state IBL approximation for the case C1. 91
4.7 Steady-state IBL predictions for the film thickness using the developed film assumption (DFA) and the boundary layer assumption (BLA) for the case C1. 92
4.8 IBL predictions for the case C2 assuming steady-state smooth film conditions, $Pr = 7$. 93
4.9 Dimensionless wall temperature vs. radial distance. Effect of convective heat transport between the liquid surface and the ambient air for the case C2 (T_a=25 °C) assuming cooling conditions with q_w=-5500 W/m^2. . . . 95
4.10 Steady-state IBL solutions for the case C3 including results for the solid-liquid mass transfer in a binary mixture, $Sc = 1196$. 97
4.11 Local Sherwood number for the case C3, $Sc = 1196$. 98
4.12 Evaluation of second-order (dashed-dotted) and third-order (solid line) c-profile assumptions for the case C3. Film thickness and thickness of individual boundary layers. 99
4.13 Depth-averaged mean species mass fraction vs. radial distance. Steady-state IBL predictions and analytical far-field solutions for the case C3. . . 100
4.14 Profile assumptions for species mass fraction for the case C3. IBL predictions using the second and third-order polynomial ansatz functions vs. analytical far-field solutions. 101
4.15 Steady-state IBL results for film thickness, thickness of individual boundary layers and depth-averaged species mass fraction for varying Schmidt numbers. 102
4.16 Instantaneous profiles of the film thickness for the case C1. 104
4.17 Time-averaged radial variation of the film thickness for the case C1. . . . 105
4.18 Time-averaged wall shear rates for the case C1. 106
4.19 Instantaneous profiles of the radial velocity component at different radial positions inside a single wave for the case C1. 107
4.20 Instantaneous profiles of the radial velocity component at different radial positions inside a single wave for the case C1. 108
4.21 Instantaneous profiles of the film thickness and the depth-averaged radial and azimuthal velocity components obtained by the unsteady IBL model for the case C1. 110
4.22 Instantaneous profiles of the film thickness, the radial surface velocity and the local wall shear rate for the case C1. 111

4.23 IBL predictions for the case C2. Temporal evolution of film thickness and radial velocity at $r = 3$. Dashed horizontal lines: time-averaged predictions of unsteady IBL model. Dotted horizontal lines: steady-state smooth film IBL predictions. 112
4.24 CFD results for the case C2. Temporal evolution of film thickness and depth-averaged radial velocity at $r = 3$. Dashed horizontal lines: time-averaged predictions of unsteady IBL model. Dotted horizontal lines: steady-state smooth film IBL predictions. 113
4.25 Time-averaged IBL predictions and 2D CFD results for the case C2, (a) film thickness vs. radial distance, (b) wall temperature vs. radial distance. 115
4.26 Temporal evolution of film thickness, depth-averaged radial velocity, and depth-averaged temperature at $r = 3$ for the case C2. Dashed horizontal lines: time-averaged predictions of unsteady IBL model. Dotted horizontal lines: steady-state smooth film IBL predictions. 116
4.27 Instantaneous profiles of the radial (red), azimuthal (blue) and vertical (green) velocity components together with the dimensionless temperature profiles (black) at selected instants of time inside a single wave at $r = 2.8$. The dashed lines refer to IBL predictions, the solid lines to CFD results. . 118
4.28 Instantaneous profiles of the radial (red), azimuthal (blue) and vertical (green) velocity components together with the dimensionless temperature profiles (black) at selected instants of time inside a single wave at $r = 2.8$. The dashed lines refer to IBL predictions, the solid lines to CFD results. . 119
4.29 Instantaneous film and concentration boundary layer thickness (black lines) together with the corresponding time-averages (red lines) for the case C3. 121
4.30 Time-averaged results for the film thickness, the surface species mass fraction, and the Sherwood number for the case C3. 122
4.31 Evolution of the film height, the surface velocity, and the Sherwood number at $r = 2.11$. Vertical dashed lines indicate selected instants of time. . . 124
4.32 Instantaneous profiles of the radial, azimuthal, and vertical velocity components together with the species mass fraction profile at selected instants of time inside a single wave at $r = 2.11$ for the case C3. The dashed-dotted lines refer to the results of the unsteady IBL model, the solid lines to the simulated profiles of the CFD, and the dashed lines refer to the polynomial profile functions evaluated with the CFD results as input. 125
4.33 Instantaneous profiles of the radial, azimuthal, and vertical velocity components together with the species mass fraction profile at selected instants of time inside a single wave at $r = 2.11$ for the case C3. The dashed-dotted lines refer to the results of the unsteady IBL model, the solid lines to the simulated profiles of the CFD, and the dashed lines refer to the polynomial profile functions evaluated with the CFD results as input. 126
4.34 Evolution of the film height, the surface velocity, and the Sherwood number at $r = 2.82$. Vertical dashed lines indicate selected instants of time. . . 128

4.35 Instantaneous profiles of the radial, azimuthal, and vertical velocity components together with the species mass fraction profile at selected instants of time inside a single wave at $r = 2.82$ for the case C3. The dashed-dotted lines refer to the results of the unsteady IBL model, the solid lines to the simulated profiles of the CFD, and the dashed lines refer to the polynomial profile functions evaluated with the CFD results as input. 129
4.36 Instantaneous profiles of the radial, azimuthal, and vertical velocity components together with the species mass fraction profile at selected instants of time inside a single wave at $r = 2.82$ for the case C3. The dashed-dotted lines refer to the results of the unsteady IBL model, the solid lines to the simulated profiles of the CFD, and the dashed lines refer to the polynomial profile functions evaluated with the CFD results as input. 130
4.37 (a)-(b): Evolution of film height at $r = 4.23$. The vertical dashed line indicates the selected instant of time.
(c)-(d): Instantaneous profiles of the radial, azimuthal, and vertical velocity components together with the species mass fraction profile at the selected instant of time inside a single wave at $r = 4.23$ for the case C3. The dashed-dotted lines refer to the results of the unsteady IBL model, the solid lines to the simulated profiles of the CFD, and the dashed lines refer to the polynomial profile functions evaluated with the CFD results as input. . . . 131
4.38 Results of unsteady IBL model using a quasi-steady kinematic boundary condition for the species mass transport. 132
4.39 Radial variation of the film thickness predicted by unsteady IBL model. Case E1, experimental data from Thomas et al.. 135
4.40 Nusselt number vs. radial distance for the case E2, IBL predictions compared against experimental data of Ozar et al. and numerical results of Rice et al., (a) 100 rpm, (b) 200 rpm. 137
4.41 Etching rate vs. radial distance for the case E3, IBL predictions compared against experimental data of Kaneko et al., (a) 100 rpm, (b) 200 rpm. . . . 139
4.42 IBL results for the radial variation of the film thickness, the thickness of the concentration boundary layer, and the depth-averaged species mass fraction for the case E3(b) with n=200 rpm. 140
4.43 IBL predictions and CFD results for the time-averaged film thickness for the case C1. Experimental data from Burns et al.. 141
4.44 Time and depth-averaged temperature vs. radial distance for the case C2. Experimental results from Staudegger. 142
4.45 Etching abrasion vs. radial distance for the case C2. Experimental results from Staudegger. 142
4.46 Radial variation of time-averaged etching rates and of the Ekman number for the case C3. 144
4.47 Radial variation of time-averaged etching rates. Exps. Staudegger et al. . . 145
4.48 Radial variation of time-averaged etching rates. Exps. Staudegger et al. . . 146

4.49 Steady-state IBL predictions for the etching rate compared against experimental data of Staudegger et al. 146
4.50 Solution of unsteady IBL model using quasi-steady "frozen-wave" kinematic boundary condition. 147

LIST OF TABLES

2.1 Profile constants for the IBL approximation of the momentum equations. . 45
2.2 Free-stream values imposed at upper boundary $z = \delta_m$ when using the boundary layer assumption (BLA) for the central impingement region. . . 59

3.1 Properties of liquids considered in the CFD simulations. 69

4.1 Considered test cases for steady-state smooth film and for wavy flow conditions. 83
4.2 Considered cases with small Ekman numbers. 134
4.3 Considered cases with large Ekman numbers. 140

1 INTRODUCTION

1.1 Motivation

Thin liquid films are encountered in a wide range of technical devices. They are also met in everyday life in the flow along a window or the windshield of a car. Thin film flow is also observed in a number of natural phenomena, as for example in lava flows, snow avalanches, and gravity currents. They are part of the general class of free boundary and interfacial flows and have received considerable attention over the past decades. Numerous technological applications are based on thin film flow, including for example distillation, water desalinization, blood oxygenation, coating, heat pumps and chemical reactors. Especially for heat and mass transfer applications thin liquid films are of great interest, since they provide a big potential for high heat and mass transfer rates on large substrates. In most cases thin liquid films are either driven by gravity or by centrifugal forces. An example of both types is shown in Fig. 1.1.
Thin film flows which are driven by the centrifugal forces are of high relevance in a variety of industrial applications. The machinery essentially uses spinning disk devices, which allow to control the film thickness by the rotational speed producing very thin liquid layers. The key benefits of these devices include strongly increased heat and mass transfer rates on the rotating surface, and furthermore, they offer the possibility of a cost-saving reduction of the working liquid.

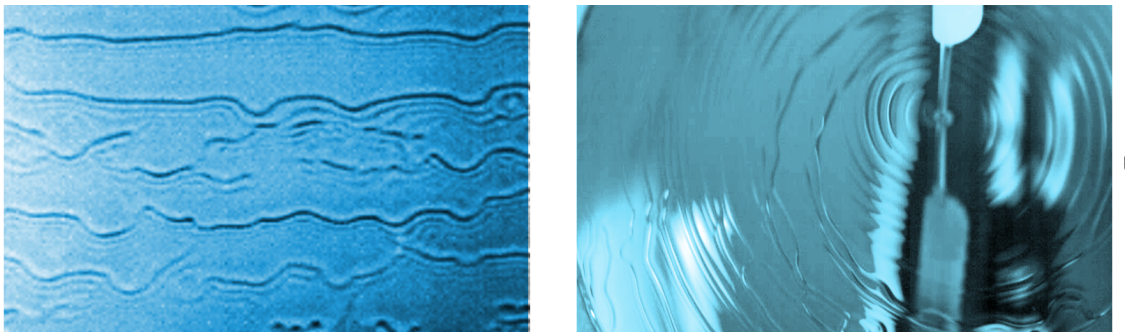

(a) Falling film. Exps. by Park and Nosoko [1]

(b) Thin film flow on a spinning disk. Exps. [2]

Figure 1.1: Thin film flow driven by (a) gravity and (b) centrifugal acceleration.

In the semiconductor industry a spinning-disk device, as the one sketched in Fig. 1.2, is used for the surface preparation of silicon wafers. To increase the efficiency of the device, the consumption of working liquid has to be kept as small as possible, while at the same time a continuous wetting of the surface has to be guaranteed to achieve uniform process results. Besides cleaning, which is one of the major tasks of the spin processor, the wet chemical etching represents a further important application. For this dissolution process of the surface of the wafer two asymptotic regimes, associated with very fast and very slow chemistry, respectively, can be distinguished. For an optimization of the surface etching process in either case a detailed analysis of the thin film flow and the associated heat and mass transfer rates is required.

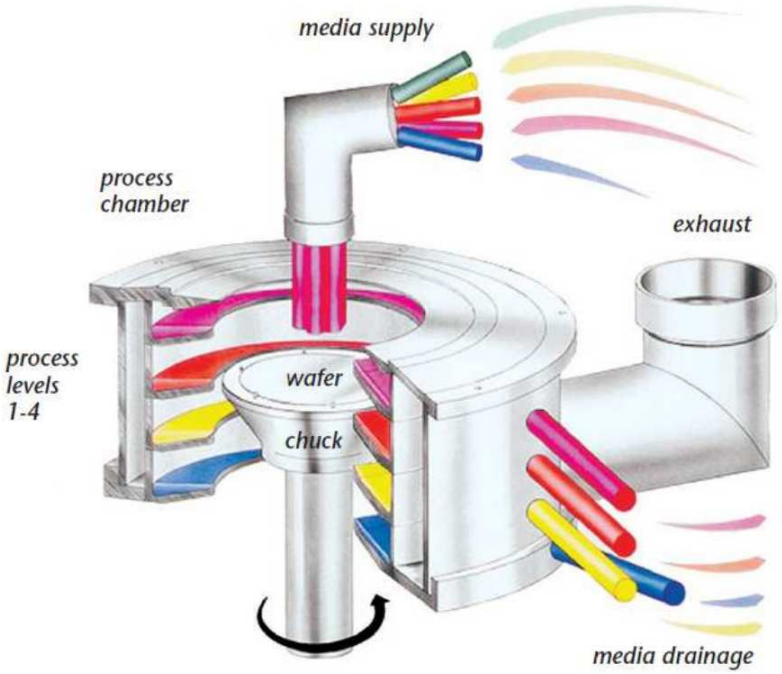

Figure 1.2: Spin Processor, Lam Research AG.

Due to the exceedingly high spatial resolution requirements, which arise from the thin film nature of the flow, resulting in a large disparity between the two governing length scales in the radial and vertical directions, a fully resolved numerical simulation is unfeasible. The spatial resolution requirements are further increased by including heat and mass transfer, as in this case the small thermal and molecular diffusivities, associated with large Prandtl and Schmidt numbers, respectively, eventually result in thin temperature and concentration boundary layers.

The complex physics which governs the flow results in a variously shaped free surface. Fig. 1.3 depicts the effect of an increase of the volumetric flowrate Q on the topology of the free surface. For moderate flow rates large scale wave structures can be observed in the radially outer region, see Fig. 1.3a. As the volumetric flowrate is increased, these large scale structures tend to break up into small-scale, three-dimensional wave structures, see Figs. 1.3b-1.3c. This highly irregular free surface, associated with complex wave dynamics, additionally challenges any numerical simulation of the flow.

(a) Q=0.36 lpm (b) Q=0.6 lpm (c) Q=1.2 lpm

Figure 1.3: Waves encountered on a spinning disk using a high-speed camera (2000 fps) considering a constant revolution speed of n=200 rpm and water as working liquid. Exps. [2].

The present work attempts to analyze computationally the wavy thin film flow and the associated heat and mass transfer characteristics on a spinning disk in order to describe and to investigate the salient features of the process of wet chemical surface etching in two asymptotic regimes, associated with very fast and very slow chemistry.

1.2 Review of previous work

Due to their high technical relevance and the complexity of the wave dynamics of the free surface flow, thin film flows have been and are still subject of numerous specific papers and scientific monographs (e.g. Chang and Demekhin [3], Kalliadasis et al. [4]). Comprehensive reviews on the dynamics of thin liquid films were presented by Oron et al. [5] and Craster and Matar [6].
While thin films driven by centrifugal forces are attracting increasingly attention in various engineering applications, due to the fact that the film thickness can be controlled by the rotational speed, historically, most effort has been put into analyzing thin liquid films flowing under the action of gravity. For these films, which are falling down a vertical wall or an inclined plane, a wide variety of waves was found and classified in various experimental studies. Typical flow quantities, such as the thickness of the liquid film, have been measured and the stability of the flow was analyzed. The modeling efforts of falling films can be basically divided in mathematical models for systems with negligible and significant inertia, resulting in a lubrication approximation for the former, and an integral boundary layer (IBL) approximation for the latter case.
Thin film flows driven by centrifugal acceleration bear in many aspects close resemblance to the falling film problem and many of the typical flow features apply to both cases. Therefore, for the sake of completeness, the present review starts with a section on falling liquid films, before it continues with thin liquid films driven by centrifugal forces.

1.2.1 Falling liquid films

In 1916 Nusselt [7] presented a steady-state base solution to the Navier-Stokes equations for a thin liquid film falling under the influence of gravity. This mathematically simple solution, which is essentially represented by a semi-parabolic streamwise velocity profile, is often referred to as Nusselt flat-film solution. In real falling liquid films flow instabilities in general produce a wide variety of surface waves, as first analyzed experimentally by Kapitza and Kapitza [8]. In a first analytical attempt to analyze the wave dynamics, the linear stability of the Nusselt flat-film solution to small perturbations was studied by several authors (e.g., Benjamin [9], Yih [10]). Applying a classical Orr-Sommerfeld linear stability analysis, the film was found to be unstable to long-wavelength disturbances above a critical Reynolds number Re_{crit}, due to inertial forces. The waves at the inception of the instability were found to travel with twice the interface velocity. Benjamin [9] found the critical Reynolds number to be

$$Re_{crit} = \frac{5}{6}\cot(\theta)\,, \tag{1.1}$$

with θ denoting the angle of inclination of the substrate. This correlation was confirmed in experiments by Binnie [11, 12], whereas the experimental findings of Tailby and Portalski

[13] on the stability of the film did not agree with Eq. (1.1). Wave inception on falling films was shown to be a convective instability (Joo and Davis [14], Cheng and Chang [15]). Disturbances at the inlet are convected downstream, where they are amplified and trigger secondary instabilities. The linear theory is therefore only applicable in the inception region. Additionally, the wave dynamics can be supposed to be very sensitive to upstream flow noise, which is often hard to control.
The extension of the stability analysis to the nonlinear regime was initiated by Benney [16], who presented a single evolution equation for the film thickness, known as Benney equation. For small Reynolds numbers this equation describes the onset of waves correctly, but it fails in practically relevant settings with moderate Reynolds numbers, since it assumes only a weak influence of inertia, which is on the other hand the key instability mechanism. In the limit of small amplitudes the Benney equation can be further reduced to an equation known as Kuramoto-Sivashinsky equation. This type of equation is often found in nonlinear long-wave simplifications of the Navier-Stokes equations, and it has been extensively studied. So it was considered by Chang [17] and Yang [18] to analyze traveling waves on falling films.
For practically relevant cases from moderate to high Reynolds numbers, a method based on a combination of the boundary-layer theory and the von Kármán-Pohlhausen integral approximation has been widely used (Kapitza [19], Shkadov [20]). This approach, often referred to as Shkadov model, leads to a coupled system of nonlinear hyperbolic partial differential equations for the film thickness and the instantaneous local flowrate. The system of equations is solved for the depth-averaged flow variables assuming polynomial profiles for the velocity variation inside the film. Wilkes and Nedderman [21] and Portalski [22] experimentally found that the streamwise velocity profile can be approximated reasonably well by a second-order polynomial, even inside a wavy film.
The equations of the Shkadov model are often referred to as integral-boundary-layer (IBL) equations. The solution of this nonlinear system of hyperbolic partial differential equations, is basically non-unique. This implies that for a fixed wave frequency and fixed process parameters several sets of solutions can exist. These sets of solutions are called wave families. The solutions in one family are categorized by the phase velocity and the height of the wave peak. The different wave families were analyzed by Shkadov [20], Bunov et al. [23] and Sisoev and Shkadov [24]. Sisoev and Shkadov [25, 26] also introduced the concept of dominating waves. These are attracting wave regimes, which are most likely to be realized, independently of the initial conditions. The dominating waves were also shown to be the waves with the greatest velocity and the largest peak height in a family. Applying the concept of dominating waves, the predictions of the Shkadov model were in good agreement with the experimental results of Alekseenko et al. [27].
An improvement to the Shkadov model was presented in the work of Ruyer-Quil and Manneville [28, 29]. They proposed a refined model for the flow inside the film by applying the method of weighted residuals to expand the streamwise velocity field on a polynomial basis. Scheid et al. [30] carried out numerical simulations for a two-dimensional formulation of this improved model in order to obtain solutions for three-dimensional film

flow. In a comparison against results from a direct numerical simulation by Salamon et al. [31], very good agreement for several traveling-wave families was found. Malamataris et al. [32] found in a direct numerical simulation (DNS) of the Navier-Stokes equations significant deviations from a semi-parabolic shape, especially in the vicinity of large solitary waves. The weighted-residual integral-boundary-layer (WRIBL) model was proven as capable to reproduce even such velocity profiles. The numerical results of the WRIBL model were also compared against experimental results of Liu and Gollub [33], Liu et al. [34], Alekseenko et al. [27, 35] and Park and Nosoko [1]. Good qualitative agreement was found and typical features, like herringbone and horseshoe shaped structures, could be reproduced.

Direct numerical simulations of the Navier-Stokes equations were considered by a number of researchers to analyze the falling film problem without any model assumptions on the velocity distributions inside the liquid. Malamataris et al. [36] and Salamon et al. [31] applied this computationally demanding approach and solved the governing set of equations numerically with a finite-element method. In these studies, similar to the numerical study carried out by Jayanti and Hewitt [37], the upper boundary condition was imposed at the interface, so that the ambient air was not part of the solution. Gao et al. [38] carried out a direct numerical simulation of the Navier-Stokes equations using the volume-of-fluid (VoF) method. They imposed a periodic forcing at the inlet to reproduce the experimentally observed wave structures. Small amplitude waves with sinusoidal-shape and a wave velocity in close agreement with the experimental observations of Kapitza [39] were found. For the large amplitude waves, the experimentally observed tendency of these waves to inherit the forcing frequency (Nosoko et al. [40]) was confirmed. Recirculation zones were found inside very large amplitude waves, located inside a confined region beneath the peak of the surface. The velocity profiles inside the liquid film were analyzed and a good overall agreement with the semi-parabolic analytical velocity profile was found in regions of the wave crests and slopes. In the wave troughs, however, where capillary ripples precede the large amplitude waves, significant deviations from the semi-parabolic velocity profiles were found. In this region also the pressure variation was found to be largest, as the strong variation of the surface curvature translates into a strong variation of the capillary pressure.

Heat and mass transfer in falling films

Heat and mass transfer in falling films was also studied with considerable interest. A detailed review on modeling advances was, for example, presented by Yih [41]. Kapitza [39] proposed an approximate model to predict transfer coefficients in a wavy film to account for the experimentally observed intensifying effect of wavy flow on the transfer characteristics. The decrease of the average film thickness due to waviness of the surface was found to provide a substantial contribution to the intensification of the heat and mass transfer rates. Other modeling efforts were rather based on constant film thickness assumptions,

which include an empirically determined eddy diffusivity to account for the intensified transfer due to the waviness.
Experimental investigations dealing with the heat transfer in falling liquid films (see, e.g. Kirkbride [42], Chun and Seban [43]) indicated an increase of the heat transfer coefficient over the steady-state Nusselt prediction. Hirshburg and Florschuetz [44, 45] used an integral method to model the wavy thin film flow and the associated heat transfer based on the semi-parabolic Nusselt profile and a linear approximation for the temperature profile. The results were found to be in good agreement with experimental data. In the numerical study of Miyara [46] the effect of local film thinning together with a convection effect of circulation flow in large amplitude waves was found to be responsible for the enhancement of the heat transfer coefficient in a falling wavy liquid film.
As for the mass transfer especially the gas-liquid mass transfer across the film surface has received considerable attention. Emmert and Pigford [47] experimentally observed an enhancement of about a factor of 2.5 for the absorption of CO_2 by water, as compared against theoretical predictions using the flat-film solution for the flow field. Solutions from an approximate model, in which a Kapitza-type velocity distribution was used to solve the convection-diffusion equation (e.g. Ruckenstein and Berbente [48]), predicted enhanced transfer rates, but the obtained magnitude of the mass transfer coefficient was still smaller than the experimentally observed magnitude. Wasden and Dukler [49] used a semi-empirical model, in which the flow solution is constructed from experimental data, to solve the diffusion equation in a coordinate system moving with the wave. The results for the absorption rates were in good agreement with the experimental findings. Sisoev et al. [50] modeled the gas absorption process in the presence of regular waves, by utilizing the dominating wave solution to solve a two-dimensional convection-diffusion equation. A number of studies were also concerned with the solid-liquid mass transfer rates at the wetted substrate. Hirose et al. [51] analyzed the dissolution of solid material from the substrate under laminar flow conditions experimentally and analytically. Analytical solutions were obtained by introducing the semi-parabolic Nusselt flat-film profile for the streamwise velocity component. They found, that in the smooth regions of the flow, the predictions of the steady-flow model matched the experimental results well. For wavy flow an enhancement in the solid-liquid mass transfer process was found and the reduction of the mean film thickness was identified as main reason for this enhancement. Brauner and Moalem-Maron [52] observed by means of simultaneous measurements of the instantaneous film thickness and the local transfer rate, a close correlation between the motion of the waves and the local mass transfer. In the same study, the major enhancement effect was found to be due to the large amplitude waves, where the transfer rates reached a local maximum beneath the propagating front of the wave.

1.2.2 Rotating films

Thin films driven by centrifugal forces bear resemblance to the problem of falling films in many aspects. The main differences, which exacerbate the modeling of these flows, arise from the radially varying acceleration and the presence of the Coriolis force. To characterize the flow it is therefore useful to consider the Rossby number Ro and the Ekman number Ek, which rate the importance of the Coriolis force relative to the inertial and viscous forces, respectively. As shown by Rauscher et al. [53] at large radii $\tilde{r}$, where the thickness of the liquid film $\tilde{\delta}$ is sufficiently small, an asymptotic solution can be found in terms of a series expansion of the Navier-Stokes equations. In the asymptotic limit of large radii the radial momentum equation is essentially governed by the balance of the centrifugal and viscous forces. This balance can be written as

$$\mathcal{O}\left(\Omega^2\tilde{r}\right) \sim \mathcal{O}\left(\nu\frac{Q}{2\pi\tilde{r}\tilde{\delta}^3}\right), \tag{1.2}$$

involving the volumetric flowrate Q and the kinematic viscosity ν of the fluid. It then follows that

$$\frac{\nu Q}{2\pi\Omega^2\tilde{r}^2\tilde{\delta}^3} \sim \mathcal{O}\left(1\right), \tag{1.3}$$

which can be rewritten as the product of the local Ekman and the Rossby numbers

$$\underbrace{\left(\frac{\nu}{\Omega\tilde{\delta}^2}\right)}_{Ek}\underbrace{\left(\frac{Q/2\pi\tilde{r}\tilde{\delta}}{\tilde{r}\Omega}\right)}_{Ro} \sim \mathcal{O}\left(1\right). \tag{1.4}$$

Since the inertial forces become insignificant at very small Rossby numbers, $Ro \ll 1$, the neglect of the inertial forces in the asymptotic limit, requires a sufficiently high Ekman number, so that

$$Ek \cdot Ro \sim \mathcal{O}\left(1\right) \tag{1.5}$$

is satisfied. It immediately follows that the more the Ekman number exceeds unity the less effect have the inertial forces. At the same time, being defined as the ratio of the viscous forces to the Coriolis forces, a large Ekman number implies negligibly small Coriolis forces.
From Eq. (1.4) it follows that the film thickness at large radii is proportional to

$$\tilde{\delta} \propto \left(\frac{1}{2\pi}\frac{Q\nu}{\Omega^2\tilde{r}^2}\right)^{1/3}. \tag{1.6}$$

In this asymptotic limit, the centrifugal force term is driving the radial motion equivalently the gravitational force term in the Nusselt flat-film solution for falling liquid films.

Based on the order of magnitude of the convective terms, which are $\mathcal{O}\left(Ro^2\right)$ relative to the leading order centrifugal term, and a length scale in vertical direction defined as

$$\delta_0 = \left(\frac{\nu}{\Omega}\right)^{1/2}, \tag{1.7}$$

Rauscher et al. [53] suggested to introduce

$$l_0 = \left(\frac{9Q^2}{4\pi^2\nu\Omega}\right)^{1/4} \tag{1.8}$$

for the characteristic radial length scale.

Experimental work

Experimental investigations on rotating films were mostly dedicated to the classification of different wave regimes and measurements of the local film thickness. The film thickness measurements were carried out using either mechanical, optical or electrical measurement techniques.

Espig and Hoyle [54] carried out the first systematic experimental investigation, utilizing a needle probe method. They reported four different flow types, including uniformly smooth film flow, flow with concentric waves, and flow with helical waves. For wavy flow the maximum film thickness, corresponding to the amplitudes of the waves, was found to be up to 40% higher than the film height predicted by the Nusselt flat-film analogon, which is proportional to Eq. (1.6) with the constant of proportionality given as $3^{1/3}$. This flat-film analogon was shown to represent the asymptotic solution of the boundary-layer equations in the limit of small Rossby numbers, $Ro \ll 1$, (Aroesty et al. [55]).
Leshev and Peev [56] measured the film thickness using alternatively water or glycerol-water solutions to investigate the validity of the asymptotic solution. While the maximum film thickness for water was found to be significantly higher than predicted by the asymptotic solution, there were only slight deviations for the higher viscous liquids, suggesting an attenuation of the waviness due to an increase of the viscosity.

While most mechanical methods constrain the film thickness measurements to the peak height of the waves, optical or electrical methods allow to obtain the time-averaged mean film thickness. Charwat et al. [57] used an infrared-absorption technique to measure the local mean film thickness of water, a water-glycerin solution, and a number of alcohols on a rotating a disk made of optical glass. The measured film thickness was found to be significantly lower than predicted by the asymptotic smooth-film solution. The smooth-film predictions exceeded the experimental results with a maximum deviation up to 50%.

Based on their experimental data Charwat et al. [57] modified the exponent as well as the pre-factor of the asymptotic smooth-film solution to obtain the correlation

$$\frac{\tilde{\delta}}{\tilde{r}} = 1.6 \left(\frac{Q\nu}{\Omega^2 \tilde{r}^5} \right)^{0.4}, \tag{1.9}$$

which provides the best fit to their film thickness measurements. Based on qualitative observations they further distinguished three wave regimes, with concentric waves, spiral waves, and irregular, wedge-like wavelets. Waveless flow was found only for small volumetric flowrates and low rotational speeds. The speed of the concentric waves was found to be a factor of 1.7-2.8 faster than the surface velocity of the smooth-film flow. The peak height of the waves was found to be up to 50% higher than the local mean film thickness.

Woods [58] measured the intensity of light that passed through a dye impregnated water film. This optical method allows for accurate measurements of the instantaneous shape of the wavy surface, see e.g., Fig. 1.4. The scaling used in Fig. 1.4 is based on the definitions (1.7) and (1.8), introduced as $\tilde{r} = r l_0$, and $\tilde{\delta} = \delta \delta_0$, as suggested by Rauscher et al. [53]. The observed waves were classified as two- or three-dimensional, and the peak height of the waves was found to be very large, with a maximum of about four times the local mean film thickness. This maximum occurred at a radial transition point, where the two-dimensional waves broke up into three-dimensional wavelets.
Ozar et al. [59] utilized the reflection of laser-light from the free surface to determine the location of the liquid-air interface. The inflow conditions were controlled by a co-rotating collar with fixed height and length. A local maximum in the film height was observed and identified as hydraulic jump. The radial position of the hydraulic jump was observed to depend on the rotational speed and a Reynolds number, which was defined using the initial velocity of the liquid and the height of the film at the exit of the collar as velocity and length scales, respectively. Three flow-regions were distinguished: an inner, inertia-dominated region, a transition region and a rotation-dominated outer region. Wavy flow with increasing wave amplitudes was observed with increasing Reynolds number.
Thomas et al. [60] considered a similar experimental setup. The local mean film thickness was measured using a capacitance technique. They observed wavy flow, in the super- and subcritical regions, before and after the hydraulic jump, respectively.

A non-intrusive technique was also used by Miyasaka [61], who focused on the radially inner flow region. In his experiments the change in the electrical resistance of a glycerin-solution was utilized to measure the film thickness with an accuracy of $\pm$ 0.01 mm. The same measurement principle was utilized by Muzhilko et al. [62], who found the mean film thickness in the radially outer region to be about 20% less than predicted by the asymptotic smooth-film solution.

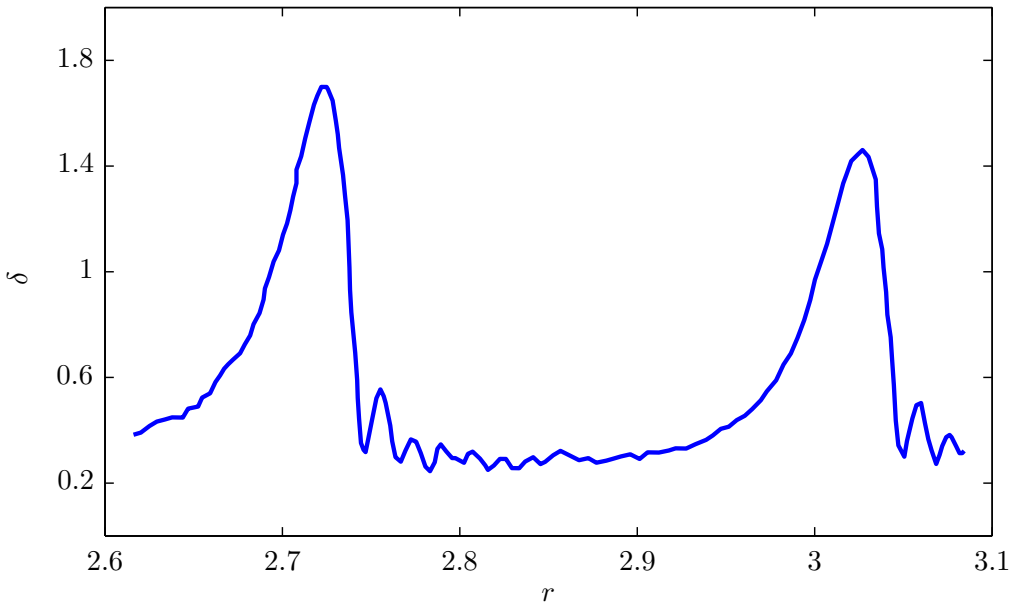

Figure 1.4: Instantaneous film thickness profile as obtained by Woods [58].
Operating conditions Q=0.78 lpm, n=400 rpm and ν=1 $\times$ 10^{-6} m^2/s.

Leneweit et al. [63] measured the velocity of the free surface. The film thickness was evaluated by assuming, that the radial and azimuthal components of the velocity agree to the leading order terms with the asymptotic smooth-film solution. They investigated the evolution of spiral waves triggered by local perturbations at the entrance of the liquid. For low flowrates, the wave velocity was found to be about twice the local surface velocity, which is in accordance with predictions from the linear stability theory.
Lim [64] used a microdensiometer technique to measure the local mean film thickness. It was found to be about 20% less than predicted by the asymptotic smooth-film solution and correlated in terms of two dimensionless groups.

Burns et al. [65] measured the time-averaged film thickness by utilizing the fact, that the film thickness is inverse proportional to the electrical resistance. The film thickness measurements were carried out for four different liquids and the results were found to be on average about 9% less than predicted by the asymptotic smooth-film solution. Three zones were identified, based on the occurrence of turning points in the radial velocity profile: an injection zone, an acceleration zone, and a synchronized zone. An estimate for the radial extensions of the two inner, inertia dominated zones was proposed as well. In Fig. 1.5 the experimental results of Burns et al. [65] are compared against the leading order term of the asymptotic solution, using the scaling quantities suggested by Rauscher et al. [53]. These results illustrate the typical observations from experimental studies in which the local mean

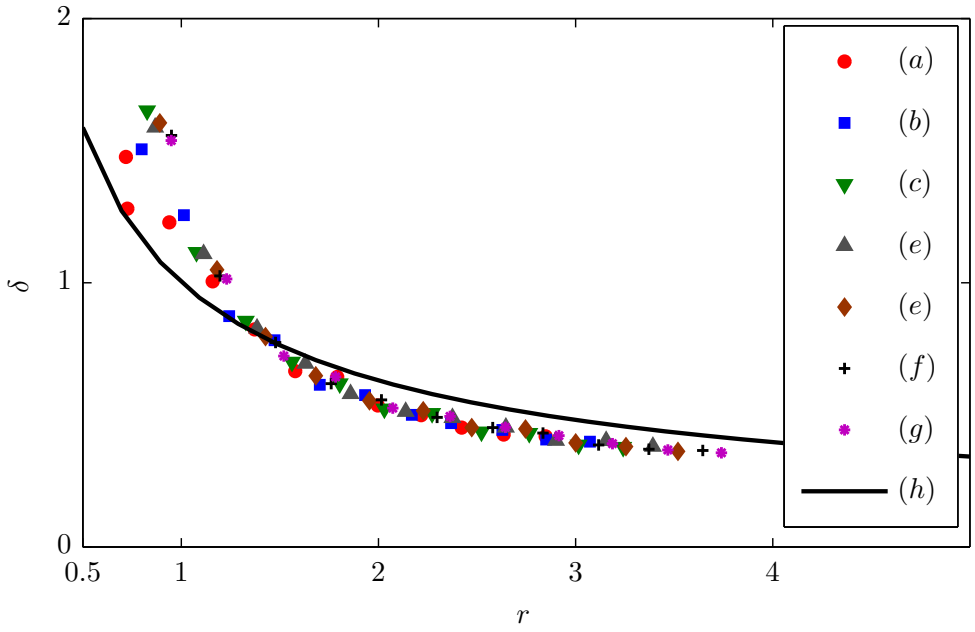

Figure 1.5: Measurements of the film thickness by Burns et al. [65] for Q=1.80 lpm, ν=1.3 $\times$ 10^{-6} m^2/s and (a) n=296 rpm, (b) n=401.1 rpm, (c) n=496.6 rpm, (d) n=601.6 rpm, (e) n=697.1 rpm, (f) n=802.1 rpm, (g) n=987.6 rpm, (h) leading-order term of asymptotic solution.

film thickness was analyzed. In the radially inner region, inertial effects dominate and the asymptotic solution is not valid. In the radially outer region the waviness of the film leads to a lower local mean film thickness than predicted by the asymptotic far-field solution.

Numerical studies of rotating films

There exist only a few studies in which the film flow on the rotating disk is investigated by performing detailed numerical simulations of the governing Navier-Stokes equations. Rice et al. [66] carried out a DNS assuming an axisymmetric flow field on an Eulerian mesh using the VoF method to track the evolution of the two-phase flow field. They compared their results for the film thickness against the experimental results of Thomas et al. [60] and Ozar et al. [59], where satisfactory agreement was found for the first, while overpredicted film heights were found for the latter.
Rahman and Faghri [67] used a curvilinear boundary-fitted coordinate system for the numerical calculation of the three-dimensional flow in a pie-shaped slice of the disk. In their approach the free surface is used as an upper boundary of the computational domain, and therefore the ambient gas was not part of the solution. In a comparison against experimen-

tal data of Thomas et al. [60] a satisfactory agreement was found. The profiles of the radial velocity component were assessed as well and found to be approximately semi-parabolic. Alike in the numerical study of Rice et al. [66], no waves were apparent, which is in contrast to the experimental findings.

Kaneko et al. [68] performed an axisymmetric simulation using the VoF method to analyze the flow on a spinning disk. They also included species transport in a binary mixture to model the diffusion controlled process of wet chemical etching of silicon wafers. The computational fluid dynamics (CFD) study was complemented by experiments, and the numerical predictions were found to be in good agreement with the experimentally observed etching rates.

Approximate models for rotating films

The mathematical modeling of films which are driven by centrifugal forces is closely related to that of falling films. The concepts for providing approximate solutions for both types of flow is therefore often based on the same methodologies. This affinity becomes obvious in the asymptotic solution of the boundary layer equations for large values of the radius. Applying the perturbation method using the dimensionless radius $r = \tilde{r}/l_0$ as expansion parameter, the leading order term of the radial velocity component resembles the Nusselt smooth-film solution (Aroesty et al. [55]) with g replaced by $\Omega^2\tilde{r}$.
Rauscher et al. [53] analyzed axisymmetric film flow on a spinning disk using an asymptotic expansion in terms of r of the full Navier-Stokes equations, imposing free-surface boundary conditions on the liquid-gas interface. This series expansion yielded leading zeroth-order terms of $\mathcal{O}\left(r^{-1/3}\right)$ for the radial component of the velocity, which are identical to the smooth-film solution derived by Aroesty et al. [55].
Needham and Merkin [69] used the method of matched asymptotic expansions and found that the asymptotic structure of the steady-state solution consists of an inner and an outer region. In the inner region there is a rapid adjustment from the inlet conditions to the thin film regime, which can cause an increase of the film thickness. In the radially outer region, the film thickness is continuously decreasing. A linear stability analysis for the outer region led to an instability criterion similar to the one obtained for the falling film problem by Benjamin [9], cf. Eq. (1.1),

$$Re_{crit} = \frac{5}{6}, \tag{1.10}$$

with a critical Reynolds number for the rotating film defined as $Re_{crit} = (Q\Omega^2)/(2\pi g\nu)$. In this stability analysis the effect of surface tension was neglected.
An analytical model for the linear stability of the rotating film was also presented by Charwat et al. [57]. In this model, which is only valid for large values of the radius and

small wave numbers, the largest amplification factors were obtained for axisymmetric perturbations, and the Coriolis force was shown to exert a stabilizing influence.
Myers and Lombe [70] analyzed the applicability of the lubrication approximation to the rotating thin film flow. They showed, that in the framework of the lubrication approximation, which is based on the assumption that inertial forces are negligible, also the contributions from the Coriolis force will be negligible, since both terms appear in the radial momentum equation with the same order of magnitude. When applying the lubrication approximation (e.g. Emslie et al. [71], Momoniat and Mason [72]), a typical feature of the rotating thin film flow is therefore omitted.

In most practically relevant settings and experimental studies the Ekman number is not large, so that the Coriolis force has to be considered. The theoretical analysis of rotating films with finite Ekman numbers is mostly based on the thin film approximation, which leads to boundary-layer-type equations. Steady-state solutions of these boundary-layer equations were obtained numerically by Dorfman [73].

In a more popular approach, the IBL approximation, which essentially relies on the methodology of the Shkadov falling-film model, is extended to the rotating disk problem. Accordingly, the von Kármán-Pohlhausen integral approximation is used to reduce the dimensionality of the problem. This method, which was for example considered by Miyasaka [61], leads to a coupled system of nonlinear hyperbolic partial differential equations for the film thickness and the radial- and azimuthal flowrates. The reduction of the dimensionality of the problem via depth-averaging requires assumptions for the profiles of the radial- and azimuthal velocity components. A popular choice for the profile of the radial velocity component is a semi-parabola (e.g. Sisoev et al. [74]). This choice is motivated by the dominating balance between the viscous and the centrifugal forces at large radii, where a parabolic velocity profile is analytically obtained, but it has also a number of shortcomings in the inner region. In the analysis of Kim and Kim [75] a quartic profile is therefore considered instead, as this fourth-order polynomial properly accounts for the effect of inertia in the radially inner region. Due to the better representation of the inertial forces in the radially inner region the results obtained using the IBL approximation with quartic velocity profiles are generally in better agreement with results from numerical simulations of the full Navier-Stokes equations, than the results obtained with an IBL approximation using a parabolic radial velocity profile. Sisoev et al. [74] and Kim and Kim [75] furthermore carried out a linear stability analysis of the IBL equations and found the wave lengths, phase velocities, and amplification factors to be in good agreement with results obtained from an eigenvalue analysis of the linearized Navier-Stokes problem, which was carried out in the work of Sisoev and Shkadov [76]. The stability analysis results obtained using the IBL approximation with quartic velocity profiles (Kim and Kim [75]) also included the effect of surface tension, and were in better agreement with the results from the Navier-Stokes equations than those of Sisoev et al. [74]. For large radii and zero surface tension the insta-

bility criterion of Needham and Merkin [69], see Eq. (1.10), was reproduced. Moreover, the leading order terms of a series expansion in r of the IBL equations for large radii were shown to be nearly identical to the leading order terms of the asymptotic expansion of the full Navier-Stokes equations.
In the limit of large Ekman numbers, i.e. negligible Coriolis forces, the IBL equations for the rotating disk problem reduce to those of the falling film (Shkadov [77]). Therefore, Sisoev et al. [78] considered in a first attempt the regular wave solutions of the falling film problem to model waves on a rotating disk. The fairly good agreement of these quasi-steady periodic waves with experimental data of Woods [58] motivated an extension of the regular wave model to finite Ekman numbers. In this extended model (Sisoev et al. [74]) a proper scaling allowed a further truncation of the IBL equations yielding localized versions of the IBL equations, where the flow is assumed to be locally homogeneous. A linear stability analysis of the localized IBL equations provided amplification factors, phase velocities and unstable wavelengths, which were close to results from the linearized Navier-Stokes problem. It was therefore concluded, that the truncated equations comprise adequately the features of the full problem. In order to obtain non-linear travelling wave solutions for the truncated IBL equations, a corresponding non-linear eigenvalue problem was solved. The dominating waves were compared against experimental data of Woods [58], where a very good quantitative and qualitative agreement was found. The stabilizing influence of the Coriolis force in the axisymmetric wave regime was confirmed.
Matar et al. [79] demonstrated that transient numerical solutions of the full IBL equations exhibit finite-amplitude waves, whose wave structure is similar to the periodic, quasi-steady wave solutions from the bifurcation analysis of the localized model. Large amplitude waves, separated by long flat-film regions were observed. Furthermore they observed a coincidence between the maxima of the depth-averaged radial flow rates and the minima of the depth-averaged azimuthal flowrates, so that the resulting Coriolis forces can effectively exert a stabilizing influence on the flow. Due to this retarding effect of the Coriolis force, waves on falling films travel faster than waves on rotating films. Furthermore it was shown, that with increasing effect of inertia the flow becomes more unstable.

Heat and mass transfer in rotating films

Experimental work

A number of experimental investigations were carried out with the focus on the heat and mass transfer in thin liquid films on rotating disks.
Among these studies are the work of Ozar et al. [80], who proposed a correlation for the local Nusselt number. Aoune and Ramshaw [81] studied the local heat transfer rates between the disk and the film. High heat transfer coefficients were found in the radially inner region, which was supposed to be a thermal entrance effect. Also in the radially outer region the heat transfer coefficients were found to be significantly higher than predicted by a simplified Nusselt smooth-film analysis.

Staudegger [82] measured the radial variation of the liquid temperature and of the etching abrasion of a silicon-dioxide layer covering the solid surface of the rotating disk. Convective cooling at the downside of the disk was realized in these experiments with a stream of nitrogen as coolant medium. As can be observed from Fig. 1.6 a notable cooling of the liquid etchant was found for increasing radii. Assuming a mainly temperature dependent chemistry as it is applicable in the asymptotic limit of reaction controlled etching, the results for the temperature translate directly into predictions for the etching abrasion. An appropriate computational model to predict heat transfer in the liquid film will therefore be of high relevance for industrial chemical surface etching applications.

Aoune and Ramshaw [81] analyzed in their study the liquid-gas mass transfer characteristics between the liquid surface and the ambient gas as well. The mass transfer coefficient was found to depend mainly on the rotational speed, while there was only a weak dependence on the flowrate, and on the radial position. The authors observed an enhancement of the heat and mass transfer rates in case of wavy flow.
Lim [64] analyzed the absorption of oxygen into water and presented a correlation for the Sherwood number. An increase in the mass transfer coefficient was observed to be related to the wave dynamics of the unsteady flow.

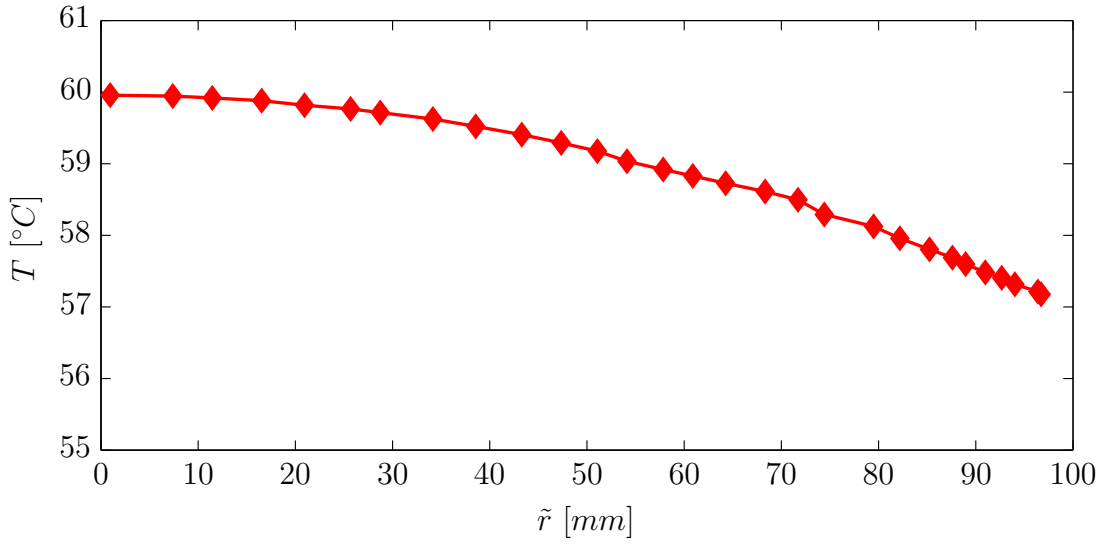

Figure 1.6: Temperature vs. radial distance. Exp. Staudegger [82], operating conditions Q=1.0 lpm, n=500 rpm and $\nu = 1 \times 10^{-6}$ m^2/s.

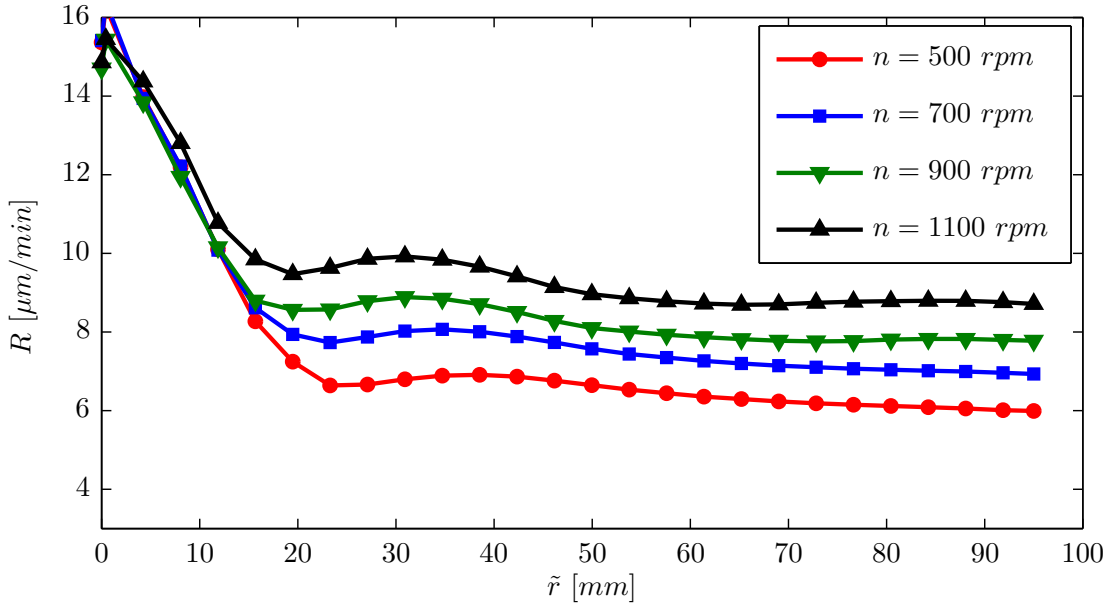

Figure 1.7: Etching rate profiles for various rotational speeds as obtained by Staudegger et al. [85]. Q=0.95 lpm and ν=2.87 $\times$ 10^{-6} m^2/s.

The solid-liquid mass transfer on the disk was experimentally analyzed by Burns and Jachuck [83], who utilized the limiting current technique for the process of copper deposition on a spinning disk. They observed an increase of the mass transfer coefficient in case of wavy flow, which is in contrast to the experimental findings of Peev et al. [84]. In the latter study the dissolution of a rotating gypsum disk was analyzed and the waviness of the liquid film was found to show no significant influence on the solid-liquid mass transfer process.

Staudegger et al. [85] and Kaneko et al. [68] analyzed the etching activity of an aqueous solution, consisting of nitric and hydrofluoric acid, flowing over a rotating silicon disk. This process is of high relevance for the semiconductor industry, where it is used for the thinning of silicon wafers, allowing for silicon chips with reduced thickness. As the chemical etching of silicon is mainly controlled by the convection-dominated mass transfer of the primary etchant component from the bulk liquid to the surface of the silicon wafer, it is essentially determined by the convection based solid-liquid mass transfer coefficient.
Fig. 1.7 shows typical etching rate profiles for various rotational speeds as obtained by Staudegger et al. [85]. The largest etching rates are observed at the center of the disk, corresponding to the stagnation region of the impinging liquid jet. In this region the etching rates are observed to be nearly unaffected by the rotational speed. Radially further downstream a local maximum, with a radial position depending on the rotational speed,

was observed. At larger radii the etching rates decrease. For the higher rotational speeds the etching rates in the radially outer region show a constant or even slightly increasing behavior. Staudegger et al. [85] additionally analyzed the influence of an increase of the volumetric flowrate and different etchant temperatures on the etching rates. It was found that an increase of the rotational speed, as well as an increase of the volumetric flowrate and an increase of the etchant temperature led in general to higher etching rates. A qualitative correlation between the observed etching rates and the corresponding approximate radial velocity profiles was obtained by considering an approximate two-parameter model for the steady-state smooth-film flow over the rotating disk.

Theoretical and computational work

Most previous theoretical work on the heat and mass transfer characteristics of the thin film flow on a spinning disk is based on the steady-state smooth-film solution of the flow field in the asymptotic limit of large radii.

Aoune and Ramshaw [81] extended the Nusselt solution obtained for the film condensation in a falling film (Nusselt [7]) to the rotating film problem. The predictions of this simplified model were compared against their experimental data. For highly viscous liquids the experimental results for the heat transfer were in satisfactory agreement with the predictions from the simplified Nusselt analysis. Significant deviations were observed, when water was used as liquid, suggesting an attenuation of the waviness due to an increase of the viscosity. Additionally, the penetration model of Higbie (Higbie [86]) was applied, to predict the liquid-gas mass transfer coefficient. Using this simple model the magnitude of the experimentally obtained mass transfer coefficient was significantly underpredicted.

Basu and Cetegen [87] applied a thin film approximation combined with the von Kármán-Pohlhausen method to analyze the thermal characteristics of a heated film flow, assuming alternatively a constant disk temperature, as well as a constant heat flux as thermal boundary condition on the surface of the rotating disk. They did not account for the influence of the Coriolis force, as the momentum equation in azimuthal direction was not considered. The thermal entry length was neglected as well. Their obtained steady-state results exhibit decreasing Nusselt numbers with increasing radii and a comparison against experimental results of Ozar et al. [80] and numerical results of Rice et al. [66] showed reasonable agreement in the radially outer region.

Peev et al. [84] applied a method, known as method of Leveque (see, e.g., Bird et al. [88]), to analyze the solid-liquid mass transfer coefficient. In this method, which was also utilized by Burns et al. [83], the concentration boundary layer is assumed to be very thin, implying

a very large Schmidt number, so that the profile of the radial velocity inside this thin layer is approximately linear. The resulting simplified convection-diffusion equation can then be solved analytically in terms of Gamma functions. The predictions of this approximate diffusion model were compared against the experimental results of Peev et al. [84], as well as against the experimental results of Burns et al. [83]. While in the former case, satisfactory agreement was found, the experimentally obtained mass transfer coefficient of the latter case was significantly underpredicted.

Rahman and Faghri [89] presented a steady-state analytical solution for the gas absorption at the gas-liquid interface and the solid dissolution at the disk surface. In their approach the radial convection velocity is prescribed using the semi-parabolic profile obtained for the steady-state smooth-film. The resulting convection-diffusion equation was cast in dimensionless form and solved using a separation of variables, yielding solutions for the dimensionless concentration in terms of confluent hypergeometric functions. The results indicated a downstream increase of the mean bulk concentration, for the case of gas absorption, as well as for the case of solid dissolution, as mass is diffused into the fluid. The Sherwood number was found to decrease with increasing radii due to the developing concentration boundary layer. The results of this asymptotic analysis were compared against their results from a fully three-dimensional numerical simulation (Rahman and Faghri [67, 89]), in which a curvilinear boundary-fitted coordinate system was used for the numerical calculation of the three-dimensional flow in a pie-shaped slice of the disk. Assuming the free surface as upper boundary of the computational domain the ambient gas was not part of the solution. A good agreement between the numerical results and the analytical solution was found in the radially outer region. In the radially inner region the analytical solution did not produce satisfactory predictions, since inertial effects, which are neglected in the far-field solution, dominate. From the numerical results a local minimum in the Sherwood number was found in the radially inner region, where a maximum in the film thickness was observed.

A rather few number of previous analytical and numerical studies scrutinized the effect of wavy flow on the heat and mass transfer characteristics. Sisoev et al. [90] solved a two-dimensional convection-diffusion equation in the framework of the localized IBL equations. Although the wave profiles were assumed to be frozen in the numerical solution of the convection-diffusion equation for the gas concentration, the obtained results indicated an enhancement of the rate of absorption due to the presence of the localized waves. This enhancement could be attributed to the deformation of the diffusion boundary layer, which increases the gas flux into the film. It was shown, that the local mass transfer rates strongly depend on the wave regimes, and therefore, for given process parameters (i.e. fixed Reynolds and Schmidt numbers), on the wave frequency. This finding attaches value to a possible frequency forcing at the inlet, which can be of high relevance in industrial

applications, when it comes to maximizing the transfer rates.

Matar et al. [91] solved for the full set of the unsteady IBL equations, where they also included a convection-diffusion equation for the concentration of the gas phase which is absorbed into the film. The necessary closure relation was provided by adopting a composite profile function for the dissolved gas concentration. A single evolution equation for the thickness of the concentration boundary layer and the base concentration is separately solved for both variables, since their total directional derivatives appear to be alternately zero, as it is dictated by the second law of thermodynamics. Numerical solutions for a wide range of parameters were obtained using a finite-element method for the discretization in space and a linear multi-step method for the time integration. While in the radially inner region smooth film flow was observed, small-amplitude waves emerged in the outer radial region. Propagating further downstream these waves steepened and eventually coalesced forming large-amplitude waves, mostly preceded by capillary ripples. The observed wavy film surface translated into significant radial variations in the thickness of the concentration boundary layer, and hence the local base concentration of the dissolved gas. On average, the base concentration was found to increase due to the presence of the nonlinear waves. Their computational results for the averaged Sherwood number were also compared against the experimental data of Aoune and Ramshaw [81] showing good agreement. The limitations of steady-state models to describe heat and mass transfer rates were also clearly demonstrated, as they are unable to capture any wave-induced enhancement of the transport.

1.3 Objectives of the present work

As it is outlined in the previous section the heat and mass transfer characteristics of thin liquid films on spinning disks were considered thus far only in a few theoretical and numerical studies despite the high relevance of these transport phenomena for various engineering applications. Most of these previous studies investigate the heat transfer or the gas-liquid mass transfer characteristics in case of waveless smooth flow. Furthermore, most of these studies are restricted to large radii, where an asymptotic solution for the flow field can be obtained (cf. Rauscher et al. [53]) and the influence of the inertial and Coriolis forces is negligible.

The present work attempts to extend the scope of these previous studies by covering the full radial extension of the rotating disk including the inner and outer region, where it puts the focus on the effect of unsteady wavy flow on the thermal conditions near the wall, as well as on the solid-liquid mass transfer characteristics. As such this work is also intended to provide essential input for the modeling of surface etching processes on a rotating wafer

in the asymptotic wet chemical etching regimes, associated with very fast and very slow chemistry, respectively.
The wavy thin film flow on a spinning disk at finite Ekman numbers shall be analyzed performing direct numerical simulations of the Navier-Stokes equations for a two-dimensional, axisymmetric flow field. The numerical analysis is based on the finite volume method, and the volume of fluid method is used to track the free surface. As the DNS of the flow is too costly for use as a computational design and optimization tool, the integral-boundary-layer method, which is less laborious in terms of computational costs, and furthermore offers the possibility for a straightforward extension to include heat and species mass transfer, is considered as an alternative approach. The predictive capability of the present IBL approximation shall be assessed using the CFD results obtained from the DNS as well as experimental measurements as reference data.

The main objectives of the present study are to

- computationally investigate the unsteady, wavy motion of the liquid film on the rotating disk based on CFD simulations and the IBL approximation,
- analyze the heat and species mass transfer between the disk and the liquid, with the focus on the effect of waviness, as described by the IBL approximation, and
- model the surface etching process in the limit of large and small Damköhler numbers on a rotating wafer.

1.4 Structure of the thesis

The present thesis is organized as follows:
In **Chapter 2**, the governing equations are presented. The problem is parameterized by non-dimensionalizing the governing equations using problem intrinsic scaling quantities. The thin film nature of the flow allows for a boundary-layer type approximation, which considerably simplifies the governing equations. Solutions to the thin film equations for the asymptotic case of very large Ekman numbers are reviewed and the integral boundary layer equations for finite Ekman numbers are presented. The IBL method, which has so far been successfully used to analyze the fluid dynamics and gas absorption into a thin film flow on a spinning disk, is then extended to model the heat transfer assuming a constant wall heat flux as thermal boundary condition, as well as to model the solid-liquid mass transfer in a binary mixture, assuming a constant species mass fraction at the wall. A simple model to estimate the etching rates for wet chemical etching in the limit of large and small Damköhler numbers is presented.
In **Chapter 3** the numerical solution of the Navier-Stokes equations using the CFD simulation software ANSYS FLUENT is outlined and some details regarding the description

of the two-phase flow using the implemented VoF method are discussed. The numerical solution procedure to solve the IBL equations, which comprise a hyperbolic system of partial differential equations, is based on a finite volume discretization and an approximate Riemann solver. The principles of Roe's approximate Riemann solver are recalled, and some details regarding the underlying wave-propagation theory, which provides flux limited higher-order correction terms, are discussed.
In **Chapter 4** the results of the IBL model for the hydrodynamic, thermal and species mass transfer characteristics are presented and discussed starting with a detailed analysis of the steady-state IBL results. The effects of wavy flow conditions on the time-averaged, as well as on the instantaneous flow field and the heat and species mass transfer characteristics are analyzed in detail. The predictions of the unsteady IBL model are assessed by comparison against results from CFD based numerical solutions of the Navier-Stokes equations assuming axisymmetric flow. In addition to the comparison against numerical results the predictive capability of the unsteady IBL model is also assessed by a comparison against available experimental data. The validation distinguishes between two different regimes based on the maximum values of the Ekman number which are reached at the outer radius of the disk.
In **Chapter 5** the basic findings are summarized, and conclusions, as well as suggestions for further work are presented.

2 MATHEMATICAL MODELING AND APPROXIMATE SOLUTIONS

2.1 Governing equations

The physical conservation laws of mass, momentum and energy provide the base for the mathematical description of the flow and the associated heat and mass transfer. Additional material properties, which govern the flow and the heat and species mass transfer characteristics, as for example viscosity, surface tension, thermal conductivity, and molecular diffusivity, are related to the nature of the fluid.
The following overview gives a synopsis of the mathematical description following textbooks on fluid mechanics, e.g. Batchelor [92], Spurk and Aksel [93], Kuhlmann [94], Pedlosky [95], or Baehr and Stephan [96].

Let $\varphi(\vec{x},\tilde{t})$ represent the amount of some arbitrary physical property of a continuous material medium per unit volume. The total amount of this general physical field quantity $\varphi(\vec{x},\tilde{t})$ present in a finite volume $V(\tilde{t})$ is then obtained through the volume integral

$$\int\limits_{V(\tilde{t})} \varphi(\vec{x},\tilde{t})\, dV. \tag{2.1}$$

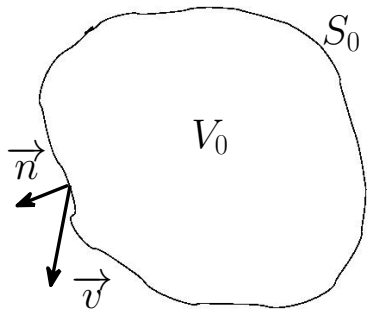

Figure 2.1: Fluid material control volume.

The Reynolds transport theorem states that the rate of change of the total amount of $\varphi(\vec{x},\tilde{t})$ within the material volume $V(\tilde{t})$, which is moving with the fluid velocity $\vec{v}$, is given by

$$\frac{D}{D\tilde{t}}\int\limits_{V(\tilde{t})}\varphi\,dV=\int\limits_{V_0}\frac{\partial\varphi}{\partial\tilde{t}}\,dV+\int\limits_{S_0}\varphi\vec{v}\cdot\vec{n}\,dS. \tag{2.2}$$

Here the stationary volume V_0, which is bounded by the surface $\partial V_0 \equiv S_0$, coincides with the material volume $V(\tilde{t})$ at $\tilde{t}=0$. The vector $\vec{n}$ denotes the outward pointing unit normal vector of the boundary S_0, see Fig. 2.1.

2.1.1 Conservation of mass

In a continuum model the mass m present in a finite volume V is obtained through the volume integral

$$m=\int\limits_{V(\tilde{t})}\rho(\vec{x},\tilde{t})\,dV. \tag{2.3}$$

Utilizing Reynolds transport theorem and replacing $\varphi(\vec{x},\tilde{t})$ by the density $\rho(\vec{x},\tilde{t})$, the conservation of mass is stated as

$$\frac{Dm}{D\tilde{t}}=\int\limits_{V_0}\frac{\partial\rho}{\partial\tilde{t}}\,dV+\int\limits_{S_0}\rho\vec{v}\cdot d\vec{S}=0, \tag{2.4}$$

or alternatively, by applying the divergence theorem (see appendix 1), as

$$\frac{Dm}{D\tilde{t}}=\int\limits_{V_0}\left(\frac{\partial\rho}{\partial\tilde{t}}+\nabla\cdot\rho\vec{v}\right)dV=0. \tag{2.5}$$

The differential form of the continuity equation is obtained in the limit $V_0\to 0$ as

$$\frac{\partial\rho}{\partial\tilde{t}}+\nabla\cdot(\rho\vec{v})=0. \tag{2.6}$$

In a $\mathcal{N}$-component system, the mass flux of the j-th species can be written as

$$\vec{\eta}_j=\rho_j\vec{v}_j. \tag{2.7}$$

Here the velocity of component j, denoted by $\vec{v}_j$, is defined relative to a stationary coordinate system. The total mass flux of the $\mathcal{N}$-component system is then given by

$$\vec{\eta}=\sum_{j=1}^{\mathcal{N}}\vec{\eta}_j=\rho\vec{v}. \tag{2.8}$$

The mass diffusion flux $\vec{f_j}$, defined relative to the motion of the mixture, reads

$$\vec{f_j} = \rho_j \left(\vec{v_j} - \vec{v}\right). \tag{2.9}$$

Incorporating the definition of the mass fraction $\tilde{c}$ for component j

$$\tilde{c_j} = \rho_j / \rho, \tag{2.10}$$

the mass flux of species j can be decomposed into a diffusive flux $\vec{f_j}$ and an overall flux of the mixture weighted with $\tilde{c_j}$

$$\vec{\eta_j} = \vec{f_j} + \tilde{c_j} \rho \vec{v}. \tag{2.11}$$

The rate of change of species j in an arbitrary control volume $V_j(t)$, moving with the species velocity $\vec{v_j}$ is balanced by the rate of production of species j, denoted by $\dot{\Gamma_j}$,

$$\frac{D}{D\tilde{t}} \int\limits_{V_j} \rho_j \, dV = \int\limits_{V_j} \dot{\Gamma_j} \, dV. \tag{2.12}$$

Utilizing Reynolds transport theorem, Eq. (2.2), together with the divergence theorem, the differential form for the mass conservation in a $\mathcal{N}$-component system, is obtained as

$$\frac{\partial \rho_j}{\partial \tilde{t}} + \nabla \cdot (\rho_j \vec{v_j}) = \dot{\Gamma_j}. \tag{2.13}$$

Employing the definition of the mass diffusion flux, Eq. (2.9), and assuming to the continuity equation for a $\mathcal{N}$-component system can be rewritten in terms of the species mass fraction as

$$\rho \frac{\partial \tilde{c_j}}{\partial \tilde{t}} + \rho \vec{v} \cdot \nabla \tilde{c_j} = -\nabla \cdot \vec{f_j} + \dot{\Gamma_j}. \tag{2.14}$$

In a two-component mixture with $j = A, B$, the diffusive flux $\vec{f_A}$ is assumed to be well approximated by Fick's law

$$\vec{f_A} = -\rho D \nabla \tilde{c}_A. \tag{2.15}$$

Considering a liquid with constant density and a constant coefficient of diffusion D, the convection-diffusion equation for the species transport in a binary mixture is given by

$$\frac{\partial \tilde{c}_A}{\partial \tilde{t}} + \vec{v} \cdot \nabla \tilde{c}_A = D \nabla^2 \tilde{c}_A + \dot{\Gamma}_A / \rho_A. \tag{2.16}$$

2.1.2 Conservation of momentum

The conservation of momentum states that the rate of change of momentum is equal to the total vector sum of the acting forces, written as

$$\frac{D\vec{I}}{D\tilde{t}} = \vec{F}. \tag{2.17}$$

In a continuum model the momentum is defined as

$$\vec{I} = \int_V \rho(\vec{x},\tilde{t})\vec{v}(\vec{x},\tilde{t})\,dV. \tag{2.18}$$

The acting forces can be classified into long-range volume forces and short-range surface forces,

$$\vec{F} = \int_V \rho\vec{f}^{\mathcal{B}}\,dV + \int_S \vec{\tau}\,dS. \tag{2.19}$$

Therein the stress vector $\vec{\tau}$ is defined as

$$\vec{\tau} = \vec{n}\cdot\mathbf{T}, \tag{2.20}$$

with the surface normal vector $\vec{n}$ and the stress tensor $\mathbf{T}$. The conservation of momentum then reads

$$\int_{V_0} \frac{\partial(\rho\vec{v})}{\partial\tilde{t}}\,dV + \int_{S_0} \rho\vec{v}\vec{v}\cdot\vec{n}\,dS = \int_{V_0} \rho\vec{f}^{\mathcal{B}}\,dV + \int_{S_0} \vec{\tau}\,dS, \tag{2.21}$$

or alternatively by applying the divergence theorem

$$\int_V \left(\frac{\partial(\rho\vec{v})}{\partial\tilde{t}} + \nabla\cdot(\rho\vec{v}\vec{v})\right) dV = \int_V \left(\rho\vec{f}^{\mathcal{B}} + \nabla\cdot\mathbf{T}\right) dV. \tag{2.22}$$

In the present work only Newtonian fluids are considered. This implies a linear stress-strain relation,

$$\mathbf{T} = -\tilde{p}\mathbb{1} + \mu\left[\nabla\vec{v} + (\nabla\vec{v})^T - \frac{2}{3}(\nabla\cdot\vec{v})\,\mathbb{1}\right] + \chi(\nabla\cdot\vec{v})\,\mathbb{1}, \tag{2.23}$$

with the dynamic viscosity μ and the volume viscosity χ. Furthermore the present analysis is restricted to the flow of incompressible fluids with constant densities of all fluids involved. Within such a framework the continuity equation, Eq. (2.6), reduces to

$$\nabla\cdot\vec{v} = 0, \tag{2.24}$$

and the stress tensor of Eq. (2.23) is given by

$$\mathbf{T} = -\tilde{p}\mathbb{1} + \mu\left[\nabla\vec{v} + (\nabla\vec{v})^T\right]. \tag{2.25}$$

Rotating reference frame

For the mathematical modeling of thin liquid films on spinning disks, a reference frame rotating with the disk's angular speed Ω represents a natural choice. The conservation of momentum stated in Eq. (2.17) is only valid in an inertial frame of reference. In order to

describe the rate of change of an arbitrary vector in a rotating reference frame correctly, an extra term, which accounts for the time derivatives of the rotating unit vectors, has to be added. The rate of change of an arbitrary vector $\vec{s}$ for an observer in an inertial reference frame is given by

$$\left(\frac{D\vec{s}}{D\tilde{t}}\right)_I = \left(\frac{D\vec{s}}{D\tilde{t}}\right)_R + \vec{\Omega} \times \vec{s}. \tag{2.26}$$

Therein the first term on the right hand side (RHS) is the rate change of $\vec{s}$ as seen by an observer in the rotating reference frame, and the second term gives the rate of change of the unit vectors of the rotating reference frame as seen by an observer in the inertial reference frame. The velocity in the inertial reference frame, $\vec{v}_I = (D\vec{x}/D\tilde{t})_I$, can be decomposed into the sum of the velocity of the origin of the rotating reference frame $\vec{v}_O$, the relative velocity in the rotating reference frame $\vec{v}_R = (D\vec{x}/D\tilde{t})_R$, and the circumferential velocity $\Omega \times \vec{x}$,

$$\vec{v}_I = \vec{v}_O + \vec{v}_R + \vec{\Omega} \times \vec{x}. \tag{2.27}$$

The acceleration in the inertial frame of reference is

$$\left(\frac{D\vec{v}_I}{D\tilde{t}}\right)_I = \left(\frac{D\vec{v}_O}{D\tilde{t}}\right)_I + \left(\frac{D\vec{v}_R}{D\tilde{t}}\right)_I + \left(\frac{D\left(\vec{\Omega} \times \vec{x}\right)}{D\tilde{t}}\right)_I. \tag{2.28}$$

Using Eq. (2.26) the total change of the relative velocity can be rewritten as

$$\left(\frac{D\vec{v}_R}{D\tilde{t}}\right)_I = \left(\frac{D\vec{v}_R}{D\tilde{t}}\right)_R + \vec{\Omega} \times \vec{v}_R. \tag{2.29}$$

Denoting the acceleration of the origin of the rotating system with $\vec{a}_O = (D\vec{v}_O/D\tilde{t})_I$, and rewriting the rightmost term in Eq. (2.28) using again Eq. (2.26) the acceleration in the inertial frame can be rewritten in terms of the rotating reference quantities

$$\left(\frac{D\vec{v}_I}{D\tilde{t}}\right)_I = \vec{a}_O + \left(\frac{D\vec{v}_R}{D\tilde{t}}\right)_R + \underbrace{2\vec{\Omega} \times \vec{v}_R}_{\text{Coriolis acc.}} + \underbrace{\vec{\Omega} \times \left(\vec{\Omega} \times \vec{x}\right)}_{\text{centrifugal acc.}} + \underbrace{\frac{d\vec{\Omega}}{d\tilde{t}} \times \vec{x}}_{\text{Euler acc.}}. \tag{2.30}$$

Considering only a non-moving origin, i.e. $\vec{a}_O = \vec{0}$, three additional forces, which arise from the motion of the reference frame itself, have to be account for. These are the Coriolis force, the centrifugal force, and the Euler force. Accordingly, the conservation of momentum for an incompressible Newtonian fluid in a reference frame rotating with constant angular velocity Ω is given by

$$\rho\left[\frac{\partial\vec{v}_R}{\partial\tilde{t}} + (\vec{v}_R \cdot \nabla)\,\vec{v}_R + 2\vec{\Omega} \times \vec{v}_R + \vec{\Omega} \times \left(\vec{\Omega} \times \vec{x}\right)\right] = -\nabla\tilde{p} + \mu\nabla^2\vec{v}_R + \rho\vec{g}. \tag{2.31}$$

It should be noted here, that the continuity equation (2.24) has the same form in the inertial and the rotating reference frame,

$$\nabla \cdot \vec{v}_I = \nabla \cdot (\vec{v}_R + \Omega \times \vec{x}) = \nabla \cdot \vec{v}_R = 0, \tag{2.32}$$

since the divergence of the curl is identical zero.
Rewriting the left hand side (LHS) of the convection-diffusion equation (2.16), as

$$\begin{aligned} \frac{\partial \tilde{c}_A}{\partial \tilde{t}} + \left(\vec{v_R} + \vec{\Omega} \times \vec{x}\right) \cdot \nabla \tilde{c}_A &= \left[\frac{\partial}{\partial \tilde{t}} + \left(\vec{\Omega} \times \vec{x}\right) \cdot \nabla\right] \tilde{c}_A + \vec{v_R} \cdot \nabla \tilde{c}_A \\ &= \left(\frac{\partial \tilde{c}_A}{\partial \tilde{t}}\right)_R + \vec{v_R} \cdot \nabla \tilde{c}_A, \end{aligned} \tag{2.33}$$

it is clear, that it remains in the same form as Eq. (2.16), when rewritten in terms of the relative velocity v_R, using the time derivative, as well as the spatial operator ∇ relative to the rotating frame.
Since in the following a rotating coordinate system is always used as reference frame, the relative velocity v_R is denoted by v, for reasons of readability.

2.1.3 Conservation of thermal energy

The conservation of thermal energy is considerably simplified when the fluid is assumed to be incompressible and Newtonian with constant thermal conductivity λ and constant heat capacity c_p. Assuming furthermore only conductive heat flux q, which is described by Fourier‘s law

$$q = -\lambda \nabla T, \tag{2.34}$$

the conservation of thermal energy can be rewritten as a convection-diffusion equation for the temperature T,

$$\frac{\partial T}{\partial \tilde{t}} + \vec{v} \cdot \nabla T = a \nabla^2 T. \tag{2.35}$$

Here a denotes the thermal diffusivity defined as

$$a = \frac{\lambda}{\rho c_p}. \tag{2.36}$$

2.1.4 Non-dimensionalization of the governing equations

The liquid film flow and the associated heat and species mass transfer for an incompressible Newtonian liquid with constant fluid properties in a reference frame rotating with the disks angular speed Ω, are governed by the following system of partial differential equations

$$\nabla \cdot \vec{v} = 0, \tag{2.37}$$

$$\frac{\partial \vec{v}}{\partial \tilde{t}} + (\vec{v} \cdot \nabla)\,\vec{v} = -\frac{1}{\rho}\nabla \tilde{p} - \vec{\Omega} \times \left(\vec{\Omega} \times \vec{x}\right) - 2\vec{\Omega} \times \vec{v} + \nu \nabla^2 \vec{v} + \vec{g}, \tag{2.38}$$

$$\frac{\partial T}{\partial \tilde{t}} + \vec{v} \cdot \nabla T = a \nabla^2 T, \tag{2.39}$$

$$\frac{\partial \tilde{c}}{\partial \tilde{t}} + \vec{v} \cdot \nabla \tilde{c} = D \nabla^2 \tilde{c}. \tag{2.40}$$

Therein, the body force due to gravity, $\vec{f}^B = \vec{g}$, is accounted for, while chemical reactions, as well as heat sources and dissipation are considered to be negligible.

The problem is considered in a cylindrical coordinate system with base vectors ($\vec{e}_r$, $\vec{e}_\phi$, $\vec{e}_z$). The angular velocity vector is aligned with $\vec{e}_z$ and is represented by $\vec{\Omega} = (0, 0, \Omega)^T$. The body force vector reads $\vec{g} = (0, 0, -g)^T$, and the position vector is given by $\vec{x} = (\tilde{r}, \tilde{\phi}, \tilde{z})^T$. The individual components of the velocity vector are denoted by $\vec{v} = (\tilde{u}, \tilde{v}, \tilde{w})^T$.

The Coriolis term from the momentum equation (2.38) becomes

$$2\vec{\Omega} \times \vec{v} = \begin{pmatrix} -2\tilde{v}\Omega \\ 2\tilde{u}\Omega \\ 0 \end{pmatrix}, \tag{2.41}$$

and the centrifugal term is

$$\vec{\Omega} \times (\vec{\Omega} \times \vec{x}) = \begin{pmatrix} -\tilde{r}\Omega^2 \\ 0 \\ 0 \end{pmatrix}. \tag{2.42}$$

To parameterize the problem the governing equations are non-dimensionalized, using the characteristic scaling quantities suggested by Rauscher et al. [53]. These scaling quantities

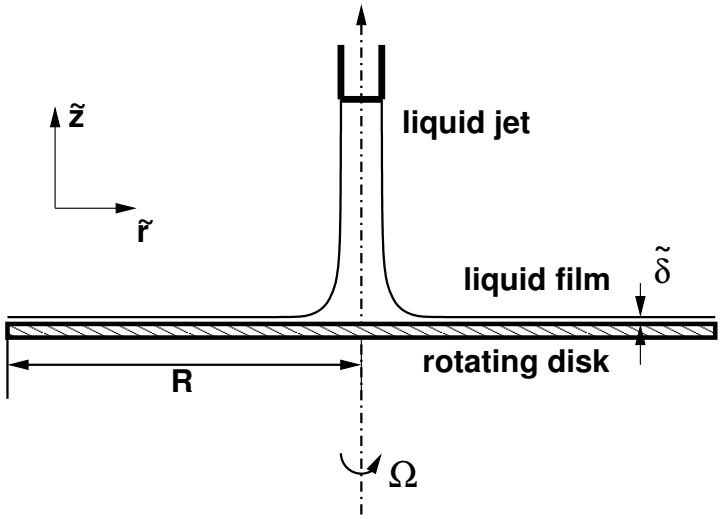

Figure 2.2: Schematics of a spinning disk device.

can be deduced from an order-of-magnitude estimate of the balance of the centrifugal and viscous forces,

$$-\tilde{r}\Omega^2 = \nu\frac{\partial^2\tilde{u}}{\partial\tilde{z}^2}, \tag{2.43}$$

which represents the asymptotic limit of Eq. (2.38) obtained in the radial direction for large radii (see Sec. 2.3.1). Denoting the velocity scale for the radial component of the velocity with u_0, and the length scale in vertical direction with δ_0, the relevant length scale in radial direction, l_0, is obtained from Eq. (2.43) as

$$l_0 \sim \frac{\nu u_0}{\Omega^2\delta_0^2}. \tag{2.44}$$

The film thickness $\tilde{\delta}$ will basically depend on the kinematic viscosity ν of the liquid and the angular speed Ω of the disk. From dimensional arguments it then follows for the vertical length scale ($\tilde{z}$-direction)

$$\delta_0 = \sqrt{\frac{\nu}{\Omega}}. \tag{2.45}$$

From Eq. (2.44) the velocity scale for the radial component is obtained as $u_0 \sim l_0\Omega$. Introducing the volumetric flow rate Q via the expression

$$Q \sim 2\pi l_0\delta_0 u_0, \tag{2.46}$$

the radial length scale l_0 is obtained as

$$l_0 \sim \left(\frac{Q^2}{4\pi^2\nu\Omega}\right)^{1/4}. \tag{2.47}$$

Rauscher [53] introduced an extra factor of $9^{1/4}$, yielding the length scale into the radial direction as

$$l_0 = \left(\frac{9Q^2}{4\pi^2 \nu \Omega} \right)^{1/4}, \tag{2.48}$$

which is used in the present work as well. The velocity scales v_0 and w_0 for the azimuthal and the vertical components of the velocity, respectively, are obtained from an order-of-magnitude analysis of the continuity equation. They are obtained as

$$v_0 = u_0, \tag{2.49}$$

and

$$w_0 = \Omega \delta_0. \tag{2.50}$$

The pressure scale is taken to be

$$p_0 = \rho \Omega^2 l_0^2, \tag{2.51}$$

and the timescale is given by

$$t_0 = l_0 / u_0 = 1/\Omega. \tag{2.52}$$

The heat transfer is investigated assuming a constant wall heat flux boundary condition at the surface of the spinning disk. Accordingly, a dimensionless temperature, which is based on the constant heat flux prescribed at the wall, q_w, and the given inflow temperature of the liquid T_i, is introduced as

$$\theta = \frac{\lambda}{q_w \delta_0} \left(T - T_i \right). \tag{2.53}$$

The solid-liquid mass transfer in a binary mixture is analyzed considering a constant species mass fraction equal to zero, $\tilde{c}_w = 0$, at the wall. In the present scaling the constant inflow species mass fraction, $\tilde{c}_i$, is used as reference quantity

$$c = \frac{\tilde{c}}{\tilde{c}_i}. \tag{2.54}$$

Introducing the characteristic scales given by Eqs. (2.45), (2.48)-(2.52), the non-dimensionalized Navier-Stokes equations read

$$\frac{1}{r} \frac{\partial}{\partial r} (ru) + \frac{1}{r} \frac{\partial v}{\partial \phi} + \frac{\partial w}{\partial z} = 0, \tag{2.55}$$

$$\begin{aligned} \frac{\partial u}{\partial t} + u \frac{\partial u}{\partial r} + \frac{v}{r} \frac{\partial u}{\partial \phi} + w \frac{\partial u}{\partial z} - \frac{v^2}{r} = \\ - \frac{\partial p}{\partial r} + 2v + r + \frac{\partial^2 u}{\partial z^2} + \epsilon^2 \left[\frac{\partial^2 u}{\partial r^2} + \frac{1}{r} \frac{\partial u}{\partial r} + \frac{1}{r^2} \frac{\partial^2 u}{\partial \phi} - \frac{2}{r^2} \frac{\partial v}{\partial \phi} - \frac{u}{r^2} \right], \end{aligned} \tag{2.56}$$

$$\frac{\partial v}{\partial t}+u\frac{\partial v}{\partial r}+\frac{v}{r}\frac{\partial v}{\partial \phi}+w\frac{\partial v}{\partial z}+\frac{uv}{r}= \\ -\frac{1}{r}\frac{\partial p}{\partial \phi}-2u+\frac{\partial^2 v}{\partial z^2}+\epsilon^2\left[\frac{\partial^2 v}{\partial r^2}+\frac{1}{r}\frac{\partial v}{\partial r}+\frac{1}{r^2}\frac{\partial^2 v}{\partial \phi^2}+\frac{2}{r^2}\frac{\partial u}{\partial \phi}-\frac{v}{r^2}\right], \tag{2.57}$$

$$\epsilon^2\left(\frac{\partial w}{\partial t}+u\frac{\partial w}{\partial r}+\frac{v}{r}\frac{\partial w}{\partial \phi}+w\frac{\partial w}{\partial z}\right)= \\ -\frac{\partial p}{\partial z}-\epsilon Fr^{-1}+\epsilon^2\frac{\partial^2 w}{\partial z^2}+\epsilon^4\left[\frac{\partial^2 w}{\partial r^2}+\frac{1}{r}\frac{\partial w}{\partial r}+\frac{1}{r^2}\frac{\partial^2 w}{\partial \phi^2}\right]. \tag{2.58}$$

Using the definition (2.53) the thermal convection-diffusion equation is obtained as

$$\frac{\partial \theta}{\partial t}+u\frac{\partial \theta}{\partial r}+\frac{v}{r}\frac{\partial \theta}{\partial \phi}+w\frac{\partial \theta}{\partial z}= \\ \frac{1}{RePr}\left[\frac{1}{r}\frac{\partial}{\partial r}\left(r\frac{\partial \theta}{\partial r}\right)+\frac{1}{r^2}\frac{\partial^2 \theta}{\partial \phi^2}+\frac{1}{\epsilon^2}\frac{\partial^2 \theta}{\partial z^2}\right], \tag{2.59}$$

and using the definition (2.54) the convection-diffusion equation for the species mass transport in a binary mixture becomes

$$\frac{\partial c}{\partial t}+u\frac{\partial c}{\partial r}+\frac{v}{r}\frac{\partial c}{\partial \phi}+w\frac{\partial c}{\partial z}= \\ \frac{1}{ReSc}\left[\frac{1}{r}\frac{\partial}{\partial r}\left(r\frac{\partial c}{\partial r}\right)+\frac{1}{r^2}\frac{\partial^2 c}{\partial \phi^2}+\frac{1}{\epsilon^2}\frac{\partial^2 c}{\partial z^2}\right]. \tag{2.60}$$

Five dimensionless parameters appear in the present non-dimensionalized formulation. These are the

- aspect ratio, $\epsilon = \delta_0/l_0$,
- Froude number, $Fr = \Omega^2 l_0/g$,
- Reynolds number, $Re = u_0 l_0/\nu$,
- Prandtl number, $Pr = \nu/a$, and the
- Schmidt number, $Sc = \nu/D$.

The thin film Reynolds number, $Re_\delta = \epsilon Re = u_0\delta_0/\nu$, does not explicitly appear in Eqs. (2.55)-(2.58), since

$$\epsilon Re_\delta = \frac{\delta_0}{l_0}\frac{u_0\delta_0}{\nu} = 1. \tag{2.61}$$

The boundary conditions for Eqs. (2.55)-(2.58) are no-slip conditions for the individual velocity components on the disk's surface and the kinematic boundary condition, as well as the stress-free conditions on the free surface, which bring about a further dimensionless parameter, a

- reduced inverse Weber number, $W^{-1} = \epsilon^3 We^{-1} = \epsilon^3 \frac{\sigma}{\rho \Omega^2 l_0 \delta_0^2} = \frac{4\pi^2 \sigma \nu^{3/2}}{9\rho \Omega^{3/2} Q^2}$.

The assumed hydrodynamic, thermal and species mass transport boundary conditions will be discussed in more detail in the next section.

From Eqs. (2.59)-(2.60) the analogy between heat and species mass transfer is obvious. Accordingly, the solutions for the temperature and species mass fraction can be related through the ratio of the Schmidt to the Prandtl number. This ratio is represented by the Lewis number

$$Le = \frac{a}{D} = \frac{Sc}{Pr}, \tag{2.62}$$

which is basically defined as the ratio of the thermal to the molecular diffusivity. For unity Lewis number, $Le = 1$, and identical non-dimensional boundary conditions Eqs. (2.59) and (2.60) would yield identical non-dimensional solutions for θ and c.

2.2 Thin film approximation

2.2.1 Governing equations and boundary conditions

Due to the thin film nature of the flow, the aspect ratio is small, $\epsilon \ll 1$, so that terms of order $\mathcal{O}(\epsilon^2)$ and smaller are neglected, yielding a boundary layer type thin film approximation for the flow on the spinning disk. In this limit the governing equations, Eqs. (2.55)-(2.60), reduce to

$$\frac{1}{r}\frac{\partial}{\partial r}(ru) + \frac{1}{r}\frac{\partial v}{\partial \phi} + \frac{\partial w}{\partial z} = 0, \tag{2.63}$$

$$\frac{\partial u}{\partial t} + u\frac{\partial u}{\partial r} + \frac{v}{r}\frac{\partial u}{\partial \phi} + w\frac{\partial u}{\partial z} - \frac{v^2}{r} = -\frac{\partial p}{\partial r} + 2v + r + \frac{\partial^2 u}{\partial z^2}, \tag{2.64}$$

$$\frac{\partial v}{\partial t} + u\frac{\partial v}{\partial r} + \frac{v}{r}\frac{\partial v}{\partial \phi} + w\frac{\partial v}{\partial z} + \frac{uv}{r} = -\frac{1}{r}\frac{\partial p}{\partial \phi} - 2u + \frac{\partial^2 v}{\partial z^2}, \tag{2.65}$$

$$0 = -\frac{\partial p}{\partial z} - \epsilon Fr^{-1}, \tag{2.66}$$

$$\frac{\partial \theta}{\partial t} + u\frac{\partial \theta}{\partial r} + \frac{v}{r}\frac{\partial \theta}{\partial \phi} + w\frac{\partial \theta}{\partial z} = \frac{1}{Pr}\frac{\partial^2 \theta}{\partial z^2}, \tag{2.67}$$

$$\frac{\partial c}{\partial t} + u\frac{\partial c}{\partial r} + \frac{v}{r}\frac{\partial c}{\partial \phi} + w\frac{\partial c}{\partial z} = \frac{1}{Sc}\frac{\partial^2 c}{\partial z^2}. \tag{2.68}$$

The Reynolds number does not explicitly appear in Eqs. (2.67)-(2.68), since

$$\frac{1}{\epsilon^2 Re} = \frac{l_0^2}{\delta_0^2}\frac{\nu}{u_0 l_0} = 1. \tag{2.69}$$

Incorporating the continuity equation (2.63) into the left hand sides of equations (2.64)-(2.68) and assuming the flow to be axisymmetric, the thin film equations can be rewritten

in conservative form as

$$\frac{1}{r}\frac{\partial}{\partial r}(ru)+\frac{\partial w}{\partial z}=0, \tag{2.70}$$

$$\frac{\partial u}{\partial t}+\frac{1}{r}\frac{\partial}{\partial r}\left(ru^2\right)+\frac{\partial}{\partial z}(uw)-\frac{v^2}{r}=-\frac{\partial p}{\partial r}+2v+r+\frac{\partial^2 u}{\partial z^2}, \tag{2.71}$$

$$\frac{\partial v}{\partial t}+\frac{1}{r}\frac{\partial}{\partial r}(ruv)+\frac{\partial}{\partial z}(vw)+\frac{uv}{r}=-2u+\frac{\partial^2 v}{\partial z^2}, \tag{2.72}$$

$$0=-\frac{\partial p}{\partial z}-\epsilon Fr^{-1}, \tag{2.73}$$

$$\frac{\partial \theta}{\partial t}+\frac{1}{r}\frac{\partial}{\partial r}(ru\theta)+\frac{\partial}{\partial z}(w\theta)=\frac{1}{Pr}\frac{\partial^2 \theta}{\partial z^2}, \tag{2.74}$$

$$\frac{\partial c}{\partial t}+\frac{1}{r}\frac{\partial}{\partial r}(ruc)+\frac{\partial}{\partial z}(wc)=\frac{1}{Sc}\frac{\partial^2 c}{\partial z^2}. \tag{2.75}$$

Hydrodynamic boundary conditions

The boundary conditions for the boundary layer approximation are the no-slip conditions on the disk's surface

$$z=0:\ u=v=w=0, \tag{2.76}$$

and the kinematic boundary condition

$$z=\delta:\ w=\frac{\partial \delta}{\partial t}+u\frac{\partial \delta}{\partial r}, \tag{2.77}$$

and stress-free conditions on the free surface at $z=\delta$:

$$\tau_{rz}=\frac{\partial u}{\partial z}=0, \tag{2.78}$$

$$\tau_{\phi z}=\frac{\partial v}{\partial z}=0, \tag{2.79}$$

$$0=-p-W^{-1}\left(\frac{1}{r}\frac{\partial}{\partial r}\left(r\frac{\partial \delta}{\partial r}\right)\right). \tag{2.80}$$

In Eq. (2.80) the reduced inverse Weber number, $W^{-1}=\sigma\delta_0/\rho\Omega^2 l_0^4$, which accounts for the influence of surface tension σ, occurs.

Thermal boundary conditions

The thermal characteristics of the flow are investigated by assuming a constant heat flux boundary condition at the surface of the spinning disk. Based on the definition of the

dimensionless temperature in Eq. (2.53), the prescribed heat flux q_w at the wall yields the condition

$$z = 0: \quad \left.\frac{\partial \theta}{\partial z}\right|_{z=0} = \frac{1}{q_w} \lambda \left.\frac{\partial T}{\partial \tilde{z}}\right|_{\tilde{z}=0} = -1 \tag{2.81}$$

for the dimensionless temperature.
Evaluating the thermal convection-diffusion equation Eq. (2.74) at $z = 0$ in the limit of steady-state conditions yields a further boundary condition at the wall as

$$z = 0: \quad \left.\frac{\partial^2 \theta}{\partial z^2}\right|_{z=0} = 0. \tag{2.82}$$

In the thermal entry region, $r < r_T$, the evolution of a thermal boundary layer δ_T is distinguished from the film height δ. The thermal entry length r_T, which is determined as the radial extension, where δ_T reaches δ, depends on the magnitude of the Prandtl number. At the height of the thermal boundary layer a zero gradient boundary condition is imposed

$$z = \delta_T: \quad \left.\frac{\partial \theta}{\partial z}\right|_{z=\delta_T} = 0. \tag{2.83}$$

Analogously, once the thermal boundary layer has reached the liquid film height, i.e. for $r \geq r_T$, the boundary condition at the free surface reads

$$z = \delta: \quad \left.\frac{\partial \theta}{\partial z}\right|_{z=\delta} = 0. \tag{2.84}$$

This basically neglects the convective heat transfer between the liquid surface and the ambient air. The effect of a possible convective heat flux at the liquid surface is addressed in Sec. 2.3.4 and its implication on the finally obtained solution will be further discussed in Sec. 4.1.2.

For completeness it is noted here, that defining the non-dimensional alternatively as

$$\theta^\star = \frac{T - T_w}{T_i - T_w}, \tag{2.85}$$

instead of using Eq. (2.53) would cover the case with constant wall temperature, which is not considered in the present work. The definition (2.85) would imply a Dirichlet boundary condition

$$z = 0: \ \theta^* = 0 \tag{2.86}$$

at the wall, while the other boundary conditions (2.82)-(2.84) would remain the same.

Boundary conditions for the species transport

When considering the species transport in a binary mixture, the boundary conditions are given as

$$z = 0 : \; c = 0, \tag{2.87}$$

and

$$z = 0 : \; \left. \frac{\partial^2 c}{\partial z^2} \right|_{z=0} = 0, \tag{2.88}$$

at the wall, where the latter is obtained by evaluating the convection-diffusion equation Eq. (2.75) at $z = 0$.

For large Schmidt numbers it is necessary to distinguish a concentration boundary layer with thickness δ_c from the film height. In the region for $r < r_c$, associated with a developing concentration boundary layer, i.e. $\delta_c < \delta$, a zero-gradient upper boundary condition is imposed

$$z = \delta_c : \; \left. \frac{\partial c}{\partial z} \right|_{z=\delta_c} = 0. \tag{2.89}$$

Analogously, once the concentration boundary layer has reached the liquid film height, i.e. for $r \geq r_c$, the boundary condition at the free surface reads

$$z = \delta : \; \left. \frac{\partial c}{\partial z} \right|_{z=\delta} = 0. \tag{2.90}$$

It is noted that for unity Lewis number, $Le = a/D = 1$, the solution obtained for the species mass fraction c would be identical with the solution for non-dimensional wall temperature for the case with constant wall temperature defined by Eq. (2.85).

2.2.2 Far field asymptotic solution for $Ek \gg 1$

As discussed in Sec. 1.2.2, an order-of-magnitude analysis yields in the limit of large radii the expression

$$Ek \cdot Ro \sim \mathcal{O}(1),$$

which implies that for high Ekman numbers, $Ek \gg 1$, the inertial, as well as the Coriolis forces are negligible. Assuming an axisymmetric and steady flow, far-field asymptotic solutions for the velocity and the film thickness can be analytically obtained in the case of $Ek \gg 1$. Based on this far-field solution for the velocity, it is possible to obtain analytical steady-state solutions for the heat and mass transfer as well.

Asymptotic momentum balance

For large radii the radial momentum balance is governed only by the viscous and centrifugal forces. Thus, assuming the flow to be axisymmetric and steady, the asymptotic momentum balance at large radii becomes

$$0 = r + \frac{\partial^2 u}{\partial z^2}, \tag{2.91}$$

which is decoupled from the momentum equation into the azimuthal direction written as

$$0 = -2u + \frac{\partial^2 v}{\partial z^2}. \tag{2.92}$$

Integration of Eq. (2.91), applying the boundary conditions of Eq. (2.76) and (2.78), and introducing the rescaled wall normal coordinate $\zeta = z/\delta$, results in

$$u(r,\zeta) = u_\delta \left(2\zeta - \zeta^2\right). \tag{2.93}$$

The maximum velocity u_δ is reached at the free surface ($\zeta = 1$), and it is related to the mean radial velocity by

$$\overline{u} = \frac{1}{\delta}\int_0^\delta u\, dz = \frac{2}{3}u_\delta. \tag{2.94}$$

The semi-parabolic velocity profile given by Eq. (2.93) represents an exact asymptotic solution in the limit of large radii, where the viscous and centrifugal forces dominate. Introducing the volumetric flowrate,

$$Q = 2\tilde{r}\pi\tilde{\delta}\tilde{\overline{u}}, \tag{2.95}$$

and recalling the length and velocity scales δ_0, l_0, and, $u_0 = l_0\Omega$, specified in Eqs. (2.45) and (2.48), the substitution of Eq. (2.93) with $u_\delta = (3/2)\overline{u}$ due to (2.94) into Eq. (2.91) yields the following radial variation of the film thickness written in dimensional form

$$\tilde{\delta} = \left(\frac{3}{2\pi}\frac{Q\nu}{\Omega^2\tilde{r}^2}\right)^{1/3} \qquad [\mathrm{m}]. \tag{2.96}$$

The asymptotic momentum balance for large radii into the azimuthal direction, Eq. (2.92), is governed by the balance between the viscous and the Coriolis forces. Integration of Eq. (2.92) using the parabolic profile for u as given by Eq. (2.93) leads to the quartic polynomial

$$v(r,\zeta) = v_\delta\left(\frac{8}{5}\zeta - \frac{4}{5}\zeta^3 + \frac{1}{5}\zeta^4\right). \tag{2.97}$$

The mean velocity into the azimuthal direction is then obtained as

$$\overline{v} = \frac{1}{\delta}\int_0^\delta v\,dz = \frac{16}{25}v_\delta, \tag{2.98}$$

and the maximum velocity v_δ, corresponding to the maximum tangential slip, is reached at the free surface, where $\zeta = 1$.

Asymptotic higher-order expansion

Based on the far-field solution $\delta = r^{-2/3}$ for the film thickness, Rauscher et al. [53] introduced the similarity variable η as

$$\eta = \frac{\tilde{z}}{\tilde{\delta}} = \frac{\tilde{z}}{\delta_0}r^{2/3}, \tag{2.99}$$

so that the radial component of the flow velocity, Eq. (2.93), expressed in terms of η is given by

$$\tilde{u} = u_0 r^{-1/3}\left(\eta - \frac{1}{2}\eta^2\right). \tag{2.100}$$

To obtain higher-order terms of the asymptotic solution for the axisymmetric flow-field, Rauscher reformulated the Navier-Stokes equations together with the corresponding boundary conditions in terms of η and $r = \tilde{r}/l_0$, and obtained the following higher-order expansions in terms of r

$$\delta = r^{-2/3} + \left(\frac{62}{315} - \frac{2}{9}\epsilon F r^{-1}\right)r^{-10/3} + \mathcal{O}(r^{-4}), \tag{2.101}$$

$$\overline{u} = \frac{1}{3}r^{-1/3} - \frac{1}{3}\left(\frac{62}{315} - \frac{2}{9}\epsilon F r^{-1}\right)r^{-3} + \mathcal{O}(r^{-11/3}), \tag{2.102}$$

$$\overline{v} = -\frac{4}{15}r^{-5/3} - \left(\frac{1156}{14175} - \frac{8}{135}\epsilon F r^{-1}\right)r^{-13/3} + \mathcal{O}(r^{-5}). \tag{2.103}$$

Far-field solutions for the solid-liquid mass transfer

Based on the asymptotic solution for the flow field it is possible to obtain an analytical solution for species mass transfer as well. Rahman and Faghri [89], for example, presented an analytical solution for species transport in case of solid dissolution at the disk surface. Neglecting convection into the vertical direction the asymptotic momentum and species transport equations ($r \gg 1$) are given by

$$\frac{\partial^2 \tilde{u}}{\partial \tilde{z}^2} = -\frac{\Omega^2 \tilde{r}}{\nu}, \tag{2.104}$$

and

$$\tilde{u}\frac{\partial \tilde{c}}{\partial \tilde{r}} = D\frac{\partial^2 \tilde{c}}{\partial \tilde{z}^2}. \tag{2.105}$$

The solution of Eq. (2.104) applying no-slip and zero-gradient boundary conditions at the disk and the free surface respectively, yields the semi-parabolic velocity profile of Eq. (2.93), which can now be substituted into Eq. (2.105), yielding

$$3\overline{\tilde{u}}\left[\frac{\tilde{z}}{\tilde{\delta}} - \frac{1}{2}\frac{\tilde{z}^2}{\tilde{\delta}^2}\right]\frac{\partial \tilde{c}}{\partial \tilde{r}} = D\frac{\partial^2 \tilde{c}}{\partial \tilde{z}^2}. \tag{2.106}$$

Rahman and Faghri [89] non-dimensionalized Eq. (2.106) by introducing the dimensionless variables

$$\Xi = \frac{\tilde{c}_w - \tilde{c}}{\tilde{c}_w - \tilde{c}_i},\ Z = \frac{\tilde{\delta} - \tilde{z}}{\tilde{\delta}},\ r^* = \frac{r}{r_i}, \tag{2.107}$$

and

$$X = 0.1733\hat{Re}_i^{-4/3}\hat{Ek}_i^{-2/3}Sc^{-1}\left(r^{*8/3} - 1\right). \tag{2.108}$$

Here the Reynolds and Ekman numbers are defined using the values at the inflow, i.e. $\hat{Re}_i = \tilde{u}_i\tilde{\delta}_i/\nu$, and $\hat{Ek}_i = \nu/\Omega\tilde{r}_i^2$. The non-dimensionalized convection-diffusion equation for the species transport in case of solid dissolution is then given by

$$\left(1 - Z^2\right)\frac{\partial \Xi}{\partial X} = \frac{\partial^2 \Xi}{\partial Z^2}, \tag{2.109}$$

and the boundary conditions read

$$Z = 0:\ \frac{\partial \Xi}{\partial Z} = 0, \tag{2.110}$$

$$Z = 1:\ \Xi = 0, \tag{2.111}$$

and

$$X = 0:\ \Xi = 1. \tag{2.112}$$

Solutions can be obtained in terms of an infinite series of confluent hypergeometric functions, $\mathcal{M}(a,b,c)$,

$$\Xi\left(X,Z\right) = \sum_{n=1}^{\infty} C_n \exp\left(-\lambda_n^2 X\right)\exp\left(\frac{-\lambda_n Z^2}{2}\right)\mathcal{M}\left(\frac{1-\lambda_n}{4}, \frac{1}{2}, \lambda_n Z^2\right), \tag{2.113}$$

as shown by Rahman and Faghri [89], who present in their study the first 15 values of the eigenvalues λ_n and coefficients C_n.

A number of authors, (see, e.g., Burns et al. [83], or Peev et al. [84]) considered a method, known as method of Leveque, to model the solid-dissolution on a spinning disk. In this method a linear approximation for the velocity profile is assumed, presuming a very thin concentration boundary layer. The resulting approximate convection-diffusion equation reads

$$\frac{3\tilde{z}}{\tilde{\delta}}\overline{\tilde{u}}\frac{\partial\tilde{c}}{\partial\tilde{r}} = D\frac{\partial^2\tilde{c}}{\partial\tilde{z}^2}, \tag{2.114}$$

which can be cast into dimensionless form using the dimensionless concentration

$$\hat{\Xi} = 1 - \Xi = \frac{\tilde{c} - \tilde{c}_i}{\tilde{c}_w - \tilde{c}_i} \tag{2.115}$$

and a similarity variable

$$\hat{\eta} = \tilde{z}\left(\frac{3\overline{\tilde{u}}}{\tilde{\delta}}\frac{1}{9D\tilde{r}}\right)^{1/3} = \tilde{z}\left(\frac{\Omega^2\tilde{\delta}}{9D\nu}\right)^{1/3}. \tag{2.116}$$

Applying the transformation into these new variables Eq. (2.114) becomes

$$\frac{d^2\hat{\Xi}}{d\hat{\eta}^2} + 3\hat{\eta}^2\frac{d\hat{\Xi}}{d\hat{\eta}} = 0, \tag{2.117}$$

with the boundary conditions

$$\hat{\Xi} = 1 \text{ at } \hat{\eta} = 0, \tag{2.118}$$

and

$$\hat{\Xi} = 0 \text{ for } \hat{\eta} \to \infty. \tag{2.119}$$

The solution of Eq. (2.117), is then obtained as

$$\hat{\Xi}(\hat{\eta}) = 1 - \frac{\gamma\left(\frac{1}{3}, \hat{\eta}^3\right)}{\Gamma\left(\frac{1}{3}\right)}. \tag{2.120}$$

Here

$$\gamma(a, x) = \int_0^x t^{a-1}e^{-t}dt, \tag{2.121}$$

denotes the incomplete gamma function, and

$$\Gamma(a) = \int_0^\infty t^{a-1}e^{-t}dt \tag{2.122}$$

is the complete, or Euler, gamma function.

2.3 Integral boundary layer approximation

A popular approach for the analysis of rotating films with finite Ekman numbers is the IBL approximation, in which depth-averaged quantities, defined by the integral average over the film thickness

$$\overline{\Upsilon} = \frac{1}{\delta}\int_0^\delta \Upsilon \, dz, \tag{2.123}$$

are considered. The governing set of partial differential equations for the IBL model is obtained by averaging the thin film equations Eqs. (2.70)-(2.75) over the film thickness.

2.3.1 IBL approximation for hydrodynamics

Using the kinematic boundary condition Eq. (2.77), and considering the flow as axisymmetric, the depth-averaging of the continuity equation Eq. (2.70) yields

$$\frac{\partial \delta}{\partial t} + \frac{1}{r}\frac{\partial}{\partial r}\int_0^\delta r u \, dz = 0, \tag{2.124}$$

which can be written in terms of the depth-averaged velocity $\overline{u}$ as

$$\frac{\partial \delta}{\partial t} + \frac{1}{r}\frac{\partial}{\partial r}\left[r\overline{u}\delta\right] = 0. \tag{2.125}$$

The integration of the thin film limit for the vertical component of the momentum equation, Eq. (2.73), yields an expression for the pressure written as

$$p = p_\delta + \epsilon Fr^{-1}\left(\delta - z\right). \tag{2.126}$$

Here p_δ denotes the pressure at the free surface, which can be computed from the stress-free boundary condition given by Eq. (2.80). The depth-averaged pressure is then obtained as

$$\overline{p} = \frac{1}{\delta}\int_0^\delta p \, dz = p_\delta + \frac{1}{2}\epsilon Fr^{-1}\delta = \frac{1}{2}\epsilon Fr^{-1}\delta - W^{-1}\left(\frac{1}{r}\frac{\partial}{\partial r}\left(r\frac{\partial \delta}{\partial r}\right)\right). \tag{2.127}$$

Depth-averaging the radial component of the momentum equation, Eq. (2.71), yields

$$\frac{\partial}{\partial t}\int_0^\delta u\,dz+\frac{1}{r}\frac{\partial}{\partial r}\int_0^\delta ru^2\,dz-\frac{1}{r}\int_0^\delta v^2\,dz= \\ -\frac{\partial}{\partial r}\int_0^\delta p\,dz+p_\delta\frac{\partial\delta}{\partial r}+r\delta+2\int_0^\delta v\,dz-\left.\frac{\partial u}{\partial z}\right|_{z=0}. \tag{2.128}$$

Herein, the boundary condition Eq. (2.78) was used and again the kinematic boundary condition Eq. (2.77) was applied to substitute the vertical component of the surface velocity w_δ.
Similarly, the depth-averaging of the azimuthal component of the momentum equation, Eq. (2.72), yields

$$\frac{\partial}{\partial t}\int_0^\delta v\,dz+\frac{1}{r}\frac{\partial}{\partial r}\int_0^\delta ruv\,dz+\int_0^\delta\frac{uv}{r}\,dz=-2\int_0^\delta u\,dz-\left.\frac{\partial v}{\partial z}\right|_{z=0}. \tag{2.129}$$

Rewriting the nonlinear convective fluxes in terms of

$$\begin{aligned}\frac{1}{\delta}\int_0^\delta u^2\,dz&=k_a\overline{u}^2,\\ \frac{1}{\delta}\int_0^\delta uv\,dz&=k_b\overline{u}\,\overline{v},\\ \frac{1}{\delta}\int_0^\delta v^2\,dz&=k_c\overline{v}^2,\end{aligned} \tag{2.130}$$

involving the profile constants k_a, k_b, k_c, and introducing the expression

$$P=\epsilon Fr^{-1}\delta-W^{-1}\left(\frac{1}{r}\frac{\partial}{\partial r}\left(r\frac{\partial\delta}{\partial r}\right)\right), \tag{2.131}$$

the depth-averaged continuity and momentum equations can be compactly rewritten as

$$\frac{\partial}{\partial t}\begin{pmatrix}\delta\\ \delta\overline{u}\\ \delta\overline{v}\end{pmatrix}+\frac{1}{r}\frac{\partial}{\partial r}\begin{pmatrix}r\delta\overline{u}\\ k_ar(\delta\overline{u})^2/\delta\\ k_br(\delta\overline{u})(\delta\overline{v})/\delta\end{pmatrix}= \\ \begin{pmatrix}0\\ k_c(\delta\overline{v})^2/(r\delta)+2(\delta\overline{v})+b_1\left(r-\frac{\partial P}{\partial r}\right)\delta-b_2(\delta\overline{u})/\delta^2\\ -k_b(\delta\overline{u})(\delta\overline{v})/(r\delta)-2(\delta\overline{u})-5(\delta\overline{v})/(2\delta^2)\end{pmatrix}. \tag{2.132}$$

Therein, $\overline{u}$, $\overline{v}$ are the depth-averages of the radial and azimuthal components of the velocity, respectively, and the constants b_1 and b_2 result from the derivatives of the radial and azimuthal components of the velocity at $z = 0$, appearing on the right hand side of Eq. (2.128) and Eq. (2.129). The depth-averaged continuity and momentum equations in Eq. (2.132) are identical to the formulation obtained by Kim and Kim [75].

The reduction of the spacial dimensionality of the problem based on depth-averaging requires approximate assumptions for the profiles of the radial and azimuthal velocity components to compute the values of the profile constants k_a, k_b, k_c, defined by Eq. (2.130), as well as b_1 and b_2. The presently assumed profiles will be discussed in the following.

Profile assumptions

Radial velocity component

A popular choice for the profile of the radial component of the velocity is the semi-parabola (e.g. Sisoev et al. [74])

$$u(r,\zeta) = u_\delta \left(2\zeta - \zeta^2\right), \tag{2.133}$$

which is basically identical to the exact asymptotic solution in the limit of large radii, Eq. (2.93), where the viscous and centrifugal forces dominate (see Sec. 2.2.2). The second-order polynomial exhibits, however, a number of shortcomings in the radially inner region, where inertial and Coriolis forces are relevant. Therefore, the assumption of a quartic polynomial was proposed as an alternative (Kim and Kim [75]) written as

$$u(r,\zeta) = u_\delta \left(\frac{8}{5}\zeta - \frac{4}{5}\zeta^3 + \frac{1}{5}\zeta^4\right) + \frac{\kappa\delta^2}{5}\zeta\,(1-\zeta)^2\left(1 - \frac{\zeta}{2}\right). \tag{2.134}$$

This profile function introduces an additional profile parameter κ, which can be determined from the radial momentum equation evaluated at $z = 0$,

$$\left.\frac{\partial^2 u}{\partial z^2}\right|_{z=0} = -r + \left.\frac{\partial p}{\partial r}\right|_{z=0} := -\kappa. \tag{2.135}$$

Azimuthal velocity component

The azimuthal component of the velocity is approximated by the quartic polynomial (see Sec. 2.2.2)

$$v(r,\zeta) = v_\delta \left(\frac{8}{5}\zeta - \frac{4}{5}\zeta^3 + \frac{1}{5}\zeta^4\right), \tag{2.136}$$

which alike Eq. (2.133) represents an exact analytical solution obtained in the limit of large radii.

Quadratic vs. quartic approximation

Substituting straightforwardly the quartic profile assumption Eq. (2.134) into Eq. (2.130) would result in very complex expressions for the integrations of the non-linear flux terms. It was therefore suggested by Kim and Kim [75] to compute the values of the profile constants k_a, k_b and k_c using rather the quadratic approximation Eq. (2.133) for the radial component of the velocity in the nonlinear integrands occurring in Eq. (2.130). The profile parameters b_1 and b_2 are still obtained using the quartic profile assumption Eq. (2.134). This approach is adopted in the present work as well, and it is referred to as quartic approximation (IBL quart.) in the following. The profile constants used for the quartic and quadratic IBL approximation of the momentum equations are listed in Tab. 2.1.

profile parameter	k_a	k_b	k_c	b_1	b_2
IBL quad.	$6/5$	$17/14$	$155/126$	1	3
IBL quart.	$6/5$	$17/14$	$155/126$	$5/6$	$5/2$

Table 2.1: Profile constants for the IBL approximation of the momentum equations.

Vertical velocity component

The profile of the vertical velocity follows implicitly from the assumptions for the other two velocity components to satisfy the continuity equation. Although the vertical velocity profile is never needed in the solution of the depth-averaged equations, the insight into the implicitly used w-profile can be helpful for the interpretation of the obtained IBL results. Considering for example the quadratic radial velocity profile, Eq. (2.133), the profile for the vertical velocity component is obtained by integrating the continuity equation, Eq. (2.63), rewritten for axisymmetric flow

$$\frac{\partial w}{\partial z} = -\frac{1}{r}\frac{\partial}{\partial r}\left[ru_\delta\left(\frac{z}{\delta}-\frac{z^2}{\delta^2}\right)\right]. \tag{2.137}$$

Using the no-slip condition at $z = 0$ integration of Eq. (2.137) yields the third-order polynomial

$$w(r,z) = \frac{z^3}{\delta^3}\left(\frac{u_\delta\delta}{3r}-\frac{2u_\delta}{3}\frac{\partial\delta}{\partial r}+\frac{1}{3}\delta\frac{\partial u_\delta}{\partial r}\right)+\frac{z^2}{\delta^2}\left(-\frac{u_\delta\delta}{r}+u_\delta\frac{\partial\delta}{\partial r}-\delta\frac{\partial u_\delta}{\partial r}\right). \tag{2.138}$$

It can be shown that this w-profile satisfies the kinematic boundary condition, Eq. (2.77), by rewriting the depth-averaged continuity equation (2.125) assuming the quadratic u-profile, Eq. (2.133), associated with $u_\delta = (3/2)\overline{u}$, as

$$\frac{\partial\delta}{\partial t} = -\frac{2}{3r}\frac{\partial}{\partial r}\left[ru_\delta\delta\right]. \tag{2.139}$$

Using (2.139) it can be easily verified, that

$$w_\delta = \frac{\partial \delta}{\partial t} + u_\delta \frac{\partial \delta}{\partial r} = -\frac{2}{3}\frac{\delta u_\delta}{r} - \frac{1}{3}u_\delta \frac{\partial \delta}{\partial r} - \frac{2}{3}\delta \frac{\partial u_\delta}{\partial r}, \tag{2.140}$$

which is identical to the RHS of Eq. (2.138) evaluated at $z = \delta$. Introducing the notation

$$a_w(r) = -\frac{3ru_\delta \frac{\partial \delta}{\partial r}}{2ru_\delta \frac{\partial \delta}{\partial r} + 4\delta\left(u_\delta + r\frac{\partial u_\delta}{\partial r}\right)}, \tag{2.141}$$

the profile for the vertical velocity component can be compactly rewritten as

$$w(r,\zeta) = w_\delta\left[\zeta^2\left(\frac{3}{2} - a_w(r)\right) + \zeta^3\left(a_w(r) - \frac{1}{2}\right)\right]. \tag{2.142}$$

The depth-averaged vertical velocity is then obtained as

$$\overline{w} = w_\delta\left(\frac{3}{8} - \frac{a_w(r)}{12}\right). \tag{2.143}$$

The validity of this implicit assumption for the profile of the vertical component of the velocity will be discussed in detail in Sec. 4.2.3.
It should be noted here, that in case of steady-state smooth flow the vertical component of the velocity tends to zero for large radii. This can easily be verified by substituting the far-field solutions ($r \gg 1$) for the film thickness $\delta = r^{-2/3}$, and the radial surface velocity, $u_\delta = (1/2)r^{-1/3}$, into the asymptotic steady-state representation of the kinematic boundary condition, Eq. (2.140), which yields

$$\lim_{r\to\infty}(w_\delta) = \lim_{r\to\infty}\left(u_\delta \frac{d\delta}{dr}\right) \approx \lim_{r\to\infty}\left(\frac{2}{3r^2}\right) = 0, \tag{2.144}$$

so that the vertical velocity profile given by Eq. (2.142) becomes identical zero.

2.3.2 IBL approximation for heat transfer

The thermal characteristics of the flow are investigated assuming a constant wall heat flux boundary condition. Depth-averaging of the thermal convection-diffusion equation (2.74) and using the boundary conditions Eq. (2.81) and (2.84) yields

$$\frac{\partial}{\partial t}\int_0^\delta \theta\, dz + \frac{1}{r}\frac{\partial}{\partial r}\int_0^\delta ru\theta\, dz = \frac{1}{Pr}. \tag{2.145}$$

To evaluate the integrals appearing on the LHS of the depth-averaged transport equation Eq. (2.145), a profile assumption for the dimensionless temperature is required. For this purpose a third-order polynomial ansatz function

$$\theta(z) = a_0 + a_1 \frac{z}{\delta_T} + a_2 \frac{z^2}{\delta_T^2} + a_3 \frac{z^3}{\delta_T^3} \tag{2.146}$$

was chosen. Introducing the dimensionless wall temperature given as

$$\theta_w = \theta|_{z=0}\,, \tag{2.147}$$

and using the boundary conditions Eqs. (2.81)-(2.82) together with Eq. (2.83), before the thermal boundary layer has reached the film surface ($\delta_T < \delta$), or, together with Eq. (2.84) thereafter ($\delta_T = \delta$), a composite profile for the dimensionless temperature is obtained as

$$\delta_T < \delta:\ \theta = \frac{2}{3}\delta_T + \delta_T \left(\frac{1}{3}\frac{z^3}{\delta_T^3} - \frac{z}{\delta_T} \right), \tag{2.148}$$

$$\delta_T = \delta:\ \theta = \theta_w + \delta \left(\frac{1}{3}\frac{z^3}{\delta^3} - \frac{z}{\delta} \right). \tag{2.149}$$

In the thermal entry region, $r < r_T$, associated with $\delta_T < \delta$, the non-dimensional wall temperature is directly related to the thickness of the thermal boundary layer as

$$\delta_T < \delta: \qquad \theta_w = \frac{2}{3}\delta_T. \tag{2.150}$$

Since the film in the radially inner region generally remains smooth, steady-state conditions are assumed within the thermal entry zone $0 < r < r_T$. Using the composite profile function given by Eqs. (2.148)-(2.149) produces the following expression for the depth-averaged temperature

$$\overline{\theta} = \frac{1}{\delta}\int_0^\delta \theta\, dz = \begin{cases} \frac{1}{4}\frac{\delta_T^2}{\delta} & \text{for } \delta_T < \delta, \\ \theta_w - \frac{5}{12}\delta & \text{for } \delta_T = \delta. \end{cases} \tag{2.151}$$

The integration of the convective heat transport term uses for simplicity again only the quadratic profile assumption of the radial velocity u given by Eq. (2.133), which yields

$$\frac{1}{\delta}\int_0^\delta u\theta\, dz = \begin{cases} \frac{\overline{u}}{120}\frac{\delta_T^3}{\delta^3}\left(24\delta - 5\delta_T\right) & \text{for } \delta_T < \delta, \\ \theta_w \overline{u} - \frac{61}{120}\delta\overline{u} & \text{for } \delta_T = \delta. \end{cases} \tag{2.152}$$

Incorporating these expressions into the approximation for the transport of heat Eq. (2.145) yields evolution equations for the thickness of the thermal boundary layer $\delta_T < \delta$

$$\frac{\partial}{\partial t}\left(\frac{\delta_T^2}{4}\right) + \frac{1}{r}\frac{\partial}{\partial r}\left[r\overline{u}\delta \left(\frac{\delta_T}{\delta}\right)^3 \left(\frac{1}{5}\delta - \frac{1}{24}\delta_T\right)\right] = \frac{1}{Pr} \tag{2.153}$$

within the thermal entry region $r < r_T$, and further downstream, when $\delta_T = \delta$, for the the dimensionless wall temperature θ_w,

$$\frac{\partial}{\partial t}\left(\delta\theta_w - \frac{5}{12}\delta^2\right) + \frac{1}{r}\frac{\partial}{\partial r}\left(r\delta\overline{u}\theta_w - \frac{61}{120}r\delta^2\overline{u}\right) = \frac{1}{Pr}. \tag{2.154}$$

2.3.3 IBL approximation for species mass transfer

Depth-averaging the species mass fraction convection-diffusion equation (2.75) and using the boundary condition Eq. (2.90) yields

$$\frac{\partial}{\partial t}\int_0^\delta c\,dz + \frac{1}{r}\frac{\partial}{\partial r}\int_0^\delta ruc\,dz = -\frac{1}{Sc}\left.\frac{\partial c}{\partial z}\right|_{z=0}. \tag{2.155}$$

The necessary closure for the solution of the depth-averaged convection-diffusion equation can be provided by choosing a third-order polynomial ansatz function for the profile of species mass fraction c, generally written as

$$\frac{c}{c_\delta(r)} = a_0 + a_1\frac{z}{\delta_c} + a_2\frac{z^2}{\delta_c^2} + a_3\frac{z^3}{\delta_c^3}. \tag{2.156}$$

Here δ_c denotes the thickness of the concentration boundary layer, and $c_\delta = c|_{z=\delta}$ denotes the value of c at the surface, which is constant in the region $r < r_c$, where the concentration boundary layer is distinguished from the film thickness. Accordingly, the surface value c_δ equals unity before the concentration boundary layer has reached the film surface ($\delta_c < \delta$), and varies with the radial position further downstream,

$$c_\delta = \begin{cases} 1 & \delta_c < \delta \\ c_\delta(r) & \delta_c = \delta. \end{cases} \tag{2.157}$$

The coefficients of the third-order polynomial are evaluated from the boundary conditions Eqs. (2.87)-(2.90), so that Eq. (2.156) is rewritten as

$$\frac{c}{c_\delta(r)} = \frac{3}{2}\frac{z}{\delta_c} - \frac{1}{2}\frac{z^3}{\delta_c^3}. \tag{2.158}$$

The entry length r_c, which is determined as the radial extension, where the concentration boundary layer δ_c reaches the free surface δ, depends on the magnitude of the Schmidt number. The diffusion coefficients of the considered species in the aqueous working liquid solutions are of the order of D=$\mathcal{O}(10^{-9}$ m^2/s), yielding a large Schmidt number of the order of Sc=$\mathcal{O}(10^3)$. Thus, the evolution of the thin concentration boundary layer will not be confined to the radially inner region associated with smooth flow. Unlike the thermal

boundary layer the concentration boundary layer has therefore to be accounted for as well, when modeling the species mass transfer in the unsteady wavy film occurring in the outer radial region.
The evolution of the concentration boundary layer under wavy flow conditions is mathematically described by introducing the variable $\beta = \delta_c/\delta$, which denotes the relative thickness of the concentration boundary layer. The composite profile assumption (2.158) can then be rewritten in terms of the rescaled wall normal coordinate $\zeta = z/\delta$, and β, as

$$c(\zeta) = \begin{cases} c_\delta \left(\frac{3}{2\beta}\zeta - \frac{1}{2\beta^3}\zeta^3 \right) & 0 \leq \zeta \leq \beta, \\ c_\delta & \beta < \zeta \leq 1. \end{cases} \tag{2.159}$$

Using the composite profile function written as Eq. (2.159) produces the following expression for the depth-averaged species mass fraction $\overline{c}$

$$\frac{1}{\delta}\int_0^\delta c\,dz = \frac{1}{\delta}\left[\int_0^{\delta_c} c\,dz + \int_{\delta_c}^{\delta} c\,dz\right] = \int_0^\beta c\,d\zeta + \int_\beta^1 c\,d\zeta = c_\delta\left(1 - \frac{3}{8}\beta\right). \tag{2.160}$$

The integration of the convective transport term yields

$$\frac{1}{\delta}\int_0^\delta uc\,dz = c_\delta\overline{u} - \frac{3}{10}\beta^2 c_\delta\overline{u} + \frac{1}{16}\beta^3 c_\delta\overline{u}. \tag{2.161}$$

Herein, only the quadratic profile assumption of the radial velocity u, given by Eq. (2.133), was used for simplicity again.

Incorporating the expressions (2.160)-(2.161) into the IBL approximation for the species transport Eq. (2.155) yields the following depth-averaged evolution equation

$$\frac{\partial}{\partial t}\left[\delta c_\delta - \frac{3}{8}\beta\delta c_\delta\right] + \frac{1}{r}\frac{\partial}{\partial r}\left[r\delta\overline{u}c_\delta - \frac{3}{10}r\delta\overline{u}c_\delta\beta^2 + \frac{1}{16}r\delta\overline{u}c_\delta\beta^3\right] = -\frac{1}{Sc}\frac{1}{\delta}\frac{3c_\delta}{2\beta}. \tag{2.162}$$

Evidently, the transport equation (2.162) contains the two unknown dependent variables β and c_δ. These two quantities are by definition alternately varying or constant, i.e.

- β varies, if $c_\delta = 1 = const.$,
- c_δ varies, if $\beta = 1 = const.$,

so that the transport equation (2.162) can be separately solved for each case. The solution follows a concept suggested by Matar et al. [91] in an IBL-based computation of gas absorption into liquid films. According to this approach Eq. (2.162) is rewritten using a newly introduced variable $\omega = \beta^2$, and recalling the depth-averaged continuity equation, Eq. (2.125), to substitute $\partial\delta/\partial t$, which yields

$$\begin{aligned}\left(\frac{16\sqrt{\omega}}{3c_\delta} - \frac{2\omega}{c_\delta}\right)\left[\frac{\partial c_\delta}{\partial t} + \frac{80-24\omega+5\omega^{3/2}}{80-30\sqrt{\omega}}\overline{u}\frac{\partial c_\delta}{\partial r}\right] \\ - \left[\frac{\partial \omega}{\partial t} + \left(\frac{8}{5}\sqrt{\omega} - \frac{1}{2}\omega\right)\overline{u}\frac{\partial \omega}{\partial r}\right] = \\ - \frac{8}{Sc}\frac{1}{\delta^2} - \frac{1}{\delta}\frac{1}{r}\frac{\partial}{\partial r}\left(r\overline{u}\delta\right)\left(2\omega - \frac{8}{5}\omega^{3/2} + \frac{1}{3}\omega^2\right).\end{aligned} \tag{2.163}$$

Defining the square-bracketed terms as total directional derivatives

$$\mathcal{D}_1 c_\delta := \left[\frac{\partial}{\partial t} + \overline{u}\frac{80-24\omega+5\omega^{3/2}}{80-30\sqrt{\omega}}\frac{\partial}{\partial r}\right] c_\delta, \tag{2.164}$$

and

$$\mathcal{D}_2 \omega := \left[\frac{\partial}{\partial t} + \overline{u}\left(\frac{8}{5}\sqrt{\omega} - \frac{1}{2}\omega\right)\frac{\partial}{\partial r}\right]\omega, \tag{2.165}$$

and abbreviating the RHS as Θ, Eq. (2.163) is compactly rewritten as

$$\left(\frac{16\sqrt{\omega}}{3c_\delta} - \frac{2\omega}{c_\delta}\right)\mathcal{D}_1 c_\delta - \mathcal{D}_2 \omega = \Theta. \tag{2.166}$$

Equation (2.166) is separately solved for ω and c_δ as their total directional derivatives become alternately zero, dependent on two distinct scenarios, which are described in the following. The first scenario is associated with $\omega < 1$. This implies that $\delta_c < \delta$ and $c_\delta = const.$, so that $\mathcal{D}_1 c_\delta = 0$ and Eq. (2.166) reduces to

$$\omega < 1: \quad \mathcal{D}_2 \omega = -\Theta. \tag{2.167}$$

The second scenario is associated with $\omega = 1 = const.$, so that the total directional derivative of ω is zero, $\mathcal{D}_2 \omega = 0$, and hence, Eq. (2.166) reads

$$\omega = 1: \quad \mathcal{D}_1 c_\delta = \frac{3c_\delta}{10}\Theta. \tag{2.168}$$

The second scenario further requires $\Theta < 0$ to avoid an unphysical increase of the surface mass fraction c_δ. This implies that the case $\Theta > 0$ is always associated with the occurrence of a concentration boundary layer $\delta_c < \delta$, and, therefore, falls into the first scenario.

Thus, the decision on which of the total directional derivatives $\mathcal{D}_1 c_\delta$ and $\mathcal{D}_2 \omega$ becomes alternatively zero, so that the transport equation (2.162) can be separately solved for ω and c_δ, is finally based on the value of ω and the sign of Θ:

- $\omega < 1$ `OR` $\Theta > 0$:

$$\frac{\partial \omega}{\partial t} + \overline{u}\left(\frac{8}{5}\sqrt{\omega} - \frac{1}{2}\omega\right)\frac{\partial \omega}{\partial r} = -\Theta, \tag{2.169}$$

- $\omega = 1$ `AND` $\Theta < 0$:

$$\frac{\partial c_\delta}{\partial t} + \overline{u}\frac{61}{50}\frac{\partial c_\delta}{\partial r} = \frac{3c_\delta}{10}\Theta. \tag{2.170}$$

The distinction between the two scenarios given by (2.169) and (2.170) is mathematically incorporated introducing the unit step function

$$\mathcal{H}(x) = \begin{cases} 0 & \text{x}<0, \\ 1 & \text{x}\geq 0, \end{cases} \tag{2.171}$$

so that Eq. (2.166) is partitioned into the two separate evolution equations

$$\frac{\partial \omega}{\partial t} + \overline{u}\left(\frac{8}{5}\sqrt{\omega} - \frac{1}{2}\omega\right)\frac{\partial \omega}{\partial r} = -\Theta\left[1 - \mathcal{H}(-\Theta)\mathcal{H}(\omega - 1)\right], \tag{2.172}$$

and

$$\frac{\partial c_\delta}{\partial t} + \overline{u}\frac{61}{50}\frac{\partial c_\delta}{\partial r} = \frac{3c_\delta}{10}\Theta\mathcal{H}(-\Theta)\mathcal{H}(\omega - 1). \tag{2.173}$$

Equations (2.172)-(2.173) cover mathematically all the possibilities described by the scenarios given by Eqs. (2.169)-(2.170).

2.3.4 Steady-state smooth film solutions

Steady-state hydrodynamics

Assuming steady-state conditions the IBL equations governing the hydrodynamics defined by Eqs. (2.132) are considerably simplified, as they reduce to ordinary differential equations for the film thickness and the depth-averaged velocity components $\overline{u}$ and $\overline{v}$,

$$\frac{d}{dr}\left(r\overline{u}\delta\right) = 0, \tag{2.174}$$

$$\frac{1}{r}\frac{d}{dr}\left(k_a r\overline{u}^2\delta\right) - \frac{k_c\overline{v}^2\delta}{r} = 2\overline{v}\delta + b_1\delta\left(r - \epsilon Fr^{-1}\frac{d\delta}{dr}\right) - b_2\frac{\overline{u}}{\delta}, \tag{2.175}$$

$$\frac{1}{r}\frac{d}{dr}\left(k_b r\overline{u}\,\overline{v}\delta\right) + \frac{k_b\overline{u}\,\overline{v}\delta}{r} = -2\overline{u}\delta - \frac{5}{2}\frac{\overline{u}}{\delta}. \tag{2.176}$$

Since the steady-state solution can only produce smooth film flow the influence of the capillary pressure will be negligible, and the pressure expression Eq. (2.131) reduces to

$$P = \epsilon Fr^{-1}\delta. \tag{2.177}$$

The integration of the continuity equation Eq. (2.174) provides a simple relation for the film thickness and the depth-averaged radial velocity,

$$r\overline{u}\delta = const. = \frac{1}{3}. \tag{2.178}$$

The value of the integration constant is chosen to be $1/3$, so that (2.178) is consistent with the volumetric flow rate Q,

$$Q = 2\pi(rl_0)(\delta\delta_0)(\overline{u}u_0). \tag{2.179}$$

Using Eq. (2.178) the radial momentum equation Eq. (2.175) can be rewritten in terms of an ordinary differential equation for the film thickness δ as

$$\frac{d\delta}{dr} = \frac{-3\beta_2 r^2 + k_a\delta + 9r^2(\beta_1 r^2 + \overline{v}(2r + k_c\overline{v}))\delta^3}{-k_a r + 9\beta_1\epsilon Fr^{-1}r^3\delta^3}. \tag{2.180}$$

Similarly, the azimuthal momentum equation can be rewritten in terms of $d\overline{v}/dr$, which yields

$$\frac{d\overline{v}}{dr} = \frac{-5r - 4r\delta^2 - 4k_b\delta^2\overline{v} - 2k_b r\delta\overline{v}\,(d\delta/dr)}{2k_b r\delta^2}. \tag{2.181}$$

To solve Eq. (2.180) and Eq. (2.181) appropriate inflow conditions have to be prescribed at the radially inner boundary, which is located at $r = r_i$. Appropriate values for $\overline{u}_i$, $\overline{v}_i$, and δ_i may be obtained from experimental data, or from a numerical simulation of the central impingement region. Extending the formulation to track the development of the boundary layers for the radial and azimuthal velocities allows for a less specific prescription of the inflow conditions. This extended concept will be discussed at the end of this section.

Far-field solution of the IBL equations

Kim and Kim [75] used the perturbation method to obtain a far-field asymptotic solution of Eqs. (2.174)-(2.176) in terms of a series expansion with $r \gg 1$ as expansion parameter written as

$$\delta = r^{-2/3} + \left(\frac{44}{225} - \frac{2}{9}\epsilon Fr^{-1}\right) r^{-10/3} + \mathcal{O}(r^{-4}), \tag{2.182}$$

$$\overline{u} = \frac{1}{3}r^{-1/3} - \frac{1}{3}\left(\frac{44}{225} - \frac{2}{9}\epsilon Fr^{-1}\right) r^{-3} + \mathcal{O}(r^{-11/3}), \tag{2.183}$$

$$\overline{v} = -\frac{4}{15}r^{-5/3} - \left(\frac{1912}{23625} - \frac{8}{135}\epsilon Fr^{-1}\right) r^{-13/3} + \mathcal{O}(r^{-5}). \tag{2.184}$$

These results are in excellent agreement with the results from the asymptotic expansion of the full Navier-Stokes equations, Eqs. (2.101)-(2.103), obtained by Rauscher et al. [53], which were presented in section 2.2.2.

Kim and Kim [75] also analyzed the asymptotic behavior in the limit of small radii, $r \ll 1$. In this limit the radial momentum balance is governed by the inertial and viscous forces, while the azimuthal momentum balance is governed by the Coriolis force as well. The asymptotic solution obtained in this inner radial region reads (cf. Kim and Kim [75])

$$\delta = \frac{C}{r} + \frac{5r^2}{2k_a}, \tag{2.185}$$

$$\overline{u} = \frac{1}{3C + 15r^3/(2k_a)}, \tag{2.186}$$

$$\overline{v} = -\frac{r}{k_b} + \frac{2r^4}{Ck_b^2} + \mathcal{O}(r^7), \tag{2.187}$$

involving a constant parameter C, which has to be determined from an appropriate inflow condition.

Steady-state heat transfer

The steady-state solution for heat transfer distinguishes a radial inner region, $r < r_T$, where the boundary layer of the temperature has not reached the surface of the film ($\delta_T < \delta$), from a outer region associated with $\delta_T = \delta$. The solution in the inner radial region $r < r_T$ is obtained by integrating Eq. (2.74), rewritten without the transient terms and incorporating the depth-averaged continuity equation $r\overline{u}\delta = 1/3$,

$$\frac{1}{r}\frac{d}{dr}\left[\frac{1}{3}\left(\frac{\delta_T}{\delta}\right)^3\left(\frac{1}{5}\delta - \frac{1}{24}\delta_T\right)\right] = \frac{1}{Pr}. \tag{2.188}$$

The integration of Eq. (2.188) yields the evolution of the thermal boundary layer thickness until it reaches the surface, such that $\delta_T = \delta$ at $r = r_T$.
For $r \geq r_T$ the steady-state depth-averaged temperature transport equation Eq. (2.154) reduces to

$$\frac{d\theta_w}{dr} = \frac{61}{120}\frac{d\delta}{dr} + \frac{3r}{Pr}. \tag{2.189}$$

IBL far-field solution for heat transfer

In the limit of large radii thermally developed flow conditions are met, i.e., $r > r_T$ and $\delta_T = \delta$, and the steady-state approximation for the film thickness is given by $\delta = r^{-2/3}$, so that Eq. (2.189) becomes

$$\frac{d\theta_w}{dr} = -\frac{61}{180}\frac{1}{r^{5/3}} + \frac{3r}{Pr}. \tag{2.190}$$

The integration of Eq.(2.190) using Eq. (2.148) evaluated at $r = r_T$ as radially inner boundary condition

$$r = r_T: \qquad \theta_w = 2\delta/3 \tag{2.191}$$

yields

$$\theta_w = \frac{61}{120}r^{-2/3} + \frac{19}{120}r_T^{-2/3} + \frac{3}{2}\frac{r^2}{Pr} - \frac{3}{2}\frac{r_T^2}{Pr}. \tag{2.192}$$

The computation of the far-field solution for heat transfer can also be useful for estimating the effect of a possible convective heat flux at the liquid surface written as

$$\left.\frac{\partial\theta}{\partial z}\right|_{z=\delta} = -\frac{\alpha\delta_0(\theta_a - \theta_\delta)}{\lambda}, \tag{2.193}$$

where θ_δ and θ_a denote the dimensionless temperatures at the liquid surface and the ambient air, respectively. The required values for the heat transfer coefficient α can be obtained using a correlation proposed for laminar flow (Wagner [97]), which is valid for subcritical values of the rotational Reynolds number, $Re_\Omega = \tilde{r}^2\Omega/\nu_a < Re_{\Omega,crit} = 250.000$,

$$Nu = \frac{\alpha\tilde{r}}{\lambda_a} = \hat{C}Re_\Omega^{1/2}. \tag{2.194}$$

The parameter $\hat{C}$ is set to 0.335, which is proposed for the value of the ambient Prandtl number Pr=0.74. Prescribing the convective heat flux given by Eq. (2.193) as upper non-adiabatic boundary condition modifies the profile function Eq. (2.149), which was obtained for the dimensionless temperature using an adiabatic upper boundary condition Eq. (2.84) to

$$\theta = \theta_w + \delta\left[\frac{1}{3}\left(1 - \frac{\alpha\delta_0(\theta_a - \theta_\delta)}{\lambda}\right)\frac{z^3}{\delta^3} - \frac{z}{\delta}\right]. \tag{2.195}$$

Using this modified profile function for the integral of the convective term in Eq. (2.145) the steady-state depth-averaged heat transfer equation in the limit of large radii is obtained as

$$\frac{d\theta_w}{dr} = \frac{3\lambda r^{2/3}\left(540r^{8/3} - 61Pr\right)}{180r^{5/3}Pr\left(3\lambda r^{2/3} - \alpha\delta_0\right)} + \frac{\alpha\delta_0\left[Pr\left(61 + 42r + 63r^{5/3}\theta_a\right) + 9r^{5/3}\theta_w\left(180r^{5/3} - 7Pr\right)\right]}{180r^{5/3}Pr\left(3\lambda r^{2/3} - \alpha\delta_0\right)}. \tag{2.196}$$

For $\alpha = 0$ equation (2.196) is identical to Eq. (2.190), which is based on the adiabatic upper boundary condition.

A comparison of the results for the dimensionless wall temperature obtained from the far-field solutions Eqs. (2.190) and (2.196), using the adiabatic and non-adiabatic surface boundary conditions, respectively, will be shown in Sec. 4.1.2.

Steady-state species mass transfer

Assuming steady-state conditions for the species mass transfer Eq. (2.163) reduces to

$$\left(\frac{16\sqrt{\omega}}{3c_\delta} - \frac{2\omega}{c_\delta}\right)\left[\frac{80 - 24\omega + 5\omega^{3/2}}{80 - 30\sqrt{\omega}}\overline{u}\frac{dc_\delta}{dr}\right] - \left[\left(\frac{8}{5}\sqrt{\omega} - \frac{1}{2}\omega\right)\overline{u}\frac{d\omega}{dr}\right] = -\frac{8}{Sc}\frac{1}{\delta^2} \tag{2.197}$$

The RHS, formerly denoted with Θ, is always negative in case of steady-state smooth flow, so that Eq. (2.197) can be separately solved for ω or c_δ depending on the development of the boundary layer δ_c:

- $\delta_c < \delta$, $\omega < 1$:

$$c_\delta = 1, \qquad \overline{u}\left(\frac{8}{5}\sqrt{\omega} - \frac{1}{2}\omega\right)\frac{d\omega}{dr} = \frac{8}{Sc}\frac{1}{\delta^2}, \tag{2.198}$$

- $\delta_c = \delta$, $\omega = 1$:

$$\omega = 1, \qquad \overline{u}\frac{dc_\delta}{dr} = -\frac{120}{61}\frac{c_\delta}{Sc}\frac{1}{\delta^2}. \tag{2.199}$$

The transition between both regions occurs at $\delta_c = \delta$, corresponding to a fixed radial position $r = r_c$, which can be determined from the condition

$$c_\delta(r_c) = 1. \tag{2.200}$$

Using the steady-state continuity equation $r\overline{u}\delta = 1/3$ Eqs. (2.198)-(2.199) can be rewritten as

$$\omega < 1: \quad \frac{d\delta_c}{dr} = \beta\frac{d\delta}{dr} + \frac{r}{Sc}\left(\frac{120}{16\beta^2 - 5\beta^3}\right), \tag{2.201}$$

$$\omega = 1: \quad \frac{dc_\delta}{dr} = -\frac{360}{61}\frac{rc_\delta}{\delta Sc}. \tag{2.202}$$

It becomes evident that for $\omega < 1$ the thickness of the boundary layer δ_c is monotonically increasing, and for $\omega = 1$ the species mass fraction at the free surface, c_δ, is decreasing with increasing radii. The latter behavior guarantees a monotonic decrease of depth-averaged species mass fraction $\overline{c}$.

IBL far-field solution for species transport

Considering the steady-state approximation for the film thickness to be given by $\delta = r^{-2/3}$, an asymptotic solution in the limit of large radii for the species mass fraction at the free surface is obtained as

$$c_\delta(r) = \exp\left[-\frac{135}{61Sc}\left(r^{8/3} - r_c^{8/3}\right)\right]. \tag{2.203}$$

Boundary layer assumption (BLA) for the central impingement region

A physically more accurate description of the flow in the central impingement region can be obtained by distinguishing the boundary layers of the radial and azimuthal velocities inside the liquid, δ_r and δ_ϕ, respectively, developing both from the point of impingement, as sketched in Fig. 2.3. Analogously to the temperature and the species mass fraction, where the thermal and the concentration boundary layers, δ_T and δ_c, are distinguished as separate sublayers, respectively, the depth-averaging procedure of the governing thin film momentum equations (2.71)-(2.72) has accordingly to be split into the subintervals $0 \leq z \leq \delta_m$, and $\delta_m \leq z \leq \delta$, symbolically written as

$$\int_0^\delta [\cdots]\, dz = \underbrace{\int_0^{\delta_m} [\cdots]\, dz}_{(\star)} + \underbrace{\int_{\delta_m}^{\delta} [\cdots]\, dz}_{(\star\star)}, \tag{2.204}$$

where δ_m represents the thickness of the considered boundary layer. Assuming constant free-stream values for the velocity, the dimensionless temperature, and the species mass fraction outside the corresponding boundary layer the contribution of the second integration $(\star\star)$ is identically zero, so that only the first integral $(\star)$ has to be considered. This

can be, for example, easily shown for the depth-averaging of the radial momentum equation, Eq. (2.71), assuming $u|_{z>\delta_r} = u_i = const.$, $v|_{z>\delta_\phi} = -r$, and $p = const.$, so that the contributions of the integration $(\star\star)$ cancel

$$\int_{\delta_r}^{\delta} -r\,dz = \int_{\delta_r}^{\delta} (-2r + r)\,dz. \tag{2.205}$$

Similarly, for the depth-averaging of the azimuthal momentum equation, Eq. (2.72), assuming $v|_{z>\delta_\phi} = -r$, the contributions of the integration $(\star\star)$ cancel as well

$$\int_{\delta_\phi}^{\delta} \left(-u - \frac{ur}{r}\right) dz = \int_{\delta_\phi}^{\delta} -2u\,dz. \tag{2.206}$$

Thus, assuming constant free-stream velocities, $u|_{z>\delta_r} = u_i$, and $v|_{z>\delta_\phi} = -r$, the depth-averaging of the steady-state momentum equations for the radial and azimuthal momentum is written as

$$\frac{1}{r}\frac{d}{dr}\int_0^{\delta_r} ru^2\,dz - \int_0^{\delta_r} \frac{v^2}{r}\,dz = 2\int_0^{\delta_r} v\,dz + r\delta_r - \delta_r \epsilon Fr^{-1}\frac{d\delta_r}{dr} - \left.\frac{\partial u}{\partial z}\right|_{z=0}, \tag{2.207}$$

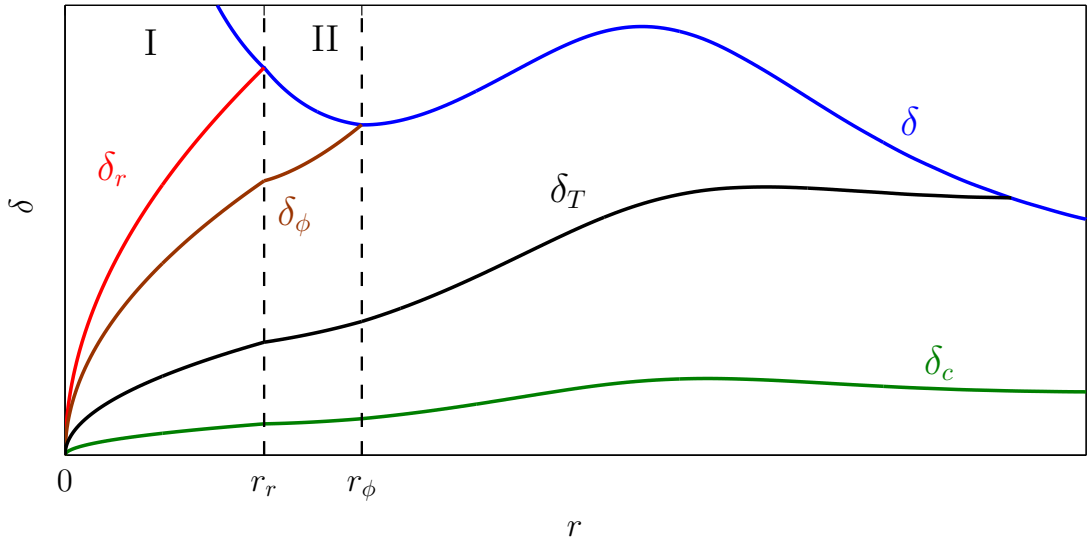

Figure 2.3: Sketch of the radial development of the boundary layers of the radial velocity, azimuthal velocity, temperature, and species mass fraction, δ_r, δ_ϕ, δ_T, and δ_c, respectively.

and

$$\frac{1}{r}\frac{d}{dr}\int_0^{\delta_\phi} ruv\,dz + \int_0^{\delta_\phi} \frac{uv}{r}\,dz = -2\int_0^{\delta_\phi} u\,dz - \left.\frac{\partial v}{\partial z}\right|_{z=0}, \tag{2.208}$$

respectively. Inside the boundary layers, $z \leq \delta_r$, and $z \leq \delta_\phi$, the velocity profile assumptions are applied, while constant free-stream values are used beyond. The stress-free boundary conditions, Eqs. (2.78) and (2.79), are consistently imposed at $z = \delta_r$ and $z = \delta_\phi$, respectively. Once the radially growing thickness of an individual boundary layer has reached the liquid surface, the corresponding upper boundary is set to the film height $\delta_r = \delta$, and $\delta_\phi = \delta$, respectively.
Accounting for the development of boundary layers also in the momentum transport basically allows for a physically sounder description of the flow in the central impingement region, as no presumptions for the film thickness and the depth-averaged velocity components are required at the inflow boundary. At the center $r = 0$ only the free stream velocity has to be prescribed as inflow boundary condition. Assuming a frictionless redirection of the vertically impinging jet the free-stream velocity, $u_i = \tilde{u}_i/u_0$, is set to the value of the vertical impingement velocity $\tilde{w}_{imp}/u_0$. As such the radial inflow velocity is computed dependent of the volumetric flow rate Q, the nozzle radius $\tilde{r}_n$, and the nozzle-to-disk distance $\tilde{h}_n$, following Bernoulli's equation

$$u_i = \frac{\tilde{w}_{imp}}{u_0} = \frac{1}{u_0}\sqrt{\left(\frac{Q}{\tilde{r}_n^2\pi}\right)^2 + 2g\tilde{h}_n}. \tag{2.209}$$

Assuming constant free-stream values, $\theta|_{z>\delta_T} = 0$, for the non-dimensional temperature, and, $c|_{z>\delta_c} = 1$, for the mass species concentration the subdivided integration, Eq. (2.204), of the convection-diffusion equations for the heat and species mass transfer, Eq. (2.74) and Eq. (2.75), respectively, yields

$$\frac{1}{r}\frac{d}{dr}\int_0^{\delta_T} ru\theta\,dz = \frac{1}{Pr}, \tag{2.210}$$

and

$$\frac{1}{r}\frac{d}{dr}\int_0^{\delta_c} ruc\,dz = -\frac{1}{Sc}\left.\frac{\partial c}{\partial z}\right|_{z=0}. \tag{2.211}$$

All the free-stream values which are imposed at the corresponding upper boundaries in the regions I and II are summarized in table 2.2.

	impingement region I				impingement region II			
independent variable	u	v	c	θ	u	v	c	θ
upper boundary at $\delta_m =$	δ_r	δ_ϕ	δ_c	δ_T	δ	δ_ϕ	δ_c	δ_T
imposed value at $z = \delta_m$:	u_i	$-r$	1	0	u_δ	$-r$	1	0

Table 2.2: Free-stream values imposed at upper boundary $z = \delta_m$ when using the boundary layer assumption (BLA) for the central impingement region.

Using the quartic profile assumption described in section 2.3.1 the evaluation of equations (2.207)-(2.208) yields inside the impingement region I two coupled ordinary differential equations for the thickness of the radial and azimuthal boundary layers written as

$$\frac{d\delta_r}{dr}\left(\delta_r \epsilon Fr^{-1} - \frac{2}{15}u_i^2\right) = \frac{2}{15}\frac{u_i^2}{r}\delta_r - \frac{r\delta_r}{5} - \frac{8u_i}{5\delta_r} + \frac{1763}{7875}r\delta_\phi, \tag{2.212}$$

and

$$\begin{aligned}\frac{d\delta_\phi}{dr}\left(\frac{28r}{75}\frac{\delta_\phi}{\delta_r} - \frac{12r}{105}\frac{\delta_\phi^2}{\delta_r^2}\right) = &\frac{8r}{5\delta_\phi u_i} + \frac{4}{35}\frac{\delta_\phi^3}{\delta_r^2} \\ &- \frac{14}{25}\frac{\delta_\phi^2}{\delta_r} - \frac{d\delta_r}{dr}\left(\frac{8r}{105}\frac{\delta_\phi^3}{\delta_r^3} - \frac{14r}{75}\frac{\delta_\phi^2}{\delta_r^2}\right),\end{aligned} \tag{2.213}$$

respectively. The film thickness in the inner impingement region I can then simply be obtained from the continuity restriction

$$Q = 2\tilde{r}\pi\tilde{\delta}\overline{\tilde{u}} = 2\tilde{r}\pi\tilde{u}_i\left(\tilde{\delta} - \tilde{\delta}_r\right) + 2\tilde{r}\pi\tilde{\delta}_r\overline{\tilde{u}}_{\tilde{\delta}_r}, \tag{2.214}$$

resulting in

$$\delta = \frac{Q}{2\tilde{r}\pi\tilde{u}_i} - \frac{\tilde{\delta}_r\overline{\tilde{u}}_{\tilde{\delta}_r}}{\tilde{u}_i} + \tilde{\delta}_r. \tag{2.215}$$

The system Eqs. (2.212)-(2.213) is extended by analogously coupled ODE's

$$\frac{d\delta_T}{dr} = \frac{180r\delta^3 - 24Pru_i\delta^2\delta_T^3 + 5Pru_i\delta\delta_T^4 + 24rPru_i\delta\delta_T^3\frac{d\delta}{dr} - 10rPru_i\delta_T^4\frac{d\delta}{dr}}{72rPru_i\delta^2 - 20rPru_i\delta\delta_T^3}, \tag{2.216}$$

for the thermal boundary layer, and by

$$\begin{aligned}\frac{d\delta_c}{dr}\left(\frac{1}{8}\frac{\delta_c^2}{\delta_r^2} - \frac{2}{5}\frac{\delta_c}{\delta_r}\right) = &-\frac{3}{2Sc\delta_c u_i} \\ &- \frac{1}{r}\left(\frac{1}{24}\frac{\delta_c^3}{\delta_r^2} - \frac{1}{5}\frac{\delta_c^2}{\delta_r}\right) - \frac{d\delta_r}{dr}\left(\frac{1}{5}\frac{\delta_c^2}{\delta_r^2} - \frac{1}{12}\frac{\delta_c^3}{\delta_r^3}\right),\end{aligned} \tag{2.217}$$

for the concentration boundary layer, when including the heat transfer, and species mass transport in a binary mixture, respectively.

In the region II the boundary layer of the radial velocity component has reached the free surface, $\delta_r = \delta$, and the following two ordinary differential equations for the film thickness and the thickness of the azimuthal boundary layer are obtained:

$$\frac{d\delta}{dr}\left(\delta\epsilon Fr^{-1} - \frac{125}{864r^2\delta^2} - \frac{10\delta}{432} + \frac{5r^2\delta^2}{4320}\right) = \frac{125}{864r^3\delta} - \frac{5}{6r\delta^2} - \frac{3r\delta^5}{4320} + \frac{5\delta^2}{432r} - \frac{r\delta}{6} + \frac{1763}{7875}r\delta_\phi, \tag{2.218}$$

and

$$\frac{d\delta_\phi}{dr}\left(\frac{14}{75}\frac{\delta_\phi}{\delta^2} - \frac{6}{105}\frac{\delta_\phi^2}{\delta^3}\right) = \frac{8r}{5\delta_\phi} + \frac{4}{105r}\frac{\delta_\phi^3}{\delta^3} - \frac{14}{75r}\frac{\delta_\phi^2}{\delta^2} - \frac{d\delta}{dr}\left(\frac{6}{105}\frac{\delta_\phi^3}{\delta^4} - \frac{14}{75}\frac{\delta_\phi^2}{\delta^3}\right). \tag{2.219}$$

If heat and mass transfer are included the system (2.218)-(2.219) is extended by Eq. (2.188) and Eq. (2.201) to compute δ_T and δ_c, respectively.

Radially downstream from the position, where the boundary layer of the azimuthal velocity component reaches the free surface, $\delta_\phi = \delta$, the original formulation given by Eqs. (2.174)-(2.176) is solved assuming steady state. The system is extended by Eqs. (2.188)-(2.189), or by Eqs. (2.201)-(2.202), when heat or species mass transfer are included, respectively.

Boundary layer assumption (BLA) vs. developed film assumption (DFA)

In the following the IBL approximation, which starts the radial integration from the center, $r_i = 0$, considering the development of the velocity boundary layers (inside region I and II, as shown in Fig. 2.4),is referred to as boundary layer assumption (BLA). On the other hand the IBL approximation, which starts the integration at a certain radial inner boundary $r = r_i$ with prescribed inlet values for δ_i, $\overline{u}_i$, and $\overline{v}_i$, is referred to as developed film assumption (DFA), as this approach assumes that both the velocity boundary layers δ_r and δ_ϕ have already reached the free surface upstream of the inner radial boundary $r = r_i$. The film thickness needed by the DFA at the inner boundary, $\delta_i = \delta_{r=r_i}$, has to be assumed, or can be taken from CFD results, if available. The required depth-averaged inflow velocities, $\overline{u}_i = \overline{u}|_{r=r_i}$, $\overline{v}_i = \overline{v}|_{r=r_i}$, can be computed from the asymptotic solutions for small radii, $r \ll 1$, given by Eqs. (2.186) and (2.187).

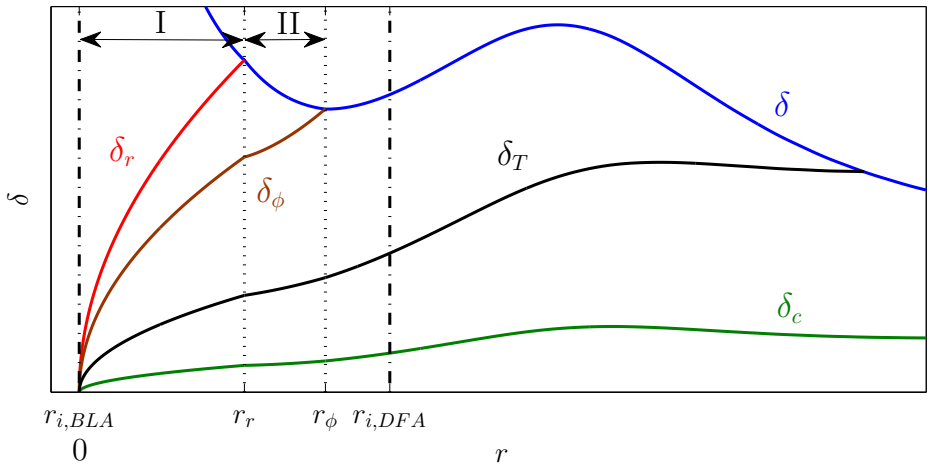

Figure 2.4: Scope of boundary layer assumption (BLA) and developed film assumption (DFA).

2.4 Modeling wet chemical surface etching

In the semiconductor industry spin processors are widely used for the surface preparation of silicon wafers. One major application in this particular spin-processing technology is the wet chemical etching. A useful parameter to determine the reaction regime of the wet chemical etching process is the Damköhler number Da. It basically relates the time scale of the chemical reaction, τ_{chem}, to the time scale of the mass transport of the etchant into the reactive layer, τ_{diff}, such that

$$Da = \frac{\tau_{diff}}{\tau_{chem}} . \tag{2.220}$$

As the mass transport essentially relies on the diffusive transport towards the wall, the corresponding time scale can be estimated in terms of the diffusivity of the etchant D and the characteristic film height $\delta_0 = (\nu/\Omega)^{1/2}$,

$$\tau_{diff} \approx \frac{\delta_0^2}{D} . \tag{2.221}$$

The reactive time scale τ_{chem} is determined by the governing chemical etching mechanism, such that it scales with the inverse of the rate determining reaction rate

$$\tau_{chem} \approx \frac{1}{\dot{\omega}} . \tag{2.222}$$

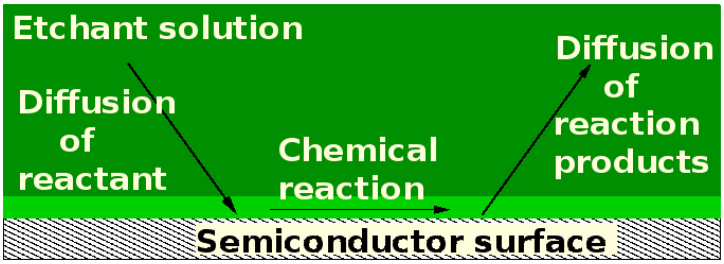

Figure 2.5: Schematic representation of main rate limiting mechanisms involved in wet chemical etching.

Based on the Damköhler number two asymptotic limits can be distinguished. The first asymptotic limit is associated with small Damköhler number and very slow chemistry as compared to the transport of the etchant towards the solid surface. In this case the etching rate will be mainly controlled by the timescale of the chemical reaction kinetics. Since the reaction kinetics strongly depends on the temperature of the liquid near the wall, one can also speak of a temperature controlled limit. In the second asymptotic limit, associated with large Damköhler number and very fast chemistry, the etching process is controlled by the mass transfer of the primary etchant component towards the solid surface.

2.4.1 Reaction controlled chemistry ($Da \ll 1$)

As an example for a reaction controlled wet chemical etching process, the present study considers the etching of silicon-dioxide (SiO_2) with diluted hydrofluoric acid (HF) as chemical system. Assuming a global one-step mechanism the overall dissolution of SiO_2 is governed by the following chemical reaction (see, e.g. Monk et al. [98])

$$SiO_2 + 6HF \rightarrow H_2SiF_6 + 2H_2O.$$

Following Staudegger [82] the rate of this reaction can be described by an Arrhenius type equation

$$k = A \exp\left[-\frac{E_a}{R_g}\frac{1}{T}\right], \tag{2.223}$$

where the prefactor A has the dimension of a velocity, E_a denotes the activation energy, and R_g is the molar gas constant with a value of R_g=8.3145 $\mathrm{J}/(\mathrm{K\,mol})$.

Staudegger [82] measured the etching abrasion

$$\Delta z_{etch} = k \cdot \tilde{t}_{etch} \tag{2.224}$$

for a given exposure time $\tilde{t}_{etch}$ in a number of experiments to obtain several values of k at varying temperature T. A best fit of Eq. (2.223) to these experimental data gave the values E_a/R_g=3978 K and A=8.29×10^5 Å/s. The so obtained reaction velocity in the considered range of temperature is always of the order of k=$\mathcal{O}(10^{-10}$ m/s). The diffusion coefficient of hydrofluoric acid in an aqueous solution is of the order of D=$\mathcal{O}(10^{-9}$ m^2/s) (see, e.g. Noulty et al. [99]). Assuming a typical film height of the order of δ_0=$\mathcal{O}(10^{-4}$ m) as a characteristic length scale the Damköhler number for this particular surface etching process can be estimated as

$$Da = \frac{\delta_0}{D} k = \mathcal{O}\left(10^{-5}\right) \ll 1, \tag{2.225}$$

so that $\tau_{chem} \gg \tau_{flow}$, and the assumption of a strongly temperature dependent, reaction controlled chemistry with abundance of the main reactive agent is justified.

2.4.2 Diffusion controlled chemistry ($Da \gg 1$)

The present study considers the etching of silicon (Si) with an aqueous etchant consisting basically of nitric acid (HNO_3) and hydrofluoric acid (HF) as an example for a diffusion controlled wet chemical etching process. Schwartz and Robbins [100] proposed a simplified two-step fast reaction mechanism for the dissolution of Si as

$$\begin{aligned} Si + 4HNO_3 &\rightarrow SiO_2 + 4NO_2 + 2H_2O \\ SiO_2 + 6HF &\rightarrow H_2SiF_6 + 2H_2O. \end{aligned}$$

Following Kaneko et al. [68], for low HNO_3 and high HF concentrations, the rate of this reaction is essentially controlled by the first reaction step. Since this key reaction is assumed as very fast, the Damköhler number is very high, $Da \gg 1$. This implies that the etching reaction is limited by the diffusive flux of the nitric acid molecules towards the surface of the wafer. The diffusion coefficient of nitric acid in an aqueous solution is D=2.4×10^{-9} m^2/s, and the typical film height is of the order of δ_0=$\mathcal{O}(10^{-4}$ m). The velocity of diffusion is thus approximately in the order of $D/\delta_0 \approx \mathcal{O}(10^{-5}$ m/s).
The etching abrasion rate R is proportional to the mass flux of dissolved silicon j_{Si}, i.e.

$$R \propto \frac{j_{Si}}{\rho_{Si}} \quad [\mathrm{m/s}]. \tag{2.226}$$

Assuming a stoichiometric oxidation of silicon by nitric acid,

$$\frac{j_{Si}}{M_{Si}} = -\frac{1}{4} \frac{j_{HNO_3}}{M_{HNO_3}}, \tag{2.227}$$

Eq. (2.226) can be rewritten as

$$R \propto -j_{HNO_3} \frac{1}{4\rho_{Si}} \frac{M_{Si}}{M_{HNO_3}} \quad [\mathrm{m/s}]. \tag{2.228}$$

The diffusive mass flux of the primary etchant species is given by

$$j_{HNO_3} = -\rho D \left. \frac{\partial \tilde{c}}{\partial \tilde{z}} \right|_{\tilde{z}=0} \quad [\mathrm{kg/(m^2 s)}], \tag{2.229}$$

which can be rewritten as in terms of the local Sherwood number

$$Sh = \left. \frac{\partial c}{\partial z} \right|_{z=0}, \tag{2.230}$$

as

$$j_{HNO_3} = -\rho D \frac{\tilde{c}_i}{\delta_0} Sh. \tag{2.231}$$

The etching rate for a diffusion controlled chemistry is proportional to the Sherwood number and computed from

$$R = \hat{k} \frac{1}{\rho_{Si}} \frac{M_{Si}}{4 M_{HNO_3}} \rho D \frac{\tilde{c}_i}{\delta_0} Sh \quad [\mathrm{m/s}] \tag{2.232}$$

using the values ρ_{Si}=2329 kg/m^3, M_{Si}=28.09 g/mol, M_{HNO_3}=63.01 g/mol, and an empirical proportionality constant $\hat{k}$.

3 NUMERICAL SOLUTIONS

3.1 Numerical solution of the Navier-Stokes equations

In the CFD based approach, the unsteady, axisymmetric Navier-Stokes equations (2.37)-(2.38), as well as the energy equation (2.39), or, alternatively, the convection-diffusion equation for a species in a binary mixture, Eq. (2.40), are discretized and numerically solved using the flow simulation software ANSYS FLUENT [101, 102]. In this general purpose CFD code a cell-centered finite-volume method is employed.

3.1.1 Finite Volume Method

The general transport equation for an arbitrary tensorial flow quantity $\varphi(\vec{x},t)$ is given by

$$\underbrace{\frac{\partial \rho\varphi}{\partial t}}_{(i)} + \underbrace{\nabla\cdot(\rho\vec{v}\varphi)}_{(ii)} = \underbrace{\nabla\cdot(\Gamma\nabla\varphi)}_{(iii)} + \underbrace{S_\varphi(\varphi)}_{(iv)}. \tag{3.1}$$

Here Γ denotes the diffusivity and $S_\varphi(\varphi)$ represents a source term. The individual terms in Eq. (3.1) represent the change per unit volume (i), the flux due to convection (ii), the transport due to diffusion (iii), and the rate of production (iv), respectively.

A finite volume discretization of Eq. (3.1) is obtained by integrating over a finite control volume V_P and time Δt,

$$\int_t^{t+\Delta t}\left[\int_{V_P}\frac{\partial\rho\varphi}{\partial t}dV + \int_{V_P}\nabla\cdot(\rho\vec{v}\varphi)\,dV\right]dt = \int_t^{t+\Delta t}\left[\int_{V_P}\left(\nabla\cdot(\Gamma\nabla\varphi)+S_\varphi(\varphi)\right)dV\right]dt. \tag{3.2}$$

The volume integral with the transient term can be approximated first-order accurate in time as

$$\int_V \frac{\partial\rho\varphi}{\partial t}dV \approx \frac{\rho_P^{n+1}\varphi_P^{n+1}-\rho_P^n\varphi_P^n}{\Delta t}V_P, \tag{3.3}$$

with $\varphi^{n+1} = \varphi(t + \Delta t)$ denoting the new value at the cell center (index P) at the time step which is solved for.

The volume integral with the convection term is discretized by transforming the volume integral into a surface integral using Gauss's theorem,

$$\int_{V_P} \nabla \cdot (\rho \vec{v} \varphi)\, dV = \int_S d\vec{S} \cdot (\rho \vec{v} \varphi) \approx \sum_f \vec{S} \cdot (\rho \vec{v})_f \, \varphi_f. \tag{3.4}$$

For the interpolation of the cell-centered values (φ_P) to the values at the cell faces (φ_f) typically second-order-accurate schemes are used.

The discretization of the volume integral with the diffusion term involving the scalar diffusion coefficient Γ, is obtained analogously to the convective flux, written as

$$\int_{V_P} \nabla \cdot (\Gamma \nabla \varphi)\, dV = \int_S d\vec{S} \cdot (\Gamma \nabla \varphi) \approx \sum_f \Gamma_f \left(\vec{S} \cdot \nabla_f \varphi \right). \tag{3.5}$$

The required gradients at the cell faces, $\nabla_f \varphi$, are computed using a second-order-accurate least-squares cell-based approach.

Introducing all the approximations for the volume integrals shown above into Eq. (3.2) the semi-discretized from of the transport equation reads

$$\int_t^{t+\Delta t} \left[\frac{\rho_P^{n+1} \varphi_P^{n+1} - \rho_P^n \varphi_P^n}{\Delta t} V_P + \sum_f \vec{S} \cdot (\rho \vec{v})_f \, \varphi_f \right] dt = \int_t^{t+\Delta t} \left[\sum_f \Gamma_f \left(\vec{S} \cdot \nabla_f \varphi \right) + S_\varphi V_P \right] dt. \tag{3.6}$$

For the temporal discretization the Euler implicit method is used, which implies for the corresponding time integrals

$$\int_t^{t+\Delta t} (\cdots)\, dt \approx (\cdots)^{n+1} \, \Delta t. \tag{3.7}$$

The finally obtained discretized formulation constitutes a set of algebraic equations for each control volume. This algebraic system of equations can be expressed in matrix form involving a sparse coefficient matrix, which is solved using an appropriate linear solver.

Dealing with incompressible flow, the continuity is satisfied based on a velocity-pressure coupling, for which a PISO-type segregated algorithm is used.

3.1.2 Volume of Fluid Method

The description of the two-phase flow is accomplished using the implemented Volume-of-Fluid method (Hirt and Nichols [103]). In this one-fluid formulation, both phases are treated as single continuum, distinguished by a phase-marker function, which is defined as

$$\gamma(\vec{x},t) = \begin{cases} 1 & \text{liquid phase,} \\ 0 & \text{gas phase,} \\ 0 < \gamma_t < 1 & \text{transitional zone.} \end{cases} \tag{3.8}$$

The interface between the phases is tracked solving the phase-marker transport equation

$$\frac{\partial \gamma}{\partial t} + \vec{v} \cdot \nabla \gamma = 0. \tag{3.9}$$

The transitional zone basically represents the interface, where the fluid properties like density or viscosity exhibit a discontinuous step in reality. This transitional zone is here considered to have a small finite thickness t, which is necessary to model the two fluids as a continuum, using the continuity and the momentum equations. The fluid properties, for example the density of the fluid, are determined using the volume-weighted average

$$\rho = \gamma \rho_L + (1-\gamma)\rho_G. \tag{3.10}$$

Here the indices L and G denote the properties of the liquid and the gas phase, respectively.

To guarantee the boundedness of the phase-marker function γ, and to prevent an unphysical smearing of the step-like change at the phase interface an adequate discretization of the phase-marker transport equation has to be employed. For this purpose, the simulation package offers different numerical methods for correcting the fluxes across the faces of the control volumes, from which the High Resolution Interface Capturing scheme (HRIC, Muzaferija et al. [104]) was chosen. This HRIC scheme represents a hybrid scheme based on the blending of bounded downwind and upwind differencing schemes.

In the framework of the implemented VoF method the effect of surface tension is modeled based on the continuum surface force (CSF) model, which was proposed by Brackbill et al. [105]. In this model the capillary force is incorporated in the momentum equations in terms of an appropriate volume force, which is proportional to the curvature of the interface.

3.1.3 Setup

The computational domain and the boundary conditions used in the CFD simulations are sketched in Fig. 3.1. At the liquid inflow boundary a uniform inlet velocity boundary condition, equivalent to the considered volumetric flowrate, was prescribed. The inflow temperature, or alternatively the inflow species mass fraction, were assumed to be constant. The radially inner boundary represents an axis of symmetry, so that symmetry boundary conditions, which are basically zero-gradient conditions, apply. At the upper and radially outer boundaries, pressure outlet boundary conditions were imposed. This boundary condition implies, that the static pressure is prescribed relative to the operating pressure, while all other flow quantities are extrapolated from the interior.

At the surface of the rotating disk a solid wall boundary condition is used, which is associated with no-slip conditions setting the velocity of the liquid equal to the rotational speed of the disk. Furthermore a constant heat flux was assumed for the thermal boundary condition at the wall, while a constant species mass fraction was assumed when modeling the mass transport in a binary mixture.

The steady-state smooth film solutions of the IBL model, presented in Sec. 2.3.4, were used to initialize the volume fraction distribution and the flow field inside the film.
The properties of the three different fluids considered as the liquid phase in the CFD simulations are listed in Tab. 3.1. For the ambient gas phase the properties of air were used, with $\rho_G = \rho_a = 1.225\ \mathrm{kg/m^3}$, $\nu_G = \nu_a = 1.46 \times 10^{-5}\ \mathrm{m^2/s}$.

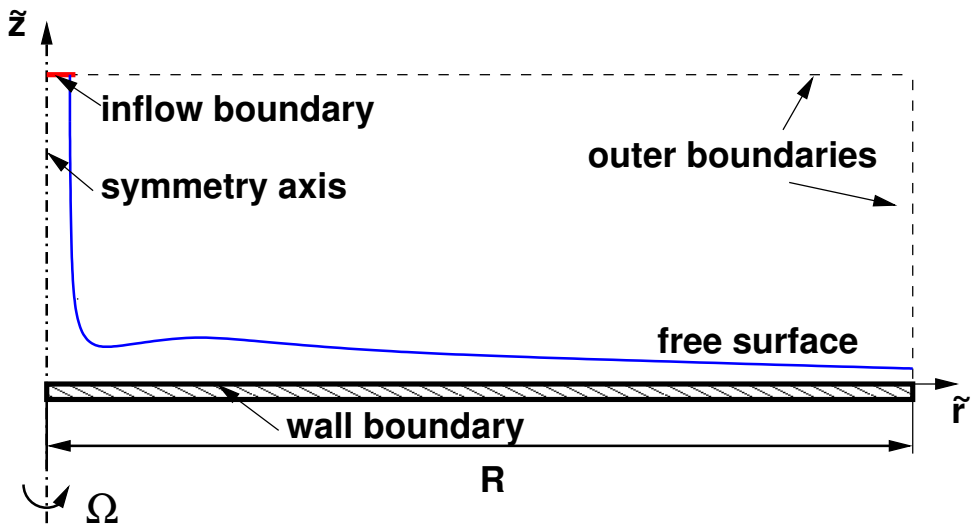

Figure 3.1: Computational domain and boundary conditions.

	ρ [kg/m^3]	ν [m^2/s]	σ [N/m]
L1	998.2	1.0×10^{-6}	0.072
L2	990	1.3×10^{-6}	0.072
L3	998.2	2.87×10^{-6}	0.072

Table 3.1: Properties of liquids considered in the CFD simulations.

The computational domain shown in Fig. 3.1 was discretized using approximately 124 thousand cells. The rectangular-shaped cells were layered in five rows. The first layer extended from the surface of the disk to $\tilde{z}$=0.005 mm and consisted of 10 rows of equally sized cells. In the second layer, which extended to $\tilde{z}$=0.1 mm, 40 rows of equally sized cells were stacked upon each other. From the third layer onwards the vertical height of the cells was successively increased. The radial region was subdivided in three evenly spaced cell columns, with a radial cell size of $\Delta\tilde{r}$=0.1 mm. In the region covered by liquid additional refinement was performed using a twice as fine resolution in both directions.

The time step size for the simulation was allowed to vary depending on the flow conditions using the Courant-Friedrichs-Lewy (CFL) criterion. The time step size typically varied between $1 \div 5 \times 10^{-5}$ s.

3.2 Numerical solution of the integral boundary layer equations

The IBL approximation leads to a nonlinear system of hyperbolic partial differential equations (PDEs), defined by Eqs. (2.132), extended by Eqs. (2.154) to model the heat transfer, and by Eq. (2.162) to model the species mass transfer.

In the following the single spacial dimension is denoted by x and the vector of the dependent state variables by $\vec{U}(x,t) \in \mathbb{R}^m$. Considering furthermore the m-dimensional flux function to be denoted with $\vec{F}(\vec{U}(x,t)) \in \mathbb{R}^m$, and the vector of source terms to be written as $\vec{S}(\vec{U}(x,t),x,t) \in \mathbb{R}^m$, the nonlinear system of hyperbolic partial differential equations can be written in general form as

$$\frac{\partial \vec{U}(x,t)}{\partial t} + \frac{\partial \vec{F}(\vec{U}(x,t))}{\partial x} = \vec{S}(\vec{U}(x,t),x,t). \tag{3.11}$$

Such time-dependent systems of PDEs are frequently encountered when modeling convection dominated transport processes. For the special case of a system of conservation laws, which is associated with $\vec{S} \equiv 0$, a change in the state variables can only be due to a net flux.

3.2.1 Hyperbolic systems

The system defined in Eq. (3.11) is called hyperbolic, if the $m \times m$ Jacobian matrix

$$J(\vec{U}) = \frac{\partial \vec{F}(\vec{U})}{\partial \vec{U}} \tag{3.12}$$

- has real eigenvalues $\lambda_p(\vec{U})$ and a corresponding complete set of m linearly independent eigenvectors $\vec{r}_p(\vec{U})$, $(p = 1, ..., m)$, and
- is diagonalizable: $J = R\Lambda R^{-1}$.

Therein, Λ is a diagonal matrix holding the real eigenvalues λ_p and R is the invertible right eigenvector matrix, with the corresponding eigenvectors $\vec{r}_p$ as its columns.
Numerical methods for solving such time-dependent hyperbolic systems are based on solving Riemann problems. For this reason the concepts of solving Riemann problems are recalled (see, e.g. Toro [106], LeVeque [107, 108]), before proceeding to the numerical approach.

Riemann problem for a linear hyperbolic system

The initial value problem (IVP) for a linear hyperbolic system

$$\frac{\partial \vec{U}(x,t)}{\partial t} + A\frac{\partial \vec{U}(x,t)}{\partial x} = 0, \tag{3.13}$$

with constant coefficient matrix A, defined together with an initial condition of the form

$$\vec{U}(x,0) = \vec{U}_0(x)\ ,\ -\infty < x < \infty \tag{3.14}$$

can be explicitly solved. For this purpose a transformation into so called characteristic variables, defined by

$$\vec{W} = R^{-1}\vec{U}, \tag{3.15}$$

is performed. The flux function is in this case simply given as

$$\vec{F}(\vec{U}(x,t)) = A\vec{U}(x,t). \tag{3.16}$$

Multiplication of Eq. (3.13) from left with R^{-1} results in

$$R^{-1}\frac{\partial \vec{U}(x,t)}{\partial t} + \Lambda R^{-1}\frac{\partial \vec{U}(x,t)}{\partial x} = 0. \tag{3.17}$$

Here the identity $A = R\Lambda R^{-1}$, or rather $R^{-1}A = \Lambda R^{-1}$, was used. Since A is constant, Eq. (3.17) can be written in terms of the characteristic variables,

$$\frac{\partial \vec{W}(x,t)}{\partial t} + \Lambda \frac{\partial \vec{W}(x,t)}{\partial x} = 0. \tag{3.18}$$

Due to the diagonal form of Λ, the linear system therefore decouples into m independent scalar advection equations

$$\frac{\partial w_p(x,t)}{\partial t} + \lambda_p \frac{\partial w_p(x,t)}{\partial x} = 0, \quad p = 1, ..., m. \tag{3.19}$$

The solution of an IVP for a linear scalar advection equation,

$$\frac{\partial v}{\partial t} + a\frac{\partial v}{\partial x} = 0, \tag{3.20}$$

with initial condition $v(x,0) = v_0$, is simply obtained as

$$v(x,t) = v_0(x - at) \quad \text{for} \quad t \geq 0. \tag{3.21}$$

Thus the initial data distribution v_0 propagates with characteristic speed a and the solution $v(x,t)$ is constant on parametric curves $x(t) = x_0 + at$ in the x-t plane. The family of the so called characteristics of the PDE is defined by the ordinary differential equation

$$\frac{dx(t)}{dt} = a, \tag{3.22}$$

and a particular characteristic is determined by supplying an initial condition at $t = 0$ as $x(t = 0) = x_0$.
The rate of change of v along $x(t) = x_0 + at$ is therefore zero,

$$\frac{dv}{dt} = \frac{\partial v}{\partial t} + \underbrace{\frac{dx}{dt}}_{a} \frac{\partial v}{\partial x} = 0. \tag{3.23}$$

In Fig. 3.2 characteristics for the linear advection equation with a positive characteristic speed $a > 0$ are sketched in the $x - t$ plane.

For the linear system defined in Eq. (3.19) this means that the solution for each of the characteristic variables $w_p(x,t)$ corresponds to the initial profiles, which have been propagated at the characteristic speed λ_p over the time t, so that

$$w_p(x,t) = w_p(x - \lambda_p t, 0). \tag{3.24}$$

The solution of the original system, defined in Eq. (3.13), is finally obtained by the inverse transformation,

$$\vec{U}(x,t) = R\vec{W}(x,t). \tag{3.25}$$

This procedure can be written in terms of an eigenvector expansion of $\vec{U}(x,t)$ with coefficients $w_p(x,t)$ as

$$\vec{U}(x,t) = \sum_{p=1}^{m} w_p(x,t)\vec{r}_p, \tag{3.26}$$

or, when using Eq. (3.24), as

$$\vec{U}(x,t) = \sum_{p=1}^{m} w_p(x-\lambda_p t,0)\vec{r}_p. \tag{3.27}$$

Thus, the solution can be interpreted as superposition of m waves with constant shape $w_p(x,0)\vec{r}_p$, which propagate independently with speed λ_p.
Denoting the rows of matrix R^{-1} by $(\vec{l}_p)^T$, the p-th component of $R^{-1}\vec{U}$ can be written as (cf. (3.15))

$$w_p(x,t) = \left(\vec{l}_p\right)^T \cdot \vec{U}(x,t). \tag{3.28}$$

Substituting this expression into the coefficients of the eigenvector expansion Eq. (3.27) can be rewritten as

$$\vec{U}(x,t) = \sum_{p=1}^{m} \left[(\vec{l}_p)^T \cdot \vec{U}(x-\lambda_p t,0)\right] \vec{r}_p. \tag{3.29}$$

A Riemann problem is generally defined by a hyperbolic PDE system together with a

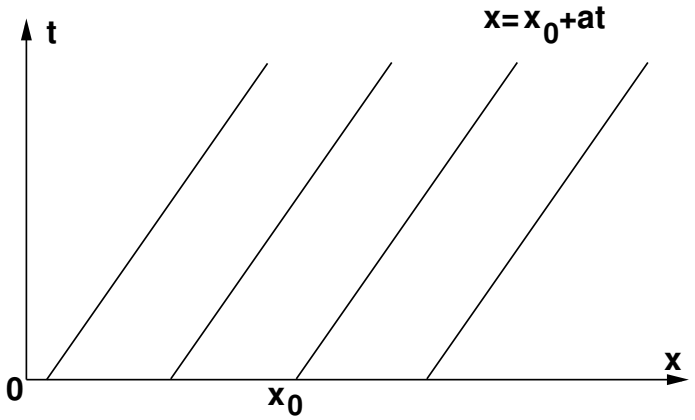

Figure 3.2: Sketch of the characteristics of the linear advection equation for a characteristic speed $a > 0$ in the $x-t$ plane.

piecewise constant initial condition of the form

$$\vec{U}(x,0) = \begin{cases} \vec{U}_L & x < 0 \\ \vec{U}_R & x > 0. \end{cases} \tag{3.30}$$

For the simple case of a linear hyperbolic system with a constant coefficient matrix A (Eq. (3.13)) the general solution is provided by Eq. (3.29). Assuming additionally, that the real eigenvalues of A are distinct and ordered,

$$\lambda_1 < \lambda_2 < ... < \lambda_m, \tag{3.31}$$

the initial condition can be written as eigenvector expansion with constant coefficients α and β as

$$\vec{U}_L = \sum_{p=1}^{m} \alpha_p \vec{r}_p \quad \text{and} \quad \vec{U}_R = \sum_{p=1}^{m} \beta_p \vec{r}_p. \tag{3.32}$$

As sketched in Fig. 3.3 the general solution of this linear Riemann problem can then be interpreted as a superposition of m waves, which originate from the point $(0,0)$ in the $x-t$ plane.

Each of these waves carries a discontinuity in each component of $\vec{U}$ and travels at constant speed λ_p. In terms of the characteristic variables, the initial condition is provided by

$$w_p(x,0) = \begin{cases} \alpha_p, & x < 0 \\ \beta_p, & x > 0 \end{cases} \tag{3.33}$$

and the solution to the scalar Riemann problems is obtained as

$$w_p(x,t) = w_p(x - \lambda_p t, 0) = \begin{cases} \alpha_p, & x - \lambda_p t < 0 \\ \beta_p, & x - \lambda_p t > 0. \end{cases} \tag{3.34}$$

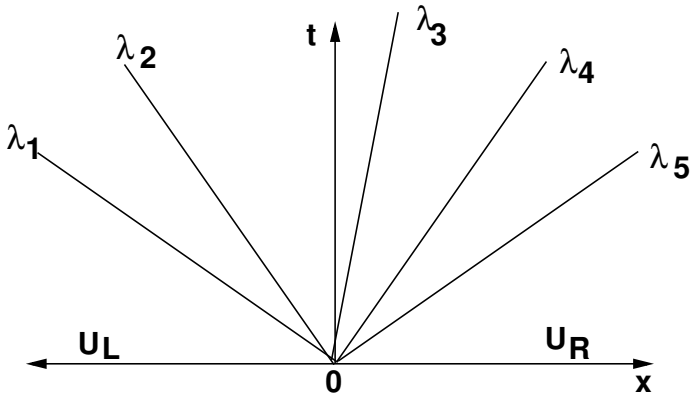

Figure 3.3: Sketch of the solution structure of a linear Riemann problem with $m = 5$ waves.

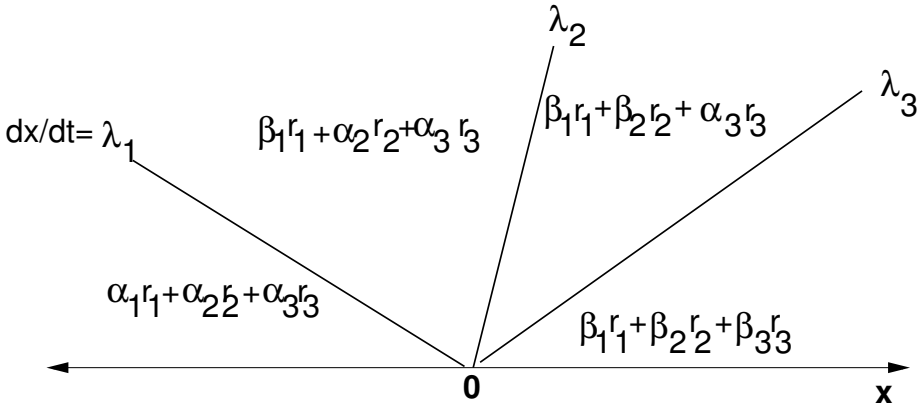

Figure 3.4: Sketch of the values of the solution in different sectors of a Riemann problem with $m = 3$ waves.

The solution to the original system can finally be written as

$$\vec{U}(x,t) = \sum_{p=1}^{P(x,t)} \beta_p \vec{r}_p + \sum_{P(x,t)+1}^{m} \alpha_p \vec{r}_p. \tag{3.35}$$

Therein, the integer $P(x,t)$ denotes the maximum value of $p \in [1,...,m]$, for which the inequality,

$$x - \lambda_p t > 0, \tag{3.36}$$

holds.

Fig. 3.4 provides an illustration for the determination of $\vec{U}(x,t)$ in case of a linear Riemann problem with $m = 3$ waves. For any point in between two characteristics, defined by $dx/dt = const.$, the solution is the same. To the left of the λ_1-characteristic the solution is simply the initial data $\vec{U}_L$. Similarly, to the right of the λ_3-characteristic, the solution is given by the initial data $\vec{U}_R$. The coefficients of the eigenvector expansion for the solutions in between the waves are determined from Eq. (3.34). As soon as one crosses the p-th characteristic, $dx/dt = \lambda_p$, the value of $x - \lambda_p t$ changes from negative to positive, corresponding to a change of the coefficient from α_p to β_p.

3.2.2 Numerical solution of hyperbolic PDE systems

Finite volume methods, which are based on the integral form of the transport equations, are especially suited for the numerical solution of hyperbolic PDE systems. The integral

form for a system of conservation laws reads

$$\frac{d}{dt}\int_{x_1}^{x_2}\vec{U}(x,t)dx = \vec{F}(\vec{U}(x_1,t)) - \vec{F}(\vec{U}(x_2,t)) \quad \forall x_1, x_2. \tag{3.37}$$

Discretizing the x-t plane utilizing a mesh of width $h = \Delta x$, and a time step size $k = \Delta t$, the discrete points (x_j, t_n) are given as

$$\begin{aligned} x_j &= jh, \quad j = ..., -1, 0, 1, 2, ... \\ t_n &= nk, \quad n = 0, 1, 2, ... \, . \end{aligned} \tag{3.38}$$

The coordinates of the left and right faces of the j-th cell are denoted by $x_{j-1/2} = x_j - h/2$ and $x_{j+1/2} = x_j + h/2$, respectively. The pointwise value of an approximation to the cell average of $\vec{U}(x,t)$ is then defined as

$$U_j^n = \frac{1}{\Delta x}\int_{x_{j-1/2}}^{x_{j+1/2}}\vec{U}(x,t_n)dx. \tag{3.39}$$

Integration of Eq. (3.37) with respect to time, between t_n and t_{n+1}, and division by Δx finally provides the discretized time integration scheme for the numerical approximation of the cell average of the j-th cell

$$U_j^{n+1} = U_j^n - \frac{\Delta t}{\Delta x}\left[F_{j+1/2}^n - F_{j-1/2}^n\right]. \tag{3.40}$$

Here $F_{j\pm1/2}^n$ is the numerical approximation of the flux vector $\vec{F}(\vec{U})$ at the left and right cell faces,

$$F_{j\pm1/2}^n \approx \frac{1}{\Delta t}\int_{t_n}^{t_{n+1}}\vec{F}(\vec{U}(x_{j\pm1/2},t))dt. \tag{3.41}$$

As sketched in Fig. 3.5, the finite volume based discretization leads to a piecewise-constant distribution of the cell averaged state variables, constituting a sequence of local Riemann problems at the cell interfaces. Thus, the task of the numerical solution of the hyperbolic PDE system is to solve these local Riemann problems to update the solution to the new time level U_j^{n+1}.

Using Godunov's method, which was developed in 1959 for gas dynamics, the independent Riemann problems are solved exactly over a short time interval. Since for nonlinear problems the solution of the sequence of Riemann problems at each time step is computationally expensive, the approximate Riemann solver is used as a more efficient approach. This approximation approach is also justified by the fact that even the Godunov scheme is only first-order accurate in space and time, due to the piecewise constant representation of the state variables.

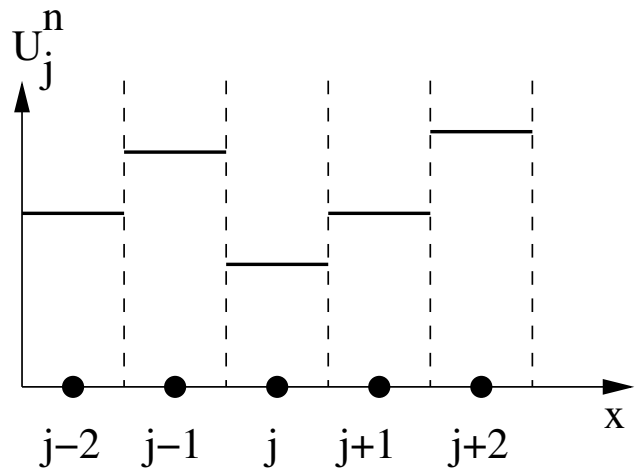

Figure 3.5: Piecewise constant distribution of a cell averaged state variable.

Roe's approximate Riemann solver

One of the most popular approximate Riemann solvers goes back to Roe [109] and is based on a linearization of the nonlinear problem. In this approach the nonlinear hyperbolic system

$$\frac{\partial \vec{U}(x,t)}{\partial t} + \frac{\vec{F}(\vec{U}(x,t))}{\partial x} = 0, \tag{3.42}$$

with initial conditions

$$\vec{U}(x,0) = \begin{cases} \vec{U}_L & x < 0 \\ \vec{U}_R & x > 0, \end{cases} \tag{3.43}$$

which results in a sequence of nonlinear Riemann problems at the individual cell interfaces, is replaced by a linear approximation

$$\frac{\partial \vec{U}(x,t)}{\partial t} + \hat{A}\frac{\partial \vec{U}(x,t)}{\partial x} = 0, \tag{3.44}$$

with a constant coefficient matrix $\hat{A}$. This Roe matrix $\hat{A}$ is assumed to be constant between two cells and is assumed to be a function of the corresponding states to the left and right of these cells, which are denoted by the subscripts L and R, respectively. As such the approximation is essentially based on a linearization together with the assumption of constant average states at the cell interfaces.

The constant coefficient Roe matrix $\hat{A}$ must guarantee the

- hyperbolicity of the system, that is $\hat{A}$ has to be diagonalizable with real eigenvalues,

- conservation across discontinuities, that is

$$\vec{F}(\vec{U}_R) - \vec{F}(\vec{U}_L) = \hat{A}(\vec{U}_R - \vec{U}_L), \tag{3.45}$$

- consistency with the exact Jacobian, that is

$$\vec{U}_L, \vec{U}_R \to \vec{\overline{U}}: \quad \hat{A} \to \frac{\partial \vec{F}(\vec{\overline{U}})}{\partial \vec{U}}. \tag{3.46}$$

A suitable approximate Jacobian $\hat{A}$ for the numerical solution of the IBL equations can be obtained using the arithmetic average for the film thickness

$$\hat{\overline{\delta}} = \frac{1}{2}\left(\delta_L + \delta_R\right), \tag{3.47}$$

and Roe averages for the remaining state variables, which is for example for the depth-averaged radial velocity $\overline{u}$ given by

$$\hat{\overline{u}} = \frac{\sqrt{\delta_L}\overline{u}_L + \sqrt{\delta_R}\overline{u}_R}{\sqrt{\delta_L} + \sqrt{\delta_R}}. \tag{3.48}$$

The obtained sequence of linearized Riemann problems is then solved exactly. For this purpose, considering exemplarily the Riemann problem at the face $x_{j-1/2}$, the left and right states at the cell interface, $U_L^n = U_{j-1}^n$ and $U_R^n = U_j^n$, respectively, are decomposed into a linear combination of right eigenvectors of $\hat{A}$

$$\begin{aligned} U_{j-1}^n &= \sum_{p=1}^{m} \alpha_{j-1}^p \hat{r}^p, \\ U_j^n &= \sum_{p=1}^{m} \beta_j^p \hat{r}^p. \end{aligned} \tag{3.49}$$

Here and below the summation index p is displayed as superscript, while the superscript denoting the current time level n is dropped in the sums on the RHS for reasons of readability.
The change in the state variables across the face between the neighboring cells is decomposed into a superposition of m waves $\mathcal{W}$,

$$\begin{aligned} (\Delta U)_{j-1/2}^n = U_j^n - U_{j-1}^n = \sum_{p=1}^{m} \left(\beta_j^p - \alpha_{j-1}^p\right) \hat{r}^p = \\ = \sum_{p=1}^{m} \gamma_{j-1/2}^p \hat{r}^p = \sum_{p=1}^{m} \mathcal{W}_{j-1/2}^p. \end{aligned} \tag{3.50}$$

The coefficients of the eigenvector expansion are determined according to Eq. (3.28), so that the p-th wave in the Riemann solution at time level n is obtained as

$$\mathcal{W}^p_{j-1/2} = \left(\hat{l}^p_{j-1/2}\right)^T (U_j - U_{j-1})\, \hat{r}^p_{j-1/2}. \tag{3.51}$$

These jumps propagate with velocities $\hat{\lambda}^p$, respectively, the eigenvalues of the system. The fluxes required for updating the averaged cell value in the j-th cell (cf. Eq. (3.40)) are determined from several right going waves with positive velocity $(\hat{\lambda}^p)^+$, starting from the $j-1/2$ cell interface, and several left going waves with negative velocity $(\hat{\lambda}^p)^-$, starting from the $j+1/2$ cell interface, respectively. The expression for updating the cell average reads

$$U^{n+1}_j = U^n_j - \frac{\Delta t}{\Delta x}\left[\sum_{p=1}^{m} \left(\hat{\lambda}^p\right)^+ \mathcal{W}^p_{j-1/2} - \sum_{p=1}^{m} \left(\hat{\lambda}^p\right)^- \mathcal{W}^p_{j+1/2}\right]. \tag{3.52}$$

Introducing the notation

$$\begin{aligned} \hat{A}^- &= \hat{R}\, \mathit{diag}\left((\hat{\lambda}_p)^-\right) \hat{R}^{-1}, \quad \hat{\lambda}^- = min(\hat{\lambda}, 0), \\ \hat{A}^+ &= \hat{R}\, \mathit{diag}\left((\hat{\lambda}_p)^+\right) \hat{R}^{-1}, \quad \hat{\lambda}^+ = max(\hat{\lambda}, 0), \end{aligned} \tag{3.53}$$

this scheme can also be written as

$$U^{n+1}_j = U^n_j - \frac{\Delta t}{\Delta x}\left[\hat{A}^+ \Delta U_{j-1/2} + \hat{A}^- \Delta U_{j+1/2}\right]. \tag{3.54}$$

Higher order correction terms and flux limiter

An extension to a high resolution method is achieved by adding an additional term, which provides limited second-order correction fluxes,

$$U^{n+1}_j = U^n_j - \frac{\Delta t}{\Delta x}\left[\hat{A}^+ \Delta U_{j-1/2} + \hat{A}^- \Delta U_{j+1/2}\right] - \frac{\Delta t}{\Delta x}\left[\tilde{F}_{j+1/2} - \tilde{F}_{j-1/2}\right]. \tag{3.55}$$

The correction fluxes are given by

$$\tilde{F}_{j\pm1/2} = \frac{1}{2}\sum_{p=1}^{m}\left(1 - \frac{\Delta t}{\Delta x}\left|\lambda^p_{j\pm1/2}\right|\right)\left|\lambda^p_{j\pm1/2}\right| \tilde{\mathcal{W}}^p_{j\pm1/2}. \tag{3.56}$$

Here $\tilde{\mathcal{W}}^p_{j\pm1/2}$ represents a limited version of the wave, which is obtained by multiplication with a limiter function $\chi\left(\mu^p_{j\pm1/2}\right)$, which measures the smoothness of the solution, as

$$\tilde{\mathcal{W}}^p_{j\pm1/2} = \chi\left(\mu^p_{j\pm1/2}\right) \mathcal{W}^p_{j\pm1/2}. \tag{3.57}$$

The parameter μ of the limiter function, is defined as

$$\mu^p_{j-1/2} = \frac{\mathcal{W}^p_{J-1/2}\mathcal{W}^p_{j-1/2}}{\left|\mathcal{W}^p_{j-1/2}\right|}, \tag{3.58}$$

with

$$J = \begin{cases} j-1 & \text{if } \lambda^p > 0 \\ j+2 & \text{if } \lambda^p < 0. \end{cases} \tag{3.59}$$

For smoothly varying data the limiter function approaches unity and the additional term in Eq. (3.55) provides a useful correction, improving the accuracy of the numerical solution. Near discontinuities the limiter modifies the wave, typically by reducing its magnitude. A popular high-resolution limiter is the superbee limiter

$$\chi(\mu) = \max\left[0, \min\left(1, 2\mu\right), \min\left(2, \mu\right)\right], \tag{3.60}$$

which was used in the present work. Linear alternative approaches are for example the upwind method ($\chi(\mu) = 0$) and the unstable Lax-Wendroff scheme with $\chi(\mu) = 1$.

Source term treatment

To properly account for the presence of source terms in the numerical solution of a hyperbolic PDE system, a popular approach is to split the problem of solving

$$\frac{\partial \vec{U}(x,t)}{\partial t} + \frac{\partial \vec{F}(\vec{U}(x,t))}{\partial x} = \vec{S}(\vec{U}(x,t), x, t). \tag{3.61}$$

into two sub-problems

$$\frac{\partial \vec{U}(x,t)}{\partial t} + \frac{\partial \vec{F}(\vec{U}(x,t))}{\partial x} = 0, \tag{3.62}$$

$$\frac{\partial \vec{U}(x,t)}{\partial t} = \vec{S}(\vec{U}(x,t), x, t). \tag{3.63}$$

The main advantage using this operator splitting approach is that for each subproblem an appropriate scheme can be chosen. Therefore, this fractional step scheme was used in the present work for the numerical solution of the governing IBL equations. In particular, Roe's approximate Riemann solver with flux-limited second-order correction terms was applied to the sub-problem associated with the homogeneous conservation laws, defined by Eq (3.62), while a two-stage Runge-Kutta scheme was chosen for the integration of the ODEs defined by Eq. (3.63).

3.2.3 Setup

For the practical implementation of the hyperbolic solver numerical routines from the Fortran-library CLAWPACK (Conservation Laws Package) [110] were used. This Fortran-library provides the wave-propagation algorithm of Eq. (3.55), which requires

- the fluctuations $\hat{A}^{\pm}\Delta U_{j-1/2}$,
- the waves $\mathcal{W}^{p}_{j-1/2}$, and
- the local speeds $\hat{\lambda}^{p}_{j-1/2}$,

for the considered system of IBL equations. To provide these input data a proper routine was programmed and implemented along with a source term routine for the fractional-step method.

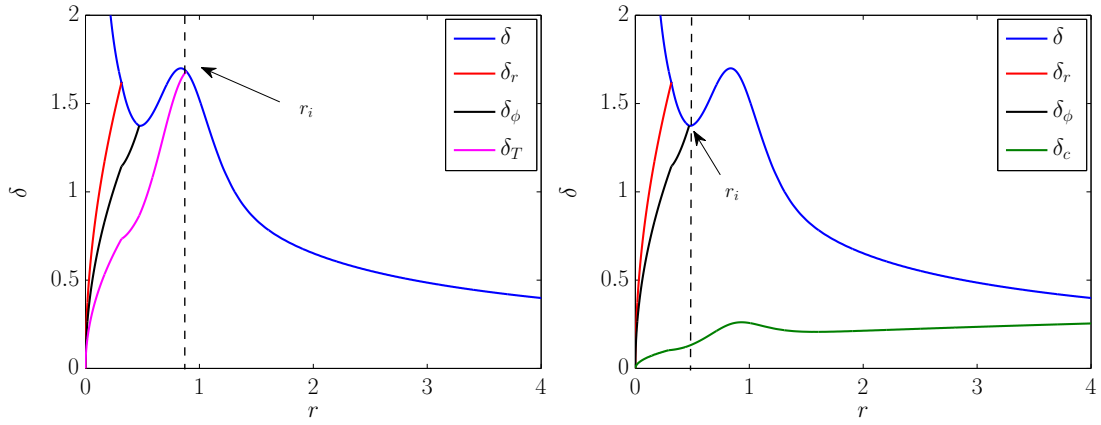

(a) (b)

Figure 3.6: Initial conditions for the film thickness and position of the inflow boundary r_i for the numerical solution of the unsteady IBL equations (a) including heat transfer, (b) including species mass transfer.

Initialization and boundary conditions

Generally the unsteady flow simulation is initialized from the corresponding steady-state solutions of the IBL model using the boundary layer assumption, as discussed in Sec. 2.3.4, computed for the whole disk.
The inflow conditions are set at a certain radial inner position r_i, where a smooth film solution can be expected, so that appropriate inlet conditions can be obtained from the

corresponding steady-state solutions. In the case of heat transfer the unsteady simulation starts from the radial position $r_i = r_T$, where the film is hydrodynamically and thermally fully developed, as shown in Fig. 3.6(a). On the other hand, in the case of species mass transfer, the unsteady IBL simulation starts from an inner radius where the flow is hydrodynamically fully developed, associated with $r_i = r|_{\delta_\phi = \delta}$, as shown in Fig. 3.6(b). This different setting of the radial inner boundary is due to the very high Schmidt numbers, which are considered in the present case. For the here relevant Schmidt number of the order of $\mathcal{O}\left(10^{-3}\right)$ the concentration boundary layers are very thin, so that they may never reach the film surface throughout the domain as exemplarily shown in Fig. 3.6(b).
At the radially outer boundary the flow quantities are linearly extrapolated from the interior.

4 RESULTS AND DISCUSSION

The following discussion of the computational results starts with a comprehensive analysis of the steady-state solutions. It is followed by the analysis of the unsteady solutions, which shall particularly highlight the effect of the unsteady surface waves on the hydrodynamics, the heat and species mass transfer. The whole discussion is based on three cases listed with their determining parameters in Tab. 4.1.

The considered cases were specially selected to cover smooth film as well as wavy film conditions, and providing also experimental data for validation.

Case	Q [lpm]	n [rpm]	ν [m^2/s]	ϵFr^{-1}	W	Pr	Sc
C1	1.8	401	1.3×10^{-6}	5×10^{-4}	1.9×10^{-7}		
C2	1	500	1×10^{-6}	4.5×10^{-4}	3×10^{-6}	7	
C3	1.25	500	2.87×10^{-6}	1.03×10^{-3}	9.35×10^{-6}		1196

Table 4.1: Considered test cases for steady-state smooth film and for wavy flow conditions.

The discussion of the hydrodynamic characteristics is mainly based on the case C1. For this particular case experimental data for the film thickness are available from Burns et al. [65]. The case C2 is focused on the investigation of the thermal characteristics of the film flow, while the case C3 is focused on the description of the species mass transfer in a binary mixture on the spinning disk. Assuming the asymptotic regimes of very small and very large Damköhler numbers for the process of wet chemical etching, the predictions for the temperature considered in case C2, and the species mass transport considered in case C3, translate directly into predictions for the etching rates, for which experimental results are available from Staudegger et al. [82, 85]. The validation of the present unsteady IBL model against the experimental data is comprehensively discussed in Sec. 4.3.

4.1 Steady-state solutions

In this section the steady-state results of the IBL equations for smooth, axisymmetric flow are discussed and compared against results from the analytical far-field solutions. The analysis of the predictions obtained for the heat transfer also includes a comparison against CFD results.

4.1.1 Hydrodynamics

The results of the steady-state solution of the IBL approximation using the developed film assumption (DFA) obtained for the case C1 are depicted in Fig. 4.1. The corresponding asymptotic solutions, which are given by Eqs. (2.185)-(2.187) for $r \ll 1$, and by Eqs. (2.182)-(2.184) for $r \gg 1$, are shown as well.

From Fig. 4.1 basically three regions can be distinguished. In the inner, inertia-dominated region, the film height is increased to a local maximum, due to the retarding effect of the viscous and Coriolis forces on the outwards directed radial motion of the liquid. In this inner region, the radial as well as the azimuthal velocities decrease from their initial values. The minima in the radial and azimuthal velocities are observed around the radial position where the local maximum in the film thickness occurs. Further downstream, beyond roughly $r > 2$, the accelerating effect of the increasing centrifugal force becomes more and more dominant and causes a continuous thinning of the liquid film. In this radially outer region the azimuthal component of the fluid velocity converges towards the disk's angular speed and the steady IBL model essentially produces the variation of the film thickness in the asymptotic limit of large radii, $\delta = r^{-2/3}$, with the asymptotic depth-averaged radial velocity $\overline{u} = (1/3)r^{-1/3}$.

The distinction between a radial inner inertia-dominated region, where the outwards directed radial motion of the liquid is retarded by the viscous and Coriolis forces, and a radial outer region dominated by centrifugal forces is also reflected by variation of the Ekman number along the disk. As can be seen from Fig. 4.2, the radial extension of the inertia dominated inner region $r \lessapprox 2$ is associated with values of the local Ekman number $Ek \lessapprox 3$. Since small local Ekman numbers imply comparatively high Coriolis forces, which effectively exert a stabilizing influence on the flow, wavy flow conditions are to be expected only in the outer radial region ($r \gtrapprox 2$), where the Ekman numbers become large ($Ek \gtrapprox 3$) and the flow is increasingly destabilized by the centrifugal acceleration. Results for the radial location of the maximum growth rate of perturbations obtained from a linear stability analysis of the IBL equations (see, e.g., Kim and Kim [75]) support this distinction concerning local onset of waviness.

Effect of the reduced inverse Froude number

To assess the influence of the only dimensionless parameter

$$\epsilon Fr^{-1} = \frac{2\pi g\nu}{3Q\Omega^2}, \tag{4.1}$$

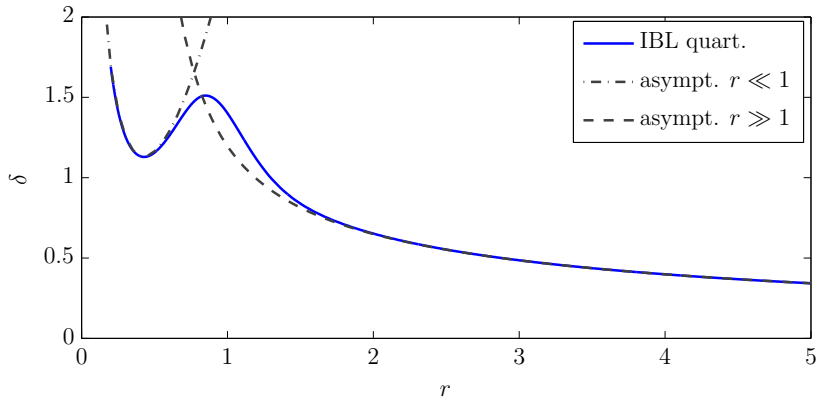

(a) Film thickness vs. radial distance.

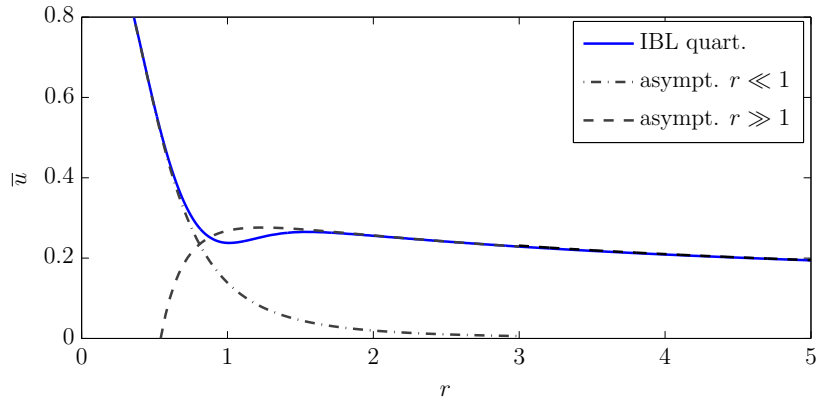

(b) Depth-averaged radial velocity vs. radial distance.

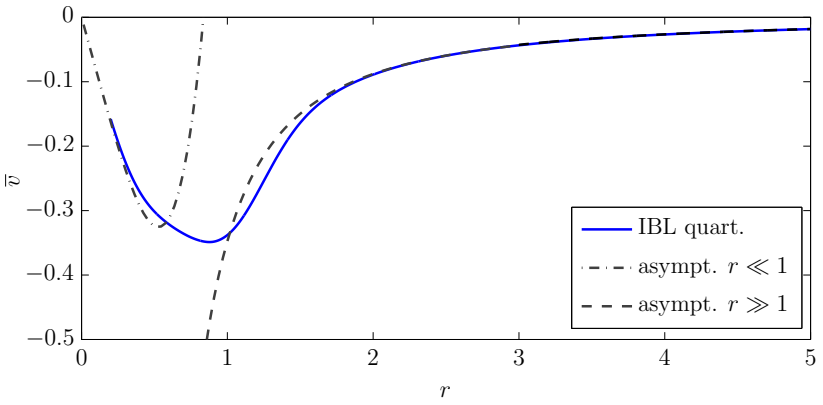

(c) Depth-averaged azimuthal velocity vs. radial distance.

Figure 4.1: Solutions of the steady-state IBL equations for the case C1 together with the asymptotic solutions in the radially inner and outer regions.

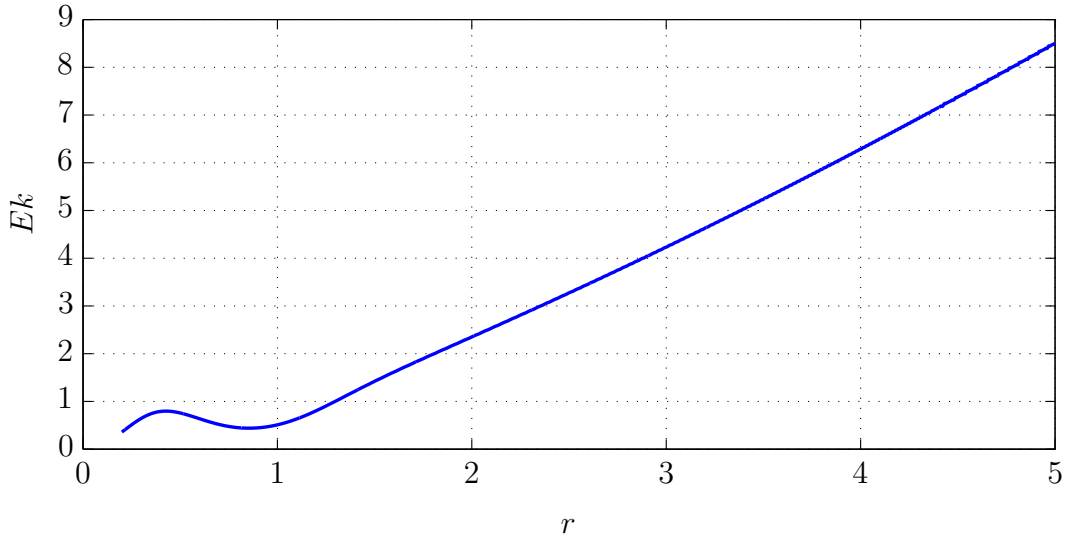

Figure 4.2: Ekman number $Ek = \nu/\Omega\tilde{\delta}^2$ vs. radial distance for the case C1.

which appears in the governing set of equations for the steady-state smooth film flow, Eqs. (2.174)-(2.176), a parametric study was carried out varying the values of the reduced inverse Froude number between 8×10^{-5} - 6×10^{-2}. This range of the reduced inverse Froude number covers most available experimental data, and is also practically relevant for the semiconductor industry, where spinning disk devices are used for the surface preparation of silicon wafers.

Fig. 4.3(a) depicts the results from the steady-state IBL model, assuming a quartic radial velocity profile (IBL quart.), obtained for a sub-range with the lower values $\epsilon Fr^{-1} \in \left[8 \times 10^{-5}, 9.3 \times 10^{-4}\right]$. The predictions for the film thickness remain very close to each other, indicating no significant effect of the reduced inverse Froude number in this sub-range. In Fig. 4.3(b) the results for the sub-range with the larger values of the reduced inverse Froude number, $\epsilon Fr^{-1} \geq 10^{-3}$, are shown. The local maximum in the film height is evidently shifted to smaller radii with increasing values of ϵFr^{-1}. Furthermore, the film thickness is found to decrease in the region of the local minimum as ϵFr^{-1} becomes larger.

The denominator in Eq. (2.180) vanishes for a critical value

$$\left(\epsilon Fr^{-1}\right)_{crit} = \frac{k_a}{9\beta_1 r^2 \delta^2}, \tag{4.2}$$

which makes the formulation singular. Due to this singularity a radially continuous integration is not possible anymore, as can for example be seen in Fig. 4.3(b) from the unphysical

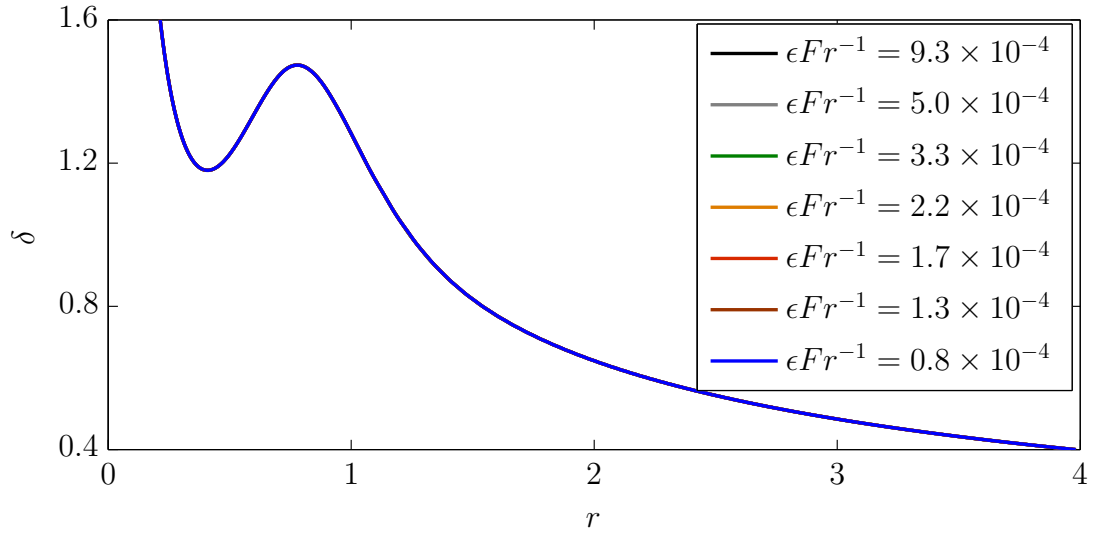

(a)

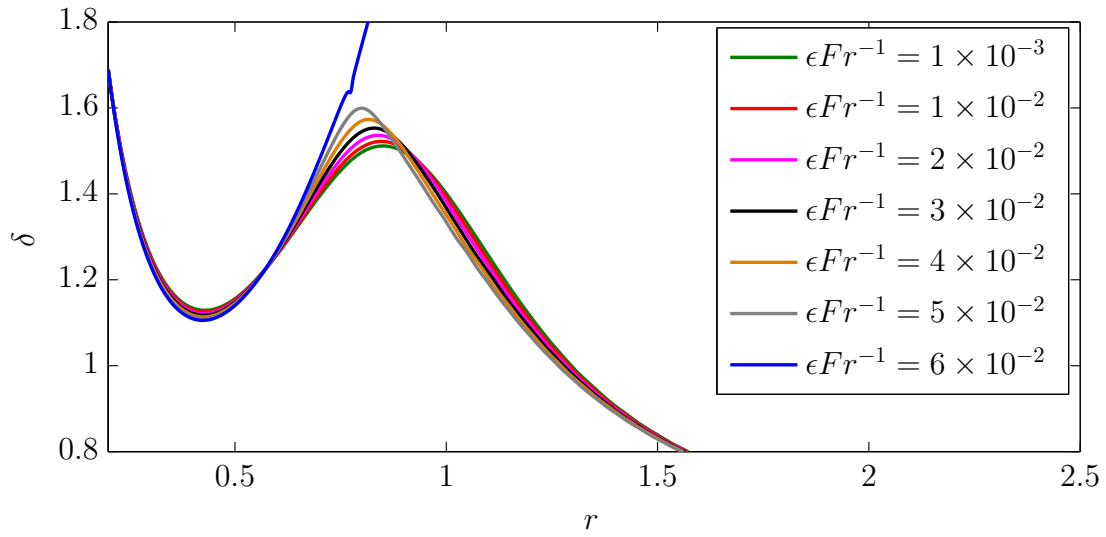

(b)

Figure 4.3: Influence of the dimensionless parameter ϵFr^{-1}. Film thickness vs. radial distance obtained from the steady-state smooth film IBL model.

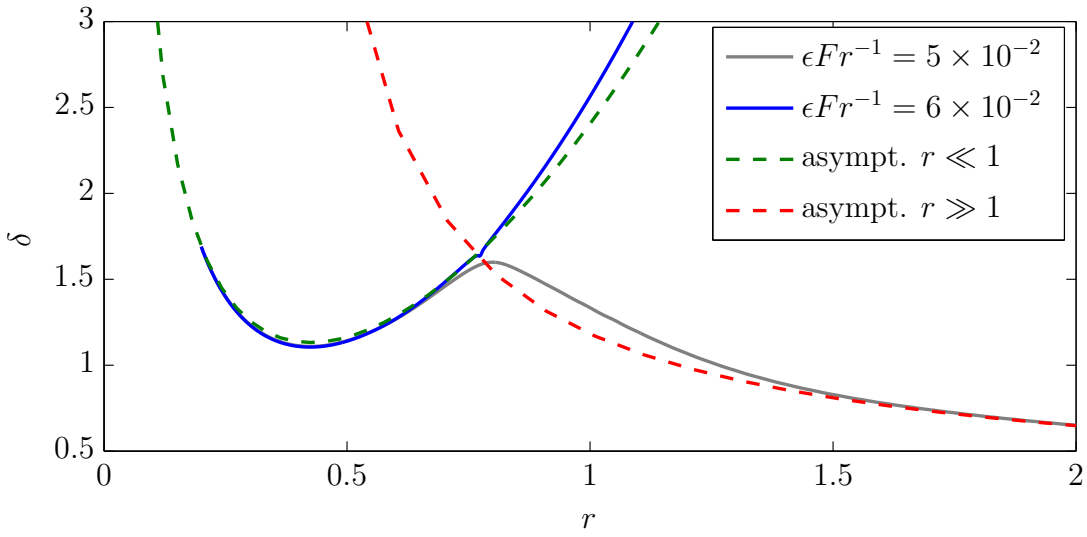

Figure 4.4: Results for a sub- and a supercritical value of ϵFr^{-1} together with asymptotic solutions for the radially inner and outer regions obtained from the steady-state smooth film IBL model.

solution for the supercritical value $\epsilon Fr^{-1} = 6 \times 10^{-2}$. Nonetheless, cases with very small rotational speeds, corresponding to large values of ϵFr^{-1}, can be described reasonably well by the asymptotic solutions on both sides of the singularity, given by Eqs. (2.185)-(2.187) for $r \ll 1$, and by Eqs. (2.182)-(2.184) for $r \gg 1$, as exemplarily shown for the film height for $\epsilon Fr^{-1} = 6 \times 10^{-2}$ in Fig. 4.4.

Evaluation of profile assumptions for the velocity

The influence of the two different profile assumptions for the radial velocity component, given by Eq. (2.133) and Eq. (2.134), on the results of the IBL approximation is examined in detail in Fig. 4.5. As seen from Fig. 4.5(b), the quartic profile predicts a lower local minimum of the radial mean velocity in the inner region downstream of the impingement, where the viscous forces successively decelerate the flow. The evidently stronger effect of the viscous forces is also indicated by bulkier quartic velocity profiles, shown at different radial positions in Fig. 4.6(a), as compared to the quadratic profile given by Eq. (2.133). The steeper gradients at the wall translate into higher wall shear rates (leading to higher wall shear stresses) shown in Fig. 4.6(b).
The retarding influence of the Coriolis force is evident in Fig. 4.5(c). The azimuthal component of the velocity lags behind the disk speed, reaching a minimum around the radial position where the maximum film thickness can be observed. The smaller negative values of $\overline{v}$ exhibited by the solution obtained with the quartic profile for $\overline{u}$ indicate a more pro-

nounced retarding effect of the Coriolis force. Accordingly, the assumption of a quartic profile produces a higher film thickness at radii $r > 1$ as seen from Fig. 4.5(a).
Towards the radial outer boundary of the domain, the differences between the results for the two profile assumptions disappear. This can also be mathematically shown in the formulation of the profile assumption given by Eq. (2.134). For large radii, the flow is determined only by the balance of viscous and centrifugal forces, so that Eq. (2.175) can be rewritten as

$$\overline{u} = \frac{\beta_1}{\beta_2} r\delta^2 = \frac{1}{3} r\delta^2. \tag{4.3}$$

Considering steady-state smooth flow in the radially outer region ($r \gg 1$) the pressure gradient is zero, so that the boundary condition Eq. (2.135) yields $\kappa = r$, and Eq. (4.3) can be rewritten as

$$\overline{u} = \frac{1}{3}\kappa\delta^2. \tag{4.4}$$

Using the quartic velocity profile Eq. (2.134), the expression for the surface velocity is given by (cf. appendix 2)

$$u_\delta = \frac{25}{16}\overline{u} - \frac{\kappa\delta^2}{48}. \tag{4.5}$$

Substituting $\overline{u} = \kappa\delta^2/3$ into Eq. (4.5) yields

$$\kappa = \frac{2u_\delta}{\delta^2}. \tag{4.6}$$

Introducing this expression for κ into the quartic velocity profile Eq. (2.134), the quartic profile becomes identical with the quadratic velocity profile, Eq. (2.133). Physically speaking, the convergence of both profile assumptions in the radially outer region indicates the vanishing effect of inertia, as this effect can only be reflected by the quartic profile.

Boundary layer assumption (BLA) for the central impingement region

As discussed in Sec. 2.3.4 the IBL approximation with BLA, which considers the development of boundary layers of the radial and azimuthal velocity components in the radially inner region, basically provides a physically more accurate description of the flow, the heat and the species mass transfer near the center.
As shown in Fig. 4.7 the predictions of the IBL model using the BLA are very close to the predictions of the IBL model using the previously discussed developed film assumption (DFA). The boundary layer of the radial velocity component, δ_r grows very fast due to the high shear rates in the impingement region. The boundary layer of the azimuthal velocity component, δ_ϕ, reaches the free surface at a radial position farther downstream than δ_r, as the growth of δ_ϕ is counteracted by the Coriolis force.

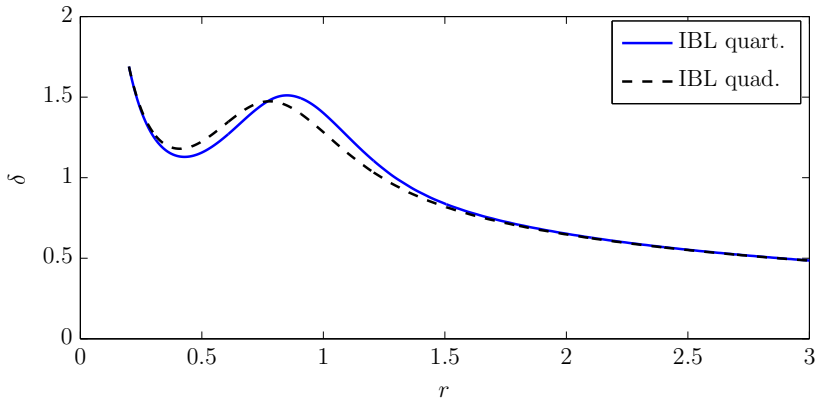

(a) Film thickness vs. radial distance.

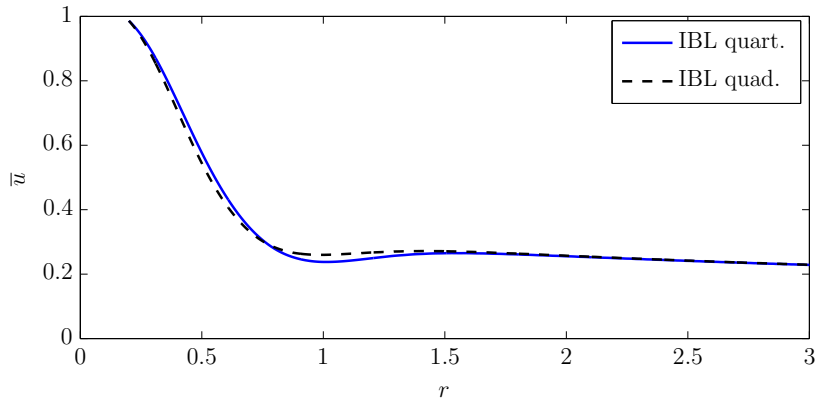

(b) Depth-averaged radial velocity vs. radial distance.

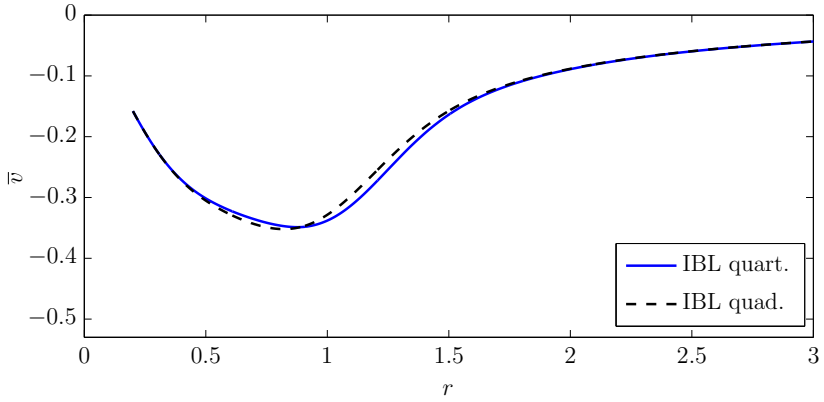

(c) Depth-averaged azimuthal velocity vs. radial distance.

Figure 4.5: Steady-state smooth film IBL predictions for the case C1 using alternatively the quadratic and quartic polynomials for the radial velocity component.

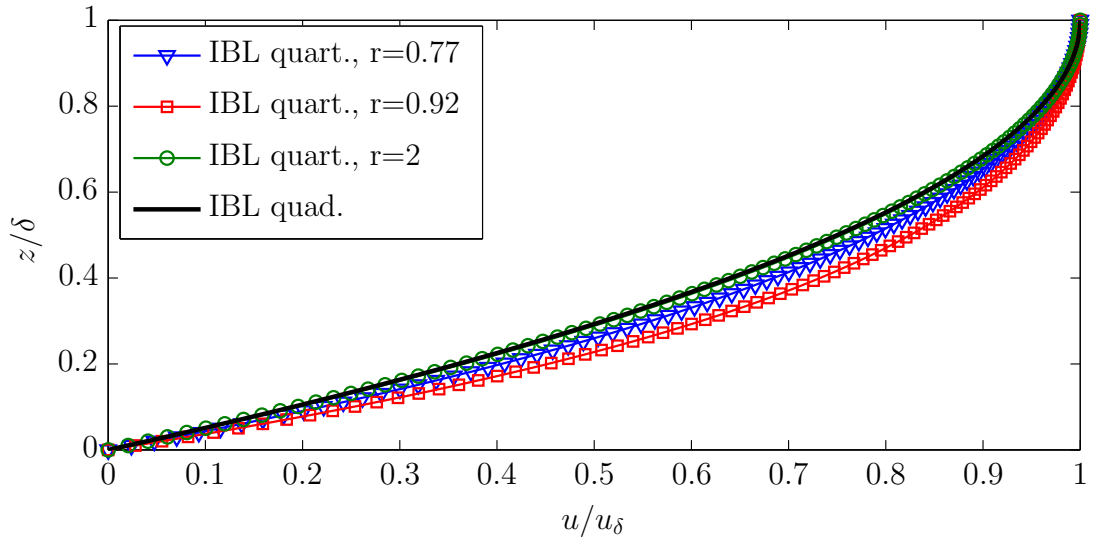

(a) Radial velocity profiles.

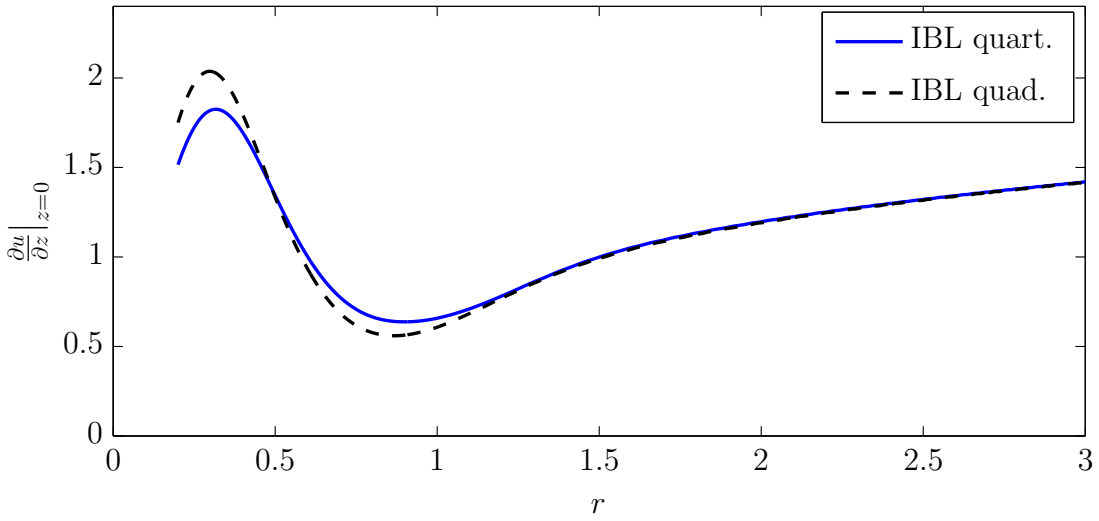

(b) Wall shear rate vs. radial distance.

Figure 4.6: Influence of the two different profile assumptions in the steady-state IBL approximation for the case C1.

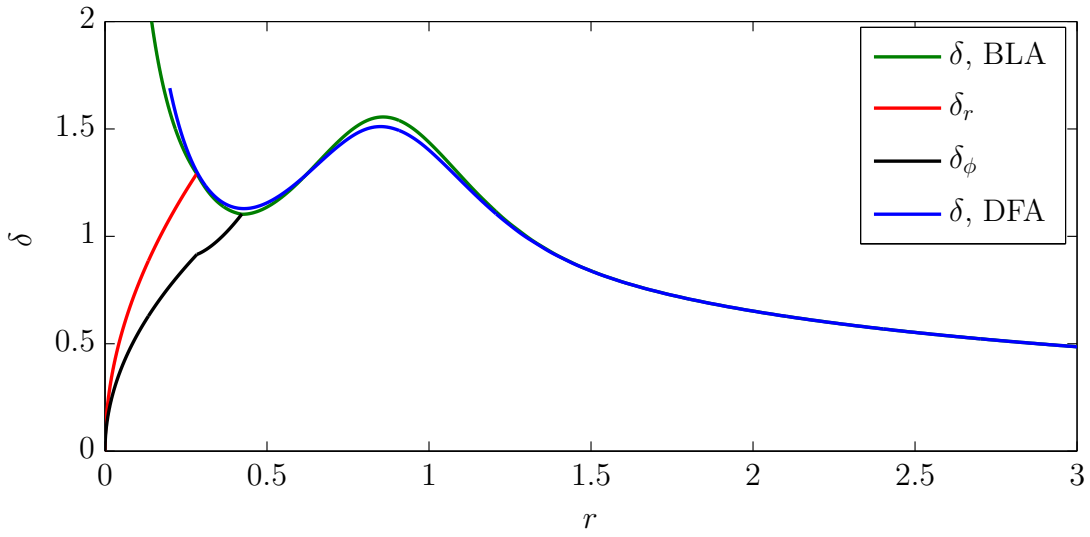

Figure 4.7: Steady-state IBL predictions for the film thickness using the developed film assumption (DFA) and the boundary layer assumption (BLA) for the case C1.

The main benefit of the IBL model using the BLA discussed in Sec. 2.3.4 resides in its role of providing a reliable description of the flow in the impingement region starting from the center, $r = 0$, with no need for prescribing any inflow conditions at an inner radius $r = r_i$.

4.1.2 Heat transfer

The heat transfer in the liquid film was examined in detail for a case assuming cooling conditions with a constant wall heat flux of $q_w = -5500\,\mathrm{W/m^2}$. The other flow relevant parameters were chosen as Q=1.0 lpm, n=500 rpm, and $\nu = 1 \times 10^{-6}\ \mathrm{m^2/s}$, which translates into the dimensionless parameters $\epsilon Fr^{-1} = 4.5 \times 10^{-4}$, $W = 3 \times 10^{-6}$, and $Pr = 7$. This parameter setting refers to the case C2 in table 4.1. The results of the steady-state solution of the IBL approximation using these parameters are depicted in Figs. 4.43(a)-(b). The radial extension of the thermal entry region, which is associated with $\delta_T < \delta$ is roughly $r_T \approx 1$, which lies within the radially inner inertia-dominated region, where the outwards directed radial motion of the liquid is retarded by viscous and Coriolis forces, so that the film height is increased to a local maximum. Within the thermal entry zone $0 < r < r_T$, where smooth, hence steady, film flow can be assumed the steady-state solution already gives a physically realistic description of the flow. As such it also provides reliable inner boundary conditions at $r = r_T$ for the unsteady solution, which is computed in the radially outer region for $r \geq r_T$, where wavy flow is expected (cf. Sec. 4.2.2).

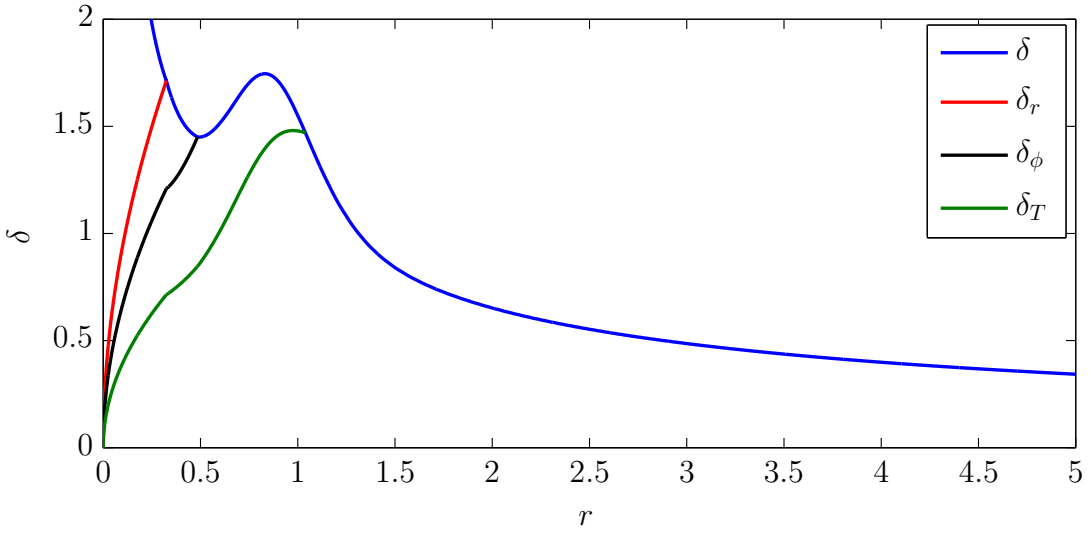

(a) Film thickness and thickness of individual boundary layers vs. radial distance.

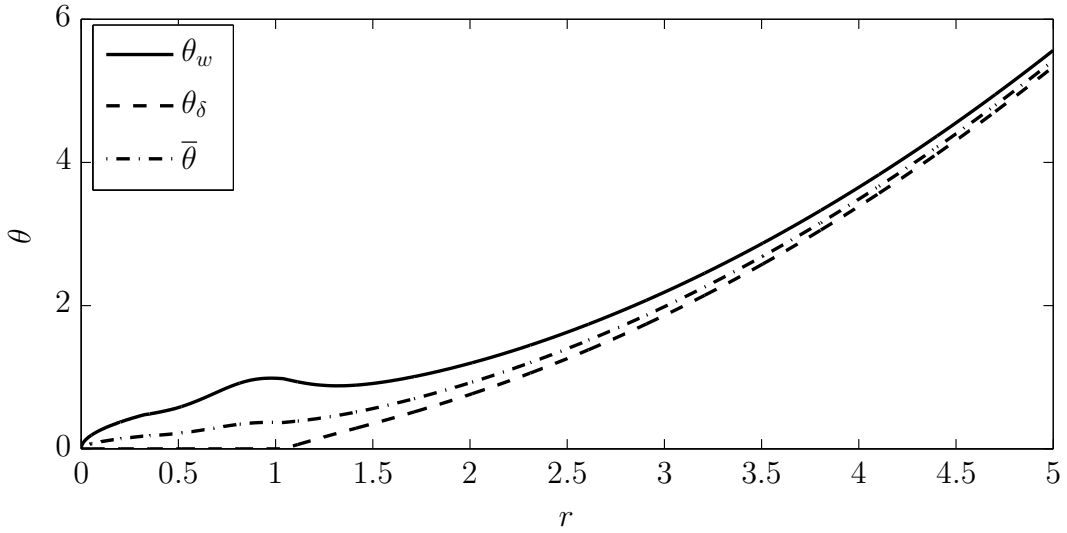

(b) Dimensionless temperature vs. radial distance.

Figure 4.8: IBL predictions for the case C2 assuming steady-state smooth film conditions, $Pr = 7$.

In Fig. 4.43(b) the steady-state IBL predictions for the radial variation of the depth-averaged dimensionless temperature $\overline{\theta}$ are shown. The local dimensionless temperatures at the disk and the liquid surface are depicted as well. The liquid surface temperature remains expectedly at its initial value in the region of the thermal entry for $r < r_T \approx 1$ and $\delta_T < \delta$, and starts to increase significantly downstream. For $r < r_T$ the radial variation of the wall temperature clearly reflects the development of the thermal boundary layer, as θ_w increases markedly faster than the depth-averaged temperature $\overline{\theta}$. Further downstream the temperature profiles tend to converge into one curve which indicates that the temperature inside the film becomes more and more uniform.

To assess the possible effect of the assumption of zero heat flux between the liquid surface and the ambient air, the predictions of the steady-state IBL model, using either an adiabatic boundary condition, or a non-adiabatic condition, are compared in Fig. 4.9(a). The far-field solution, which was obtained with the non-adiabatic upper boundary conditions using the Nusselt number correlation Eq. (2.194) for the heat transfer coefficient and assuming a typical ambient temperature T_a=25 °C, evidently remains fairly close to the predictions of the IBL model using an adiabatic upper boundary condition.
This observation could also be confirmed by a CFD-based analysis. The numerical results obtained from two axisymmetric CFD simulations, using either adiabatic or non-adiabatic surface conditions, respectively, show no significant differences (Fig. 4.9(b)), although the CFD simulations capture the effects of the surface waviness. As only minor differences are observed in the results for the temperature variations, the assumption of an adiabatic free surface appears to be justified.

4.1.3 Species mass transfer

As explained in section 2.4.2 the species mass transfer has to be included in the IBL solution in order to model the process of wet chemical surface etching in the limit of large Damköhler numbers. The operating liquid is assumed as a binary mixture of a primary etchant component diluted into a chemically inert carrier component. Due to the typically small molecular diffusivities the values of the considered Schmidt numbers are large when compared against the considered Prandtl numbers for aqueous solutions. Thus, the radial extension of the region, in which a concentration boundary layer has to be distinguished, is considerably larger. This exacerbates the modeling of diffusion controlled etching processes.

The mass transfer characteristics are examined in detail for a case which is referred to as case C3 in table 4.1. The flow parameters of this case were chosen as Q=1.25 lpm, n=500 rpm, and ν=2.87 $\times$ 10^{-6} m^2/s, which translates into the dimensionless parameters

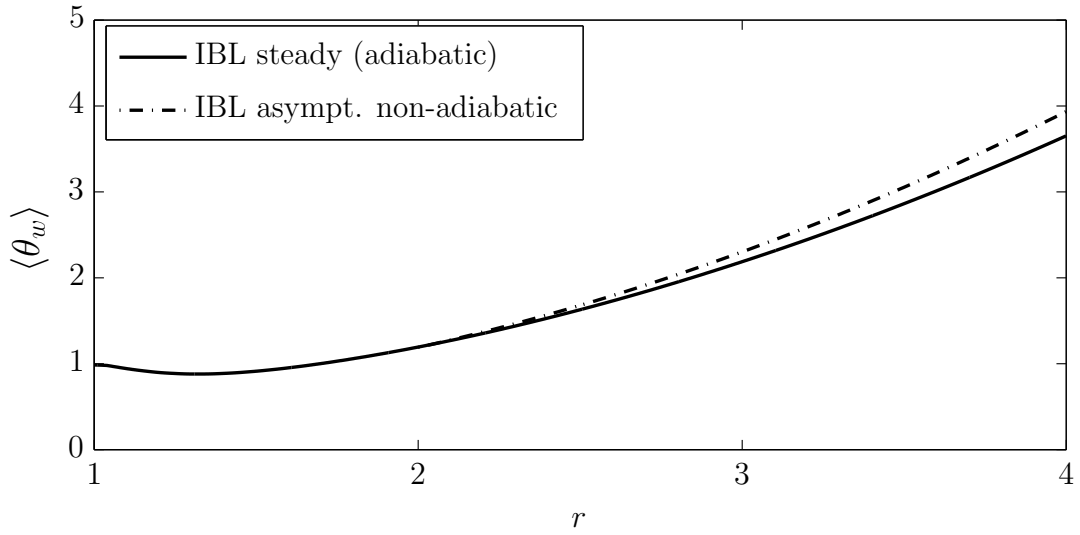

(a) IBL prediction

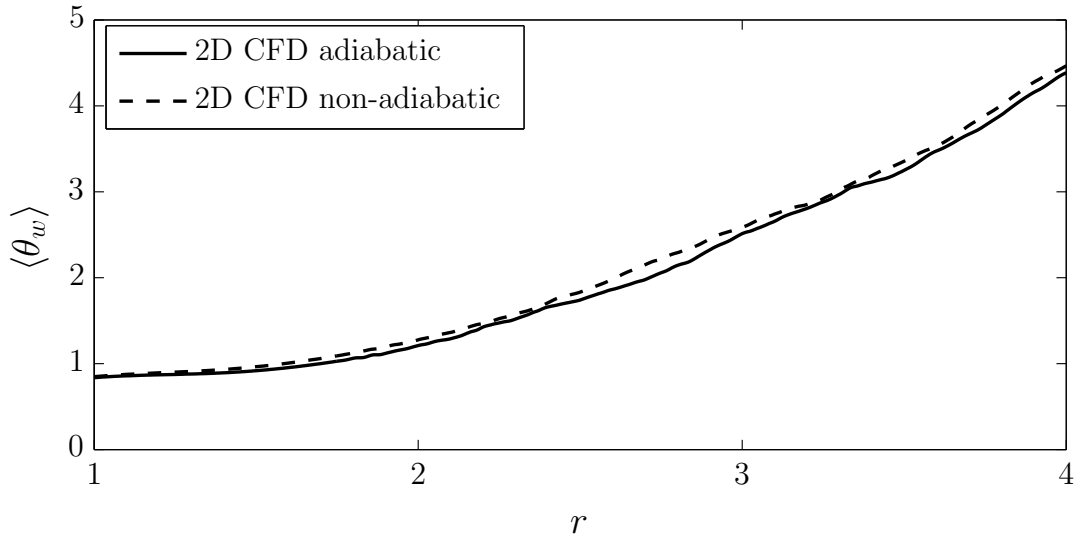

(b) CFD simulation

Figure 4.9: Dimensionless wall temperature vs. radial distance. Effect of convective heat transport between the liquid surface and the ambient air for the case C2 (T_a=25 °C) assuming cooling conditions with q_w=-5500 W/m^2.

$\epsilon Fr^{-1} = 1.03 \times 10^{-3}$, $W = 9.35 \times 10^{-6}$, and $Sc = 1196$.
Fig. 4.10(a) shows the film thickness together with the thickness of the individual boundary layers, including the concentration boundary layer, δ_c. The concentration boundary layer monotonously increases up to a local maximum which coincides with the local maximum of the film thickness. In the radial inner region the radial variation of δ_c evidently follows quite closely the trend of the film height, which indicates that the first term on the RHS of Eq. (2.201) dominates over the second term representing the diffusive transport. Further downstream the common trend disappears as the film height δ decreases, while the concentration boundary layer δ_c restarts growing. This opposite trend points at a dominance of the second (diffusive) term on the RHS of Eq. (2.201).
As can be seen from Fig. 4.10(b) the species mass fraction at the free surface, c_δ, decreases from its initial value, radially downstream of $r = r_c \approx 6$, where the concentration boundary layer reaches the film surface. It is interesting to note that the also depicted variation of the depth-averaged species mass fraction decreases almost linearly with the radial distance throughout the domain showing no sensitivity to the development of the boundary layers, especially not to δ_c.

In Fig. 4.11 the radial variation of the Sherwood number is examined. Assuming a third-order polynomial for the profile of the species mass fraction, the Sherwood number is determined by the following expression for the dimensionless species mass fraction gradient at the wall

$$Sh = \left.\frac{\partial c}{\partial z}\right|_{z=0} = \frac{3c_\delta}{2\delta_c}\,. \tag{4.7}$$

This implies that for $r < r_c$, where $c_\delta = 1$, the diffusive flux at the wall is proportional to the inverse of the thickness of the concentration boundary layer, i.e.,

$$\left.\frac{\partial c}{\partial z}\right|_{z=0} \propto \frac{1}{\delta_c}. \tag{4.8}$$

For $r > r_c$, where c_δ decreases, the diffusive flux at the wall is proportional to the ratio

$$\left.\frac{\partial c}{\partial z}\right|_{z=0} \propto \frac{c_\delta}{\delta}. \tag{4.9}$$

so that it scales with the inverse of the film height. The first proportionality can be clearly seen from Figs. 4.10(a) and 4.11, where the local minimum in the Sherwood number corresponds to the local maximum in the thickness of δ_c, located at a dimensionless radius of about $r \approx 0.9$. The monotonic increase of δ_c occurring further downstream translates into a slow radial decrease of Sh. Downstream of the radial position $r = r_c$, where the boundary layer thickness δ_c reaches the film height δ the Sherwood number exhibits a plateau-like variation. According to Eq. (4.9) the decrease of c_δ starting at $r = r_c$ is evidently compensated by the decrease of the film height resulting in nearly constant Sherwood numbers.

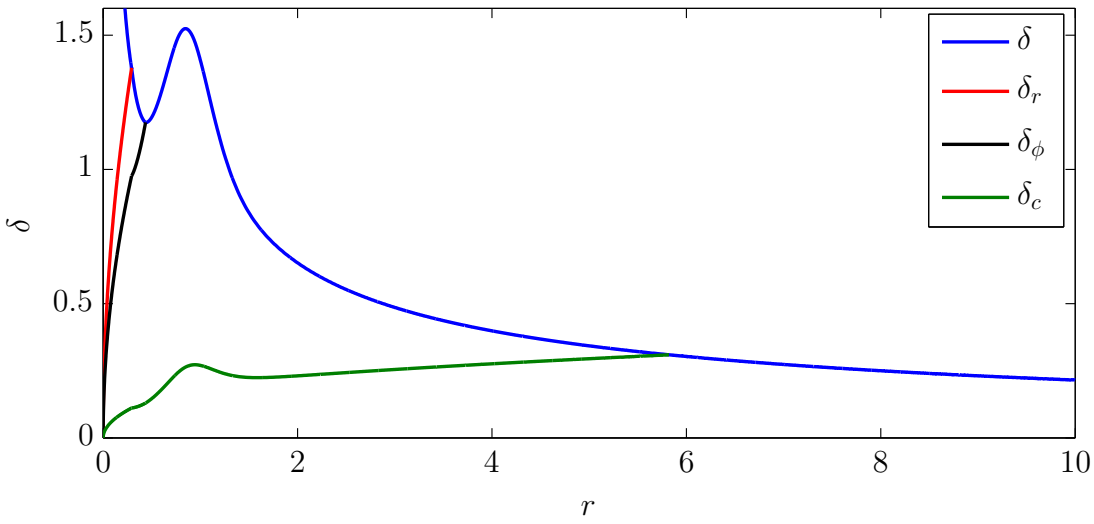

(a) Film thickness and thickness of individual boundary layers.

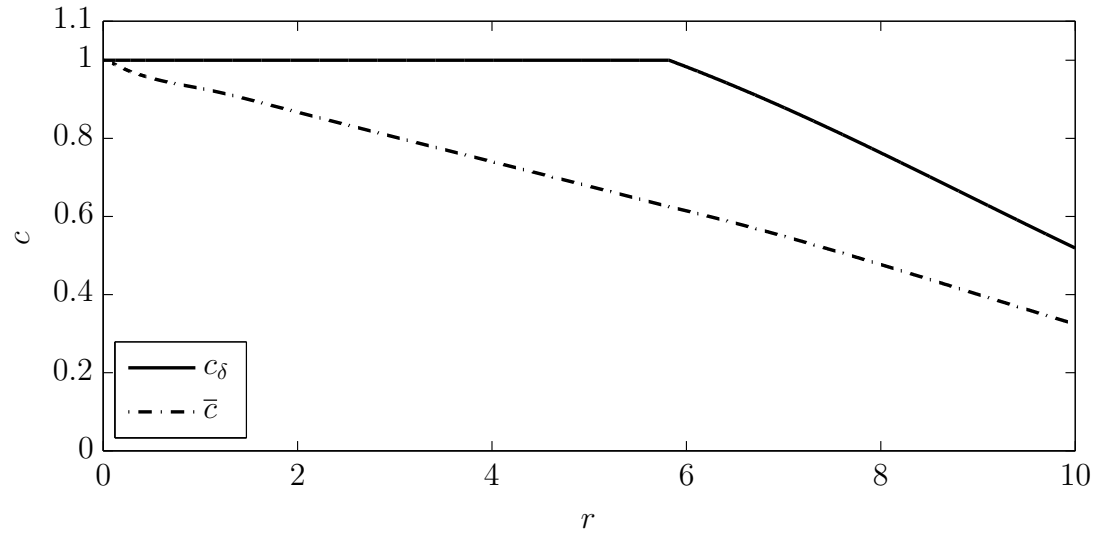

(b) Surface and depth-averaged species mass fraction vs. radial distance.

Figure 4.10: Steady-state IBL solutions for the case C3 including results for the solid-liquid mass transfer in a binary mixture, $Sc = 1196$.

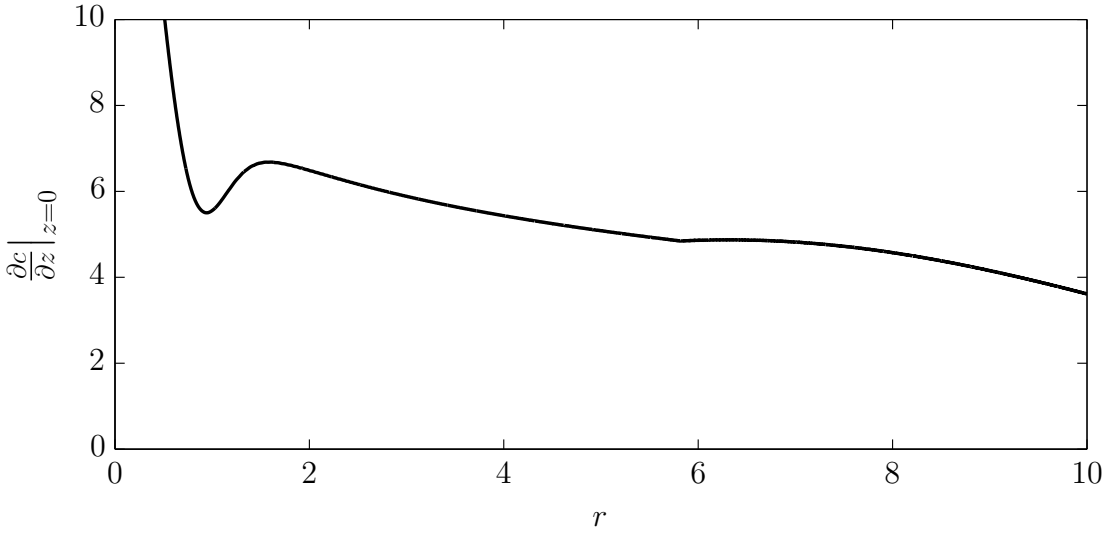

Figure 4.11: Local Sherwood number for the case C3, $Sc = 1196$.

Evaluation of profile assumptions for the species mass fraction

In Figs. 4.12-4.13 the influence of the order of the polynomial ansatz function for the profile of the species mass fraction is examined. The available boundary conditions allow the coefficients of a third-order polynomial to be fully determined. If a second-order polynomial is considered instead (see appendix 3 for details) the IBL model predicts a faster growth of the concentration boundary layer, as can be seen from Fig. 4.12. The faster growth of δ_c immediately follows from the larger concentration gradient of the second-order polynomial at the wall, since

$$\frac{\partial}{\partial z}\left[c_\delta\left(2\frac{z}{\delta_c}-\frac{z^2}{\delta_c^2}\right)\right]_{z=0} > \frac{\partial}{\partial z}\left[c_\delta\left(\frac{3}{2}\frac{z}{\delta_c}-\frac{1}{2}\frac{z^3}{\delta_c^3}\right)\right]_{z=0}. \tag{4.10}$$

The larger gradient results in faster decrease of the bulk concentration, and thus a faster growth of δ_c. Furthermore, the use of a second-order polynomial conflicts with the zero-curvature condition at the wall, Eq. (2.88), as the second derivative reads

$$\frac{\partial^2}{\partial z^2}\left[c_\delta\left(2\frac{z}{\delta_c}-\frac{z^2}{\delta_c^2}\right)\right] = -2\frac{c_\delta}{\delta_c^2}. \tag{4.11}$$

The shortcomings of the second-order polynomial in the near wall region are therefore greatest in the radially inner region, where the thickness of the concentration boundary layer is smallest. Radially further downstream the error introduced by the quadratic approximation for the c-profile will decrease as the surface species mass fraction approaches zero, $c_\delta \to 0$. The faster increase of the thickness of the concentration boundary layer is

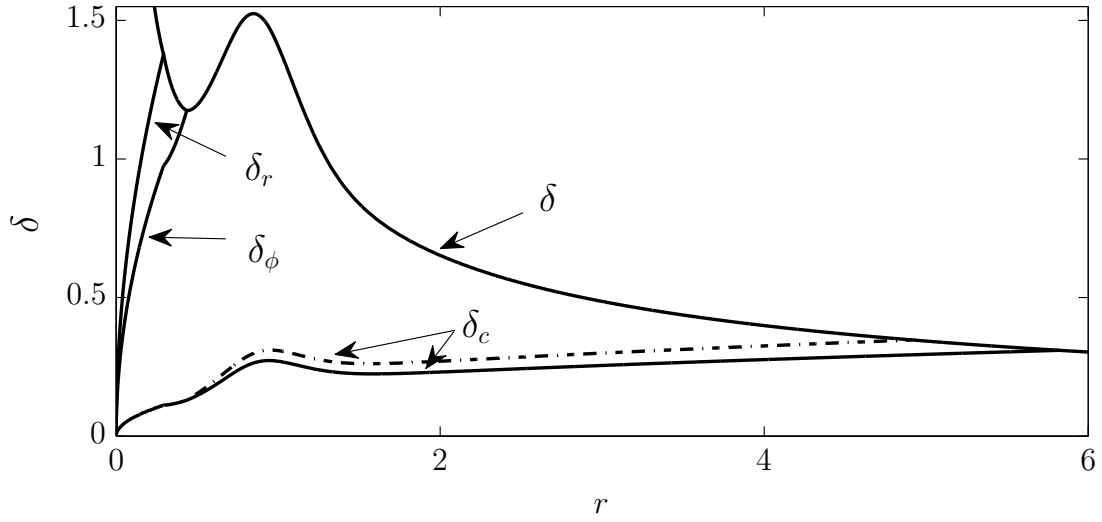

Figure 4.12: Evaluation of second-order (dashed-dotted) and third-order (solid line) c-profile assumptions for the case C3. Film thickness and thickness of individual boundary layers.

associated with an upstream shift of the radial position of r_c. This effectively leads to a faster decrease of the depth-averaged mean species mass fraction $\overline{c}$ in the film, as shown in Fig. 4.13. In this figure the results from the analytical far-field solutions for the species mass fraction, which were discussed in Sec. 2.2.2, are depicted as well. These analytical solutions, which are assumed to be valid for large radii, $r \gg 1$, were obtained by considering alternatively the semi-parabolic radial velocity profile given by Eq. (2.93) (Rahman and Faghri [89]), which represents an exact asymptotic solution in the limit of large radii, or alternatively, by assuming a linear approximation for the u-profile, which implies a very thin concentration boundary layer.
Fig. 4.13 makes evident, that the IBL predictions for the depth-averaged mean species mass fraction using the third-order polynomial for the c-profile are in very good agreement with the analytical far-field solution provided by Rahman and Faghri [89] in the radially outer region. The IBL prediction using the second-order polynomial for the profile of the species mass fraction lies significantly below this far-field solution, due to the faster growth of the concentration boundary layer, which finally leads to a faster decrease of the bulk concentration as noted above.
The analytical solution obtained assuming a very thin concentration boundary layer and approximating the radial velocity profile by a linear function deviates most significantly from all other solutions.

Fig. 4.14 shows a comparison between the the species mass fraction profiles using either the second- or the third-order polynomial ansatz functions for several radial positions in-

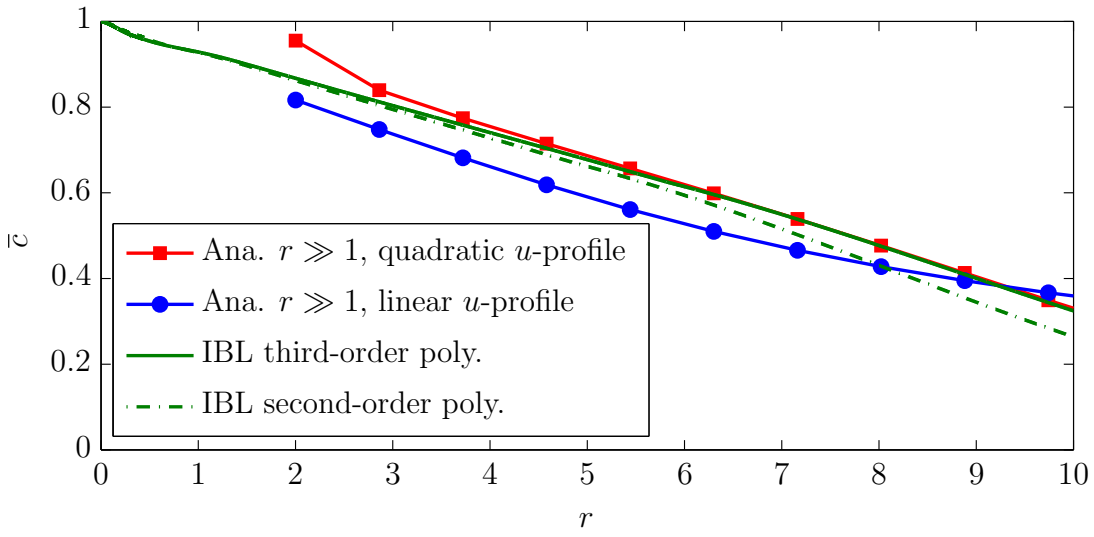

Figure 4.13: Depth-averaged mean species mass fraction vs. radial distance. Steady-state IBL predictions and analytical far-field solutions (Rahman and Faghri [89]) for the case C3, $Sc = 1196$.

side the liquid film. The analytical far-field solutions are depicted as well. As can be seen from Figs. 4.14(a)-(b), there is a good agreement between the IBL solutions and the exact analytical solution using the quadratic u-profile (Rahman and Faghri [89]), especially in the near wall region. The IBL predictions for the height of the concentration boundary layer using the third-order polynomial are in very good agreement with the exact far-field solution, while the IBL results using a second-order polynomial predict a faster increase of the concentration boundary layer. At larger radii, where $\delta_c = \delta$, (see Figs. 4.14(c)-(d)), the second-order polynomial predicts significantly lower values for the surface species mass fraction c_δ than the IBL model using the third-order polynomial and the analytical far-field solution, which show good agreement. This behavior is due to the fast growth of the concentration boundary layer and the resulting more rapid decrease of the species mass fraction at the free surface when using the second-order polynomial ansatz function.

Significant deviations from the other solutions are observed in the analytical far-field results using a linear approximation for the radial velocity profile. This analytical solution exhibits generally lower wall gradients, and a markedly higher thickness of the concentration boundary layer at $r = 4$. The assumption of a linear velocity profile inside the liquid film is evidently inadequate at larger radii, where the analytical far-field solution yields the semi-parabola (2.93), and the radially continuously increasing concentration boundary layer is not significantly thinner than the film thickness.

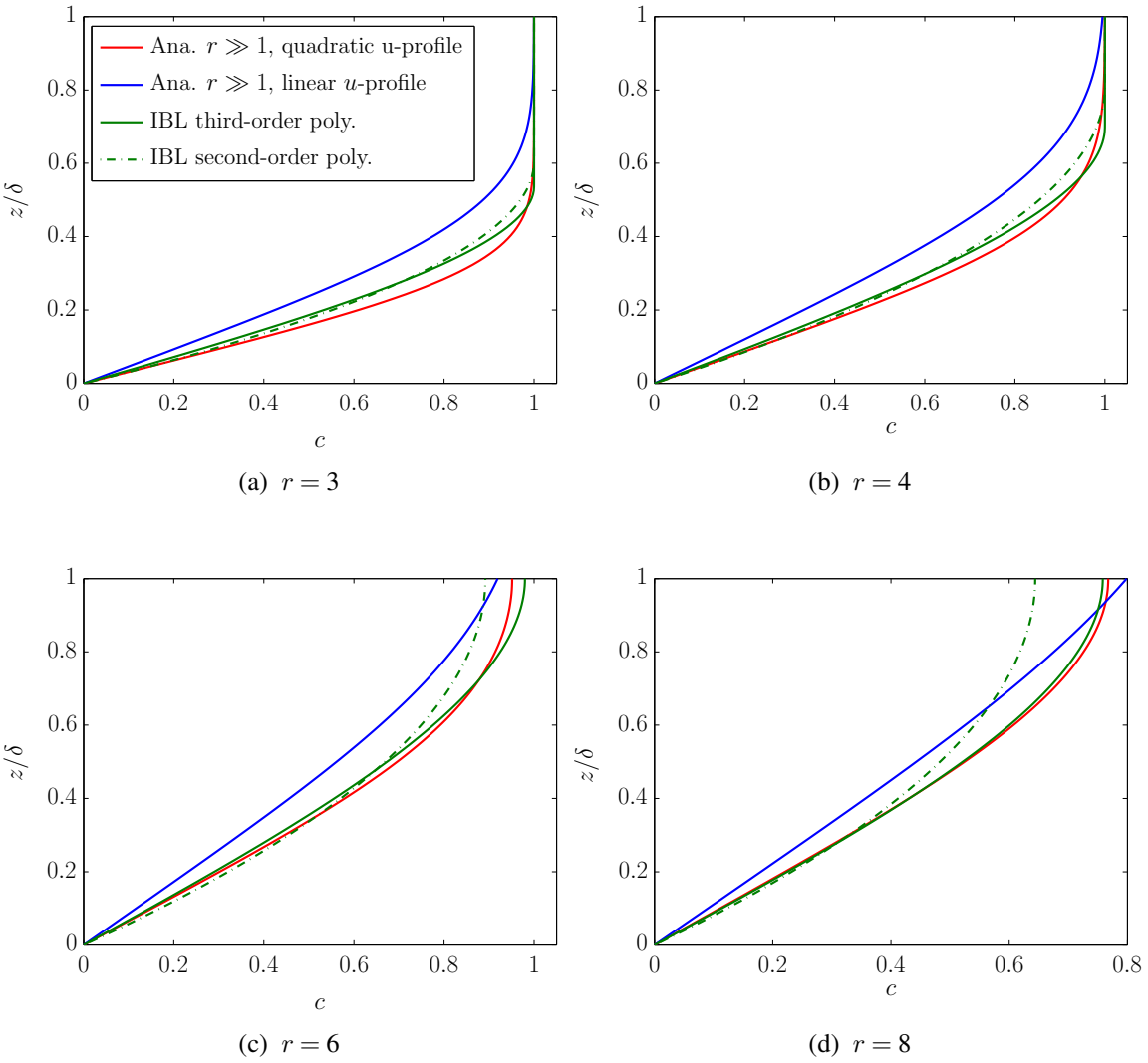

(a) $r = 3$ (b) $r = 4$

(c) $r = 6$ (d) $r = 8$

Figure 4.14: Profile assumptions for species mass fraction for the case C3. IBL predictions using the second and third-order polynomial ansatz functions vs. analytical far-field solutions (Rahman and Faghri [89]).

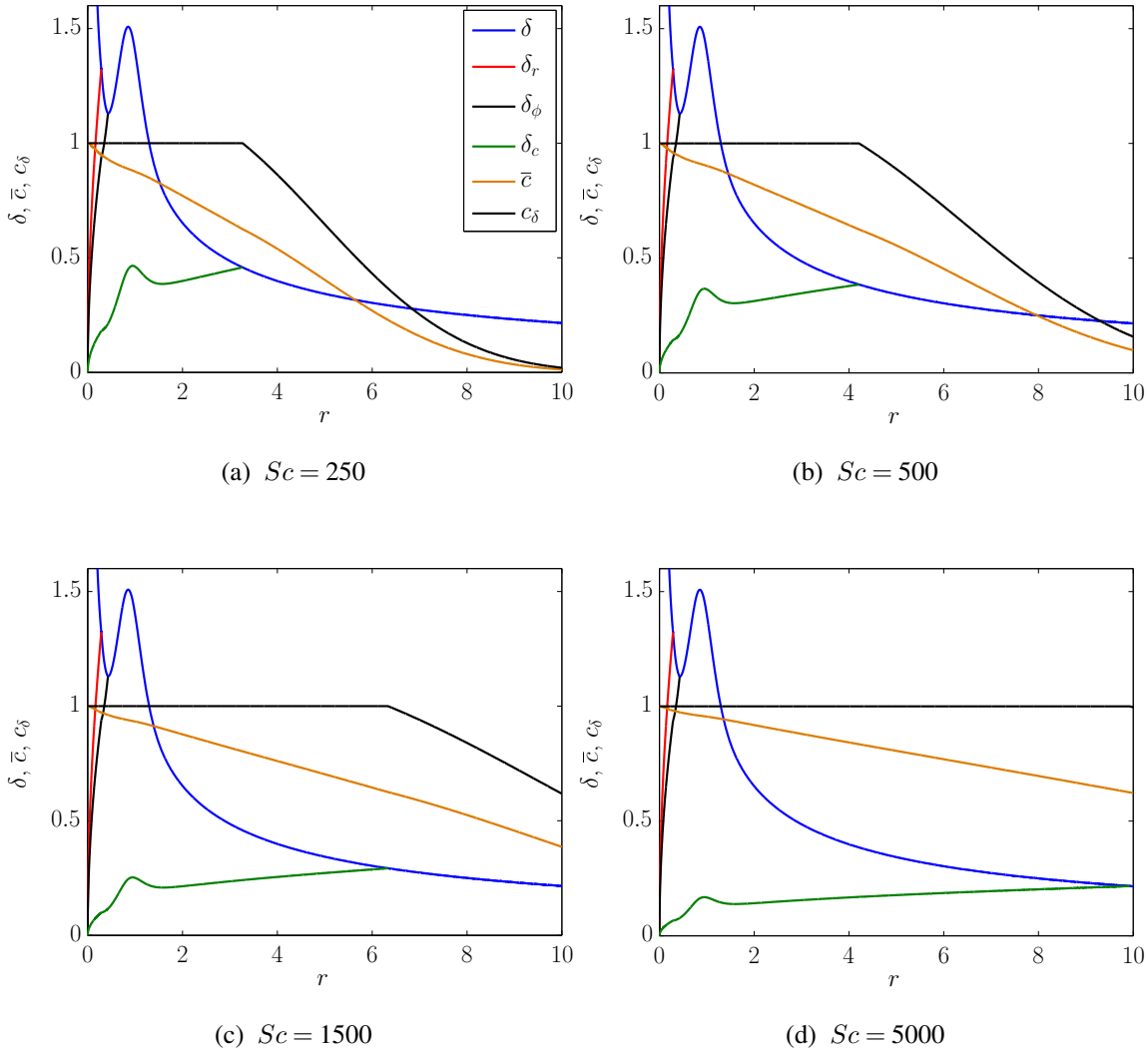

(a) $Sc = 250$

(b) $Sc = 500$

(c) $Sc = 1500$

(d) $Sc = 5000$

Figure 4.15: Steady-state IBL results for film thickness, thickness of individual boundary layers and depth-averaged species mass fraction for varying Schmidt numbers.

In summary, it can be stated that the predictions of the IBL approximation assuming a third-order polynomial profile for the species mass fraction are generally in very good agreement with the analytical results, which are obtained by integrating the asymptotic species mass transport equation in the far-field for large radii assuming a semi-parabolic velocity profile.

Effect of the Schmidt number

In Figs. 4.15(a)-(d) the effect of an increase of the Schmidt number on the thickness of the concentration boundary layer δ_c and the depth-averaged mean species mass fraction $\overline{c}$ is examined. The setting of the hydrodynamical parameters follows again case C3 in table 4.1 For the lowest Schmidt number, $Sc = 250$, the radial extension of the entry length $0 < r < r_c$ is smallest as expected. The concentration boundary layer increases rapidly and reaches the free surface already at $r_c \approx 3.3$. The depth-averaged mean species mass fraction decreases fastest with increasing radii and approaches zero in the radially outer region. An increase of the Schmidt number results in a shift of r_c radially further downstream, as can be seen from Figs. 4.15(b)-(d). Consistently the radial decrease of the depth-averaged mean species mass fraction becomes slower the larger the Schmidt number.

4.2 Effect of wavy flow

In this section the effects of wavy flow conditions on the dynamics and the heat and species mass transfer characteristics are analyzed in detail, considering again the three cases which were discussed in the analysis of the steady-state smooth film solutions (cf. Tab. 4.1). To validate the predictions of the unsteady IBL model comparisons against results from numerical CFD simulations are shown as well.

4.2.1 Hydrodynamics

In Fig. 4.16 the predictions of the unsteady IBL model for the instantaneous radial variations of the film thickness for the case C1, are depicted together with result from an axisymmetric CFD simulation. In the radially inner region both computational results exhibit a smooth film and are in very good agreement. Radially further downstream small disturbances are amplified and the generated sequence of small waves with nearly sinusoidal-shape merges into large amplitude waves with steep fronts, preceded by capillary ripples. Good agreement is found for the radial position of wave inception and their evolution radially downstream. The integral method evidently reproduces waves with similar amplitudes and wave lengths as obtained in the axisymmetric CFD simulation. It is interesting to note that at larger radii the radial extension of the thin film regions, which separate the large amplitude waves, increases.

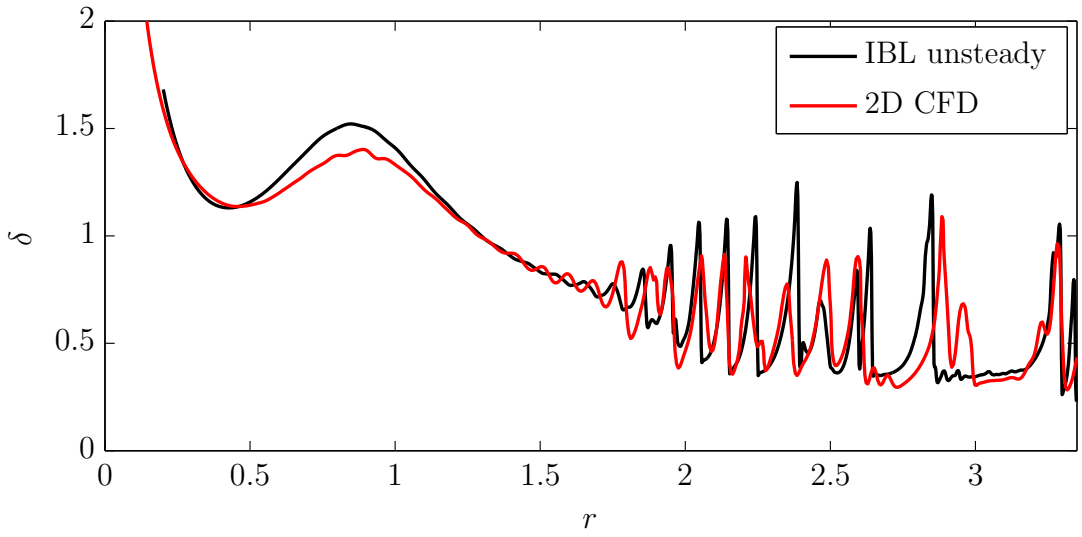

Figure 4.16: Instantaneous profiles of the film thickness for the case C1.

Fig. 4.17 shows the time-averaged profiles of the film thickness predicted by the unsteady IBL model together with the time-averaged profiles obtained from the axisymmetric CFD simulation. The asymptotic far-field solution in the limit of large radii, $\delta = r^{-2/3}$, is depicted as well. In the radial inner region, which is associated with small Ekman numbers, both results exhibit smooth non-wavy film surfaces, so that the shown time-averages do not differ from the instantaneous solution presented in Fig. 4.16. In the wavy region further downstream a very good agreement is seen only between the predictions of the unsteady IBL model and the predictions of the CFD simulation. In this outer radial region the prediction of the asymptotic far-field solution, which basically represents the steady-state smooth film IBL solution for large radii, lies well above the time-averaged film height of the unsteady wavy film results. This decrease of the average film thickness associated with wavy flow, which is very well reproduced by the unsteady IBL model, exerts a significant effect on the heat and mass transfer as well, as will be discussed in Sec. 4.2.2 and Sec. 4.2.3, respectively. It is therefore of central importance to capture this salient flow feature when modeling the etching process.

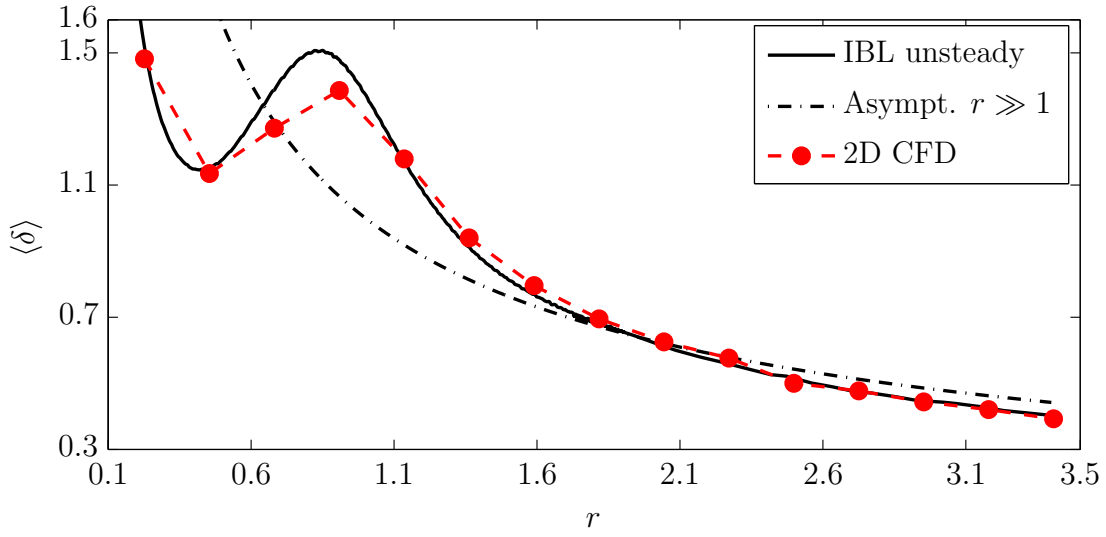

Figure 4.17: Time-averaged radial variation of the film thickness for the case C1.

As seen from Fig. 4.18, the time-averaged wall shear rates of the numerical results and the predictions of the IBL model are also in very good agreement. As a salient feature, the radial wall shear rates of the wavy film lie always well below the prediction of the steady-state smooth-film solution in the radially outer region, where waviness appears. The largest difference between the predictions of the unsteady IBL model, using either a quartic or a quadratic profile for the radial component of the velocity, is again observed in the inertia

dominated radially inner region ($r \leq 2$), where, as to be expected, the quartic approximation gives a slightly better estimate for the local wall shear rates when compared against the CFD results. Radially further downstream due to the vanishing effect of the inertial forces no significant discrepancies can be observed in the time-averaged predictions of the IBL model using either profile assumptions for the radial component of the velocity.

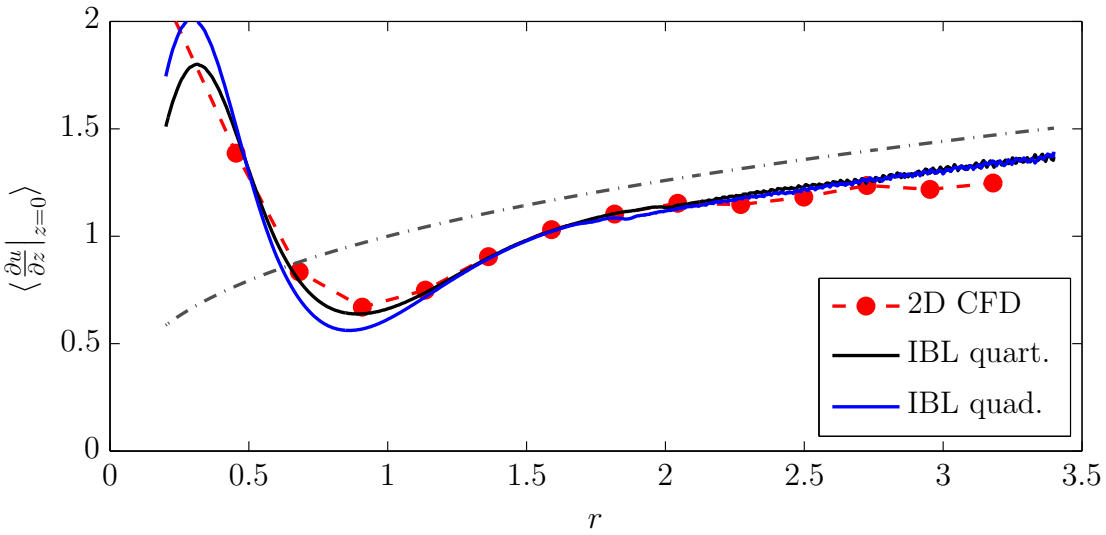

Figure 4.18: Time-averaged wall shear rates for the case C1.

To examine the profile assumptions, which were required for the depth-averaging in the framework of the IBL model, a comparison with the instantaneous profiles obtained from the CFD simulation was carried out. Figs. 4.19 and 4.20 show a comparison between the assumed profile functions and the instantaneous velocity profiles obtained from the CFD analysis at several radial positions inside a single wave. While the assumed profiles agree very well with the instantaneous profiles obtained from the CFD simulation at position 1 (Fig. 4.19(b)), some deviations from the CFD results are observed upstream of the wave crests, at positions 2 and 3 (Figs. 4.19(c)-(d)). At position 2, the quartic profile assumption comes closer to the CFD prediction, giving a better approximation for the radial component of the surface velocity. Still, both profile assumptions slightly overpredict the magnitude of the numerically obtained result for the surface velocity of the radial velocity component. An opposite tendency can be observed at position 3, where both profile assumptions of the IBL model practically coincide. At this position the profile obtained from the CFD simulation indicates a faster moving layer at the top of the film. At positions 4-6, the analytically assumed profiles again match the instantaneous velocity profiles obtained with the CFD simulation very well, as shown in Fig. 4.20.

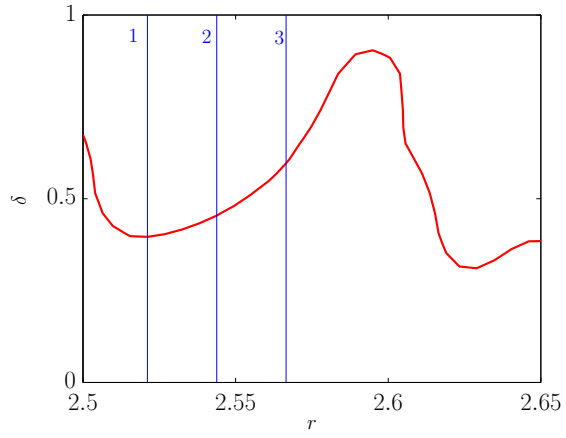

(a) Selected radial position inside an instantaneous wave profile

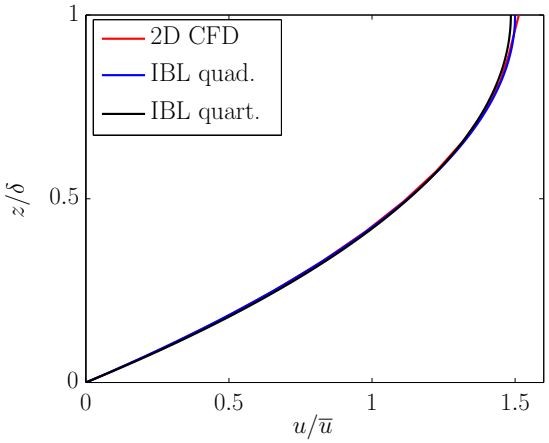

(b) Position 1

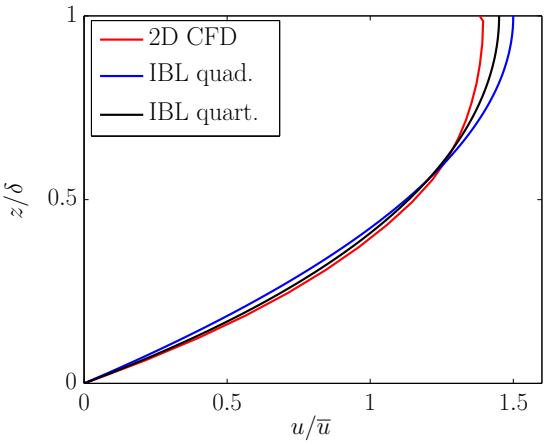

(c) Position 2

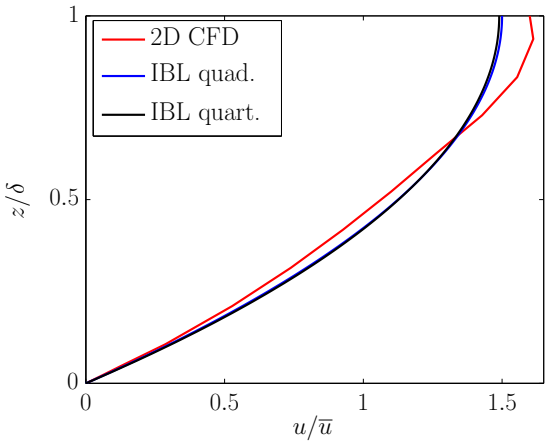

(d) Position 3

Figure 4.19: Instantaneous profiles of the radial velocity component at different radial positions inside a single wave for the case C1.

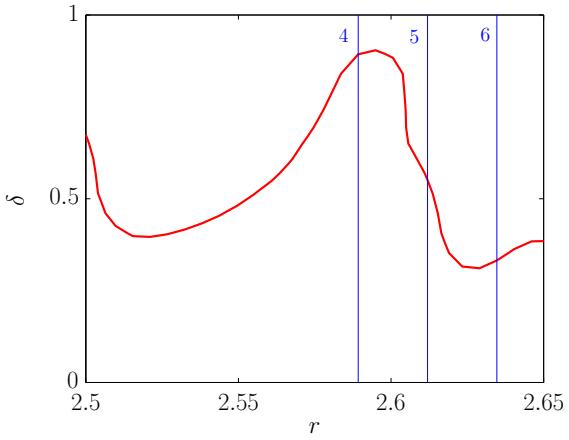

(a) Selected radial position inside an instantaneous wave profile

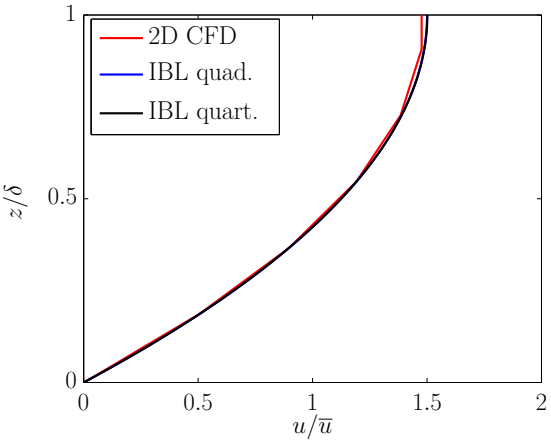

(b) Position 4

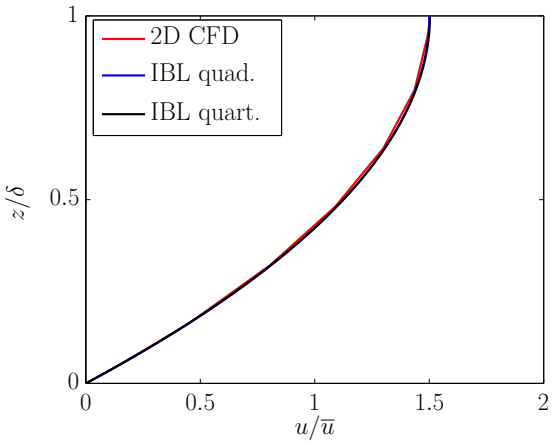

(c) Position 5

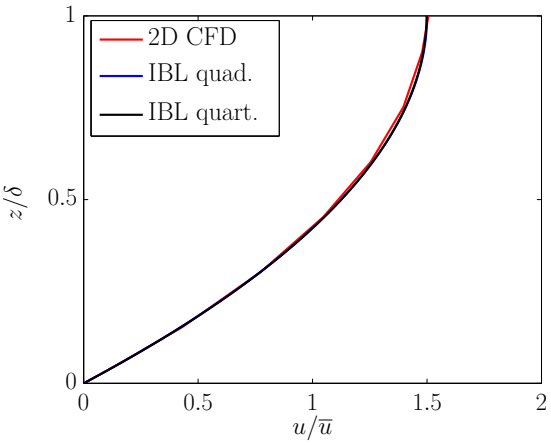

(d) Position 6

Figure 4.20: Instantaneous profiles of the radial velocity component at different radial positions inside a single wave for the case C1.

Very importantly, it has to be noted that no significant deviation of the velocity profiles in the near wall region was observed. This can be considered as a promising aspect, when extending the IBL approximation to include heat and species mass transfer between the liquid and the disk‘s surface.
Concerning the assumption for the profile of the radial velocity it is further noted that the quartic profile (IBL quart.) was used in all IBL results presented in the following, unless it is specifically indicated as quadratic (IBL quad.).

The reduction of the time averaged film height observed in the wavy region can be explained by taking a closer look at the evolution of the instantaneous flow quantities.

In Fig. 4.21(a) the predictions of the unsteady IBL model for the film thickness are depicted together with the instantaneous depth-averaged radial velocity $\overline{u}$. The shown signals are evidently well in phase, so that the spatial maxima in δ and $\overline{u}$ coincide. From Fig. 4.21(b) it can be observed that the azimuthal component of the velocity significantly lags behind the disk speed beneath the wave peaks, while it differs only slightly from the speed of the solid body rotation in the wave troughs. This indicates the retarding effect of the azimuthal component of the velocity on the flow caused by the Coriolis force, which has already been pointed out by Matar et al. [79, 90]. Due to this effect waves are propagated at lower speeds in rotating films than in corresponding falling films.

In Fig. 4.22 the instantaneous profiles of the film thickness, the radial component of the velocity at the free surface, and the local wall shear rates are examined in detail. From the numerical results of the axisymmetric CFD based solution of the Navier-Stokes equations, depicted in Fig. 4.22(a), it is obvious that the variations of the surface velocity are in phase with to the film thickness, and the values become obviously largest at the wave peaks and smallest in the wave troughs. Exactly the same behavior is observed in the predictions of the IBL model, which are shown in a close-up view in Fig. 4.22(b).
The radial position of the maximum in the local wall shear rate predicted by the CFD simulation is observed in the strongly ascending part on the tail side of the waves, while the minima are reached in the wave troughs. In the results of the IBL model local minima and maxima in the wall shear rates appear at the same positions relative to the wave. Adomeit and Renz [111] experimentally observed the same positions for the extrema of the local wall shear rate relative to the waves in the case of falling liquid films. They analyzed the instantaneous, laminar falling film flow for a large range of Reynolds numbers. In their experimental study the maxima in the instantaneous flow rate always coincided with wave crests. Moreover the radial velocity profile was found to be approximately parabolic throughout the wavy domain. As such these experimental observations for falling films are well in line with the computational results of the IBL model and the CFD results for the instantaneous flow on the spinning disk obtained in the present study.

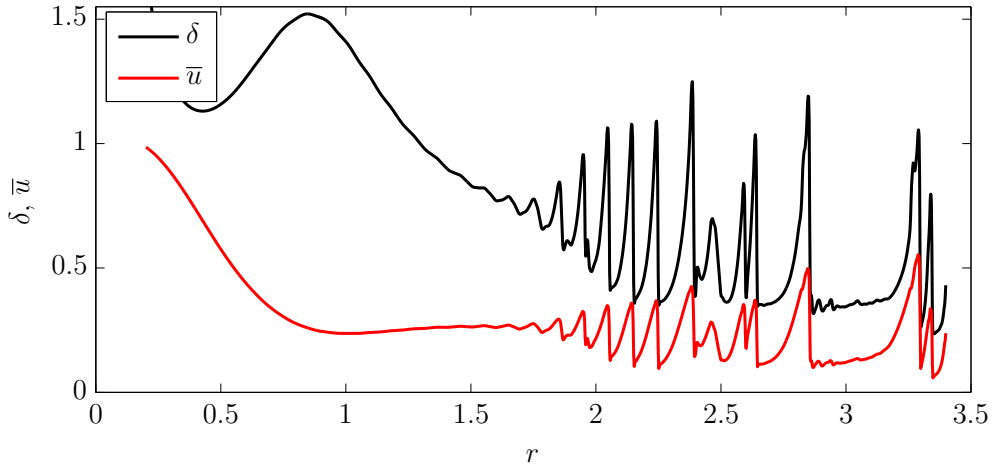

(a) Instantaneous film thickness together with depth-averaged radial velocity.

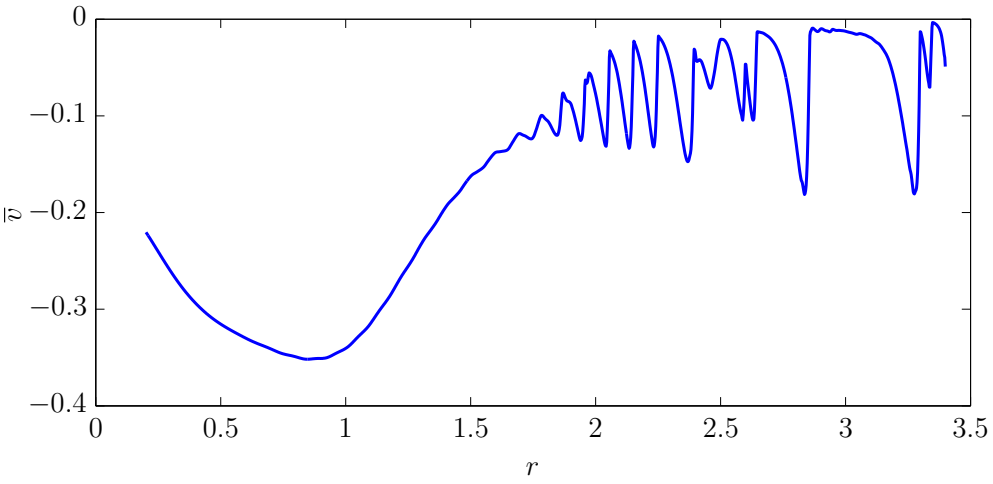

(b) Instantaneous depth-averaged azimuthal velocity.

Figure 4.21: Instantaneous profiles of the film thickness and the depth-averaged radial and azimuthal velocity components obtained by the unsteady IBL model for the case C1.

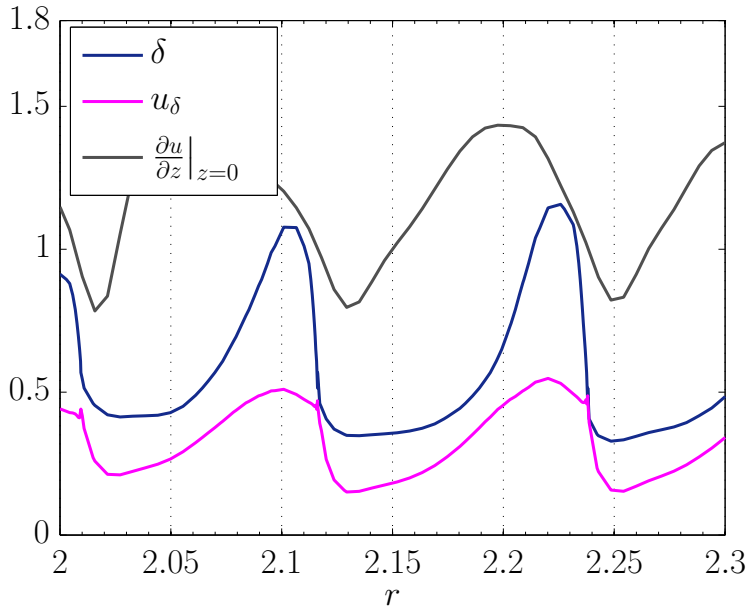

(a) 2D CFD

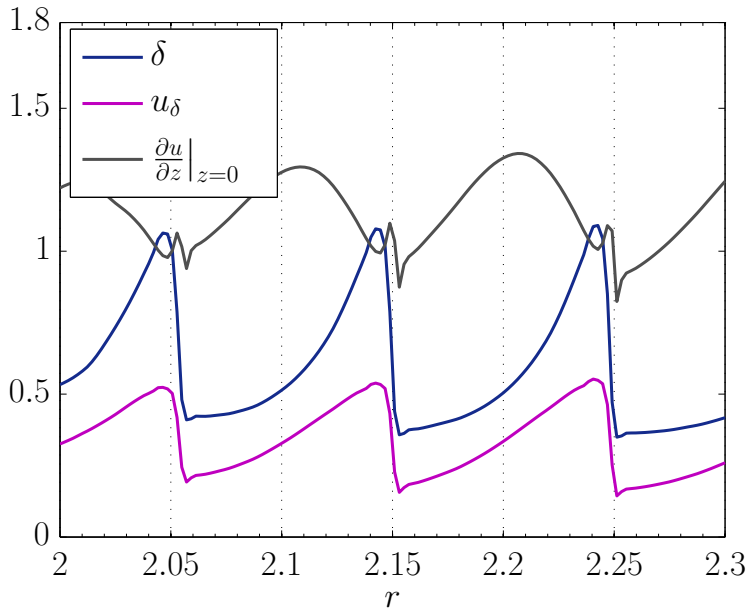

(b) unsteady IBL

Figure 4.22: Instantaneous profiles of the film thickness, the radial surface velocity and the local wall shear rate for the case C1.

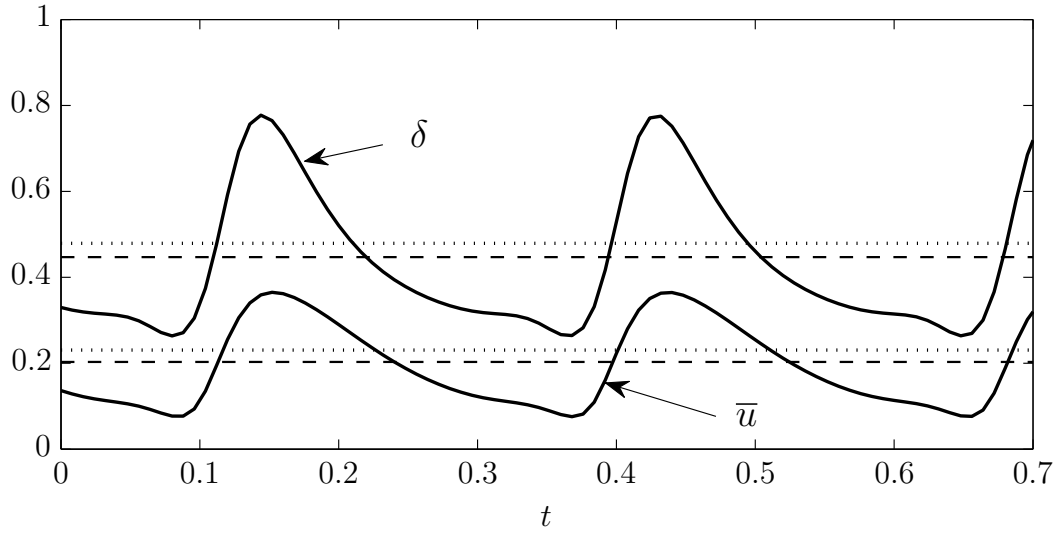

Figure 4.23: IBL predictions for the case C2. Temporal evolution of film thickness and radial velocity at $r = 3$. Dashed horizontal lines: time-averaged predictions of unsteady IBL model. Dotted horizontal lines: steady-state smooth film IBL predictions.

A closer look at the evolution of the instantaneous flow quantities in time is shown in Fig. 4.23 for the case C2. This particular case will also be considered in the next section, where the effect of the wavy flow on the heat transfer is examined. In Fig. 4.23 the evolution of the instantaneous film thickness is plotted together with the evolutions of the instantaneous depth-averaged radial velocity $\overline{u}$, at a fixed radial position $r = 3$. The corresponding time-averaged mean values of the unsteady and the steady-state smooth film solutions are indicated by the horizontal dashed and dotted lines, respectively. The shown time signals make evident again that the depth-averaged radial velocity is in phase with the film height. It can be inferred from the coincidence of the maxima/minima in δ and $\overline{u}$ that a considerable part of the liquid volume passes the disk in shape of fast moving solitary waves. The comparatively longer periods associated with a very thin film coverage occurring between the passage of the large waves effectively lead to smaller time-averaged film heights.

The present findings based on the temporal evolution of the relevant dynamic quantities predicted by the unsteady IBL model are again supported by numerical results obtained from a CFD simulation. As seen from Fig. 4.24, the different time signals from the CFD analysis feature the same wave pattern as it was obtained from the unsteady IBL solution.

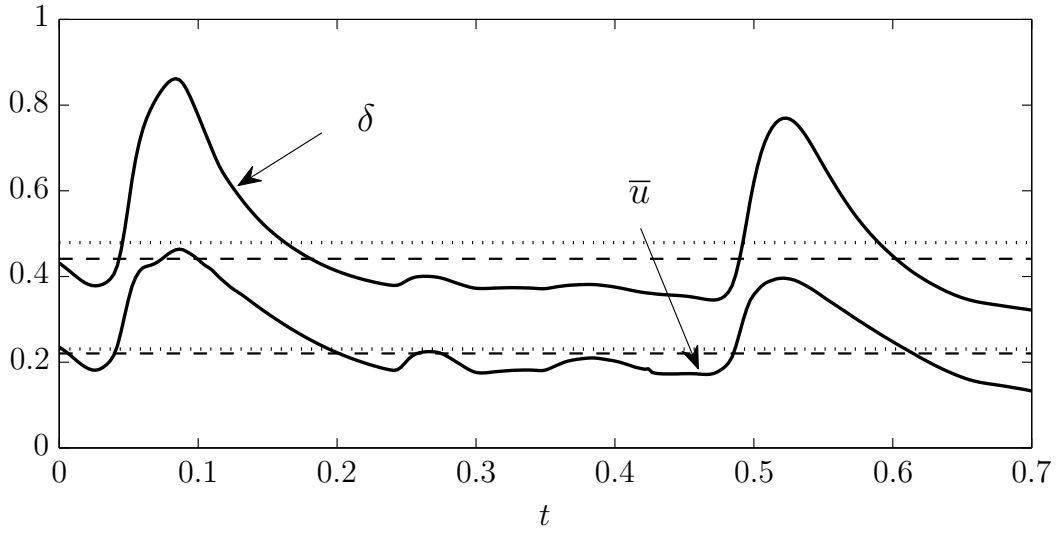

Figure 4.24: CFD results for the case C2. Temporal evolution of film thickness and depth-averaged radial velocity at $r = 3$. Dashed horizontal lines: time-averaged predictions of unsteady IBL model. Dotted horizontal lines: steady-state smooth film IBL predictions.

Summing up, it can be stated that the present unsteady IBL model is capable to capture the essential instantaneous hydrodynamic features of the thin film flow at a high descriptive level.

4.2.2 Heat transfer

Fig. 4.25(a) shows the time-averaged profiles of the film thickness for the case C2 as obtained from the IBL model using the steady-state and the unsteady formulation, as well as the results of the axisymmetric CFD simulation. In the radial inner region for $r \lessapprox 2$, which is associated with small Ekman numbers $Ek \lessapprox 3$, both the steady and the unsteady IBL solutions exhibit smooth non-wavy film surfaces. This behavior is also shown by the CFD results. In the wavy region further downstream for $r > 2$ and larger values of the local Ekman number the steady IBL model essentially produces the variation of the film thickness in the asymptotic limit of large radii, $\delta = r^{-2/3}$, which again evidently lies well above the time-averaged film height of the unsteady wavy film results. This decrease of the time-average film thickness associated with wavy flow is again very well reproduced by the unsteady IBL model.
The radial variations of the dimensionless wall temperature predicted by the unsteady IBL model and the axisymmetric CFD simulation clearly reflect the effect of waviness as well,

as it is seen from Fig. 4.25(b). Both the predictions of the unsteady IBL model and the CFD show in good agreement an enhanced radial increase of $\langle\theta_w\rangle$ in the wavy region ($r > 2.5$). In contrast, the smooth film solution of the steady IBL model predicts a considerably slower radial increase of $\langle\theta_w\rangle$ resulting in markedly lower values for the dimensionless wall temperature in the outer radial region, associated with local Ekman numbers $Ek \gtrapprox 3$ and surface waves.
According to the definition (2.53) a higher dimensionless wall temperature corresponds to a lower wall temperature T_w, when cooling conditions, prescribed in terms of a negative wall heat flux q_w, are assumed. Thus, the unsteady IBL solution, which captures the formation and propagation of the surface waves, evidently produces on average lower wall temperatures as compared to the steady-state smooth film results. Analogously, in the case of a heated film, associated with a positive wall heat flux ($q_w > 0$) in the definition (2.53), the wall temperature in the wavy film solution would be higher.

The increase of the time-averaged dimensionless wall temperature θ_w, observed in the wavy region can again be explained by taking a closer look at the evolution of the instantaneous flow and thermal quantities in time.
Fig. 4.26(a) shows the evolution of the instantaneous film thickness plotted together with the evolutions of the instantaneous depth-averaged radial velocity $\overline{u}$ and the depth-averaged dimensionless temperature $\overline{\theta}$, at a fixed radial position $r = 3$. The corresponding time-averaged mean values of the unsteady and the steady-state smooth film solutions are indicated by the horizontal dashed and dotted lines, respectively. The temporal maxima/minima in δ and $\overline{u}$ are found again to coincide. Furthermore, the time signals of the shown dimensionless temperatures are all in phase with the film height and the velocity as well, but here the minima in the $\overline{\theta}$-values coincide with the maxima in δ, or $\overline{u}$, and vice versa. Assuming heated film flow conditions ($q_w > 0$), this implies that during the periods with small film heights and slow radial motion the temperature of the thin liquid layer is increased very fast by the heating from below. The temperature inside the liquid also becomes more uniform as seen from the converging tendency of the individual θ-signals (Fig. 4.26(a)). The comparatively long periods associated with higher temperature levels of the liquid finally explains the increased temporal averages of the non-dimensional wall temperature θ_w obtained for the unsteady IBL solution in the wavy region.

The present findings based on the temporal evolution of the relevant dynamic and thermal quantities are also supported by numerical results obtained from a CFD simulation. As seen from Fig. 4.26(b), the different time signals show the same behavior, as it was seen in the results of the unsteady IBL solution.

An assessment of the instantaneous velocity and temperature profiles at several time instants inside a single wave is shown in Figs. 4.27-4.28. The velocity profiles are normalized with the corresponding absolute value of the surface velocity, so that the signs of the

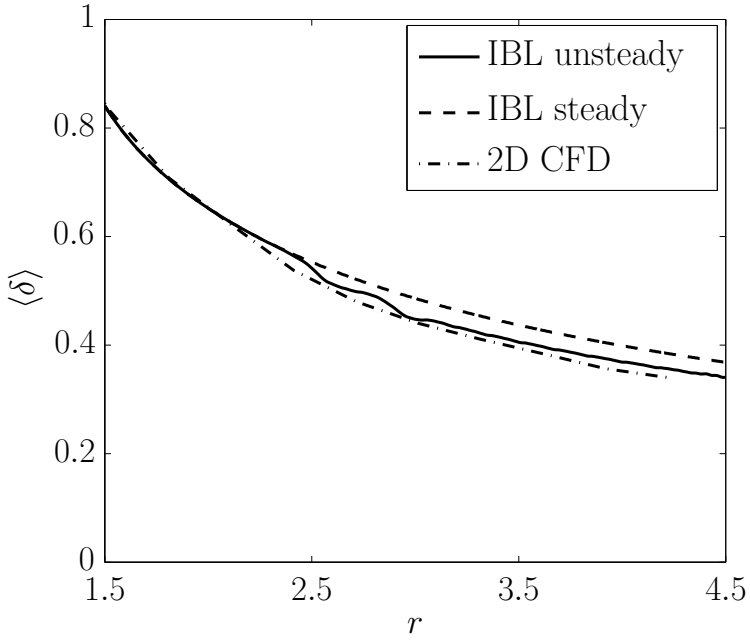

(a)

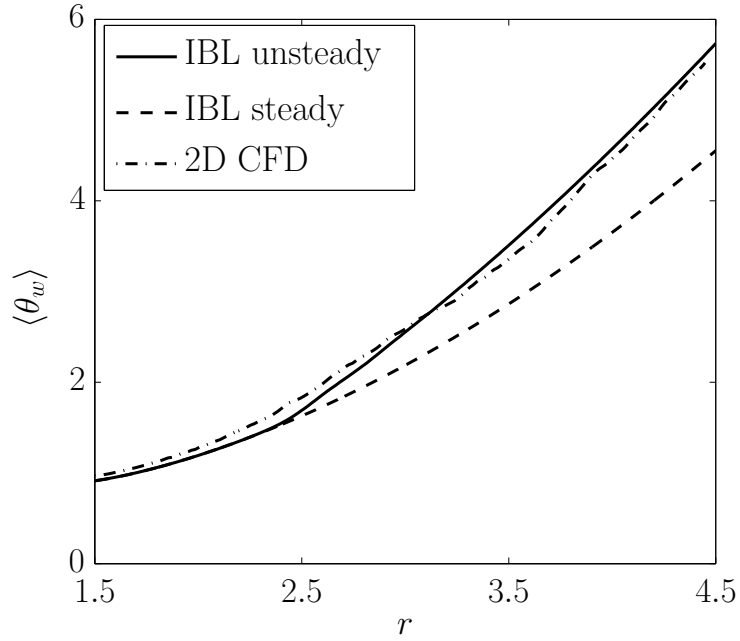

(b)

Figure 4.25: Time-averaged IBL predictions and 2D CFD results for the case C2, (a) film thickness vs. radial distance, (b) wall temperature vs. radial distance.

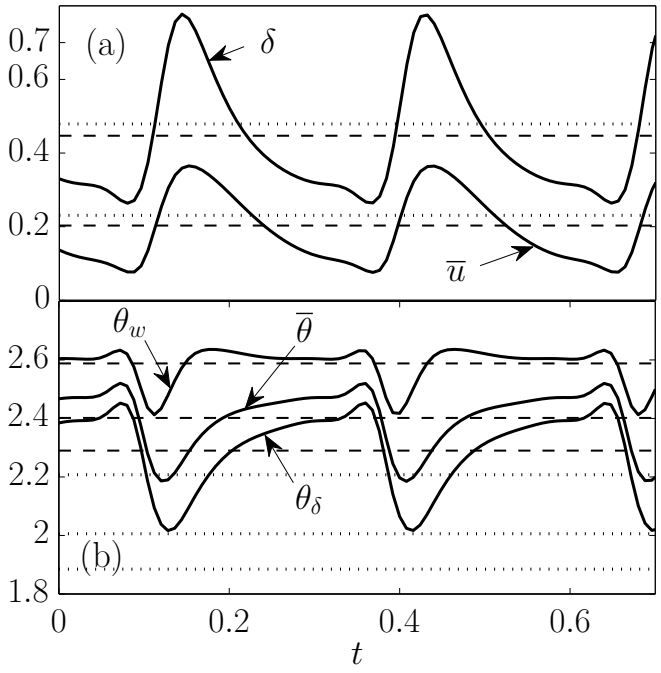

(a) IBL model

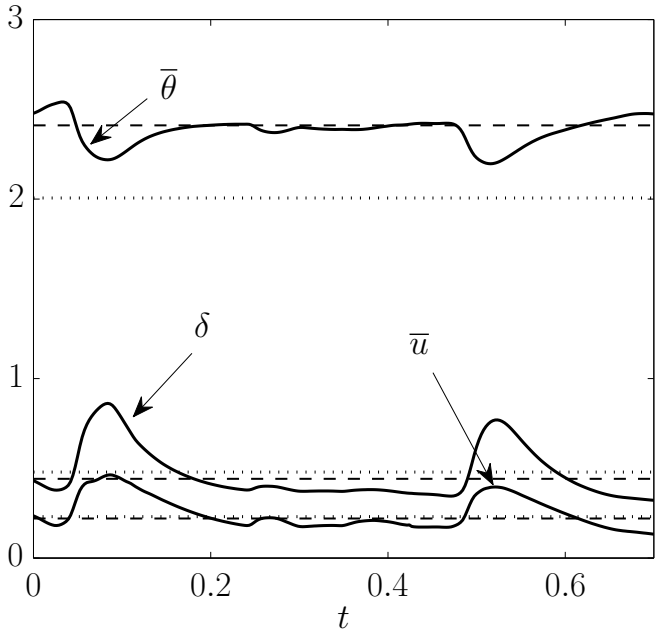

(b) 2D CFD

Figure 4.26: Temporal evolution of film thickness, depth-averaged radial velocity, and depth-averaged temperature at $r = 3$ for the case C2. Dashed horizontal lines: time-averaged predictions of unsteady IBL model. Dotted horizontal lines: steady-state smooth film IBL predictions.

normalized velocities indicate the orientation of the motion at the surface relative to the rotating disk. One should also bear in mind that in the wavy region the maximum values of the relative azimuthal and wall normal velocity components are at least one order of magnitude smaller than the radial surface velocities. The dashed curves always refer to the profiles of the IBL model, where the radial and the azimuthal velocity components are determined by the assumed quartic polynomials, Eqs. (2.134) and (2.136), respectively, and the vertical wall normal velocity is computed from Eq. (2.142).
At the instants of time associated with the passage of a wave trough, Figs. 4.27(b)-(c), a fairly good agreement between the assumed velocity profiles and the instantaneous profiles obtained from the CFD simulation is found. Moreover, also the assumed third-order polynomial for the temperature reproduces very well the temperature distribution obtained from the CFD results. Between time instant 2 and 3 the sign of the vertical surface velocity switches from negative to positive. Within this short interval of time (see e.g. Fig. 4.27(d)) a steep wave front passes by, and all profiles associated with the IBL model significantly deviate from the corresponding CFD results. Here the CFD results suggest a two-layered flow with a fast moving surface layer and a slowly moving bottom layer. These short periods associated with the passage of steep wave fronts make the limitations of the current IBL model, or rather its profile assumptions, evident. Aside from these discrepancies, as can be observed from Fig. 4.28, a very good agreement between the IBL profiles and the instantaneous profiles obtained from the CFD simulation is found again at instants 4-6. These instants of time refer to the passage of the descending tail side parts of the waves.

Dynamically speaking, the observed wave propagation is driven by the centrifugal force, which pushes the liquid towards the front faces of the waves crests. In effect, as indicated by the sign of the vertical component of the surface velocity, the liquid motion is directed upwards when the steep front faces of the waves are passing, while it is directed downwards otherwise. Thus, the action of the centrifugal force effectively steepens the waves resulting in the formation of large solitary waves, which are separated by relatively large thin film regions. The wave crests are moving relatively faster than the liquid in the bottom layer as indicated by the S-shaped profile seen in Fig. 4.27(d).

Since the deviations of the profiles used for the IBL model from the corresponding CFD results occur only during comparatively short periods of time, the predictions of the present unsteady IBL model still provide a very reliable description of the wavy film flow including heat transfer. Nonetheless, the assumed profile functions required by the IBL approach still represent an important limitation of this model when considering wavy flow.

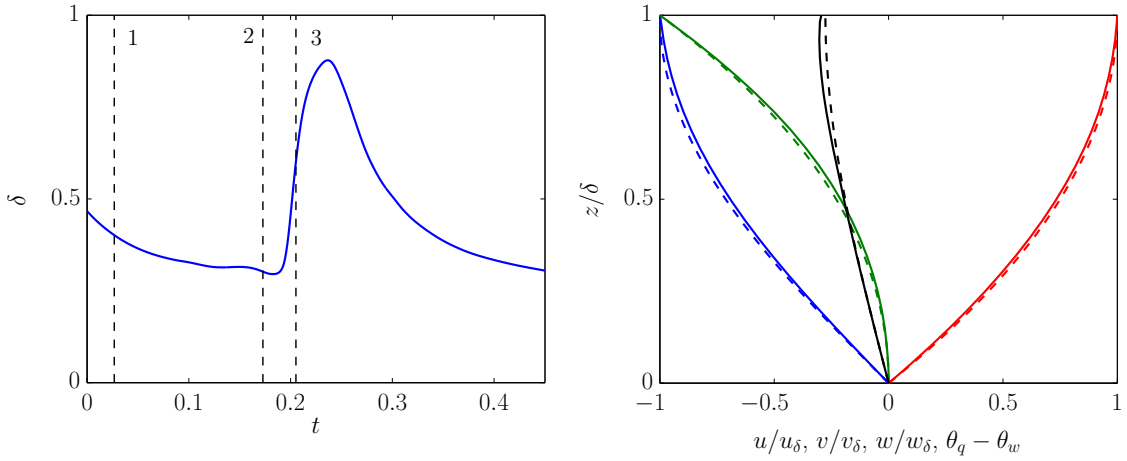

(a) Evolution of film height at $r = 2.8$ and selected instants of time.

(b) Instant 1

(c) Instant 2

(d) Instant 3

Figure 4.27: Instantaneous profiles of the radial (red), azimuthal (blue) and vertical (green) velocity components together with the dimensionless temperature profiles (black) at selected instants of time inside a single wave at $r = 2.8$. The dashed lines refer to IBL predictions, the solid lines to CFD results.

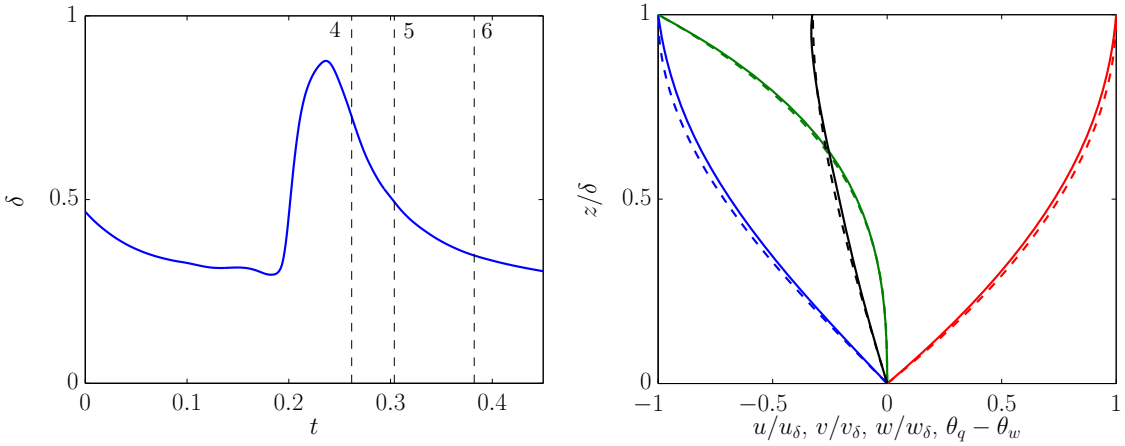

(a) Evolution of film height at $r = 2.8$ and selected instants of time.

(b) Instant 4

(c) Instant 5

(d) Instant 6

Figure 4.28: Instantaneous profiles of the radial (red), azimuthal (blue) and vertical (green) velocity components together with the dimensionless temperature profiles (black) at selected instants of time inside a single wave at $r = 2.8$. The dashed lines refer to IBL predictions, the solid lines to CFD results.

4.2.3 Species mass transfer

To assess the predictive capability of the unsteady IBL model for species mass transfer in wavy films the case referred to as C3 in table 4.1 was considered. Fig. 4.29(a) shows the IBL predictions for the instantaneous film thickness and the thickness of the concentration boundary layer, together with the corresponding time-averaged results denoted by the red lines. The corresponding results for the film thickness and the height of the concentration boundary layer of a CFD simulation, which was carried out as well to validate the results of the unsteady IBL solution, are shown in Fig. 4.29(b). In the radially inner region, the CFD results as well as the predictions of the IBL model exhibit a smooth film. The time-averaged film thickness and the thickness of the concentration boundary layer remain close to the steady-state solution in the region associated with $r \lessapprox 2$, and both computational results agree well with each other. Radially further downstream the formation of nonlinear waves on the film surface leads to strong variations of the thickness of the concentration boundary layer in the predictions of the IBL model. With growing amplitudes of the surface waves the local maxima in the thickness of the concentration boundary layer increase as well. As a consequence, a fast radial increase of the time-averaged concentration boundary layer is observed in the region $2.5 \lessapprox r \lessapprox 3$. In contrast, the time-averaged concentration boundary layer thickness increases notably more slowly in the CFD results in this interval. Radially further downstream the time-averaged thickness of the concentration boundary layer predicted by the IBL model follows closely the trend of the time-averaged film height.

Fig. 4.30 shows the time-averaged results for the radial variation of the film thickness, the surface species mass fraction, and the Sherwood number. While for the time-averaged film thickness again very good agreement between the predictions of the unsteady IBL model and the CFD results is found, the time-averaged results for the species transport differ significantly. The IBL model predicts a much faster decrease of the species mass fraction at the surface from its initial value in the radially outer region. Moreover, the predictions of the unsteady IBL model show a very fast radial decrease of the time-averaged non-dimensional concentration gradient at the wall represented by the Sherwood number in comparison to the steady-state smooth film solution. This behavior results from the sudden increase of the thickness of the concentration boundary layer as can be immediately seen from Eq. (4.7). In contrast to the unsteady IBL predictions the time-averaged local Sherwood number of the CFD solution remains almost constant in this region. In the outer radial region they even come very close to the results of the steady-state smooth film IBL model.

The inability of the present unsteady IBL model to capture correctly the effect of waviness on the species transport can be explained by taking a closer look at the evolution of the instantaneous flow quantities and the assumed profile functions for the velocity components and the species mass fraction in time.

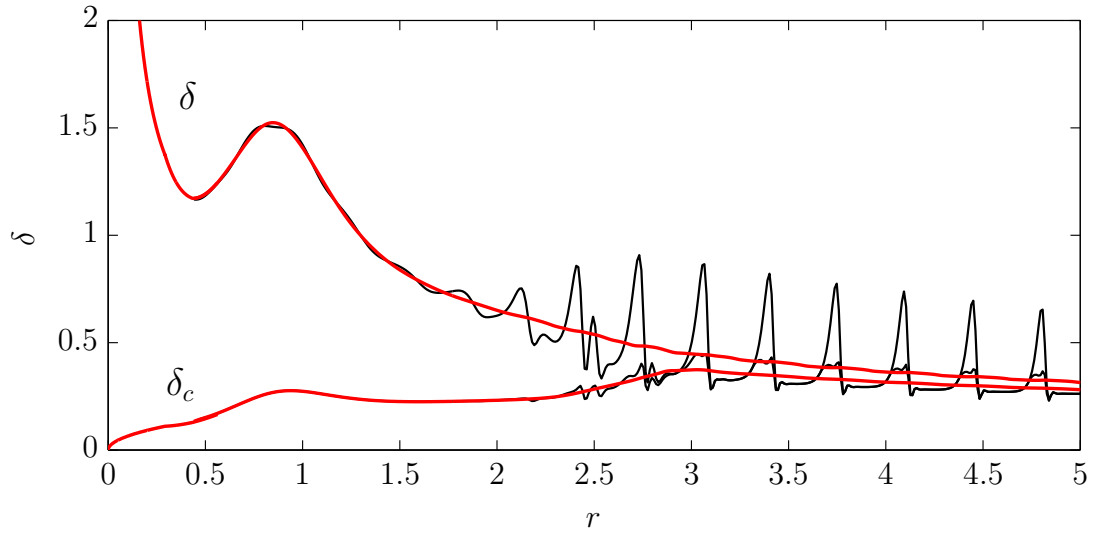

(a) IBL model

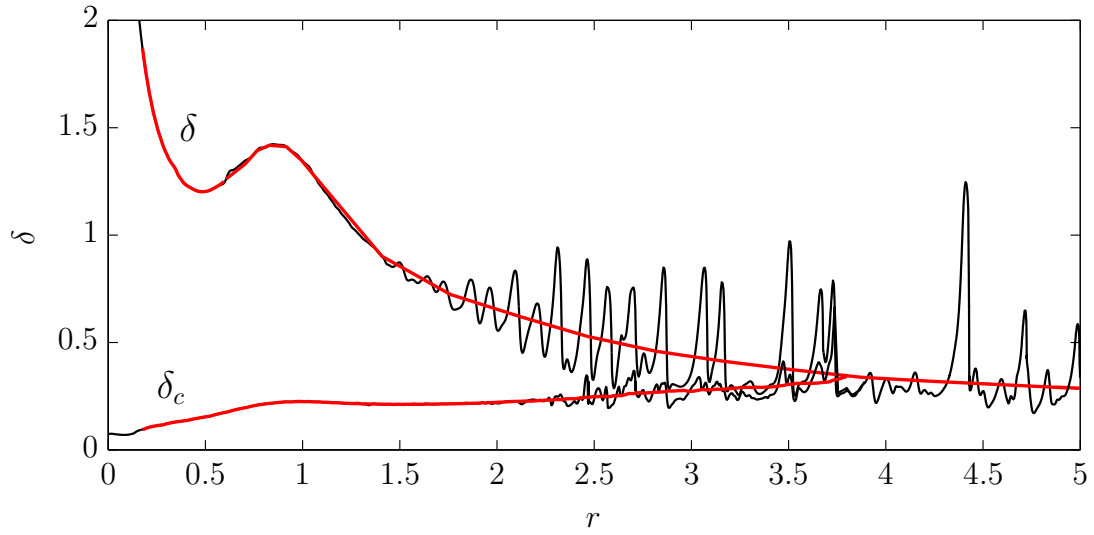

(b) 2D CFD

Figure 4.29: Instantaneous film and concentration boundary layer thickness (black lines) together with the corresponding time-averages (red lines) for the case C3.

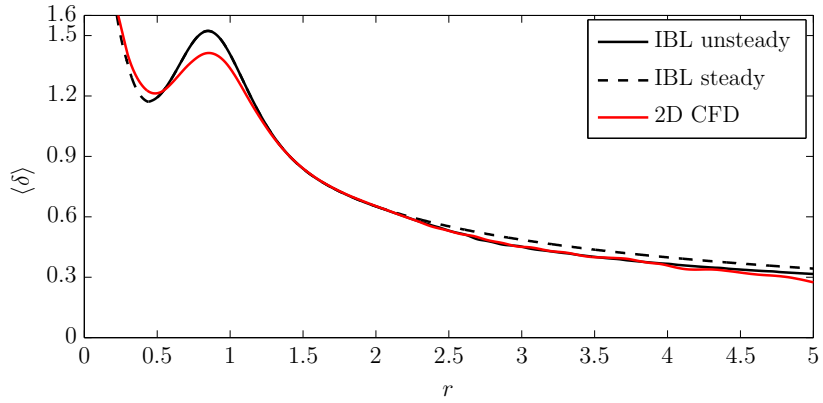

(a) Film thickness

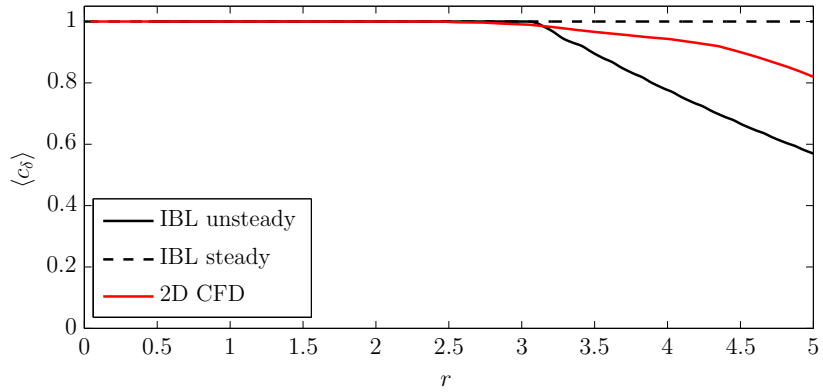

(b) Surface species mass fraction

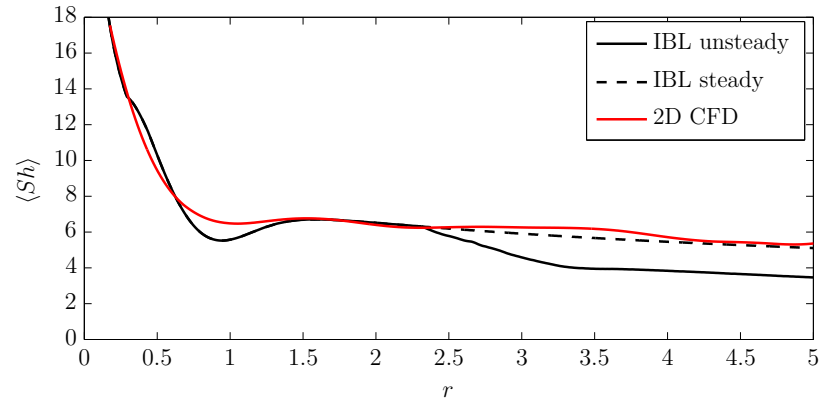

(c) Sherwood number

Figure 4.30: Time-averaged results for the film thickness, the surface species mass fraction, and the Sherwood number for the case C3.

Figs. 4.31(a)-(b) show the evolution of the instantaneous film thickness at the radial position $r = 2.11$ as obtained from the CFD simulation and the IBL model, respectively. This radial position is associated with small amplitude waves, whose evolution is shown here for two typical representatives taken from the CFD and IBL results, respectively. The predictions of the IBL model and the CFD simulation for the species transport agree very well, as seen from Figs. 4.31(e) and 4.31(f), where the temporal evolution of the Sherwood number is depicted. Figs. 4.31(c) and 4.31(d) show the temporal evolution of the components of the surface velocity. While the IBL predictions for the radial and azimuthal surface velocities agree very well with the CFD results, the IBL predictions for the vertical component of the velocity significantly exceed the CFD results in the interval between the instants 1 and 3, or correspondingly, i and iii, associated with the passage of the wave front. In Figs. 4.32-4.33 the instantaneous velocity and species mass fraction profiles at the selected instants of time marked by dashed lines in Figs. 4.31(a)-(f) are depicted. In the left columns (i.e. in Figs. 4.32(a),(c) and Figs. 4.33(a),(c)) the CFD results are compared against the polynomial profile functions for the individual velocity components and the species mass fraction, which were obtained using the local instantaneous CFD results for δ, δ_c and c_δ as input into the formulation of the polynomials. For the shown instantaneous conditions the shapes of the polynomial profiles reproduce very well the simulated counterparts obtained in the CFD. The profiles taken from the unsteady IBL solutions at corresponding instantaneous flow conditions at instants i-iv, which are shown in Figs. 4.32(b) and (d), and Figs. 4.33(b) and (d), respectively, are in good agreement with the CFD results, as well.

Next, the temporal evolutions of the instantaneous flow quantities and the profiles of the velocity components and the species mass fraction are examined at the radial position $r = 2.82$, which is associated with large amplitude waves, considering again two comparable representative conditions taken from the CFD and the IBL solutions, respectively. As can be seen from Figs. 4.34(a)-(d) a good agreement between the CFD results and the IBL predictions for the film thickness and the radial and azimuthal components of the surface velocities is found again. During the passage of the steep wave front occurring closely before instant 2 and, correspondingly, instant ii, the IBL model predicts again a significantly higher magnitude of the vertical component of the surface velocity in comparison to the CFD results. Unlike in the IBL results obtained radially upstream at $r = 2.11$ shown in Fig. 4.31(f) the rapid strong increase of the vertical surface velocity is reflected by a significant temporal variation of the local Sherwood number, as seen from Fig. 4.34(f). In contrast, the CFD simulation predicts a notably higher Sherwood number, which remains almost constant showing no sensitivity to the variations of the vertical velocity component, as seen from Fig. 4.34(e).

Figs. 4.35 and 4.36 show the instantaneous profiles of the radial, azimuthal, and vertical velocity components, as well as the species mass fraction profiles obtained from the

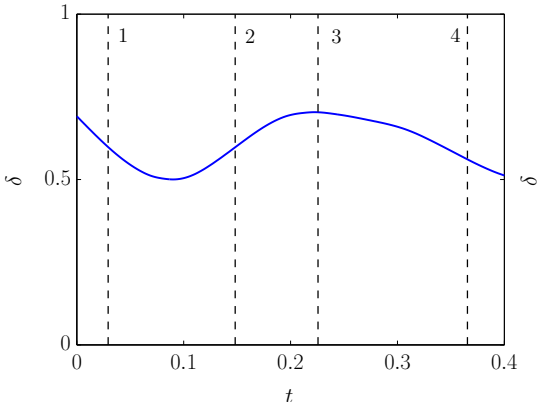

(a) 2D CFD: film height at $r = 2.11$.

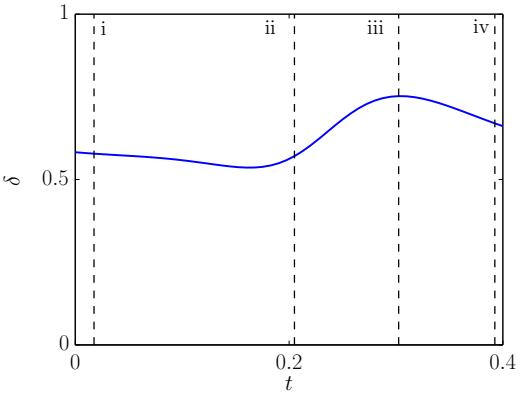

(b) IBL model: film height at $r = 2.11$.

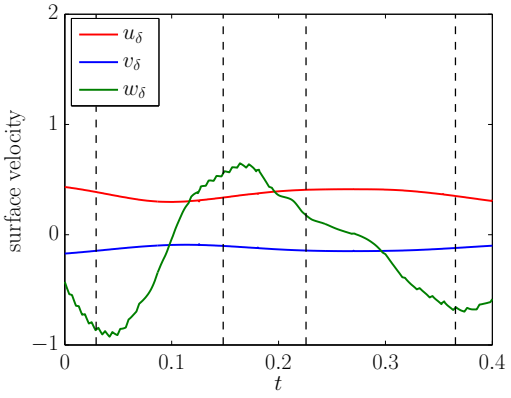

(c) 2D CFD: surface velocity

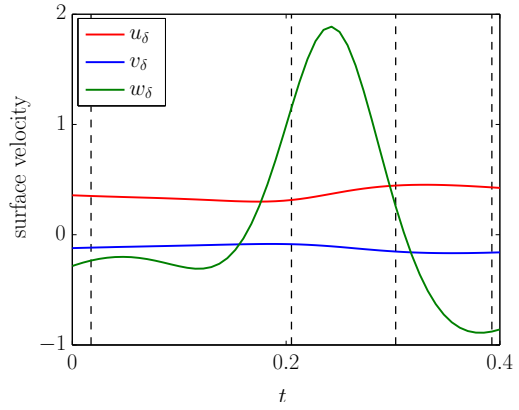

(d) IBL model: surface velocity

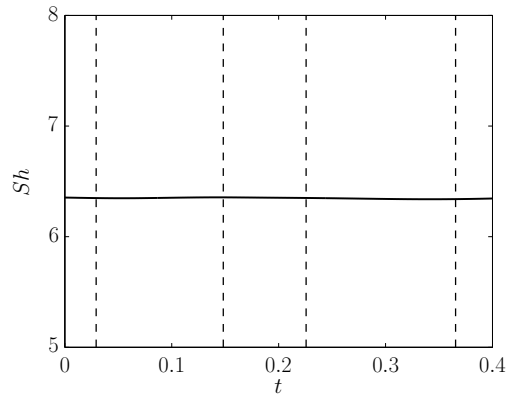

(e) 2D CFD: Sherwood number

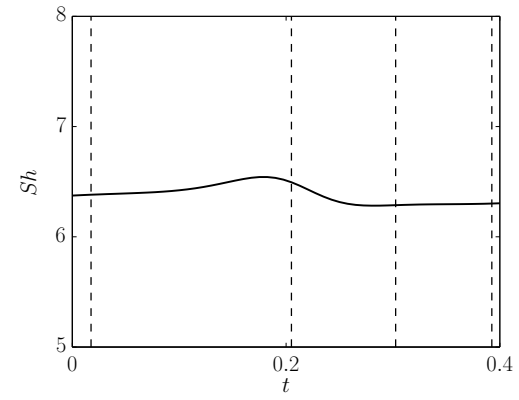

(f) IBL model: Sherwood number

Figure 4.31: Evolution of the film height, the surface velocity, and the Sherwood number at $r = 2.11$. Vertical dashed lines indicate selected instants of time.

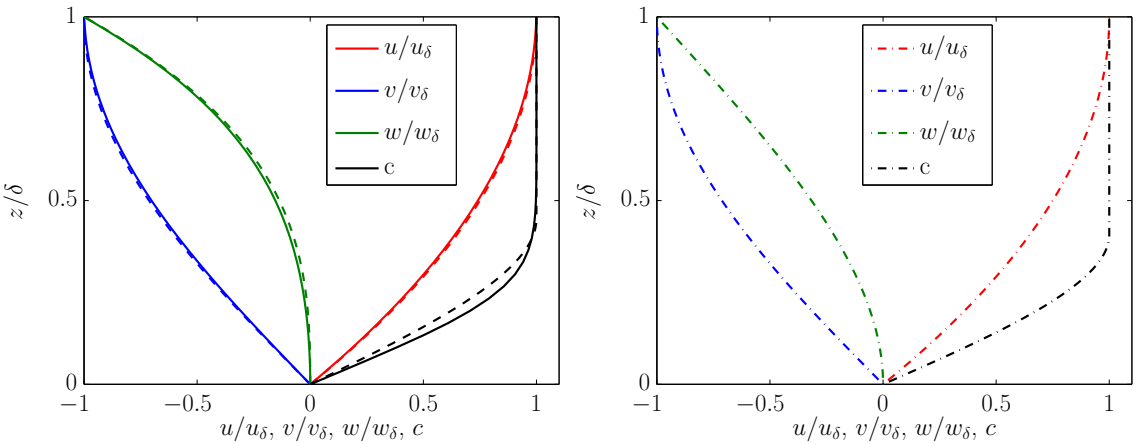

(a) 2D CFD, instant of time 1

(b) IBL model, instant of time i

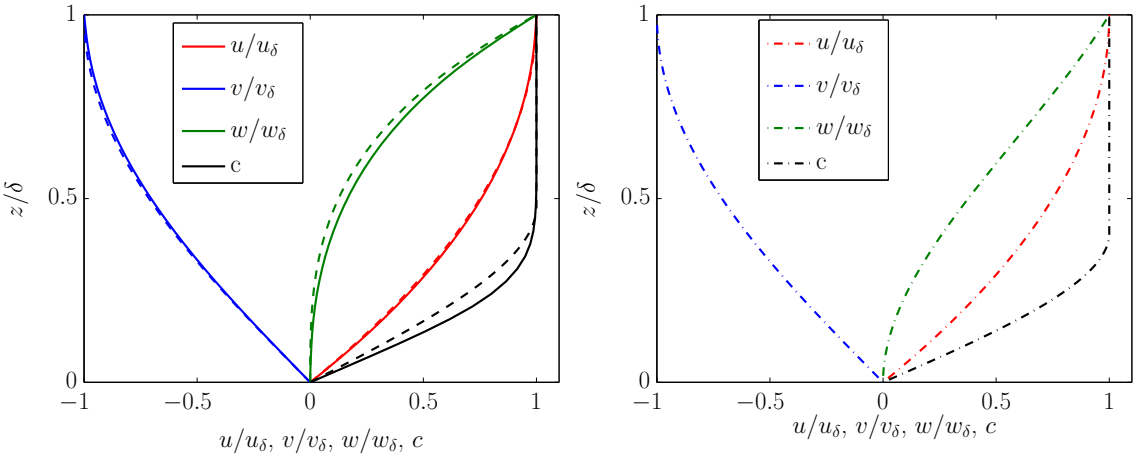

(c) 2D CFD, instant of time 2

(d) IBL model, instant of time ii

Figure 4.32: Instantaneous profiles of the radial, azimuthal, and vertical velocity components together with the species mass fraction profile at selected instants of time inside a single wave at $r = 2.11$ for the case C3. The dashed-dotted lines refer to the results of the unsteady IBL model, the solid lines to the simulated profiles of the CFD, and the dashed lines refer to the polynomial profile functions evaluated with the CFD results as input.

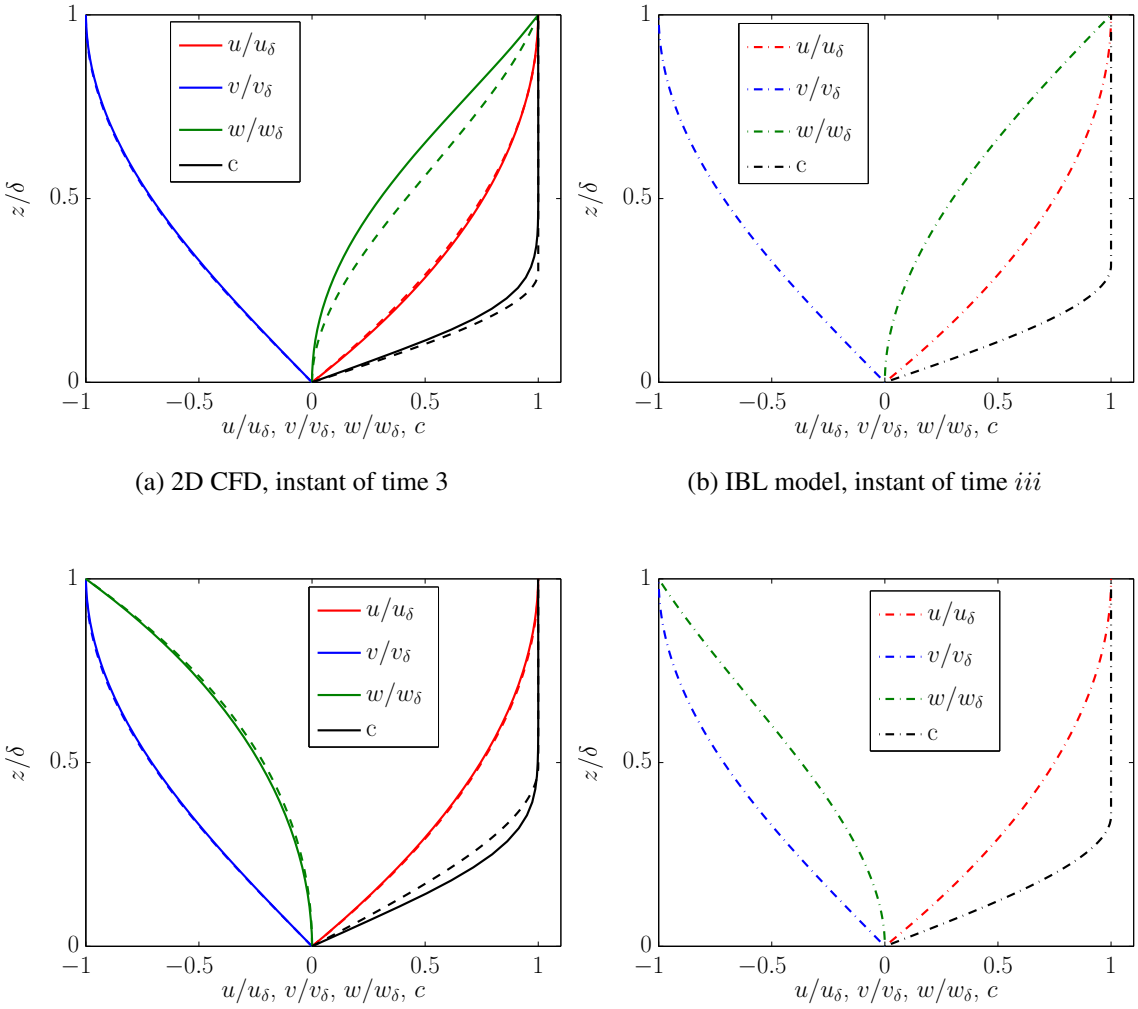

(a) 2D CFD, instant of time 3

(b) IBL model, instant of time iii

(c) 2D CFD, instant of time 4

(d) IBL model, instant of time iv

Figure 4.33: Instantaneous profiles of the radial, azimuthal, and vertical velocity components together with the species mass fraction profile at selected instants of time inside a single wave at $r = 2.11$ for the case C3. The dashed-dotted lines refer to the results of the unsteady IBL model, the solid lines to the simulated profiles of the CFD, and the dashed lines refer to the polynomial profile functions evaluated with the CFD results as input.

CFD and the IBL solution at four selected instants of time within the interval shown in Fig. 4.34. While a fairly good agreement between the CFD results and the polynomial profile assumptions is generally found for the radial and azimuthal velocity components, large deviations are observed for the vertical component of the velocity, especially at the instant 2 associated with the passage of the peak of the wave. At the instants of time 3 and 4, and correspondingly, iii and iv, i.e., after the passage of the wave peak, a fairly good agreement with the CFD results is observed again for all components. This observation applies to the polynomial functions using the CFD solution as input, as well as those taken from the unsteady IBL solution.
Marked deviations in the w-profiles do not only appear during the passage of the wave peaks. They were also observed, less pronounced, after the passage of the large solitary waves, as seen from Fig. 4.37 showing conditions obtained further downstream at $r = 4.23$. As for the mass transfer, the simulated profiles for the species mass concentration exhibit always a higher wall gradient than the polynomial functions. This explains the higher level of the local Sherwood number predicted by the CFD seen from Figs. 4.34(e)-(f), which is also reflected by the radial variations of the time-averaged Sherwood number in the outer wavy region shown in Fig. 4.30(c).

The detailed discussion of the velocity profiles above suggests that the observed deficits of the unsteady IBL model in the description of the species mass transfer can be mainly attributed to some inherent limitations of the assumed profile functions required by the depth-averaging. These limitations become most evident in the discrepancies observed for the w-profiles, which are implicitly determined by the polynomials assumed for the radial and azimuthal velocities. According to the definition of the profiles for u, v, c, and implicitly, for w, they essentially scale with the thickness of the film δ, so that a strong temporal variation of the height of the liquid surface in the wavy region practically rescales the whole profiles down to the wall while leaving the prescribed shape of the polynomials unchanged. As a consequence, the onset of surface waviness always leads to a very fast increase of the thickness of the concentration boundary layer, which in turn leads to a marked radial decrease of the time-averaged Sherwood number due to $Sh \propto 1/\delta_c$, as seen from Fig. 4.30(c). This inherent feature is especially problematic for the here considered high Schmidt number, $Sc = 1196$. High Schmidt numbers imply very thin concentration boundary layers, which are expected to be less sensitive to the unsteady motion of the liquid in the wavy surface layer, than it is inherently imposed by the polynomial profile functions.

The present reasoning is also supported by a simple test assuming quasi-steady "frozen waves" by neglecting the transient term in the kinematic boundary condition, Eq. (2.77), such that

$$w_\delta = u_\delta \frac{\partial \delta}{\partial r}. \tag{4.12}$$

Using this quasi-steady formulation in the depth-averaged mass transport equation (2.163)

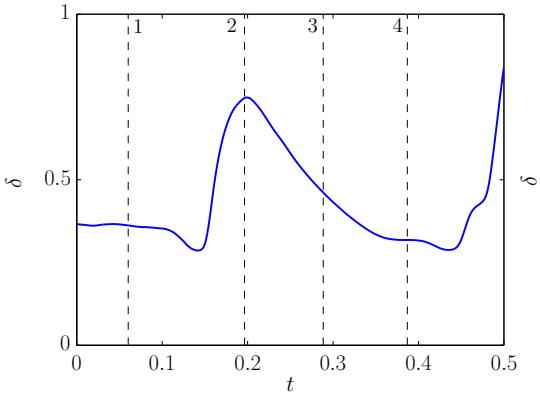

(a) 2D CFD: film height at $r = 2.82$

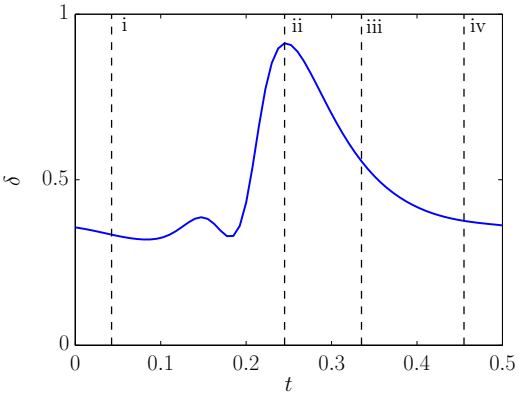

(b) IBL model: film height at $r = 2.82$

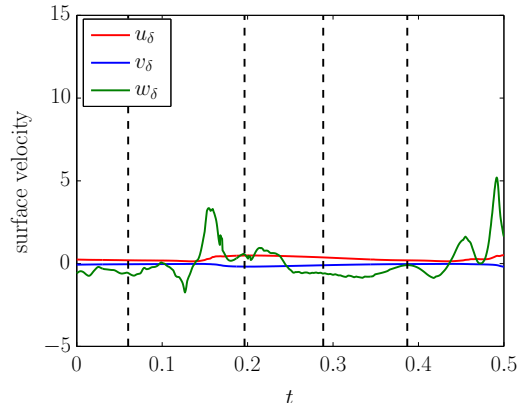

(c) 2D CFD: surface velocity

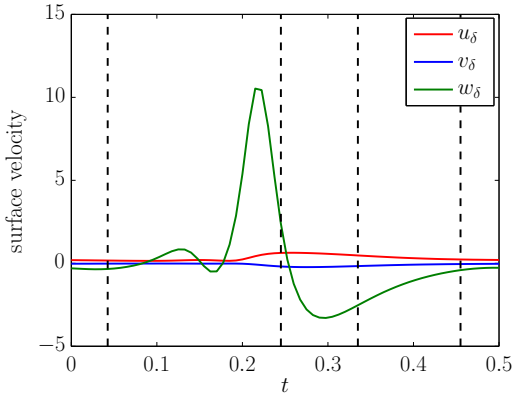

(d) IBL model: surface velocity

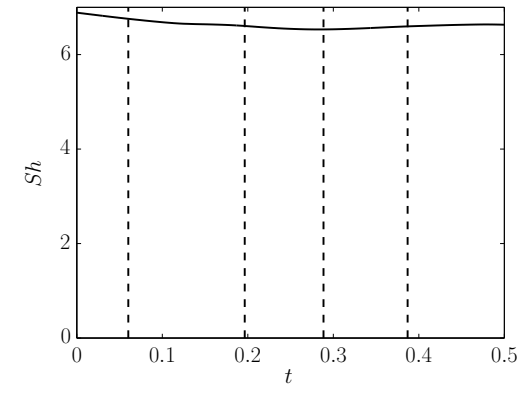

(e) 2D CFD: Sherwood number

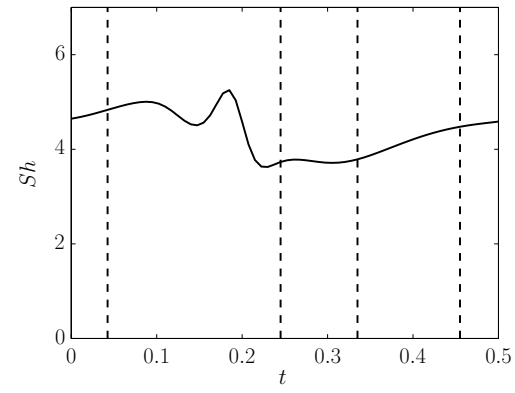

(f) IBL model: Sherwood number

Figure 4.34: Evolution of the film height, the surface velocity, and the Sherwood number at $r = 2.82$. Vertical dashed lines indicate selected instants of time.

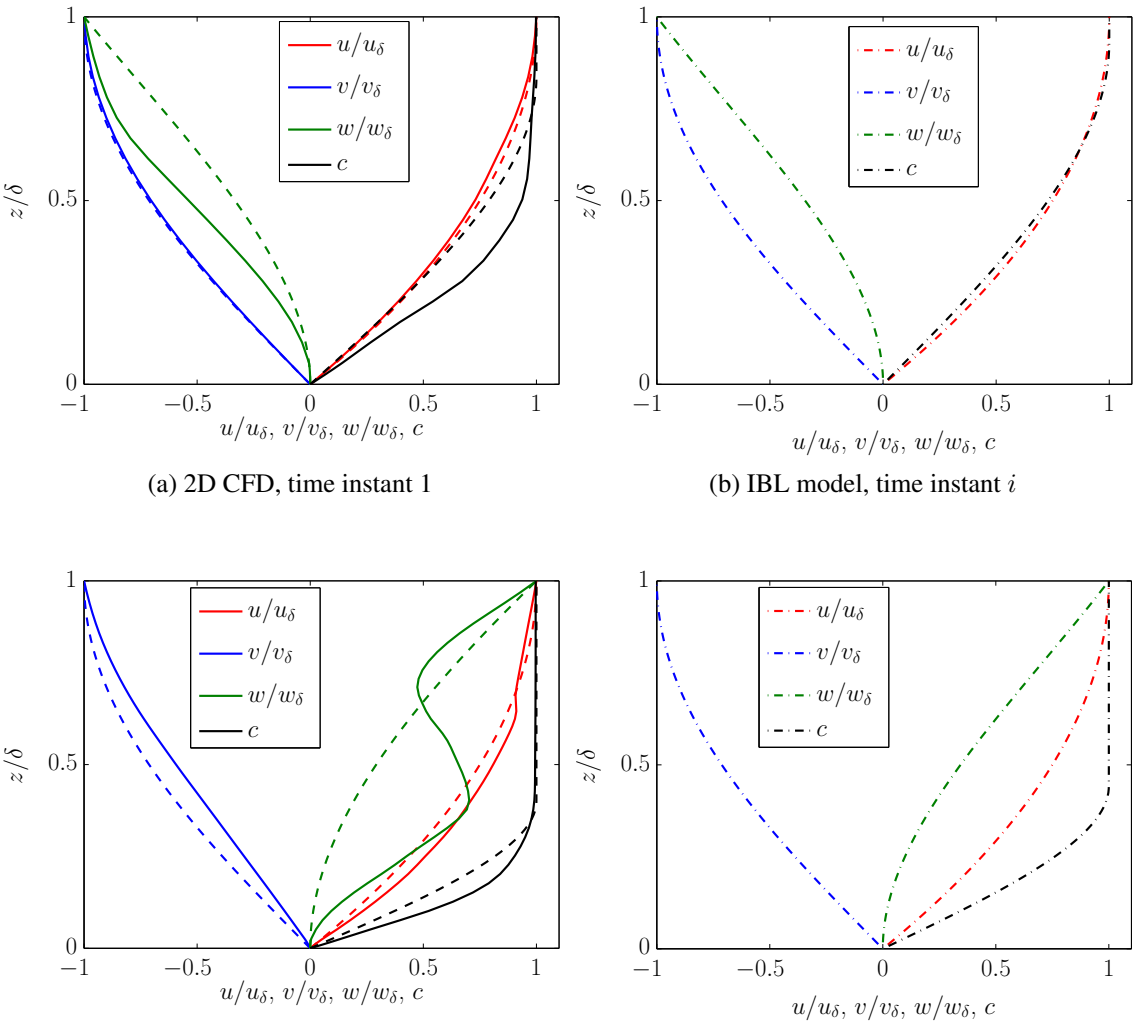

(a) 2D CFD, time instant 1

(b) IBL model, time instant i

(c) 2D CFD, time instant 2

(d) IBL model, time instant ii

Figure 4.35: Instantaneous profiles of the radial, azimuthal, and vertical velocity components together with the species mass fraction profile at selected instants of time inside a single wave at $r = 2.82$ for the case C3. The dashed-dotted lines refer to the results of the unsteady IBL model, the solid lines to the simulated profiles of the CFD, and the dashed lines refer to the polynomial profile functions evaluated with the CFD results as input.

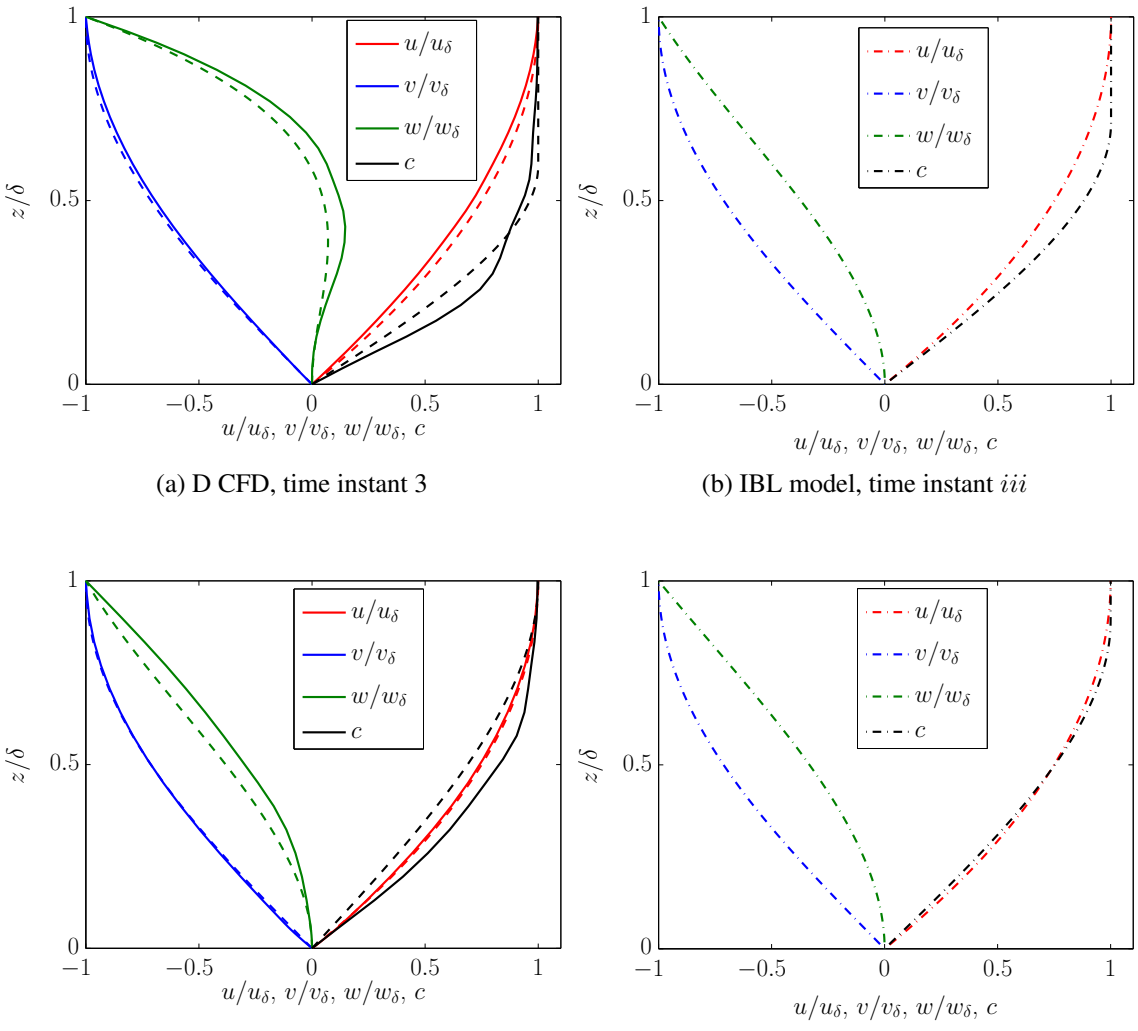

(a) D CFD, time instant 3

(b) IBL model, time instant iii

(c) 2D CFD, time instant 4

(d) IBL model, time instant iv

Figure 4.36: Instantaneous profiles of the radial, azimuthal, and vertical velocity components together with the species mass fraction profile at selected instants of time inside a single wave at $r = 2.82$ for the case C3. The dashed-dotted lines refer to the results of the unsteady IBL model, the solid lines to the simulated profiles of the CFD, and the dashed lines refer to the polynomial profile functions evaluated with the CFD results as input.

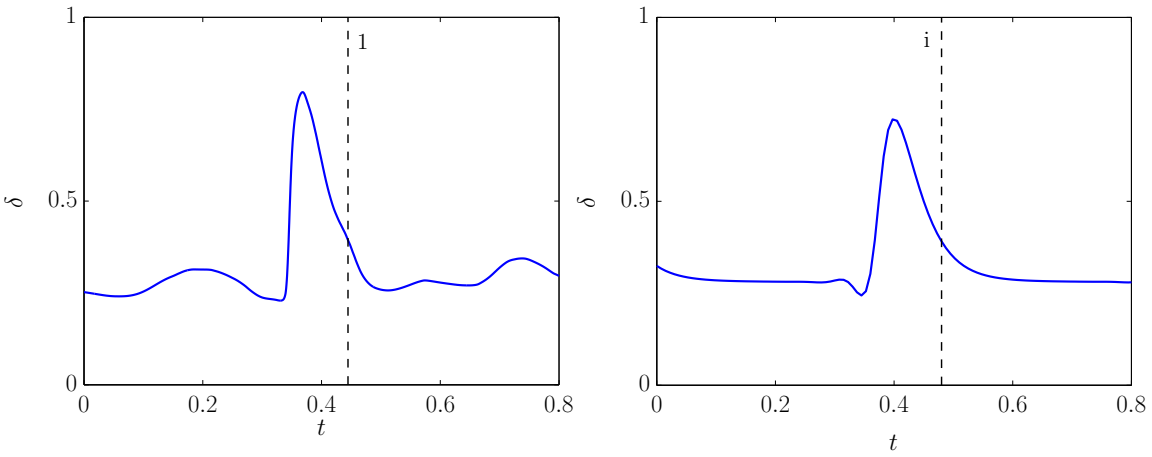

(a) 2D CFD: film thickness at $r = 4.23$

(b) IBL model: film thickness at $r = 4.23$

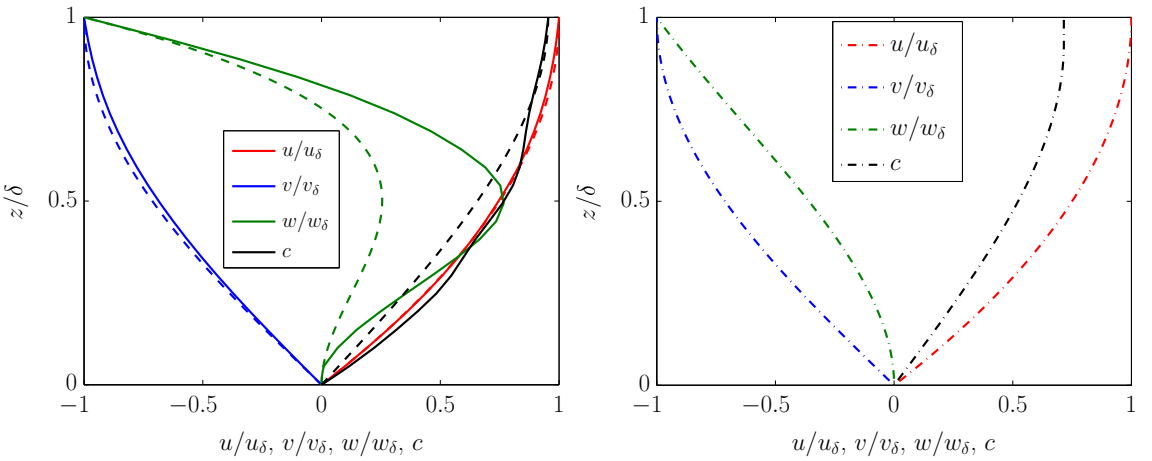

(c) 2D CFD, time instant 1

(d) IBL model, time instant i

Figure 4.37: (a)-(b): Evolution of film height at $r = 4.23$. The vertical dashed line indicates the selected instant of time.
(c)-(d): Instantaneous profiles of the radial, azimuthal, and vertical velocity components together with the species mass fraction profile at the selected instant of time inside a single wave at $r = 4.23$ for the case C3. The dashed-dotted lines refer to the results of the unsteady IBL model, the solid lines to the simulated profiles of the CFD, and the dashed lines refer to the polynomial profile functions evaluated with the CFD results as input.

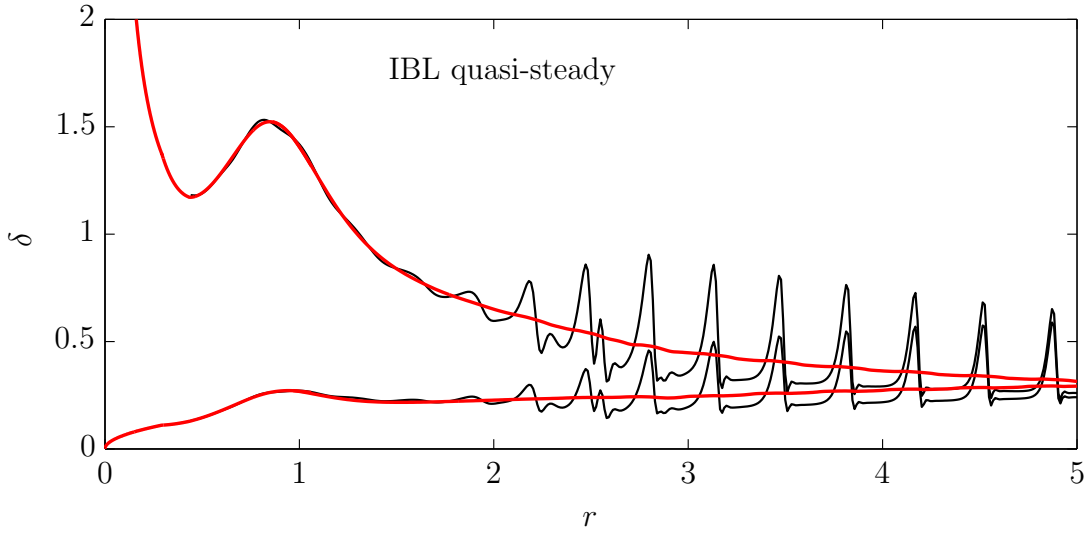

(a) Instantaneous (black lines) and time-averaged (red lines) film and concentration boundary layer thickness.

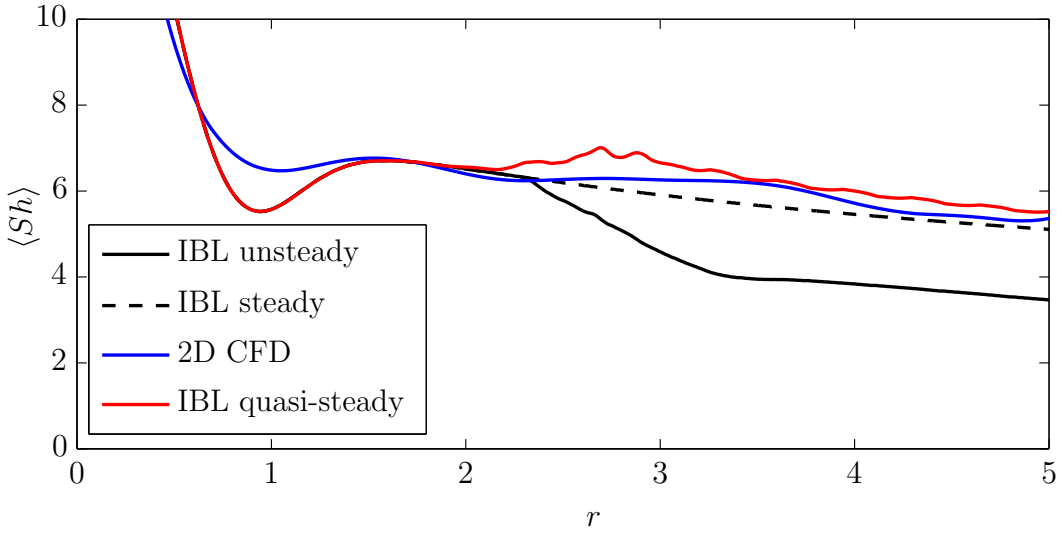

(b) Time-averaged Sherwood number.

Figure 4.38: Results of unsteady IBL model using a quasi-steady kinematic boundary condition for the species mass transport.

practically decouples the solution for the species mass transfer from the local temporal change of the film thickness represented by the transient term $\partial\delta/\partial t$.
A comparison of Fig. 4.38(a) against Fig. 4.29(a) makes evident that using the quasi-steady kinematic boundary condition leads to a much slower increase of the thickness of the concentration boundary layer downstream of $r = 2.5$. The resulting radial variation of the time-averaged Sherwood number shown in Fig. 4.38(b) remains in the outer wavy region on even a higher level than the CFD solution.

4.3 Validation against experiments

In addition to the comparison against numerical results from CFD simulations, which was presented in the previous section, the predictive capability of the present unsteady IBL model is also assessed by a comparison against available experimental data. The validation distinguishes between two different regimes based on the maximum values of the Ekman number which are reached at the outer radius of the disk.

4.3.1 Small Ekman numbers

Small values of the maximum Ekman number ($Ek_{max} \lessapprox 3$) imply that the whole flow domain basically belongs to the inner radial region, which is essentially governed by a balance of the inertial and the retarding Coriolis and viscous forces. The accelerating centrifugal forces are too small to destabilize the flow, generating a wavy surface. The considered cases for this regime are listed in Tab. 4.2.

Case	E1	E2		E3	
		(a)	(b)	(a)	(b)
Exp. reference	Thomas et al. [60]	Ozar et al. [80]		Kaneko et al. [68]	
Q [lpm]	7	3		0.7	
n [rpm]	200	100	200	100	200
$\nu \times 10^6$ [m^2/s]	1	0.66		2.87	
Ek_{max}	2.2	2.6	3.3	2.8	3.6
$\epsilon Fr^{-1} \times 10^4$	4	24.6	6.16	482	120
$W \times 10^6$	0.24	2	0.7	364	129
Pr		4.36			
Sc				1196	

Table 4.2: Considered cases with small Ekman numbers.

Hydrodynamics

The first considered case was experimentally investigated by Thomas et al. [60], who applied a capacitance technique to measure the local mean film thickness. The experimental conditions of this case correspond to dimensionless parameters $\epsilon Fr^{-1} = 4.0 \times 10^{-4}$ and $W = 2.4 \times 10^{-8}$. This case is associated with a fairly small maximum Ekman number ($Ek_{max} = 2.2$) evaluated at the outer edge of the disk. Fig. 4.39 shows a comparison of the predicted film thickness against the experimental data. The shown instantaneous results of

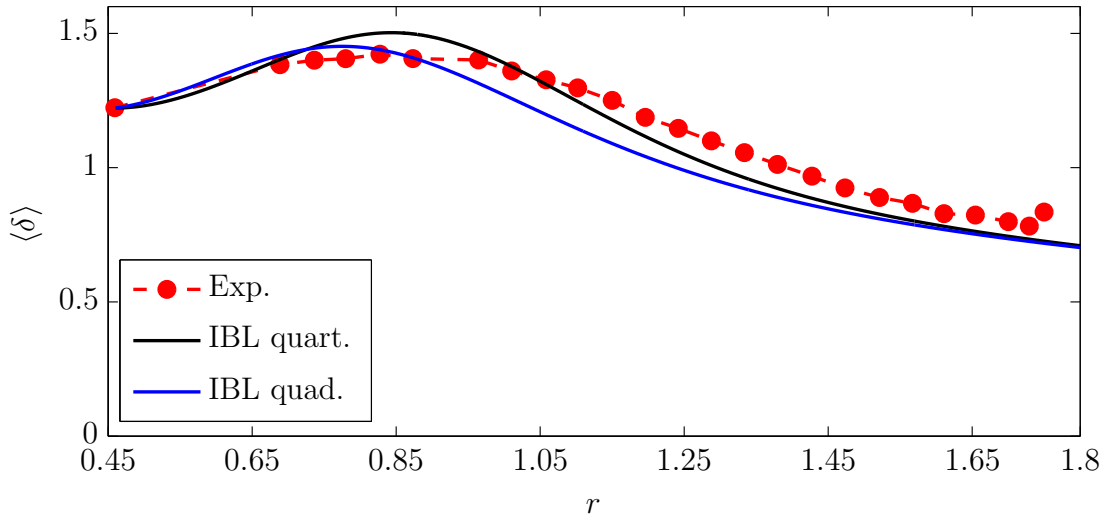

Figure 4.39: Radial variation of the film thickness predicted by unsteady IBL model. Case E1, experimental data from Thomas et al. [60].

the unsteady IBL model were obtained using alternatively quadratic and quartic polynomials for the radial velocity component, Eq. (2.133) and Eq. (2.134), respectively, to examine the effect of the profile assumption.

Dealing with a low Ekman number regime the unsteady IBL model produces expectedly a non-wavy surface, which basically represents the steady-state smooth film solution, and is evidently in close agreement with the experimental data. Assuming a quartic radial velocity profile (IBL quart.) produces a slightly higher film thickness, which translates into a better prediction for the radial position of the local maximum in the film thickness.
Apart from this test case all IBL results presented in the following were obtained using the quartic profile assumption.

Heat transfer

The case E2 in table 4.2 was considered to evaluate the predictive capability of the present IBL model for film flow with heat transfer. For this particular case experimental as well as numerical results for the radial variation of the Nusselt number are available from Ozar et al. [80] and Rice et al. [66], respectively. Ozar et al. [80] experimentally measured the local Nusselt number for a film of water on a rotating disk uniformly heated from below at constant power of H=4500 W. The water was supplied at a constant volumetric flowrate of Q=3 lpm through an annular gap with a certain height at the center of the disk. The inflow

temperature of the water was T_i=40 °C. Accordingly, the fluid properties used for the IBL computation were set to ν=0.658 $\times$ 10^{-6} m^2/s, λ=0.629 $W/(mK)$ and c_p=4179 $J/(kgK)$. Given the uniformly heated area in the experiments the constant heat flux imposed at the wall is simply obtained as

$$q_w = \frac{H}{\pi(\tilde{r}_D^2 - \tilde{r}_i^2)}. \tag{4.13}$$

As suggested by Ozar et al. [80], the constant wall heat flux is also used in the definition of the local Nusselt number written as

$$Nu = \frac{q_w \tilde{r}_i}{\lambda(T_w - T_i)}. \tag{4.14}$$

According to this definition, the Nusselt number varies only dependent of the local wall temperature T_w. The comparison against the IBL predictions considers the experimental and computational results obtained for two different rotation speeds, n=100 rpm and n=200 rpm. Based on the aforementioned flow rate and material properties the dimensionless parameters read $\epsilon Fr^{-1} = 24.6 \times 10^{-4}$, $W = 1.9 \times 10^{-6}$, and $Pr = 4.36$, for the case E2(a), and $\epsilon Fr^{-1} = 6.16 \times 10^{-4}$, $W = 7 \times 10^{-7}$, and $Pr = 4.36$, for the case E2(b). For both considered cases the maximum Ekman number is again fairly small ($Ek_{max} \leq 3.3$), and the unsteady IBL model consistently produced non-wavy smooth film solutions.

The radial variation of the Nusselt number, defined in Eq. (4.14), obtained for the rotational speeds n=100 and 200 rpm are shown in Figs. 4.40(a) and (b) respectively. In both cases the predictions of the IBL model agree evidently very well with the experimentally obtained results in the whole flow region covered by the measurements. It is interesting to note that the observed overall agreement is even better than for the numerical results of Rice et al. [66], which show notable deviations at small radii.

Species mass transfer

As discussed in Sec. 2.4.2, the wet chemical etching of silicon using an etchant, which basically consists of nitric acid, is associated with large values of the Damköhler number and very fast chemistry. Thus, the etching process is mainly controlled by the mass transfer of the HNO_3 molecules towards the solid surface. In this limit of very large Damköhler numbers the etching rate is therefore proportional to the local Sherwood number, see Eq. (2.232).
Fig. 4.41 shows a comparison of the IBL predictions for the etching rate obtained from Eq. (2.232) against experimental data from Kaneko et al. [68]. The liquid etchant was supplied at a constant volumetric flowrate of Q =0.67 lpm through an impinging jet emerging from a nozzle with a diameter d_n =6.5 mm. Two rotational speeds, n=100 rpm and

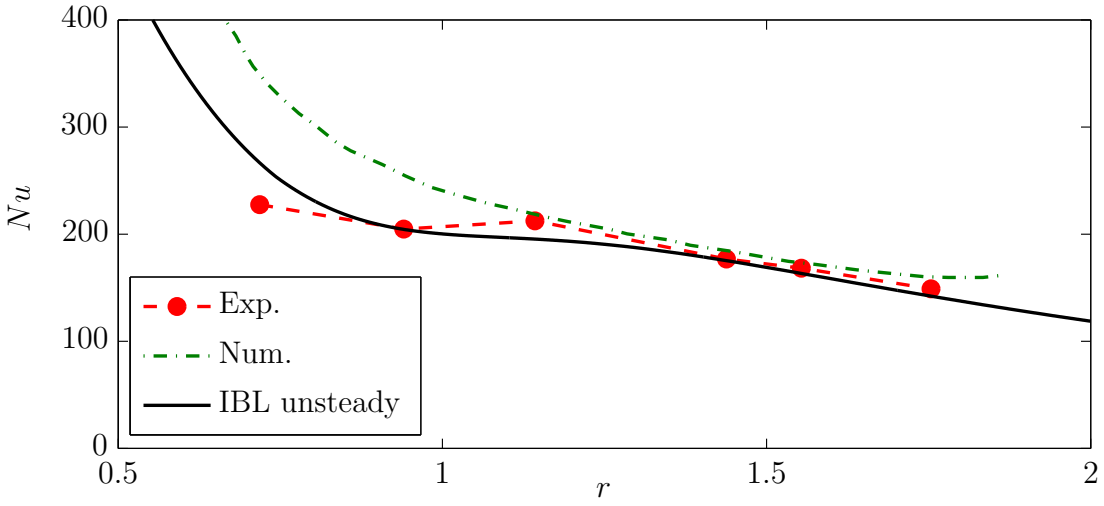

(a)

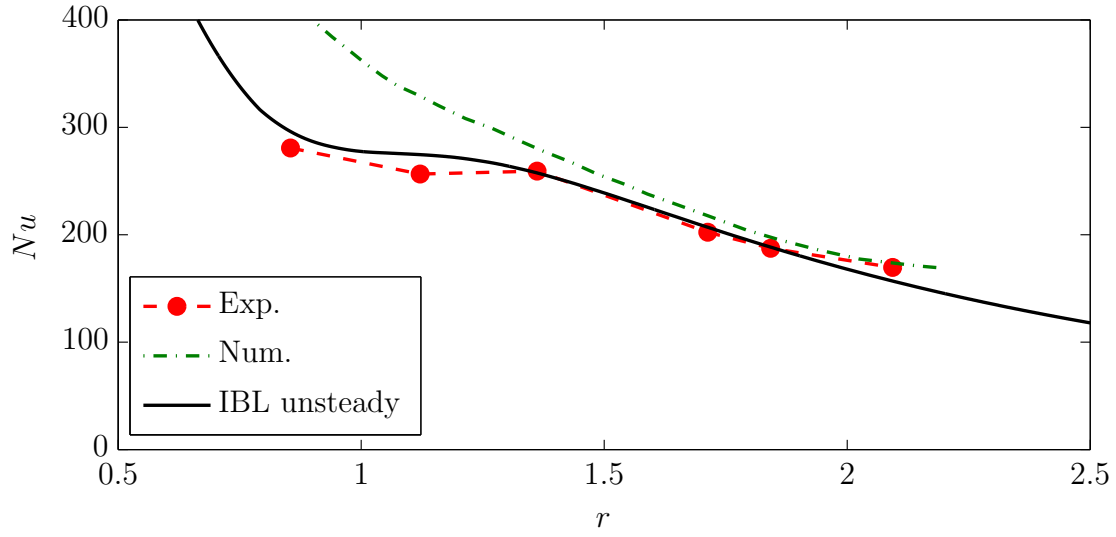

(b)

Figure 4.40: Nusselt number vs. radial distance for the cases E2(a)-(b), IBL predictions compared against experimental data of Ozar et al. [80] and numerical results of Rice et al. [66], (a) 100 rpm, (b) 200 rpm.

n=200 rpm were considered, which yield together with the aforementioned operating conditions the dimensionless parameters referred to as cases E3(a)-(b) in Tab. 4.2.

As can be seen from Fig. 4.41, the IBL predictions capture evidently very well the essential features of the etching activity on the disk in the small Ekman number regime ($Ek \lessapprox 3.6$), so that a good agreement with experimental results from Kaneko et al. [68] is observed. Aside from some deviations around $\tilde{r} \approx$20 mm the IBL model also predicts very well the highly intensified etching activity in the impingement region near the center. The development of the concentration and velocity boundary layers, and the associated near-wall conditions determining the wall fluxes, are evidently described very reliably by the present model. A quantitative case-to-case comparison of the etching behavior in the outer radial region further unveils that the etching rates reach a higher level for the higher rotational speed. This tendency is conceivable, as for increasing rotational speeds the film height δ is decreasing, which in turn leads to a thinner concentration boundary layer being related to δ through the given Schmidt number. The reduced thickness of the concentration boundary layer finally leads to increased wall gradients, and hence, wall mass fluxes, or, equivalently etching rates. The quantitative behavior is also reflected by the IBL model very well. Recalling the dependence

$$\left.\frac{\partial c}{\partial z}\right|_{z=0} \propto \frac{1}{\delta_c},$$

valid in this region (cf. Fig. 4.42), it can be concluded that the etching rate in the small Ekman number regime ($Ek \lessapprox 3.6$) is essentially determined by the growth of the concentration boundary layer at the given Schmidt number $Sc = 1196$.

4.3.2 Large Ekman numbers

For many practically relevant operation conditions the local Ekman number reaches in the outer radial region of the disk values considerably larger than $Ek = 3$. Due to the prevailing effect of the accelerating centrifugal forces the regime with $Ek \gtrapprox 3$ is associated with a wavy flow pattern emerging in the outer radial region. The three considered cases for this regime are basically the same as those listed in Tab. 4.1 in section 4.1. The essential parameters of these cases are rewritten below in table 4.3 including the corresponding experimental references and the maximum Ekman numbers.

Hydrodynamics

The case C1 involves a maximum Ekman number of $Ek_{max} = 5.1$. The film thickness measurements for this case were carried out by Burns et al. [65], where they investigated

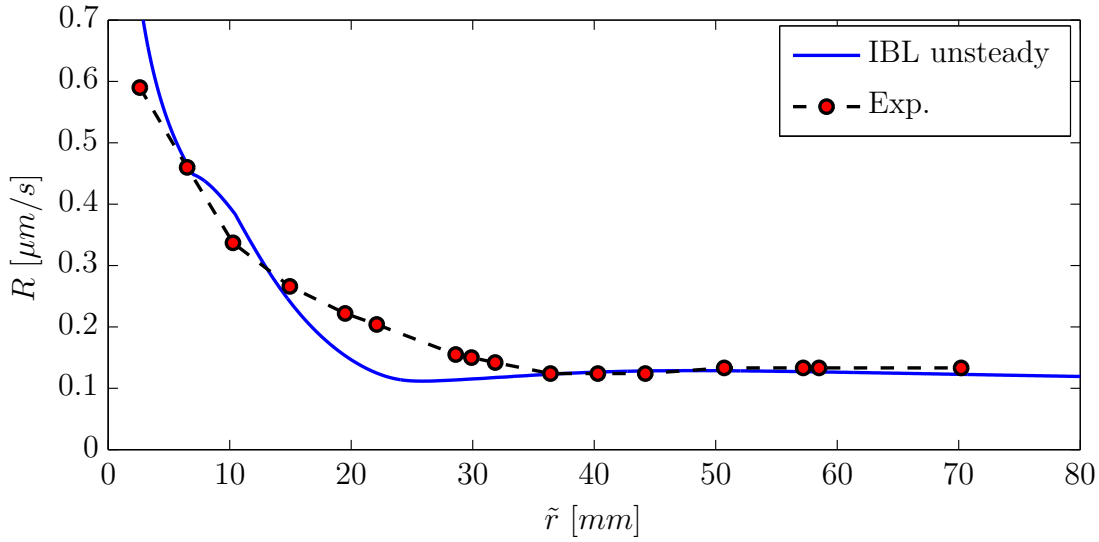

(a)

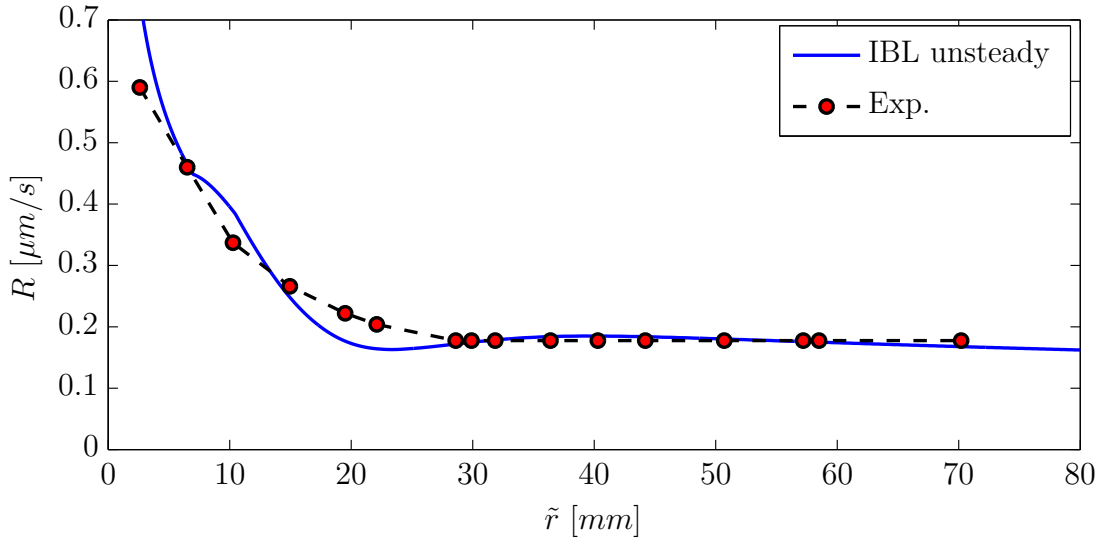

(b)

Figure 4.41: Etching rate vs. radial distance for the cases E3(a)-(b), IBL predictions compared against experimental data of Kaneko et al. [68], (a) 100 rpm, (b) 200 rpm.

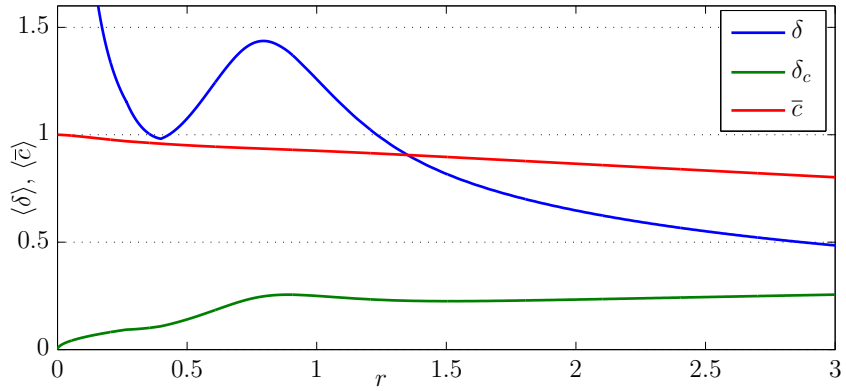

Figure 4.42: IBL results for the radial variation of the film thickness, the thickness of the concentration boundary layer, and the depth-averaged species mass fraction for the case E3(b) with n=200 rpm.

a setup with a volumetric flowrate of Q=1.8 lpm, a rotational speed of n=401 rpm and a liquid with viscosity ν=1.3 $\times 10^{-6}$ m^2/s.

Fig. 4.43 shows the time-averaged profiles of the film thickness predicted by the unsteady IBL model together with the time-averaged profiles obtained from an axisymmetric CFD simulation, and the experimental data of Burns et al. [65]. In the radially inner smooth region, associated with $r < 2$ and $Ek < 3$, the IBL predictions again capture very well the height and the radial position of the local maximum of the film thickness and show a satisfactory overall agreement with the experimental as well as the numerical results.

Case	C1	C2	C3
Exp. reference	Burns et al. [65]	Staudegger [82]	Staudegger et al. [85]
Q $[lpm]$	1.8	1	1.25
n $[rpm]$	401	500	500
$\nu \times 10^6$ $[m^2/s]$	1.3	1	2.87
Ek_{max}	5.1	4.3	5.3
$\epsilon Fr^{-1} \times 10^4$	5	4.5	10.3
$W \times 10^6$	0.19	3	9.35
Pr		7	
Sc			1196

Table 4.3: Considered cases with large Ekman numbers.

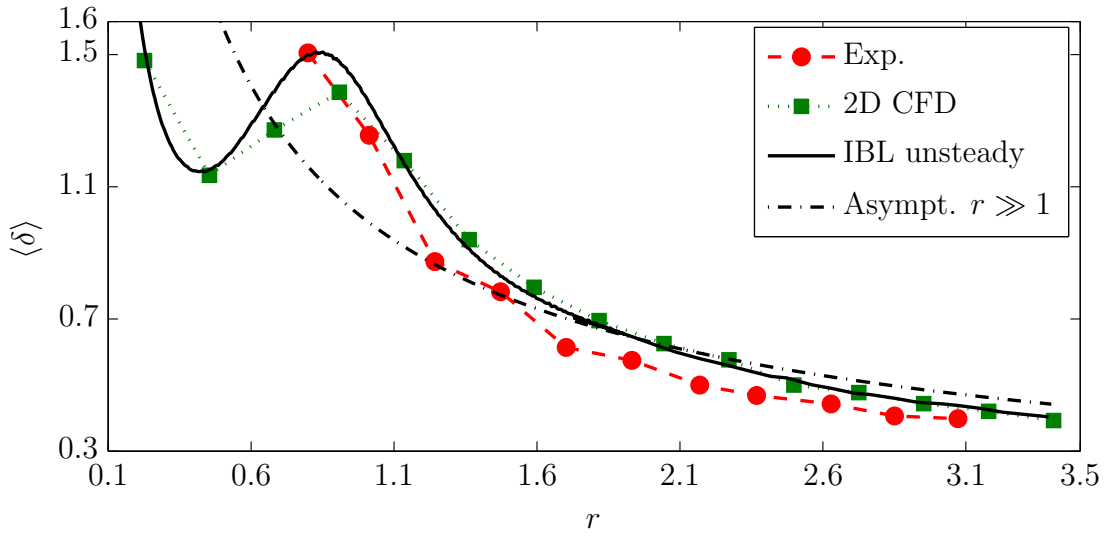

Figure 4.43: IBL predictions and CFD results for the time-averaged film thickness for the case C1. Experimental data from Burns et al. [65].

In the radially outer region ($Ek \geq 3$) a very good agreement between the predictions of the unsteady IBL model and the predictions of the CFD analysis is observed. As a salient feature both computational results exhibit a reduced time-averaged film thickness in the wavy outer region. This is clearly indicated by their deviation from the corresponding asymptotic smooth film solution obtained in the limit of large radii $r \gg 1$. Yet, in comparison to the experiments, both computational results still predict somewhat higher average heights in the outer radial region. This discrepancy may be due to three-dimensional effects, which are not captured by both computational approaches, but can also be attributed to higher uncertainties in the measurements of the average film height in wavy films.

Heat transfer

The case C2 listed in table 4.3 is very close to a real industrial process of surface etching. As this case also provides experimental data on a chemical etching process, the validation of the unsteady IBL model includes the predictions for the chemical abrasion as well. The operating conditions of the considered experiments were Q=1.0 lpm, n=500 rpm, and ν=1×10^{-6} m^2/s. The maximum Ekman number, which is calculated at the radius of the outer edge of the disk of $\tilde{r}$=100 mm, is $Ek_{max} = 4.3$. The experiments were carried out by Staudegger [82], who measured the radial variation of the liquid temperature and of the etching abrasion of the SiO_2 layer covering the solid surface of the rotating disk. The inflow temperature of the aqueous etchant was T_i=60 °C. The convective cooling at the

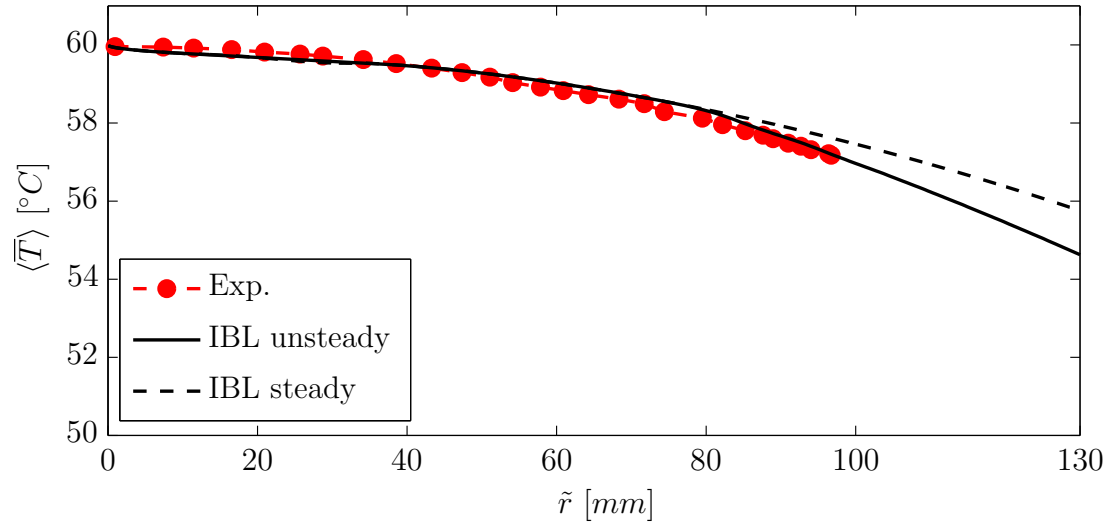

Figure 4.44: Time and depth-averaged temperature vs. radial distance for the case C2. Cooling conditions q_w=-5500 W/m^2. Experimental results from Staudegger [82].

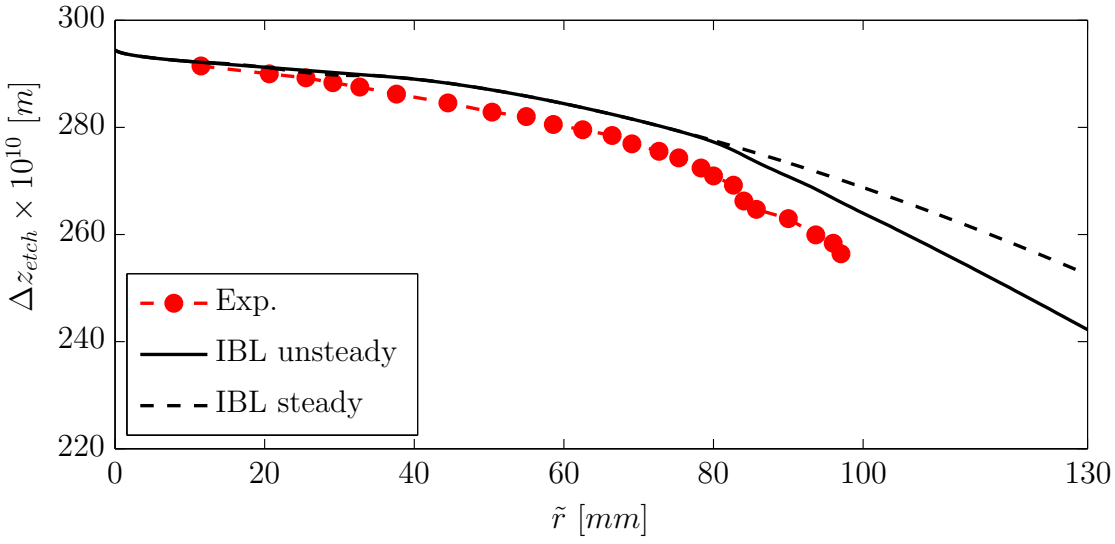

Figure 4.45: Etching abrasion vs. radial distance for the case C2. Cooling conditions q_w=-5500 W/m^2. Experimental results from Staudegger [82].

downside of the disk, which was realized in the experiments with a stream of nitrogen as coolant medium, was prescribed in terms of a constant wall heat flux q_w=-5500 $\mathrm{W/m^2}$ in the computation.
As seen from Fig. 4.44, the time-averaged predictions from the IBL approximation for the depth-averaged temperature agree very well with the experimentally obtained data. A comparison against the corresponding steady-state smooth film solution underlines again the importance of capturing the unsteady waviness in the outer radial region. This aspect is also clearly reflected by the predictions for the etching abrasion shown in Fig. 4.45. Assuming a mainly temperature dependent model for the chemistry, as it is applicable in the here considered limit of very small Damköhler numbers (cf. Sec. 2.4.1), the improved predictions for the temperature translate directly into better predictions for the etching results.

Species mass transfer

The here considered case is referred to as C3 in Tab. 4.3. In contrast to the reaction controlled case C2, the case C3 involves a diffusion controlled chemistry assuming very fast etching reactions. In this limit of high Damköhler number the etching rate is basically determined by the species mass flux of the etchant into the wall as given by Eq. (2.232). As such the etching rate is equivalent to the Sherwood number.

In Fig. 4.46 the computed time-averaged etching rate is compared against experimental data obtained by Staudegger et al. [85]. In the radially inner smooth region, associated with $r \lessapprox 2$ and $Ek \lessapprox 3$, the IBL predictions again capture very well the experimentally observed etching rates. Dealing with high Schmidt number flow the thickness of the concentration boundary layer remains smaller than the film thickness in this region, (compare, e.g. Fig. 4.29, for the case C3 with $Sc = 1196$), so that the radial variation of the etching rate is essentially determined by the growth of the concentration boundary layer. The region, where good agreement with the experiments is observed, is evidently restricted to the inner and middle region associated with $Ek \lessapprox 4$, as can be seen from Fig. 4.46(b). In the outer region, the unsteady IBL solution predicts a significant decrease of the local time-averaged Sherwood number, which translates into a decrease of the etching rate. This peculiar feature is evidently not supported by the experiments, as seen from the significant deviations in the radially outer region.

A very similar tendency is seen in the predictions for the etching rates obtained for a wide range of operating conditions, as shown in Figs. 4.47-4.48. While generally very good agreement is found in the radially inner and middle regions, the unsteady IBL model always underpredicts the experimentally observed rates in the radially outer region associated with $Ek \gtrapprox 4$. As seen from Figs. 4.49(a)-(b), which exemplarily depict the steady-state

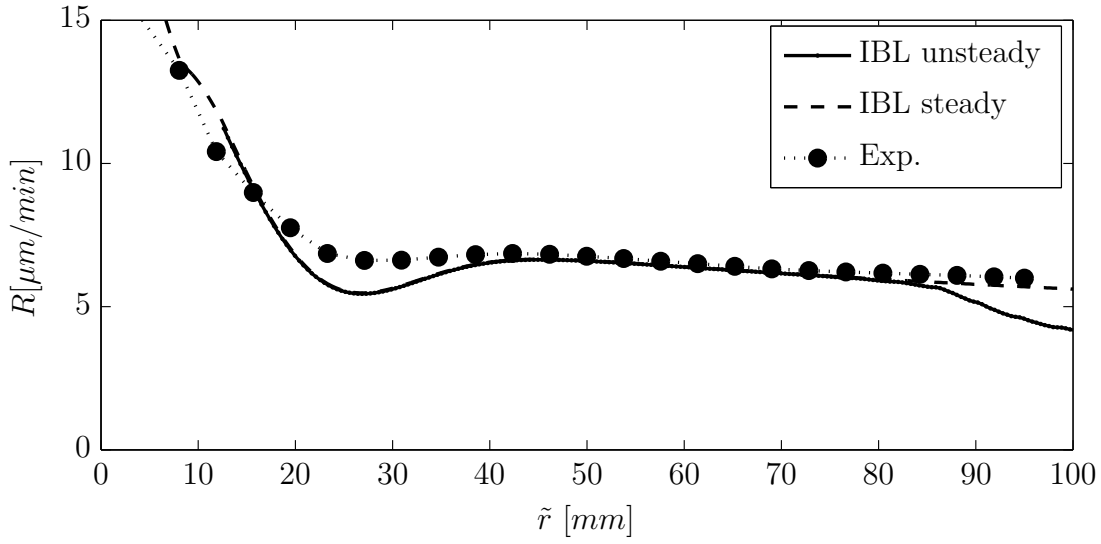

(a) Etching rate vs. radial distance.

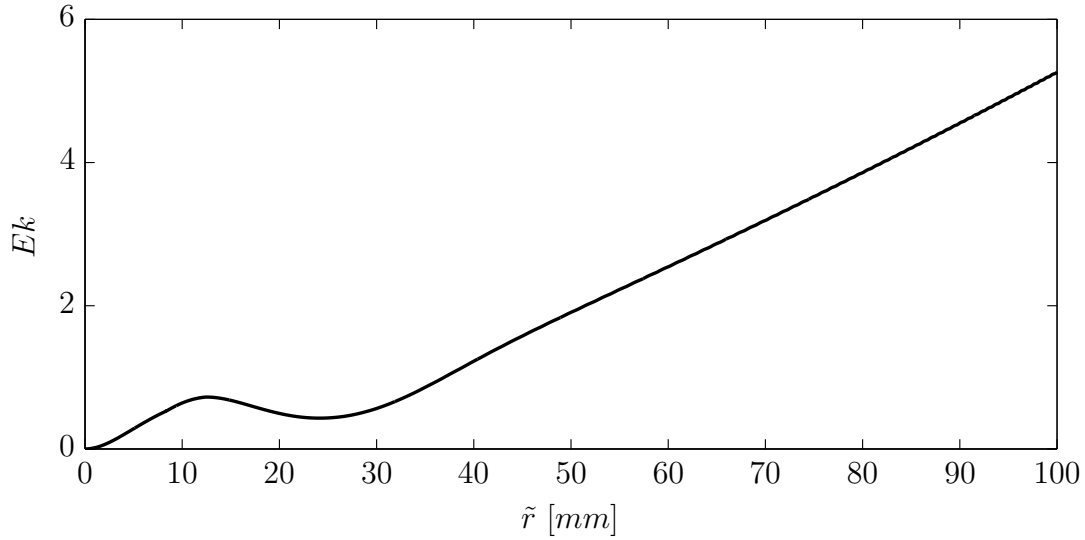

(b) Ekman number vs. radial distance.

Figure 4.46: Radial variation of time-averaged etching rates and of the Ekman number for the case C3. Experimental results from Staudegger et al. [85].

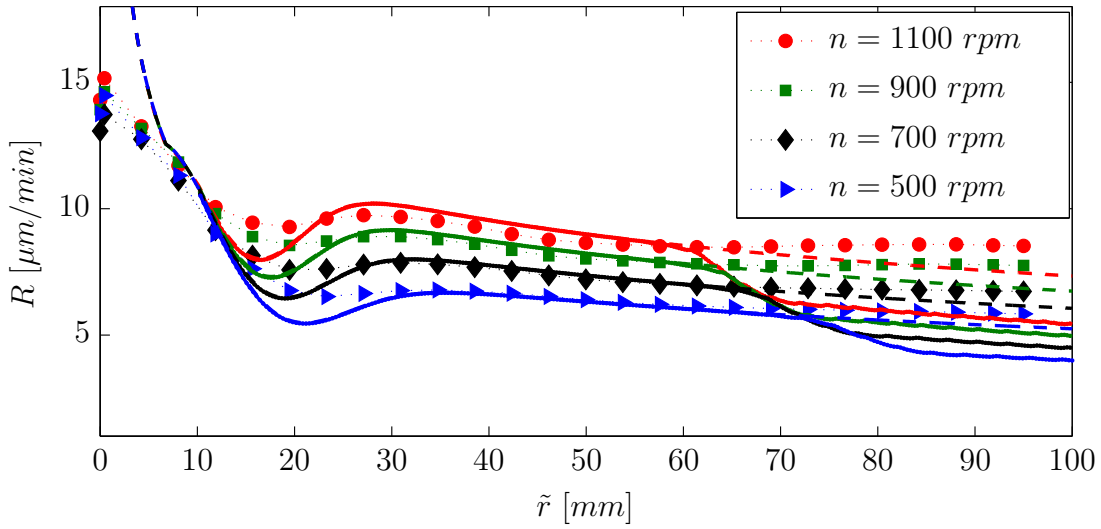

Figure 4.47: Radial variation of time-averaged etching rates, Q=0.78 lpm. Experimental results from Staudegger et al. [85] (markers), unsteady IBL model (solid lines), steady-state IBL model (dashed lines).

predictions of the IBL model for cases with the operating conditions set to Q=0.78 lpm, n=700 rpm, and Q=0.95 lpm, n=1100 rpm, respectively, the steady-state IBL model still gives better results in this region, although it does not account for any waviness. The possible reasons for the underpredicted etching rates observed for the unsteady IBL model were already addressed in the discussion of the predicted species mass concentration profiles and the resulting wall fluxes in section 4.2.3.

Using the quasi-steady "frozen wave" formulation for the kinematic boundary condition, Eq. (4.12), which was introduced to decouple the solution for the species mass transfer from the instantaneous changes of the film height, produces a better agreement with the experiments, especially in the radially outer region, as shown in Fig. 4.50. This underlines again, that the significant deviations produced by the unsteady IBL model can be attributed to the strong coupling between the wall gradients and the instantaneous film thickness, which is inherently imposed by the assumed profile functions. Possible further improvements of the present unsteady IBL model should address this issue aiming at a consistently modified formulation rather than introducing the ad hoc assumption of quasi-steady frozen waves.

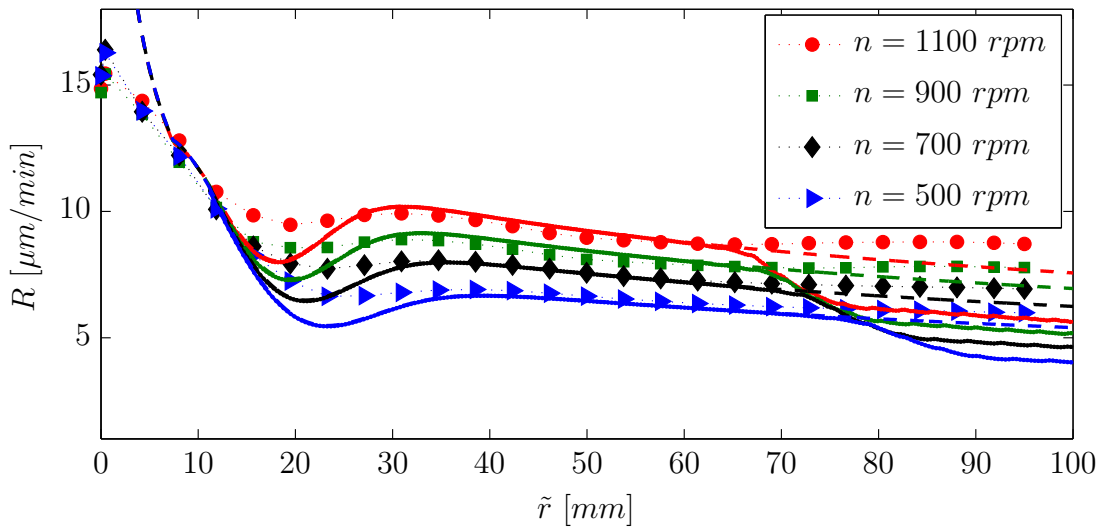

Figure 4.48: Radial variation of time-averaged etching rates, Q=0.95 lpm. Exps. Staudegger et al. [85] (markers), unsteady IBL model (solid lines), steady-state IBL model (dashed lines).

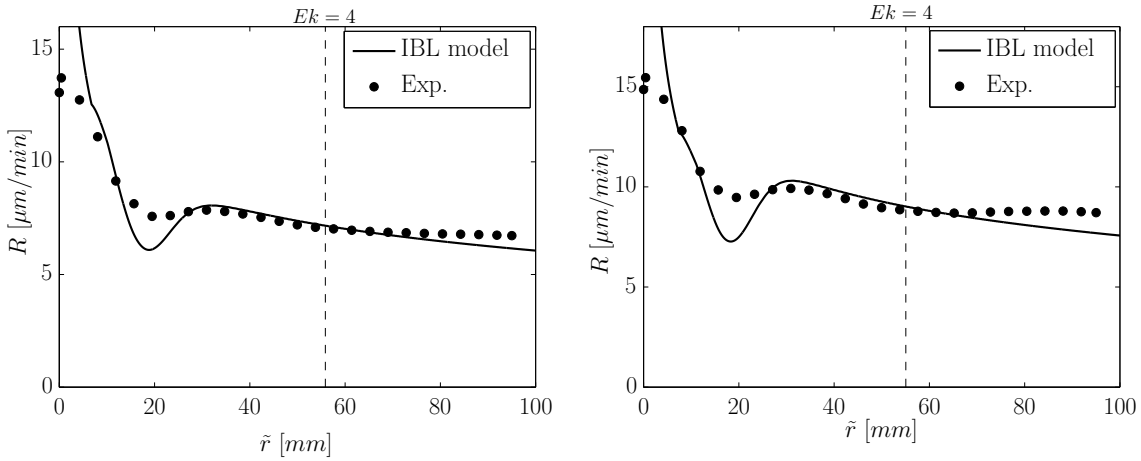

(a) Q=0.78 lpm, n=700 rpm, $Ek_{max} = 8.2$

(b) Q=0.95 lpm, n=1100 rpm, $Ek_{max} = 8.3$

Figure 4.49: Steady-state IBL predictions for the etching rate compared against experimental data of Staudegger et al. [85].

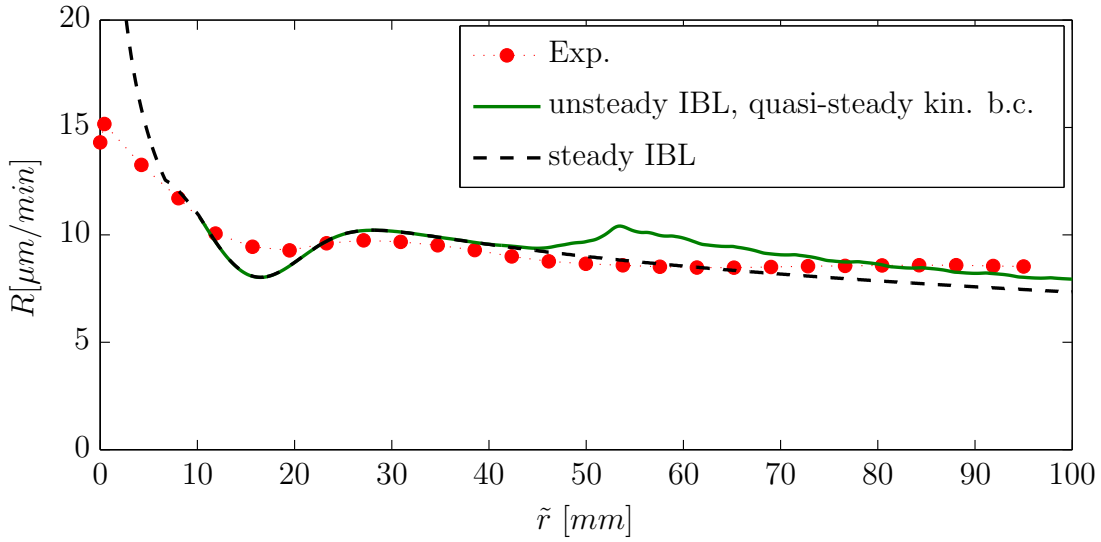

Figure 4.50: Solution of unsteady IBL model using quasi-steady "frozen-wave" kinematic boundary condition for Q=0.78 lpm, n=1100 rpm.

5 CONCLUSIONS AND RECOMMENDATIONS FOR FURTHER WORK

The present work investigated computationally the hydrodynamic, heat and species mass transfer of thin liquid film flow on rotating disks using an unsteady integral boundary layer (IBL) model. In the framework of this model the governing unsteady boundary layer type equations are averaged over the film height, assuming polynomial ansatz functions for the profiles of the individual velocity components, the dimensionless temperature, and the species mass fraction. Aside from the analysis of the salient steady-state features met in the smooth film regime the focus was particularly put on the effect of the unsteady surface waves on the momentum, heat and species mass transfer.

In the inner radial region, $r \lessapprox 2$, associated with small Ekman numbers, $Ek \lessapprox 3$, where Coriolis forces exert a stabilizing influence, the predictions of the present unsteady IBL model consistently exhibit a non-wavy smooth surface. It can be inferred that the small Ekman number regime allows for the computationally simpler steady-state IBL model, which can describe only smooth film flow. The results which were obtained with the IBL model in this region for the radial variation of the film thickness, the Nusselt number, and the Sherwood number are in very good agreement with corresponding experimental data.
In the cases with larger values of the local Ekman number, $Ek \geq 3$, the unsteady computations reproduced very well the formation and further propagation of surface waves triggered by the destabilizing influence of the radially increasing centrifugal forces. A comparison of the time-averaged results of the unsteady IBL model against corresponding steady-state smooth film solutions unveiled a reduced averaged film thickness as one of the major effects of the waviness. As for the heat transfer the waviness led to an increased/decreased film temperature in the heating/cooling wall heat flux cases. The reason for these most salient effects, which are also observed in experiments, could be identified by a close analysis of the evolution of the instantaneous flow and thermal quantities. In the wavy region most of the liquid volume is transported by fast moving surface waves, whose passage is generally intermittent with comparatively longer periods with very thin liquid coverage, which effectively reduces the average film thickness. The thin liquid layers occurring between the surface waves are more easily heated-up/cooled-down by the heating/cooling wall heat flux, which explains the increased/decreased film temperatures in the wavy regime.
The practical importance of accounting appropriately for the effects of surface waviness is highlighted by including a wet chemical etching model valid for low Damköhler numbers.

Applying the so extended unsteady IBL model to a technically relevant test case yielded a markedly improved agreement with available experimental data as compared to a corresponding steady-state smooth film solution.

The high level of description demonstrated by the present unsteady IBL model for the hydrodynamics and the heat transfer in the unsteady wavy regime was not observed for the species mass transfer. In contrast to experiments and CFD simulations the IBL results always exhibited a rapid decrease in the wall mass flux at the onset of waviness.
In a detailed analysis of the velocity and mass fraction profiles it was found that the observed deficits of the present unsteady IBL model can be mainly attributed to some inherent limitations of the assumed profile functions. In particular, large discrepancies were observed for the w-profile, which is implicitly determined by the polynomials assumed for the radial and azimuthal components of the velocity. In addition the assumed profile functions scale with the film height. This inherently imposes a strong coupling between the instantaneous local variations in the height of the liquid and the near wall conditions inside the concentration boundary layer, which finally produces an exaggeratedly strong thickening of the concentration boundary layer when the surface becomes wavy. This descriptive limitation is specially relevant for the high Schmidt number cases considered in this work ($Sc \approx 1200$). The very thin concentration boundary layers are expected to be less influenced by the flow condition at the liquid surface, which speaks against the strong coupling incorporated by the assumed profile functions.

Summing up, it can be stated that the present unsteady IBL method was shown to capture the essential hydrodynamic and thermal features of the wavy thin film flow on a spinning disk at a high level of description. Major restrictions only become evident when considering species mass transfer in a binary mixture for the particular case with very large Schmidt numbers. Aside from this limitation, the present unsteady IBL approximation has proven as a reliable and computationally efficient approach to investigate wavy flow on rotating disks, including heat and mass transfer. As such the present concept offers a great potential as computational design and optimization tool for spinning disk devices, which are widely used for various wet processing applications.

Recommendations for further work

Relevant topics for further studies are an improvement of the present IBL model by utilizing the weighted residual integral boundary layer (WRIBL) approach (see, e.g. Ruyer-Quil & Manneville [28, 29], Trevelyan et al. [112]) instead of simple polynomial profile assumptions, as the major limitations of the present model were found to be related to the polynomial ansatz functions, which are required for the depth-averaging. In the framework of the WRIBL approach it should be possible to model the recirculation zones, which

appear inside solitary waves. An appropriate modeling of these recirculation zones is expected to improve also the predictions for heat and species mass transfer.

Furthermore the present IBL model should be extended to model three-dimensional flow (2D IBL model, see e.g. appendix 4), as the assumption of axisymmetric conditions is only valid in a very restricted range of operating conditions. A three-dimensional model would additionally offer the possibility to model cases with off-center impingement, which are highly relevant for various industrial applications. In this framework also a proper ansatz for the description of the formation of dry spots will have to be included.
It may be also interesting to include edge effects, as the fluid flow over disk edge typically results in the formation of a liquid rim due to the increased pressure caused by the surface tension.

A further validation of the IBL predictions and the CFD results against more comprehensive experimental data, including experimental data describing instantaneous flow features, would be desirable.

Appendices

1 Divergence (Gauss's) theorem

Gauss's theorem relates the volume integral of the divergence of a vector, $\nabla \cdot \vec{F}$, over the volume V, with the surface integral over the boundary of this volume, $\partial V \equiv S$, by

$$\int_V \left(\nabla \cdot \vec{F}\right) dV = \int_S \vec{F} \cdot d\vec{S}. \tag{1}$$

Physically this can be interpreted as conservation law, which states that the net flux across the boundary S equals the source rate inside V.

2 Relations and profile parameters for the IBL model

2.1 Quadratic approximation

$$\overline{u} = \frac{1}{\delta}\int_0^\delta u(z)dz = \int_0^\zeta u_\delta \left(2\zeta - \zeta^2\right) d\zeta = \frac{2}{3}u_\delta \tag{2}$$

$$\overline{v} = \frac{1}{\delta}\int_0^\delta v(z)dz = \int_0^\zeta v_\delta \left(\frac{8}{5}\zeta - \frac{4}{5}\zeta^3 + \frac{1}{5}\zeta^4\right) d\zeta = \frac{16}{25}v_\delta. \tag{3}$$

$$\begin{aligned}\overline{w} =& \frac{1}{\delta}\int_0^\delta w(z)dz = \\ & \int_0^\zeta w_\delta \left[\zeta^2\left(\frac{3}{2} - a_w(r)\right) + \zeta^3\left(a_w(r) - \frac{1}{2}\right)\right] d\zeta \\ & = w_\delta\left(\frac{3}{8} - \frac{a_w(r)}{12}\right).\end{aligned} \tag{4}$$

$$k_a = \frac{\int_0^\zeta u_\delta^2 \left(2\zeta - \zeta^2\right)^2 d\zeta}{\overline{u}^2} = \frac{6}{5} \tag{5}$$

$$k_b = \frac{\int_0^\zeta u_\delta \left(2\zeta - \zeta^2\right) v_\delta \left(\frac{8}{5}\zeta - \frac{4}{5}\zeta^3 + \frac{1}{5}\zeta^4\right) d\zeta}{\overline{u}\overline{v}} = \frac{17}{14} \tag{6}$$

$$k_c = \frac{\int_0^\zeta v_\delta^2 \left(\frac{8}{5}\zeta - \frac{4}{5}\zeta^3 + \frac{1}{5}\zeta^4\right)^2 d\zeta}{\overline{v}^2} = \frac{155}{126} \tag{7}$$

$$\left.\frac{\partial u}{\partial z}\right|_{z=0} = 3\frac{\overline{u}}{\delta} \tag{8}$$

$$\left.\frac{\partial v}{\partial z}\right|_{z=0} = \frac{5}{2}\frac{\overline{v}}{\delta} \tag{9}$$

2.2 Quartic approximation

$$\overline{u} = \frac{1}{\delta}\int_0^\delta u(z)dz = \frac{16}{25}u_\delta + \frac{\kappa\delta^2}{75} \tag{10}$$

$$u_\delta = \frac{25}{16}\overline{u} - \frac{\kappa\delta^2}{48} \tag{11}$$

$$\overline{v} = \frac{1}{\delta}\int_0^\delta v(z)dz = \frac{16}{25}u_\delta + \frac{\kappa_2\delta^2}{75} \tag{12}$$

$$v_\delta = \frac{25}{16}\overline{u} - \frac{\kappa\delta^2}{48}. \tag{13}$$

$$\left.\frac{\partial u}{\partial z}\right|_{z=0} = \frac{5}{2}\frac{\overline{u}}{\delta} + \frac{1}{6}\kappa\delta \tag{14}$$

$$\left.\frac{\partial v}{\partial z}\right|_{z=0} = \frac{5}{2}\frac{\overline{v}}{\delta} + \frac{1}{6}\kappa 2\delta \tag{15}$$

3 Second-order polynomial ansatz function for the species mass fraction

The necessary closure for the solution of the depth-averaged convection-diffusion equation (2.155) can be provided by choosing a second-order polynomial ansatz function for c, generally written as

$$\frac{c}{c_\delta(r)} = a_0 + a_1\frac{z}{\delta_c} + a_2\frac{z^2}{\delta_c^2}. \tag{16}$$

The surface value c_δ equals unity before the concentration boundary layer has reached the film surface, and varies with the radial position further downstream, as defined in Eq. (2.157). The coefficients of the second-order polynomial are evaluated from the boundary conditions Eqs. (2.87), (2.89), and (2.90), yielding

$$\frac{c}{c_\delta(r)} = 2\frac{z}{\delta_c} - \frac{z^2}{\delta_c^2}. \tag{17}$$

Introducing the variable $\beta = \delta_c/\delta$, the composite profile assumption (17) is written in terms of the rescaled wall normal coordinate ζ, and β, as

$$c(\zeta) = \begin{cases} c_\delta\left(\frac{2}{\beta}\zeta - \frac{1}{\beta^2}\zeta^2\right) & 0 < \zeta < \beta \\ c_\delta & \beta < \zeta < 1. \end{cases} \tag{18}$$

Using the composite profile function rewritten as Eq. (18) produces the following expression for the depth-averaged species mass fraction $\overline{c}$

$$\frac{1}{\delta}\int_0^\delta c\,dz = \frac{1}{\delta}\left[\int_0^{\delta_c} c\,dz + \int_{\delta_c}^{\delta} c\,dz\right] = \int_0^\beta c\,d\zeta + \int_\beta^1 c\,d\zeta = c_\delta\left(1 - \frac{1}{3}\beta\right). \tag{19}$$

The integration of the convective transport term yields

$$\frac{1}{\delta}\int_0^\delta uc\,dz = c_\delta\overline{u} - \frac{1}{4}\beta^2 c_\delta\overline{u} + \frac{1}{20}\beta^3 c_\delta\overline{u}. \tag{20}$$

Incorporating these expressions into the IBL approximation for the species transport equation (2.155) yields the following depth-averaged evolution equation

$$\frac{\partial}{\partial t}\left[\delta c_\delta - \frac{1}{3}\beta\delta c_\delta\right] + \frac{1}{r}\frac{\partial}{\partial r}\left[r\delta\overline{u}c_\delta - \frac{1}{4}r\delta\overline{u}c_\delta\beta^2 + \frac{1}{20}r\delta\overline{u}c_\delta\beta^3\right] = -\frac{1}{Sc}\frac{1}{\delta}\frac{2c_\delta}{\beta}. \tag{21}$$

Reformulating Eq. (21) in terms of the total directional derivatives, considering additionally the flow to be axisymmetric, yields

$$\left(\frac{6\sqrt{\omega}}{c_\delta}-\frac{2\omega}{c_\delta}\right)\left[\frac{\partial c_\delta}{\partial t}+\frac{15\omega-3\omega^{3/2}-60}{20\sqrt{\omega}-60}\overline{u}\frac{\partial c_\delta}{\partial r}\right]- \left[\frac{\partial \omega}{\partial t}+\left(\frac{3}{2}\sqrt{\omega}-\frac{9}{20}\omega\right)\overline{u}\frac{\partial \omega}{\partial r}\right]= -\frac{12}{Sc}\frac{1}{\delta^2}-\frac{1}{\delta}\frac{\partial \delta}{\partial t}\left(-2\omega+\frac{3}{2}\omega^{3/2}-\frac{3}{10}\omega^2\right). \tag{22}$$

Again Eq. (22) can be separately solved for ω and c_δ as their total directional derivatives become alternately zero.

Steady-state species mass transfer

Utilizing the second-order polynomial ansatz function given by Eq. (17), the depth-averaged convection-diffusion equation for the steady-state species mass transfer reduces to

$$\begin{aligned}\beta<1, c_\delta=1:&\quad \frac{d\delta_c}{dr}=\beta\frac{d\delta}{dr}+\frac{r}{Sc}\left(\frac{360}{30\beta^2-9\beta^3}\right),\\ \beta=1, c_\delta<1:&\quad \frac{dc_\delta}{dr}=-\frac{15}{2}\frac{rc_\delta}{\delta Sc}.\end{aligned} \tag{23}$$

Considering the steady-state approximation for the film thickness to be given by $\delta=r^{-2/3}$, an asymptotic solution in the limit of large radii for the species mass fraction at the free surface is obtained as

$$\beta=1, c_\delta<1:\quad s_\delta(r)=\exp\left[-\frac{45}{16Sc}\left(r^{8/3}-r_c^{8/3}\right)\right]. \tag{24}$$

4 IBL approximation for three-dimensional film flow

In the limit of the thin film approximation the governing equations for the three-dimensional flow on a spinning disk are given by Eqs. (2.63)-(2.68). The kinematic boundary condition reads

$$z=\delta:\ w=\frac{\partial\delta}{\partial t}+u\frac{\partial\delta}{\partial r}+\frac{v}{r}\frac{\partial\delta}{\partial\phi}, \tag{25}$$

and the stress-free conditions on the free surface at $z=\delta$ are given by

$$\tau_{rz}=\frac{\partial u}{\partial z}=0, \tag{26}$$

$$\tau_{\phi z}=\frac{\partial v}{\partial z}=0, \tag{27}$$

$$0=-p-W\left(\frac{1}{r}\frac{\partial}{\partial r}\left(r\frac{\partial\delta}{\partial r}\right)+\frac{1}{r^2}\frac{\partial^2\delta}{\partial\phi^2}\right). \tag{28}$$

The depth-averaged continuity equation for the three-dimensional flow is obtained as

$$\frac{\partial\delta}{\partial t}+\frac{1}{r}\frac{\partial}{\partial r}\left[r\overline{u}\delta\right]+\frac{1}{r}\frac{\partial}{\partial\phi}\left[\overline{v}\delta\right]=0. \tag{29}$$

Introducing an improved profile assumption for the azimuthal component of the velocity as (see, e.g., Kim & Kim [75])

$$v(\zeta)=v_\delta\left(\frac{8}{5}\zeta-\frac{4}{5}\zeta^3+\frac{1}{5}\zeta^4\right)+\frac{\kappa_2\delta^2}{5}\zeta\left(1-\zeta\right)^2\left(1-\frac{\zeta}{2}\right). \tag{30}$$

the depth-averaged momentum equations in radial and azimuthal direction read

$$\frac{\partial\left(\delta\overline{u}\right)}{\partial t}+\frac{k_a}{r}\frac{\partial}{\partial r}\left(r\delta\overline{u}^2\right)+\frac{k_b}{r}\frac{\partial}{\partial\phi}\left(\overline{u}\,\overline{v}\delta\right)-\frac{k_c\delta\overline{v}^2}{r}= \beta_1\delta\left(r-\frac{\partial P}{\partial r}\right)+2\delta\overline{v}-\beta_2\frac{\overline{u}}{\delta}, \tag{31}$$

and

$$\frac{\partial\left(\delta\overline{v}\right)}{\partial t}+\frac{k_b}{r}\frac{\partial}{\partial r}\left(r\delta\overline{u}\,\overline{v}\right)+\frac{k_c}{r}\frac{\partial}{\partial\phi}\left(\overline{v}^2\delta\right)+\frac{k_b\delta\overline{u}\,\overline{v}}{r}= -\frac{5}{6}\frac{\delta}{r}\frac{\partial P}{\partial\phi}-2\delta\overline{u}-\frac{5}{2}\frac{\overline{v}}{\delta}, \tag{32}$$

respectively.
Depth averaging of the convection-diffusion equation for the transport of a general passive scalar quantity, denoted by s, yields

$$\frac{\partial}{\partial t}\left[\delta\Phi\right]+\frac{1}{r}\frac{\partial}{\partial r}\left[r\delta\Psi\right]+\frac{1}{r}\frac{\partial}{\partial\phi}\left[\delta\Pi\right]=-\frac{1}{K}\left.\frac{\partial s}{\partial z}\right|_{z=0}. \tag{33}$$

Here K is the characteristic dimensionless variable for the transport of the passive scalar, e.g. the Schmidt number in case of species transport ($s \equiv c$). The capital Greek letters supersede the integrals

$$\Phi=\frac{1}{\delta}\int_0^\delta s dz, \tag{34}$$

$$\Psi=\frac{1}{\delta}\int_0^\delta u s dz, \tag{35}$$

and

$$\Pi=\frac{1}{\delta}\int_0^\delta v s dz. \tag{36}$$

Assuming a Dirichlet boundary condition for the passive scalar

$$s|_{z=0}=0, \tag{37}$$

the depth-averaged transport equation is obtained as

$$\begin{aligned}&\frac{\partial}{\partial t}\left[\delta s_\delta-\frac{3}{8}\beta\delta s_\delta\right]+\frac{1}{r}\frac{\partial}{\partial r}\left[r\delta\overline{u}s_\delta-\frac{3}{10}r\delta\overline{u}s_\delta\beta^2+\frac{1}{16}r\delta\overline{u}s_\delta\beta^3\right]\\&+\frac{1}{r}\frac{\partial}{\partial\phi}\left[\delta\overline{v}s_\delta-\frac{1}{4}\delta\overline{v}s_\delta\beta^2+\frac{3}{112}\delta\overline{v}s_\delta\beta^4-\frac{1}{256}\delta\overline{v}s_\delta\beta^5\right]=-\frac{1}{K}\frac{1}{\delta}\frac{3s_\delta}{2\beta}.\end{aligned} \tag{38}$$

Therein a third-order polynomial ansatz function was chosen as closure relation. Reformulating Eq. (38) in terms of ω, utilizing the depth-averaged continuity equation, Eq. (29) to

substitute $\partial\delta/\partial t$, yields

$$
\begin{aligned}
&\left(\frac{16\sqrt{\omega}}{3s_\delta}-\frac{2\omega}{s_\delta}\right)\\
&\left[\frac{\partial s_\delta}{\partial t}+\frac{80-24\omega+5\omega^{3/2}}{80-30\sqrt{\omega}}\overline{u}\frac{\partial s_\delta}{\partial r}+\frac{448\omega-48\omega^2+7\omega^{5/2}-1792}{672\sqrt{\omega}-1792}\frac{\overline{v}}{r}\frac{\partial s_\delta}{\partial\phi}\right]\\
&-\left[\frac{\partial\omega}{\partial t}+\left(\frac{8}{5}\sqrt{\omega}-\frac{1}{2}\omega\right)\overline{u}\frac{\partial\omega}{\partial r}+\left(\frac{4}{3}\sqrt{\omega}-\frac{2}{7}\omega^{3/2}+\frac{5}{96}\omega^2\right)\frac{\overline{v}}{r}\frac{\partial\omega}{\partial\phi}\right]=\\
&-\frac{8}{K}\frac{1}{\delta^2}-\frac{1}{\delta}\frac{1}{r}\frac{\partial}{\partial r}\left(r\overline{u}\delta\right)\left(2\omega-\frac{8}{5}\omega^{3/2}+\frac{1}{3}\omega^2\right)\\
&-\frac{1}{\delta}\frac{1}{r}\frac{\partial}{\partial\phi}\left(\overline{v}\delta\right)\left(2\omega-\frac{4}{3}\omega^{3/2}+\frac{1}{7}\omega^{5/2}-\frac{1}{48}\omega^{7/2}\right).
\end{aligned}
\tag{39}
$$

BIBLIOGRAPHY

[1] C. Park and T. Nosoko, "Three-dimensional wave dynamics on a falling film and associated mass transfer," *AIChE Journal*, vol. 49, no. 11, pp. 2715–2727, 2003.

[2] D. Prieling, H. Steiner, W. Meile, and G. Brenn, "High-speed camera recordings of wavy liquid films on spinning disks," tech. rep., Institute of Fluid Mechanics and Heat Transfer, Graz University of Technology, 2010.

[3] H.-C. Chang and E. Demekhin, *Complex wave dynamics on thin films*. Elsevier Science, 2002.

[4] S. Kalliadasis, C. Ruyer-Quil, B. Scheid, and M. Velarde, *Falling liquid films*. Springer Verlag, 2011.

[5] A. Oron, S. Davis, and S. Bankoff, "Long-scale evolution of thin liquid films," *Reviews of Modern Physics*, vol. 69, no. 3, pp. 931–980, 1997.

[6] R. Craster and O. Matar, "Dynamics and stability of thin liquid films," *Reviews of Modern Physics*, vol. 81, no. 3, pp. 1131–1198, 2009.

[7] W. Nusselt, "Die Oberflächenkondensation des Wasserdampfes," *Zeitschrift des Vereins Deutsche Ingenieure*, vol. 60, pp. 541–546, 1916.

[8] P. Kapitza and S. Kapitza, "Wave flow of thin fluid layers of liquid," *Soviet Journal of Experimental and Theoretical Physics*, vol. 19, pp. 105–120, 1949.

[9] T. Benjamin, "Wave formation in laminar flow down an inclined plane," *Journal of Fluid Mechanics*, vol. 2, no. 6, pp. 554–573, 1957.

[10] C. Yih, "Stability of liquid flow down an inclined plane," *Physics of Fluids*, vol. 6, no. 3, pp. 321–334, 1963.

[11] A. Binnie, "Experiments on the onset of wave formation on a film of water flowing down a vertical plate," *Journal of Fluid Mechanics*, vol. 2, no. 6, pp. 551–553, 1957.

[12] A. Binnie, "Instability in a slightly inclined water channel," *Journal of Fluid Mechanics*, vol. 5, no. 4, pp. 561–570, 1959.

[13] S. Tailby and S. Portalski, "The hydrodynamics of liquid films flowing on vertical surface," *Transactions of the Institution of Chemical Engineers*, vol. 38, pp. 324–330, 1960.

[14] S. Joo and S. Davis, "Instabilities of three-dimensional viscous falling films," *Journal of Fluid Mechanics*, vol. 242, no. 1, pp. 529–547, 1992.

[15] M. Cheng and H. Chang, "Competition between subharmonic and sideband secondary instabilities on a falling film," *Physics of Fluids*, vol. 7, no. 1, pp. 34–54, 1995.

[16] D. Benney, "Long waves on liquid films," *Journal of Mathematical Physics*, vol. 45, no. 2, pp. 150–155, 1966.

[17] H. Chang, "Travelling waves on fluid interfaces: Normal form analysis of the kuramoto-sivashinsky equation," *Physics of Fluids*, vol. 29, no. 10, pp. 3142–3147, 1986.

[18] T. Yang, "On traveling-wave solutions of the Kuramoto-Sivashinsky equation," *Physica D: Nonlinear Phenomena*, vol. 110, no. 1, pp. 25–42, 1997.

[19] P. Kapitza, "Wave flow of thin viscous fluid layers," *Soviet Journal of Experimental and Theoretical Physics*, vol. 18, no. 1, pp. 3–28, 1948.

[20] V. Shkadov, "Wave modes in the gravity flow of a thin layer of a viscous fluid," *Izv. Akad. Nauk. SSSR, Mekh. Zhid. i Gaza*, vol. 1, pp. 43–51, 1967.

[21] J. Wilkes and R. Nedderman, "The measurement of velocities in thin films of liquid," *Chemical Engineering Science*, vol. 17, no. 3, pp. 177–187, 1962.

[22] S. S. Portalski, "Velocities in film flow of liquids on vertical plates," *Chemical Engineering Science*, vol. 19, no. 8, pp. 575–582, 1964.

[23] A. Bunov, E. Demekhin, and V. Shkadov, "On the non-uniqueness. of non-linear wave solutions in a viscous layer," *Journal of Applied Mathematics and Mechanics*, vol. 48, no. 4, pp. 495–499, 1984.

[24] G. Sisoev and V. Shkadov, "On two-parametric manifold of the waves solutions of equation for falling film of viscous liquid," *Doklady Physics*, vol. 44, no. 7, pp. 454–459, 1999.

[25] G. Sisoev and V. Shkadov, "Dominant waves in a viscous liquid flowing in a thin sheet," *Doklady Physics*, vol. 42, no. 12, pp. 683–686, 1997.

[26] G. Sisoev and V. Shkadov, "Development of dominating waves from small disturbances in falling viscous-liquid films," *Fluid Dynamics*, vol. 32, no. 6, pp. 794–792, 1997.

[27] S. Alekseenko, V. Nakoriakov, B. Pokusaev, and T. Fukano, *Wave flow of liquid films*. Begell House, New York, 1994.

[28] C. Ruyer-Quil and P. Manneville, "Modeling film flows down inclined planes," *The European Physical Journal B-Condensed Matter and Complex Systems*, vol. 6, no. 2, pp. 277–292, 1998.

[29] C. Ruyer-Quil and P. Manneville, "Improved modeling of flows down inclined planes," *The European Physical Journal B-Condensed Matter and Complex Systems*, vol. 15, no. 2, pp. 357–369, 2000.

[30] B. Scheid, C. Ruyer-Quil, and P. Manneville, "Wave patterns in film flows: modelling and three-dimensional waves," *Journal of Fluid Mechanics*, vol. 562, no. 1, pp. 183–222, 2006.

[31] T. Salamon, R. Armstrong, and R. Brown, "Traveling waves on vertical films: Numerical analysis using the finite element method," *Physics of Fluids*, vol. 6, no. 6, pp. 2202–2220, 1994.

[32] N. Malamataris, M. Vlachogiannis, and V. Bontozoglou, "Solitary waves on inclined films: Flow structure and binary interactions," *Physics of Fluids*, vol. 14, no. 3, pp. 1082–1094, 2002.

[33] J. Liu and J. Gollub, "Solitary wave dynamics of film flows," *Physics of Fluids*, vol. 6, no. 5, pp. 1702–1712, 1994.

[34] J. Liu, J. Schneider, and J. Gollub, "Three-dimensional instabilities of film flows," *Physics of Fluids*, vol. 7, no. 1, pp. 55–67, 1995.

[35] S. Alekseenko, V. Antipin, V. Guzanov, S. Kharlamov, and D. Markovich, "Three-dimensional solitary waves on falling liquid film at low Reynolds numbers," *Physics of Fluids*, vol. 17, no. 12, pp. 121704.1–121704.4, 2005.

[36] N. Malamataris and T. Papanastasiou, "Unsteady free surface flows on truncated domains," *Industrial & Engineering Chemistry Research*, vol. 30, no. 9, pp. 2211–2219, 1991.

[37] S. Jayanti and G. Hewitt, "Hydrodynamics and heat transfer of wavy thin film flow," *International Journal of Heat and Mass Transfer*, vol. 40, no. 1, pp. 179–190, 1997.

[38] D. Gao, N. Morley, and V. Dhir, "Numerical simulation of wavy falling film flow using VOF method," *Journal of Computational Physics*, vol. 192, no. 2, pp. 624–642, 2003.

[39] P. Kapitza, *Collected papers by P. L. Kapitza*. New York: Macmillan, 1964.

[40] T. Nosoko, P. Yoshimura, T. Nagata, and K. Oyakawa, "Characteristics of two-dimensional waves on a falling liquid film," *Chemical Engineering Science*, vol. 51, no. 5, pp. 725–732, 1996.

[41] S. Yih, "Modelling heat and mass transport in falling liquid films," in *Handbook of Heat and Mass Transfer*, vol. 2, ch. 5, pp. 111–210, 1986.

[42] C. Kirkbride, "Heat transfer by condensing vapors on. vertical tubes," *Transactions of American Institute of Chemical Engineers*, vol. 30, pp. 170–193, 1934.

[43] K. Chun and R. A. R.A. Seban, "Heat transfer to evaporating liquid films," *Journal of Heat Transfer*, vol. 93, pp. 391–396, 1971.

[44] R. Hirshburg and L. Florschuetz, "Laminar wavy-film flow: Part I, hydrodynamic analysis," *Journal of Heat Transfer*, vol. 104, no. 3, pp. 452–458, 1982.

[45] R. Hirshburg and L. Florschuetz, "Laminar wavy-film flow: Part II, condensation and evaporation," *Journal of Heat Transfer*, vol. 104, no. 3, pp. 459–464, 1982.

[46] A. Miyara, "Numerical analysis on heat transfer enhancement by waves on falling liquid film," *Journal of Thermal Science*, vol. 9, pp. 236–242, 2000.

[47] R. Emmert and R. Pigford, "Interfacial resistance-gas absorption in falling liquid film," *Chemical Engineering Progress*, vol. 50, pp. 87–93, 1954.

[48] E. Ruckenstein and C. Berbente, "Mass transfer in wavy flow," *Chemical Engineering Science*, vol. 20, pp. 795–801, 1965.

[49] F. Wasden and A. Dukler, "A numerical study of mass transfer in free falling wavy films," *A.I.Ch.E. Journal*, vol. 9, no. 36, pp. 1379–1390, 1990.

[50] G. Sisoev, O. Matar, and C. Lawrence, "Absorption of gas into a wavy falling film," *Chemical Engineering Science*, vol. 60, no. 3, pp. 827–838, 2005.

[51] T. Hirose, Y. Mori, and Y. Sato, "Solid-liquid mass transfer in falling liquid films on single spheres," *Journal of Chemical Engineering of Japan*, vol. 7, no. 1, pp. 19–24, 1974.

[52] N. Brauner and D. Moalem-Maron, "Characteristics of inclined thin films, waviness and the associated mass transfer," *International Journal of Heat and Mass Transfer*, vol. 25, no. 1, pp. 99–110, 1982.

[53] J. Rauscher, R. Kelly, and J. Cole, "An asymptotic solution for the laminar flow of a thin film on a rotating disk," *Journal of Applied Mechanics*, vol. 40, no. 1, pp. 43–47, 1973.

[54] H. Espig and R. Hoyle, "Waves in a thin liquid layer on a rotating disk," *Journal of Fluid Mechanics*, vol. 22, no. 4, pp. 671–677, 1965.

[55] J. Aroesty, J. Gross, M. Illickal, and J. Maloney, "Blood oxygenation: A study in bioengineering mass transfer," tech. rep., The Rand Corporation, Santa Monica, California, 1967.

[56] I. Leshev and G. Peev, "Film flow an a horizontal rotating disk," *Chemical Engineering and Processing*, vol. 42, no. 11, pp. 925–929, 2003.

[57] A. Charwat, R. Kelly, and C. Gazley, "The flow and stability of thin liquid films on a rotating disk," *Journal of Fluid Mechanics*, vol. 53, no. 2, pp. 227–255, 1972.

[58] W. Woods, *The hydrodynamics of thin liquid films flowing over a rotating disc*. Dissertation, University of Newcastle upon Tyne, 1995.

[59] B. Ozar, B. Cetegen, and A. Faghri, "Experiments on the flow of a thin liquid film over a horizontal stationary and rotating disk surface," *Experiments in Fluids*, vol. 34, no. 5, pp. 556–565, 2003.

[60] S. Thomas, A. Faghri, and W. Hankey, "Experimental analysis and flow visualization of a thin liquid film on a stationary and rotating disk," *Journal of Fluids Engineering*, vol. 113, pp. 73–80, 1991.

[61] Y. Miyasaka, "On the flow of a viscous free boundary jet on a rotating disk: 1st report theoretical analysis," *Bulletin of JSME*, vol. 17, pp. 1461–1468, 1974.

[62] A. Muzhilko., V. Rifert, and P. Barabash, "Flow of liquid film over the surface of a rotating disk," *Heat Transfer - Soviet Research*, vol. 15, no. 5, pp. 1–6, 1983.

[63] G. Leneweit, K. Roesner, and R. Koehler, "Surface instabilities of thin liquid film flow on a rotating disk," *Experiments in Fluids*, vol. 26, no. 1, pp. 75–85, 1999.

[64] S. Lim, *Hydrodynamics and mass transfer processes associated with the absorption of oxygen in liquid films flowing across a rotating disc*. Dissertation, University of Newcastle Upon Tyne, 1980.

[65] J. Burns, C. Ramshaw, and R. Jachuck, "Measurement of liquid film thickness and the determination of spin-up radius on a rotating disc using an electrical resistance technique," *Chemical Engineering Science*, vol. 58, no. 11, pp. 2245–2253, 2003.

[66] J. Rice, A. Faghri, and B. Cetegen, "Analysis of a free surface film from a controlled liquid impinging jet over a rotating disk including conjugate effects, with and without evaporation," *International Journal of Heat and Mass Transfer*, vol. 48, no. 25, pp. 5192–5204, 2005.

[67] M. Rahman and A. Faghri, "Numerical simulation of fluid flow and heat transfer in a thin liquid film over a rotating disk," *International Journal of Heat and Mass Transfer*, vol. 35, no. 6, pp. 1441–1453, 1992.

[68] K. Kaneko, A. Tamenori, N. Alleborn, and F. Durst, "Numerical and experimental investigation of wet chemical etching of silicon wafers," *ECS Transactions*, vol. 2, no. 6, pp. 295–303, 2007.

[69] D. Needham and J. Merkin, "The development of nonlinear waves on the surface of a horizontally rotating thin liquid film," *Journal of Fluid Mechanics*, vol. 184, pp. 357–379, 1987.

[70] T. Myers and M. Lombe, "The importance of the Coriolis force on axisymmetric horizontal rotating thin film flows," *Chemical Engineering and Processing*, vol. 45, pp. 90–98, 2006.

[71] A. G. Emslie, F. Bonner, and L. Peck, "Flow of a viscous liquid on a rotating disk," *Journal of Applied Physics*, vol. 29, no. 5, pp. 858–862, 1958.

[72] E. Momoniat and D. Mason, "Investigation of the effect of the Coriolis force on a thin fluid film on a rotating disk," *International Journal of Non-Linear Mechanics*, vol. 33, no. 6, pp. 1069–1088, 1998.

[73] L. Dorfman, "Flow and heat transfer on a viscous fluid layer on a rotating disk," *Inzhenerno-Fizicheskii Zhurnal*, vol. 12, pp. 309–316, 1967.

[74] G. Sisoev, O. Matar, and C. Lawrence, "Axisymmetric wave regimes in viscous liquid film flow over a spinning disk," *Journal of Fluid Mechanics*, vol. 495, pp. 385–411, 2003.

[75] T. Kim and M. Kim, "The flow and hydrodynamic stability of a liquid film on a rotating disc," *Fluid Dynamics Research*, vol. 41, no. 3, pp. 35504.1–35504.28, 2009.

[76] G. Sisoev and V. Shkadov, "Flow stability of a film of viscous liquid on the surface of a rotating disk," *Journal of Engineering Physics and Thermophysics*, vol. 52, no. 6, pp. 671–674, 1987.

[77] V. Shkadov, "Some methods and problems of the theory of hydrodynamic stability," in *Scientific Proceedings Institute of Mechanics of Lomonosov, Moscow*, 1973.

[78] G. Sisoev, O. Matar, and C. Lawrence, "Modelling of film flow over a spinning disk," *Journal of Chemical Technology and Biotechnology*, vol. 78, no. 2, pp. 151–155, 2003.

[79] O. Matar, G. Sisoev, and C. Lawrence, "Evolution scales for wave regimes in liquid film flow over a spinning disk," *Physics of Fluids*, vol. 16, no. 5, pp. 1532–1545, 2004.

[80] B. Ozar, B. Cetegen, and A. Faghri, "Experiments on heat transfer in a thin liquid film flowing over a rotating disk," *Journal of Heat Transfer*, vol. 126, no. 2, pp. 184–192, 2004.

[81] A. Aoune and C. Ramshaw, "Process intensification: heat and mass transfer characteristics of liquid films on rotating discs," *International Journal of Heat and Mass Transfer*, vol. 42, no. 14, pp. 2543–2556, 1999.

[82] F. Staudegger, *Advanced Process Control für Halbleiterätzmaschinen*. Dissertation, Graz University of Technology, 2008.

[83] J. Burns and R. Jachuck, "Determination of liquid–solid mass transfer coefficients for a spinning disc reactor using a limiting current technique," *International Journal of Heat and Mass Transfer*, vol. 48, no. 12, pp. 2540–2547, 2005.

[84] G. Peev, A. Nikolova, and D. Peshev, "Solid dissolution in a thin liquid film on a horizontal rotating disk," *Heat and Mass Transfer*, vol. 43, no. 4, pp. 397–403, 2007.

[85] F. Staudegger, M. Hofbaur, and H.-J. Kruwinus, "Analyses and modeling of a wet-chemical-etch process on rotating silicon wafers with an impinging etchant jet," *Journal of the Electrochemical Society*, vol. 156, no. 5, pp. 340–345, 2009.

[86] R. Higbie, "The rate of absorption of pure gas into a still liquid during short periods of exposure," *Transactions of American Institute of Chemical Engineers*, vol. 35, pp. 365–373, 1935.

[87] S. Basu and B. Cetegen, "Analysis of hydrodynamics and heat transfer in a thin liquid film flowing over a rotating disk by the integral method," *Journal of Heat Transfer*, vol. 128, no. 3, pp. 217–225, 2006.

[88] R. Bird, W. Stewart, and E. Lightfoot, *Transport Phenomena*. New York: John & Sons, 1960.

[89] M. Rahman and A. Faghri, "Gas absorption and solid dissolution in a thin liquid film on a rotating disk," *International Journal of Heat and Mass Transfer*, vol. 36, no. 1, pp. 189–199, 1993.

[90] G. Sisoev, O. Matar, and C. Lawrence, "Gas absorption into a wavy film flowing over a spinning disc," *Chemical Engineering Science*, vol. 60, no. 7, pp. 2051–2060, 2005.

[91] O. Matar, C. Lawrence, and G. Sisoev, "The flow of thin liquid films over spinning disks: Hydrodynamics and mass transfer," *Physics of Fluids*, vol. 17, no. 5, pp. 052102.1–052102.20, 2005.

[92] F. Batchelor, *An Introduction to Fluid Dynamics*. Cambridge University Press, 1967.

[93] J. Spurk and N. Aksel, *Strömungslehre: Einführung in die Theorie der Strömungen*. Springer Verlag, 2010.

[94] H. Kuhlmann, *Strömungsmechanik*. Pearson Studium, 2007.

[95] J. Pedlosky, *Geophysical Fluid Dynamics*. Springer, 1st ed., 1979.

[96] H. Baehr and K. Stephan, *Wärme- und Stoffübertragung*. Springer Verlag, 2006.

[97] C. Wagner, "Heat transfer from a rotating disk to ambient air," *Journal of Applied Physics*, vol. 19, pp. 837–839, 1948.

[98] D. Monk, D. Soane, and R. Howe, "A review of the chemical reaction mechanism and kinetics for hydrofluoric acid etching of silicon dioxide for surface micromachining applications," *Thin Solid Films*, vol. 232, no. 1, pp. 1–12, 1993.

[99] R. Noulty and D. Leaist, "Diffusion of aqueous hydrofluoric acid and aqueous potassium fluoride," *Electrochimica Acta*, vol. 30, no. 8, pp. 1095–1099, 1985.

[100] B. Schwartz and H. Robbins, "Chemical etching of silicon. A temperature study in the acid system," *Journal of the Electrochemical Society*, vol. 108, no. 4, pp. 365–372, 1961.

[101] ANSYS, Inc., *ANSYS FLUENT 12.0 Theory Guide*, 2009.

[102] ANSYS, Inc., *ANSYS FLUENT 12.0 User's Guide*, 2009.

[103] C. Hirt and B. Nichols, "Volume of fluid VOF method for the dynamics of free boundaries," *Journal of Computational Physics*, vol. 39, pp. 201–225, 1981.

[104] S. Muzaferija, M. Peric, P. Sames, and T. Schellin, "A two-fluid Navier-Stokes solver to simulate water entry," *22nd Symposium on Naval Hydrodynamics, Washington*, 1998.

[105] J. Brackbill, D. Kothe, and C. Zemach, "A continuum method for modeling surface tension," *Journal of Computational Physics*, vol. 100, no. 2, pp. 335–354, 1992.

[106] E. Toro, *Riemann solvers and numerical methods for fluid dynamics: a practical introduction*. Springer, 2009.

[107] R. LeVeque, *Numerical Methods for Conservation Laws*. Birkhäuser Verlag, 1992.

[108] R. LeVeque, *Finite volume methods for hyperbolic problems*. Cambridge University Press, 2002.

[109] P. Roe, "Approximate Riemann solvers, parameter vectors, and difference schemes," *Journal of Computational Physics*, vol. 43, no. 2, pp. 357–372, 1981.

[110] R. LeVeque, M. Berger, *et al.*, "Clawpack software v4.6.1," *www.clawpack.org*, 2012.

[111] P. Adomeit and U. Renz, "Hydrodynamics of three-dimensional waves in laminar falling films," *International Journal of Multiphase Flow*, vol. 26, no. 7, pp. 1183–1208, 2000.

[112] P. Trevelyan, B. Scheid, C. Ruyer-Quil, and S. Kalliadasis, "Heated falling films," *Journal of Fluid Mechanics*, vol. 592, pp. 295–334, 2007.